The

Role of Wing Morphology

in the

Aerodynamics of Insect Flight

by

Robert R. Harbig

A thesis submitted to Monash University

for the degree of

Doctor of Philosophy

February 2014

Department of Mechanical and Aerospace Engineering

Monash Universty

Copyright Notices

Notice 1

Notice 2

Statement of Originality

This thesis contains no material that has been accepted for the award of a degree or diploma in this or any other university. To the best of the candidate's knowledge and belief, this thesis contains no material previously published or written by another person except where due reference is made in the text of this thesis.

_____

Candidate: Robert Harbig

February 2014

Think before you swat.

Michael Dickinson, 2013.

Abstract

Recent interest in developing micro air vehicles (MAVs) for a variety of both civil and military uses has driven significant research into the aerodynamics of natural flyers, such as insects, birds and bats. Insects, in particular, exhibit desirable flight characteristics that MAV designers wish to incorporate into their designs, however our understanding of how these animals fly is still limited. Research into insect flight has shown that they employ a number of unsteady mechanisms, the most prevalent of these being the formation of a leading-edge vortex (LEV) which provides the wing with enhanced lift. While this research has greatly improved our understanding of insect flight, the effect of the wing's shape on these unsteady mechanisms is not well understood. This thesis describes an investigation into the effect of two wing morphological parameters, aspect ratio and camber, on the flow structures around flapping and rotating wings in an insect-like flight regime.

The effect of wing aspect ratio is first explored at different Reynolds numbers using a numerical model of an altered fruit fly wing revolving at a constant angular velocity. Increasing the Reynolds number for an aspect ratio of 2.91 resulted in the development of a dual LEV structure, however increasing aspect ratio at a fixed Reynolds number generated the same flow structures. This result shows that the effects of Reynolds number and aspect ratio are linked. An alternate flow scaling method, using the wing span as the characteristic length, is presented to decouple the effects of Reynolds number from those of aspect ratio. This resulted in a span-based Reynolds number, which can be used to independently describe the development of the LEV. Indeed, universal behaviour was found for various parameters using this scaling. The effect of aspect ratio on the vortex structures was then assessed at different span-based Reynolds numbers and it was found the wing aspect ratio had the effect of shortening the wing's chord length relative to a fixed LEV size. Scaling the flow using the wing span was found to apply for revolving wings at large angles of attack, such that the flow separates from the leading-edge and a strong spanwise velocity is generated on the leeward side of the wing. These conditions are typical of those seen in nature, and hence this scaling could be applied to similar investigations involving insects and birds as well as nature-mimicking MAVs.

The effect of wing aspect ratio was then explored at different advance ratios using a numerical model that mimicked a flapping insect wing. It was demonstrated that

increasing the advance ratio enhances vorticity production at the leading-edge during the downstroke, and this results in more rapid growth of the LEV for non-zero advance ratios. This effect, combined with that of aspect ratio, determines whether the LEV remains stably attached to the wing or if it is shed. For high advance ratios and large aspect ratios the LEV was observed to quickly grow to envelop the entire wing during the early stages of the downstroke. Continued rotation of the wing resulted in the LEV being eventually shed as part of a vortex loop that peels away from the wing's tip. It is shown that the shedding of the LEV for high aspect ratio wings at non-zero advance ratios leads to reduced aerodynamic performance of these wings. This helps to explain why a number of insect species have evolved to have low aspect ratio wings, as they outperform high aspect ratios across a wide range of flight speeds.

Finally, wing deformation is observed during the flight of some insect species, which results in the wing becoming cambered throughout each half stroke. In this study, the effect of wing camber on the flow structures and aerodynamic forces for insect-like wings is investigated using the rotating-wing numerical model. Both positive and negative camber was investigated at Reynolds numbers of 120 and 1500, along with the chordwise location of maximum camber. It was found that negatively cambered wings produce similar LEV structures to non-cambered wings at both Reynolds numbers, but high positive camber resulted in the formation of multiple streamwise vortices at the higher Reynolds number, which disrupt the development of the main LEV. Despite this, positively cambered wings were found to produce higher lift on drag ratios than flat or negatively cambered wings. It was determined that a region of low pressure near the wing's leading edge, combined with the curvature of the wing's upper surface in this region, resulted in a vertical tilting of the net force vector for positively cambered wings, which explains how insects can benefit from wing camber.

Acknowledgments

First and foremost, I would like to thank my supervisors, Prof. Mark Thompson and Prof. John Sheridan, for their help and guidance throughout the project. I would also like to thank Prof. Don Rockwell and Dr. Cem A. Ozen from Lehigh University whose extensive knowledge of the subject helped guide the project, particularly in its early formulation.

I would like to acknowledge the Department of Mechanical and Aerospace Engineering, Monash University, for providing the office space and resources necessary to complete this study. I am grateful for the financial backing of the Australian Government provided through an Australian Postgraduate Award scholarship. This research was undertaken with the assistance of resources provided at the NCI National Facility systems at the Australian National University through the National Computational Merit Allocation Scheme supported by the Australian Government.

I would also like to thank my fellow PhD students at Monash and Lehigh Universities, both past and present, for their insightful discussions on fluid mechanics. Finally, I would like to thank my wife, Annika, for proof reading all my work and putting up with me talking endlessly about flapping wings and leading-edge vortices.

Publications Relating to Thesis

HARBIG, R.R., SHERIDAN, J. & THOMPSON, M.C. 2012 Observations of flow structure changes with aspect ratio for rotating insect wing planforms. *In proceedings of the 42nd AIAA Aerospace Sciences Meeting and Exhibit*, New Orleans, LA, USA, June 2012.

HARBIG, R.R., SHERIDAN, J. & THOMPSON, M.C. 2013 Reynolds number and aspect ratio effects on the leading-edge vortex for rotating insect wing planforms. *Journal of Fluid Mechanics* **717**, 166–192.

HARBIG, R.R., SHERIDAN, J. & THOMPSON, M.C. 2013 Relationship between aerodynamic forces, flow structures and wing camber for rotating insect wing planforms. *Journal of Fluid Mechanics* **730**, 52–75.

HARBIG, R.R., SHERIDAN, J. & THOMPSON, M.C. 2014 The role of advance ratio and aspect ratio in determining leading-edge vortex stability for flapping flight. *Journal of Fluid Mechanics*, in press.

Nomenclature

A list of the abbreviations and symbols used throughout the thesis is included here in the following order; mathematical symbols, Greek alphabet nomenclature and English alphabet nomenclature.

Symbol	Description
$\S$	Thesis section
$\int$	Integration
$\sum$	Summation
∇	Vector gradient operator (grad)
∇^*	Dimensionless vector gradient operator (grad)
∇^2	Del squared (or div grad) operator
$\wedge$	Exterior product
$\frac{\mathrm{d}}{\mathrm{d}t}$	Temporal differential
$\frac{\partial}{\partial t}$	Partial temporal differential
$\lvert \ \rvert$	Magnitude
$(\ )^T$	Transpose
$(\ )_n$	Solution value at current time step
$(\ )_{n-1}$	Solution value at previous time step
$(\ )_{n-2}$	Solution value at two time steps back
α	Geometric angle of attack
α_i	Angle of incidence
α_0	Geometric angle of attack at mid-downstroke
β	Stroke plane angle,
	Blend factor scheme variable,

Continued on the next page.

Symbol	Description
	Iterative order of convergence variable
Γ_z	Spanwise component of circulation
γ_1	Vortex axis identification scalar field
γ_2	Vortex core identification scalar field
$\Delta \boldsymbol{r}$	Vector from the upwind node to integration point
Δt	Time step
ϵ	Relative error
ϵ_{12}	Relative error between finest two grids
ϵ_{23}	Relative error between coarsest two grids
θ	Stroke deviation angle
θ_M	Angle between velocity vector and radius vector
λ_2	Second eigenvalue of the symmetric part of the velocity gradient tensor
μ	Fluid viscosity
ν	Fluid's kinematic viscosity
ξ	Flight velocity angle
ρ	Fluid density,
	Previous iterate for order of convergence
$\boldsymbol{\tau}$	Stress tensor
Φ	Peak to peak amplitude of wing flap
ϕ	Stroke position angle,
	Rotation angle
χ	Body angle
ψ	A solution variable
ψ_{ip}	Solution variable at integration point
ψ_{up}	Solution variable at upwind node
Ω	Rotational velocity constant
$\boldsymbol{\Omega}$	Rotational velocity vector
$\boldsymbol{\Omega}^*$	Dimensionless rotational velocity vector
Ω_θ	Solid body rotational velocity of the vortex

Symbol	Description
Ω_y	Rotational velocity about y-axis
$\dot{\Omega}$	Time-averaged angular acceleration amplitude
$\dot{\boldsymbol{\Omega}}$	Angular acceleration vector
$\dot{\boldsymbol{\Omega}}^*$	Dimensionless angular acceleration vector
ω	Relaxation factor
$\boldsymbol{\omega}$	Vorticity vector
ω_x	Streamwise component of vorticity
ω_z	Spanwise component of vorticity
AR	Single wing aspect ratio
a	Vortex core radius
$\boldsymbol{a}$	Acceleration vector of a boundary
C_D	Drag coefficient
C_{Di}	Instantaneous drag coefficient
C_F	Net force coefficient
C_L	Lift coefficient
C_{Li}	Instantaneous lift coefficient
C_P	Pressure coefficient
CFD	Computational fluid dynamics
c	Local chord length
$\bar{c}$	Wing's mean chord length
D	Aerodynamic drag force
DNS	Direct numerical simulation
DPIV	Digital particle image velocimetry
F	Net aerodynamic force
F_s	Safety factor
f_1	Solution value on the fine grid
f_2	Solution value on the intermediate grid
f_3	Solution value on the coarse grid
GCI	Grid convergence index

Symbol	Description
GCI_{coarse}	Grid convergence index for the coarse grid
GCI_{fine}	Grid convergence index for the fine grid
GCI_{12}	Grid convergence index for the finest two grids
GCI_{23}	Grid convergence index for the coarsest two grids
GGI	General grid interface
HSV	Horseshoe-shaped vortex
$\boldsymbol{I}$	Identity matrix
J	Advance ratio
L	Aerodynamic lift force
LEV	Leading-edge vortex
LEV_D	Leading-edge vortex formed during the downstroke
LEV_U	Leading-edge vortex formed during the upstroke
LEV 1	Upstream co-rotating vortex in dual LEV structure
LEV 2	Downstream co-rotating vortex in dual LEV structure
l	Radial distance from the vortex axis
M	Grid point
MAV	Micro air vehicle
m	Magnitude of wing camber
N	Number of grid points
N_1	Number of mesh elements for the finer grid
N_2	Number of mesh elements for the coarser grid
n	Flapping frequency
$\boldsymbol{n}$	Wall unit normal vector
P	Central grid point
PIV	Particle image velocimetry
p	Pressure,
	Chordwise position of maximum camber,
	Order of convergence
p^*	Dimensionless pressure

Symbol	Description
p_0	Ambient pressure
Q	Second invariant of the velocity gradient tensor
R	Wing span
Re	Chord-based Reynolds number
Re_R	Span-based Reynolds number
Ro	Rossby number
$\boldsymbol{\mathcal{R}_{PM}}$	Radius vector from P to M
RSV	Rotational starting vortex
r	Spanwise location,
	Grid refinement ratio
$\boldsymbol{r}$	Location vector
$\boldsymbol{r}^*$	Dimensionless location vector
r_g	Radius of gyration
r_{12}	Refinement ratio between finest two grids
r_{23}	Refinement ratio between coarsest two grids
S	Wing area
s	Distance along wing boundary
SV	Secondary counter-rotating vortex in dual LEV structure
T	Total simulation time,
	Flapping cycle period
TEV	Trailing-edge vortex
TEV_D	Trailing-edge vortex formed during the downstroke
TEV_U	Trailing-edge vortex formed during the upstroke
TV	Tip vortex
TV_D	Tip vortex formed during the downstroke
TV_U	Tip vortex formed during the upstroke
t	Time
t^*	Dimensionless time,
	Fraction of cycle period starting at ventral reversal

Continued from previous page.

Symbol	Description
t_r	Half the stroke reversal time,
	Half the flip duration
t'_1	Dimensionless stroke reversal time for ventral reversal
t'_2	Dimensionless stroke reversal time for dorsal reversal
U	Reference velocity
U_θ	Vortex azimuthal velocity
$U_{\theta max}$	Maximum azimuthal velocity
U_a	Vortex axial velocity
U_i	Instantaneous relative velocity
$\boldsymbol{U_M}$	Velocity vector at M
$\boldsymbol{U_P}$	Local advection velocity vector around P
U_{rg}	Velocity at the wing's radius of gyration
$\bar{U}_{rg}$	Cycle averaged flapping velocity at the wing's radius of gyration
U_{tip}	Velocity at the wing's tip
$\bar{U}_{tip}$	Cycle averaged flapping velocity at the wing's tip
$\boldsymbol{u}$	Velocity vector viewed in the rotating frame
$\boldsymbol{u}^*$	Dimensionless velocity vector viewed in the rotating frame
$\boldsymbol{u_{abs}}$	Velocity vector viewed in the absolute (stationary) frame
u_n	Velocity component normal to boundary
V	Flight speed,
	Integration volume
w	Spanwise velocity component
x'	Abscissa of a point on the chord line
x_c	Distance from the leading-edge to a point on the chord line
y_c	Mean camber line
$\boldsymbol{z}$	Unit normal vector

Contents

Introduction

In recent years, there has been significant interest in developing micro air vehicles (MAVs) for a variety of both civil and military uses, as they have the potential to revolutionise our surveying and information gathering capabilities. MAVs are classified as aircraft with a maximum dimension of less than 15cm (Pines & Bohorquez 2006; Stanford *et al.* 2008). Many types of MAVs have already been proposed including fixed wing, rotary wing and flapping wing designs (for examples see Mueller & DeLaurier 2003; Jones *et al.* 2004; Pines & Bohorquez 2006). Many early MAV designs were of the fixed wing type, as these designs were adapted from conventional fixed wing aircraft. However, fixed wing MAVs suffer from laminar boundary-layer separation, roll instabilities and sensitivity to wind gusts (Mueller & DeLaurier 2003; Stanford *et al.* 2008). These issues create problems with lift generation and flight control, particularly as their size is reduced.

Natural flyers, such as insects, birds and bats, exhibit incredible aerodynamic manoeuvrability, efficiency and insensitivity to wind gusts. MAV designers wish to incorporate these desirable flight characteristics into their designs, and consequently significant research has been devoted to investigating rotating and flapping wing designs, as these concepts take significant inspiration from nature. Despite some progress, the performance of these MAVs is still inferior to that of natural flyers (Pines & Bohorquez 2006). To bridge this gap in flight performance, further advances in our understanding of the aerodynamics of flapping and rotating wings is required. MAVs are expected to operate in urban environments and therefore require the ability to fly through buildings and tunnels, as well as to perch or hover for long periods of time (Pines & Bohorquez 2006). Due to the obvious links between flapping wing MAVs and natural flyers, much work has directly focused on the study of insect and bird species in an attempt to understand how these animals fly. Insects are of particular interest because of their ability to hover and manoeuvre in tight spaces.

1

The flight regime of insects is unique for a number of reasons. Firstly, insects operate at Reynolds numbers between 10 and 10^4 (Shyy *et al.* 2010), which are much lower than Reynolds numbers typical of conventional aircraft and also lower than the Reynolds number of most birds. Additionally, because of the wing's flapping motion the flow around them is highly unsteady. Insect wings are also thin and function at very high angles of attack that are well in excess of typical stall angles associated with conventional aircraft wings, however they are still able to generate large amounts of lift. As such, insects operate in an alternate flight regime and exploit different mechanisms to achieve the lift coefficients required for flight. Research into insect flight has shown that they employ a number of unsteady mechanisms. These are the clap and fling mechanism (Weis-Fogh 1973), delayed stall mechanism (Ellington *et al.* 1996), rapid pitch rotation (Dickinson *et al.* 1999) and wake capture (Dickinson *et al.* 1999).

The most prevalent of these is the delayed stall mechanism, which it is associated with the formation of a leading-edge vortex (LEV). This LEV is a common occurrence in the insect world, and it has been identified for many species of insect (e.g. Ellington *et al.* 1996; Srygley & Thomas 2002; Liu & Aono 2009). The LEV forms at the beginning of each half cycle and remains attached to the wing throughout the wing's rotation. The LEV provides the wing with additional circulation and enhanced lift. Consequently, the ability of the LEV to remain attached to the wing is a key characteristic that is required in order to maintain high lift throughout the wing's stroke. However, the mechanism that provides this stability for the LEV is still debated (Ellington *et al.* 1996; Birch & Dickinson 2001; Lentink & Dickinson 2009b; Jones & Babinsky 2010). The lift generated by the LEV is analogous to the vortex lift produced by the LEVs that form over delta wing aircraft (Polhamus 1971; Sane 2003) and to a large extent explains how insects are able to produce the lift coefficients that are required for flight.

While recent research has greatly improved our understanding of insect flight, the effect of the wing's geometry on the aerodynamic performance of these insects is still not understood. Due to the vastly different flow regime of insect flight compared to normal aircraft, conventional reasoning on the effect of wing morphological parameters does not apply to insect flight (Usherwood & Ellington 2002a). One critical wing design parameter for large aircraft is wing aspect ratio (AR), where large aspect ratios are considered to be more efficient (McCormick 1995). Different insect species employ a variety of wing aspect ratios (e.g. Ellington 1984b; Shyy *et al.* 2010) and many insects

have evolved to have relatively low aspect ratio wings compared to most conventional aircraft, however the reason for this is unknown. Indeed, it is still unclear whether aspect ratio is a significant design parameter for optimal aerodynamic performance in insect/MAV flight.

Additionally, wing deformation is observed during the flight of some insect species (e.g. Weis-Fogh 1973; Wootton 1981; Ellington 1984c), which is a result of the wing's passive response to inertial and aerodynamic forces. These deformations result in wing shapes that exhibit significant twist, camber and spanwise bending. Most investigations into flapping and rotating wings have been performed under the assumption that the wing is rigid and flat, and consequently, the effect of these wing deformations is still unclear. Research into wing camber has shown that it has the potential to improve the wing's aerodynamic performance (e.g. Tsuzuki *et al.* 2007; Du & Sun 2008; Young *et al.* 2009), however the effect of camber on the LEV has not been investigated and therefore an explanation of how camber works in insect flight regimes is lacking. Therefore, a study into the effect of different wing morphological parameters on the flow structures and aerodynamic performance of flapping and rotating wings is required.

This thesis outlines a study into the effect of two wing shape parameters, wing aspect ratio and wing camber, in insect-like flight regimes. A numerical model is used to investigate the flow structures generated by flapping and rotating wings with different aspect ratios and camber, along with the aerodynamic forces they produce. The results of this work provide insight into the evolution of insect and bird flight as well as to provide foundations from which future flapping and rotating wing MAVs can be designed.

Chapter 1

Aerodynamics of Insect Flight

In this chapter, a review of the relevant literature on the aerodynamics of flapping and rotating wings under insect-like flight regimes will be presented. Such flows can be classified as for wings rotating about their root at a large angle of attack such that flow separation occurs at the leading-edge.

The equations that govern the flow around flapping and rotating wings are first presented. The types of wing kinematics that insects employ, as well as the variation in aerodynamic forces throughout the wing's stroke are then detailed. This provides the foundation from which the flow mechanisms that insects exploit are discussed. Next, a review of the literature that has investigated the effect of the wing's shape on these mechanisms is presented. Finally, a summary of this literature review is given, in which the specific aims of this study are highlighted.

1.1 Governing Equations and Scaling Laws

The flow around a flapping or rotating wing is governed by the incompressible Navier-Stokes equations cast in a non-inertial rotating frame of reference,

$$\rho \frac{\mathrm{D}\boldsymbol{u}}{\mathrm{D}t} + \rho \dot{\boldsymbol{\Omega}} \times \boldsymbol{r} + \rho \boldsymbol{\Omega} \times (\boldsymbol{\Omega} \times \boldsymbol{r}) + \rho 2\boldsymbol{\Omega} \times \boldsymbol{u} = -\boldsymbol{\nabla} p + \mu \boldsymbol{\nabla}^2 \boldsymbol{u} \qquad (1.1)$$

and

$$\boldsymbol{\nabla}{\cdot}\boldsymbol{u} = 0, \qquad (1.2)$$

where ρ is the fluid density, $\boldsymbol{u}$ is the velocity vector in the rotating frame, p is the pressure, μ is the fluid viscosity, $\boldsymbol{\Omega}$ is the rotational velocity vector, $\dot{\boldsymbol{\Omega}}$ is the angular acceleration vector and $\boldsymbol{r}$ is the location vector. Equation 1.1 is the momentum equation, where $\frac{\mathrm{D}\boldsymbol{u}}{\mathrm{D}t} = \frac{\partial \boldsymbol{u}}{\partial t} + \boldsymbol{u} \cdot \boldsymbol{\nabla}\boldsymbol{u}$ is the material derivative. The next three terms are the angular, centrifugal and Coriolis acceleration terms respectively, which are due to

the rotating frame. $\boldsymbol{\nabla} p$ is the pressure gradient term and $\mu \boldsymbol{\nabla}^2 \boldsymbol{u}$ is the diffusion term. Equation 1.2 is the continuity constraint, which follows from the incompressibility of the fluid.

Lentink & Dickinson (2009a) provide a framework with which to scale these governing equations for flapping and rotating wings. The following parameters were selected to scale the terms in the Navier-Stokes equations;

$$\boldsymbol{u}^* = \frac{\boldsymbol{u}}{U}, \quad t^* = \frac{Ut}{\bar{c}}, \quad \boldsymbol{\nabla}^* = \bar{c} \cdot \boldsymbol{\nabla}, \quad \dot{\boldsymbol{\Omega}}^* = \frac{\dot{\boldsymbol{\Omega}}}{\dot{\Omega}}, \qquad (1.3a, b, c, d)$$

$$\boldsymbol{\Omega}^* = \frac{\boldsymbol{\Omega}}{\Omega}, \quad \boldsymbol{r}^* = \frac{\boldsymbol{r}}{R}, \quad p^* = \frac{p}{p_0}, \qquad (1.3e, f, g)$$

where U is the reference velocity, $\bar{c}$ is the wing's mean chord length, R is the wing's span, p_0 is the ambient pressure, Ω is the time-averaged rotational velocity and $\dot{\Omega}$ is the time-averaged angular acceleration amplitude. Substituting equations 1.3 into equations 1.1 and 1.2 and normalising by $\rho U^2 / \bar{c}$ results in the following dimensionless equations;

$$\frac{\mathrm{D}\boldsymbol{u}}{\mathrm{D}t} + \frac{\dot{\Omega}R\bar{c}}{U^2}\dot{\boldsymbol{\Omega}} \times \boldsymbol{r} + \frac{\Omega^2 R\bar{c}}{U^2}\boldsymbol{\Omega} \times (\boldsymbol{\Omega} \times \boldsymbol{r}) + \frac{\Omega^2 R\bar{c}}{U^2}2\boldsymbol{\Omega} \times \boldsymbol{u} = -\frac{p_0}{\rho U^2}\boldsymbol{\nabla}p + \frac{\mu}{\rho U\bar{c}}\boldsymbol{\nabla}^2\boldsymbol{u} \quad (1.4)$$

and

$$\boldsymbol{\nabla} \cdot \boldsymbol{u} = 0, \qquad (1.5)$$

where * is omitted for clarity. Equation 1.4 shows that the centrifugal and Coriolis accelerations scale with $1/Ro$, where $Ro = U^2/\Omega^2 R\bar{c}$ is the Rossby number. The Rossby number is the ratio of inertial to Coriolis forces and is a measure of the rotation of a system compared to its translation. The angular acceleration term scales with $\frac{\dot{\Omega}R\bar{c}}{U^2}$ which Lentink & Dickinson call the inverse of the acceleration number, which is a measure of the unsteadiness of the flow induced by rotational acceleration. Lentink & Dickinson show that this term depends on the stroke amplitude of the wing and is therefore defined by the wing's kinematics. The diffusion term scales with the inverse of the Reynolds number,

$$Re = \frac{\rho U\bar{c}}{\mu}, \qquad (1.6)$$

which is the ratio of inertial and viscous forces in the fluid. For insect flight, the wing's mean chord length is typically used as the characteristic length for the calculation of Reynolds number. The velocity at the wing's radius of gyration (U_{rg}) is often used as the reference velocity, although the velocity at the wing tip is also sometimes used. The
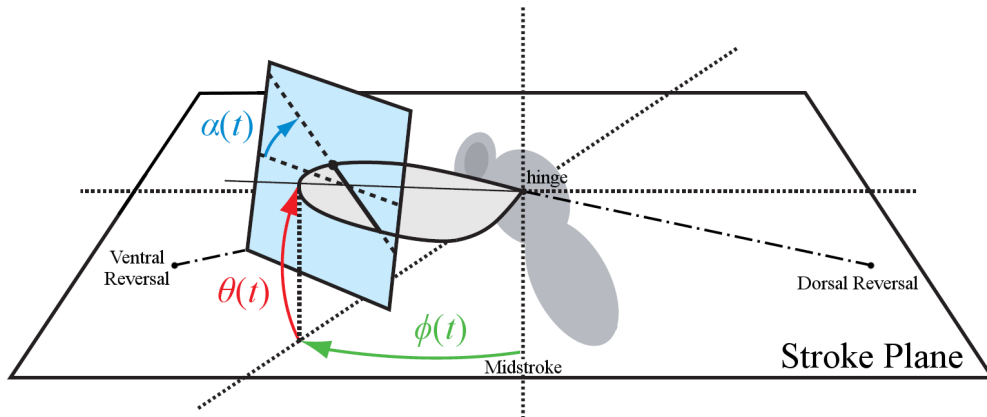
FIGURE 1.1: Schematic of kinematic angles used to define the wing's position with respect to the stroke plane (adapted from Fry *et al.* 2005). $\phi(t)$ is the stroke position, $\theta(t)$ is the stroke deviation and $\alpha(t)$ is the angle of attack. The white plane is the stroke plane while the blue plane is a plane that is perpendicular to the base-to-tip line of the wing and cuts through the wing along the wing's chord, shown here as a line with a filled circle denoting the leading-edge.

radius of gyration (r_g) is also referred to as the radius of the second moment of wing area, and is therefore a measure of the wing's shape (Ellington 1984b). It is calculated by

$$r_g^2 = \frac{1}{S} \int_0^R c(\boldsymbol{r})\boldsymbol{r}^2 d\boldsymbol{r}, \tag{1.7}$$

where S is the wing area.

1.2 Stroke Kinematics and Aerodynamic Forces

An insect flaps its wings by rotating them about a hinge which connects the wing to the insect's body. The position of the wing can therefore be described at each instant in time by the time variation of three Euler angles which are defined with respect to the stroke plane (see figure 1.1). The stroke position $(\phi(t))$ is the angular position of the wing in the stroke plane, measured from the mid-point of a wing stroke, and the stroke deviation $(\theta(t))$ is the angle that the base-to-tip line on the wing makes with the stroke plane. The instantaneous angle of attack $(\alpha(t))$ defined here is a geometric angle and is the angle that the wing chord makes with the stroke plane in the direction of the wing's motion. The wing's true angle of attack depends on the wing's kinematics, the insect's flight velocity and the downwash velocity.

To define the position of the wing with respect to the insect's body a coordinate
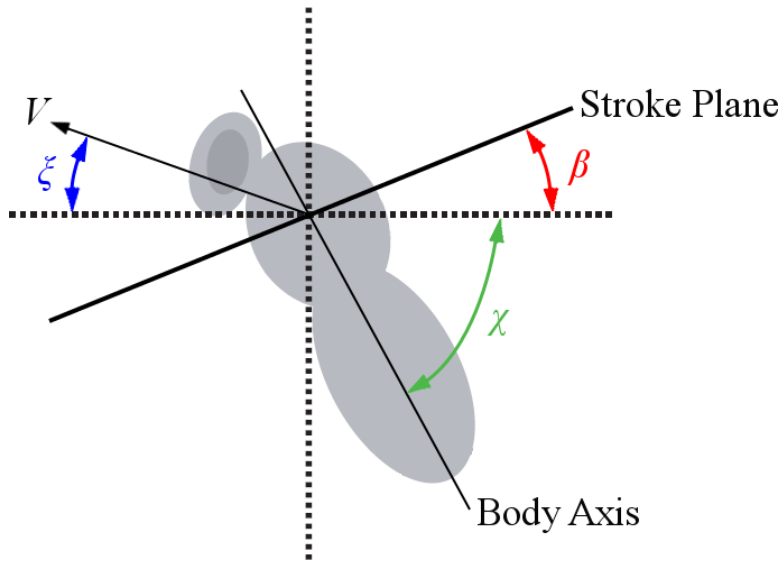
FIGURE 1.2: Schematic of stroke plane angle (β), body angle (χ) and angle of the flight velocity vector (ξ) (adapted from Ellington 1984c; Fry *et al.* 2005).

system fixed to the body is used (see figure 1.2). The stroke plane angle (β) is then defined as the angle that the stroke plane makes with the horizontal axis and the body angle (χ) is the angle between the longitudinal body axis and the horizontal. The flight velocity angle (ξ) can also be defined as the angle between the mean flight velocity and the horizontal axis.

An example of how these kinematic angles vary throughout the course of a flapping cycle for a real insect is shown in figure 1.3a. This data was measured by Fry *et al.* (2005) during the hovering flight of the fruit fly *Drosophila Melanogaster* by filming free flying insects using three orthogonally aligned high-speed cameras. Figure 1.3a shows that the wing's motion is complex. Each flapping cycle consists of two half cycles; an upstroke and a downstroke, and two stroke reversals. The upstroke is from ventral reversal to dorsal reversal, while the downstroke is from dorsal reversal to ventral reversal. During hovering, a fruit fly flaps its wings along an almost horizontal stroke plane ($\beta \approx 0°$) and the wing's position varies according to an approximately sinusoidal function. The peak to peak amplitude of the wing flap (Φ) is 140° with a flapping frequency (n) of 218Hz, but these values vary significantly for other insects. For example, a hoverfly hovers at $\Phi = 66°$ and $n = 141$Hz while a ladybird hovers at $\Phi = 177°$ and $n = 54$Hz (Ellington 1984c). Figure 1.3a also shows that the wing follows a shallow U shaped arc during the up- and downstrokes. At the end of each stroke the wing rotates up through a 90°
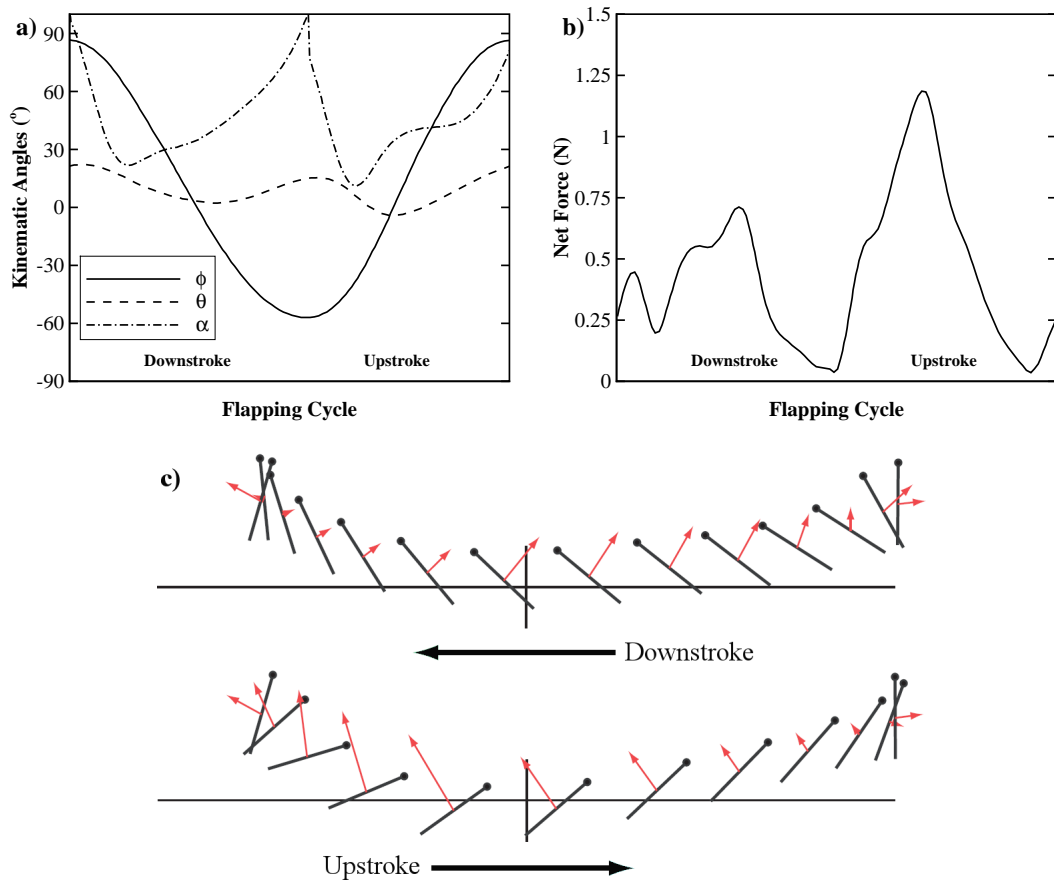
FIGURE 1.3: Kinematics and net aerodynamic force of a hovering fruit fly (adapted from Fry *et al.* 2005). (a) Variation of kinematic angles during a flapping cycle. (b) Change in measured net aerodynamic force throughout a flapping cycle. The net force was measured using a dynamically scaled robotic wing and is therefore larger than what a real fruit fly would produce. (c) Two-dimensional representation of the wing tip path during a flapping cycle. Wing is shown as a line with a filled circle at one end, which indicates the wing's leading-edge. Red arrows are the net force vectors and the axes indicate the range of stroke position between -90° to 90° horizontally and -10° to 10° vertically.

angle of attack in preparation for the next half cycle. The angle of attack during each stroke is large compared to that for a conventional aircraft wing and is approximately 35° for the fruit fly at midstroke. These large angles of attack are typical for insect flight and generally range between 25° and 45° (Ellington 1984c).

Fry *et al.* (2005) used this information to simulate the flapping cycle, utilising a dynamically scaled mechanical wing to measure the aerodynamic forces. Figure 1.3b shows that the net aerodynamic force varies dramatically throughout the flapping cycle and is highly time dependent. The net force vectors are also plotted in figure 1.3c

throughout the flapping cycle and show that they always act approximately perpendicular to the wing's chord line. Despite the complex variation in the net aerodynamic force with time, the thrust produced by the wing perfectly balances out to zero over the course of a flapping cycle during hovering and the mean lift is sufficient to support the weight of the insect.

1.2.1 Hovering Styles and Simplification of Kinematics

With the diversity of insects seen in nature there is an equally wide variety in hovering kinematics that insects employ. However, Weis-Fogh (1973) undertook an extensive survey of hovering insects, including flies, bees, butterflies, dragonflies and beetles, and noticed that most employ a symmetric back and forth kinematic stroke in a near horizontal plane. This type of hovering style was called "normal hovering" and its basic form is illustrated in figure 1.4a. In this simplified motion the stroke plane is horizontal and the stroke deviation is assumed to be zero throughout the flapping cycle. Additionally, the kinematics for the up- and downstrokes are usually made to be symmetric to further simplify the wing's motion. During each half cycle the wing travels at a constant angle of attack and flips over at stroke reversal in preparation for the next half cycle. It is often assumed that the variation of the stroke position with time follows either a sinusoidal or rounded triangular motion and that the angle of attack varies according to a smoothed trapezoidal function. For this type of motion, the lift that is produced supports the weight of the insect, while the drag from each half cycle cancels out.

A further simplification of a normal hovering stroke is often made in order to remove the effects of stroke reversal. Here the wing is rapidly accelerated from rest and then continues to rotate about its base at a constant angular velocity (figure 1.4c). The angle of attack is kept constant throughout the motion. The impulsive start is comparable to the beginning to middle section of a half cycle of a normal hovering stroke and thus produces comparable flow structures (Poelma *et al.* 2006; Lentink & Dickinson 2009b). The wing is often allowed to rotate beyond its normal flapping kinematic limit as this allows a quasi-steady flow state to develop and be maintained for the majority of the wing's motion (Dickinson *et al.* 1999; Poelma *et al.* 2006; Lentink & Dickinson 2009b).

While normal hovering is the most common form of hovering stroke, a few insects employ an asymmetric hovering stroke along an inclined plane (figure 1.4b). This type of
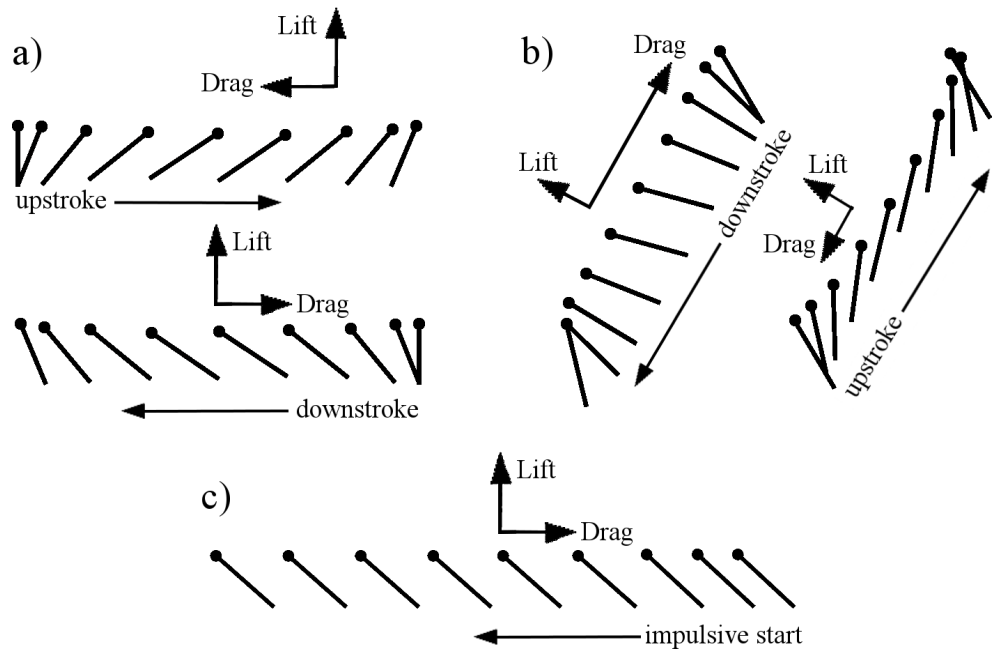
10

FIGURE 1.4: Two-dimensional representation of wing tip path for (a) normal hover, (b) drag based hover and (c) impulsive start kinematics (adapted from Wang 2005; Poelma *et al.* 2006). Circle depicts wing's leading-edge.

kinematic stroke resembles a rowing motion, where the weight supporting force is mainly produced during the downstroke and is primarily drag based (Sun 2004; Wang 2005). Again, the simplification of this stroke assumes that the stroke deviation throughout the cycle is zero. Here the stroke plane angle is large and is close to vertical. During the downstroke, the wing travels at a high angle of attack to produce a large drag force that is sufficient to support the weight of the insect. Throughout the upstroke, the wing is at a low angle of attack in order to minimise the downwards force on the wing. The horizontal component of lift that is produced during the cycle acts to balance out the horizontal component of drag that is produced due to the inclined stroke plane. Two insects that use this type of hovering stroke are dragonflies and hoverflies. Both of these insects are incredibly good at hovering and it has therefore been suggested that this type of hovering stroke may be more efficient than normal hovering (Wang 2005).

1.2.2 Transition to Forward Flight

Insects that employ normal hover kinematics transition to forward flight by tilting their body forward (reducing χ) and thus increasing the stroke plane angle of their wings (see figure 1.5). This is similar to the way a conventional helicopter would add forward
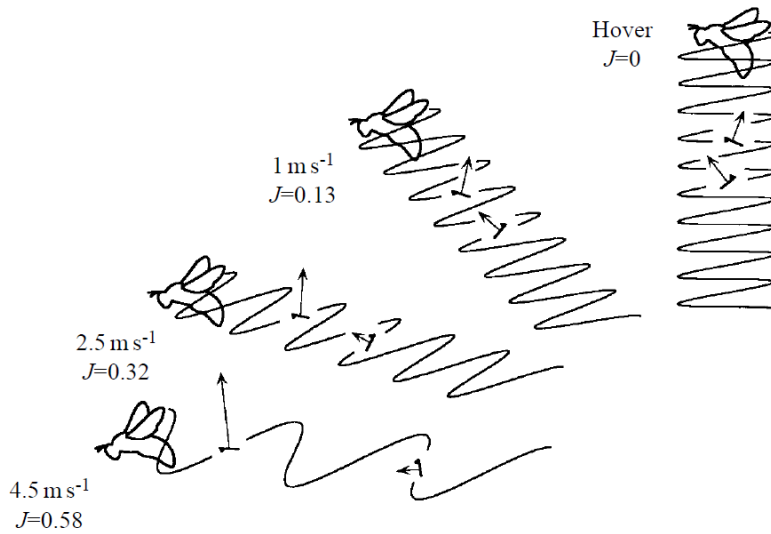
FIGURE 1.5: Two-dimensional view of the wing tip path for a bumblebee at different flight speeds (from Ellington 1999). Resultant aerodynamic forces are shown for representative up- and downstrokes. The anatomical lower wing surface is marked by a triangle at the leading-edge. The advance ratio (J) is shown for each forward flight speed.

cyclic in order to tilt the rotor disk forward to produce thrust for forward flight. At top speed the insect's body is close to horizontal and stroke plane angles of up to 40° have been measured for bumblebees (Dudley & Ellington 1990) and up to 60° for hawkmoths (Willmott & Ellington 1997a). The kinematic angles appear to vary little between hovering and fast forward flight (Ellington 1999). One exception is the geometric angle of attack relative to the stroke plane. This angle varies with forward speed such that the effective angle of attack remains approximately constant for each half cycle (Ellington 1999). Additionally, the amplitude of the flapping stroke has been found to decrease slightly with increasing speed for some insects (Dudley & Ellington 1990; Willmott & Ellington 1997a).

Ellington (1984c) characterised the flight speed of an insect using the advance ratio (J), which is defined by equation 1.8.

$$J = \frac{V}{2\Phi nR} \tag{1.8}$$

The advance ratio is the ratio of the insect's flight speed (V) to the average velocity at the wing's tip due to its rotation. Ellington (1984c) arbitrarily defined hovering flight as being for $J < 0.1$ and Ellington (1999) suggested that $J \approx 1$ is the theoretical upper limit for insect flight.

The transition to forward flight has a substantial impact on the aerodynamic forces that are produced for each half cycle. As the advance ratio is increased, the downstroke increasingly dominates the force balance, due to the larger relative velocity experienced by the wing for this half of the flapping cycle (Ellington 1999). Dickson & Dickinson (2004) investigated this by measuring the aerodynamic forces on a wing that combined a revolving motion with a uniform freestream velocity that acted in the plane of the wing's rotation. They showed that the aerodynamic forces are non-constant for non-zero advance ratios, where they varied with both the advance ratio and with the wing's stroke position angle (ϕ). They suggested that this variation in aerodynamic forces could be characterised by a single variable (at a constant angle of attack); the tip velocity ratio. At fast forward flight, the powerful downstroke becomes primarily responsible for weight support and some thrust, but the feeble upstroke produces a small amount of thrust only (see figure 1.5). The required thrust for forward flight is not very large, even at high speeds, and is only 10-20% of the insect's weight (Ellington 1999). The net aerodynamic force is therefore nearly vertical and is tilted forwards by less than approximately 10°.

1.3   Unsteady Mechanisms in Insect Flight

Early aerodynamic analysis of insect flight was based on the blade-element theory of propellers, which was modified by Osborne (1951) for flapping flight. In these models the wing is segmented into blade elements at varying radial distances along the wing's span. By applying the wing's kinematics to each element and estimating the downwash velocity, the aerodynamic force per unit span on the wing can be calculated using steady-state lift and drag coefficients measured from wind tunnel experiments. As such, these models assume that the aerodynamic force at any instant in time is the same as its steady-state value.

This method requires the stroke position, stroke deviation, the geometric angle of attack and the section profile to all be known as a function of time, and for a suitable estimate of the downwash velocity to be made, making it difficult to apply and prone to error (Ellington 1999). Consequently, a modification of this method is often used to simplify the analysis called the "mean coefficients method". Here the lift and drag coefficients are assumed to be constant over a half-stroke and by relating the net weight and thrust of the insect to the aerodynamic forces, a more accurate estimate of the mean

lift and drag coefficients can be calculated.

In a series of papers, Ellington (1984a,b,c,d,e,f) applied the mean coefficients method to a number of insects and used "proof by contradiction" to show that the quasi-steady assumption does not rigorously hold for insect flight. For many insects the mean lift coefficient required for weight support exceeded the maximum steady flow lift coefficient, sometimes by factors of two or three (Ellington 1984a; Willmott & Ellington 1997b; Ellington 1999). These results show that insects cannot fly according to the conventional laws of aerodynamics and that unsteady high-lift mechanisms must be employed instead.

Since this work, a number of unsteady mechanisms have been identified which are utilised by insects to enhance the wing's lift. These are the LEV, clap and fling, rapid pitch rotation and wake capture. They are described below.

1.3.1 The Leading-Edge Vortex

By far the most important flow feature of insect flight is the presence of an attached LEV. Most insects rely on this mechanism to generate the aerodynamic forces required for flight (Ellington 1999; Shyy *et al.* 2008; Liu & Aono 2009). While early studies theorised that such a vortex must exist (Maxworthy 1979; Ellington 1984d; Dickinson & Gotz 1993), direct evidence that insects actually create a LEV came from Ellington *et al.* (1996), who visualised the LEV on a real hawkmoth which was tethered in a wind tunnel (see figure 1.6). In order to examine the LEV more closely, Ellington *et al.* (1996) also built a scaled robotic hawkmoth wing and used it to visualise the LEV in a simulated hawkmoth hovering stroke. The LEV was observed to form above the top surface of the wing during the downstroke. It remained attached along the wing's span for most of the downstroke and joined with the tip vortex at the wing tip. During the latter half of the stroke the vortex was seen to break down at 60-70% of the wing span. A significant spanwise velocity that was comparable to the wing's tip velocity was also observed. This resulted in a conical spiral shaped LEV structure that enlarged towards the wing tip.

A schematic of the general two- and three-dimensional flow topology is shown in figure 1.7. As the wing is thin and at a high angle of attack, the flow separates from the leading-edge, but later reattaches to the upper surface, enclosing the LEV. The reattachment of the flow to the wing downstream of the LEV allows it to leave the
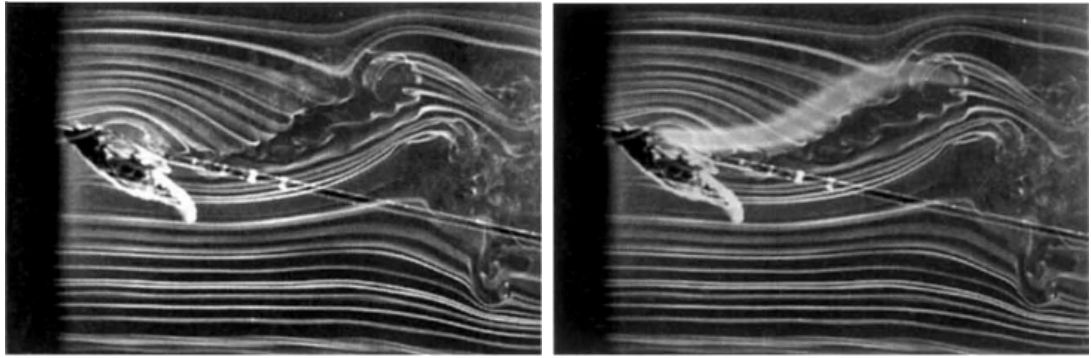
FIGURE 1.6: Flow visualisation around a hawkmoth's wing late in the downstroke (from Ellington *et al.* 1996). Left image shows raw smoke traces. Right image shows drawing of main vortex structure superimposed onto the left image.
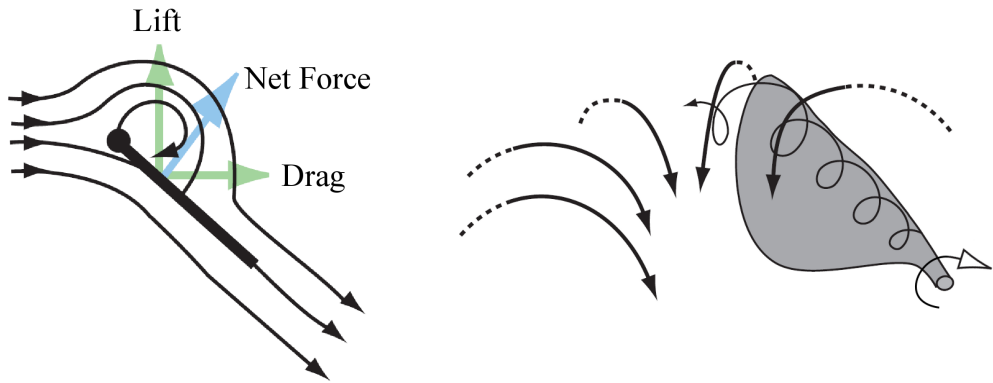

FIGURE 1.7: General flow structure schematics (adapted from Sane 2003). Two-dimensional cross-section of the flow is shown on the left and three-dimensional structure is shown on the right. Wing section is depicted as the thick line with a filled circle (leading-edge) in the left image. Thick black arrows in the right image indicate the downwash due to the vortex system.

trailing-edge smoothly (i.e. the Kutta condition is maintained). Due to the wing's rotation, a strong spanwise component of velocity is present on the wing. This spanwise flow is thought to stabilise the LEV to the wing's surface by limiting the growth of the vortex (see §1.3.1.3) and results in a spiralling vortex structure that increases in size along the wing's span.

Ellington *et al.* (1996) suggested that the LEV was responsible for generating the high lift required for hovering hawkmoths and remarked at its similarity to the LEVs found on delta wing aircraft. In the same way that a vortex on a delta wing increases the wing's lift, the LEV on a flapping wing increases lift by producing a region of

15

low pressure above the wing. The extra lift can also be explained as an enhanced circulation around the wing due to the vortex. These two explanations are equivalent (Ellington *et al.* 1996). Usherwood & Ellington (2002a) demonstrated, using model hawkmoth wings ($Re = 8071$), that the pressure force dominates, and accordingly the resultant force on a thin flat wing acts perpendicular to the wing's surface (see figure 1.7). Consequently, the added suction due to the LEV acts to increase both lift and drag. This was further explored by Birch *et al.* (2004) who showed that at a Reynolds number of 1400 the angle of the net force vector to the wing's surface quickly reaches $90°$ as the angle of attack of the wing is increased from $0°$. This state is reached more slowly at a lower Reynolds number of 120 due to the increased skin friction force.

The LEV has been shown to be a common flow feature in flapping wing aerodynamics at Reynolds numbers of the order of 10^4 and lower and, to a large extent, explains the enhanced lift required for the flight of many insect species (Shyy & Liu 2007; Liu & Aono 2009).

1.3.1.1 Development Throughout a Flapping Cycle

The formation of the LEV was investigated by Poelma *et al.* (2006) using digital particle image velocimetry (DPIV) of the flow around an impulsively started rotating wing. The results of their study are shown in figure 1.8. At the beginning of the wing's motion the LEV forms as part of a horseshoe-shaped vortex (HSV) that surrounds the wing. This HSV is made up of a trailing-edge vortex (TEV) or starting vortex, the tip vortex (TV) and the LEV. As the wing continues to rotate the TEV separates from the wing's trailing-edge. Poelma *et al.* (2006) surmised that the HSV was part of a ring vortex system, where the TEV connects back to the wing at the wing's root. Later numerical studies confirmed this to be correct and showed that the ring vortex system creates a strong downwash velocity in the wake of the wing (Aono *et al.* 2008; Liu & Aono 2009; Jardin *et al.* 2012). Poelma *et al.* (2006) showed that the LEV grows in size and strength during the early stages of the wing's motion, particularly nearer the wing tip. As the wing's rotation continues, the LEV's growth stops and it remains attached to the wing regardless of the distance that the wing travels (Dickinson *et al.* 1999; Poelma *et al.* 2006; Lentink & Dickinson 2009b), which results in a quasi-steady flow state being formed around the wing.
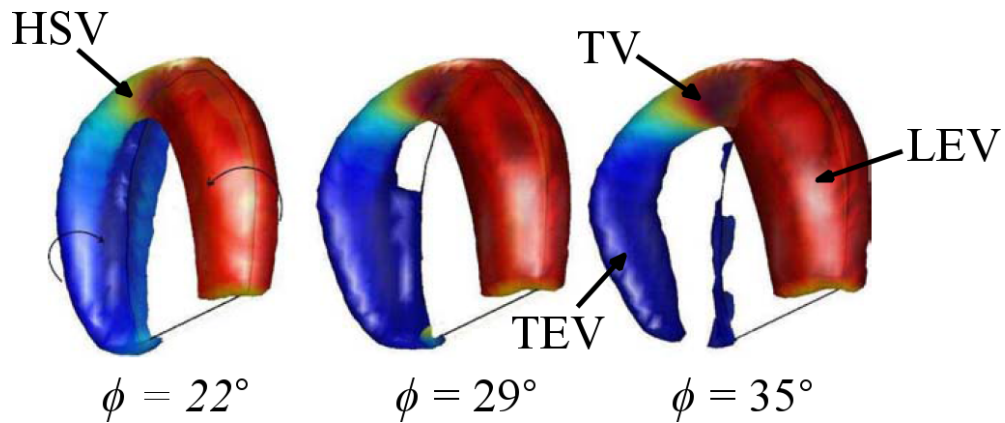
FIGURE 1.8: Development of the vortex structures during the early stages of an impulsively-started wing at a constant angle of attack (from Poelma *et al.* 2006). The root of the wing, which the wing is rotating about, is not shown in the images and the view point moves with the wing's rotation. Vortex structures are visualised by iso-surfaces of the second invariant of the velocity gradient tensor which are coloured by the spanwise component of vorticity, clockwise (blue) and counterclockwise (red) as indicated by the thin arrows.

Poelma *et al.* (2006), Aono *et al.* (2008), Liu & Aono (2009) and Jardin *et al.* (2012) all investigated the development of the vortex structures around flapping wings, and the simulations of Jardin *et al.* for one half of the flapping cycle are shown in figure 1.9. For a flapping wing, the development of the ring vortex system is the same as an impulsively started wing, only with the added complexity of stroke reversal. Figure 1.9 shows that a similar HSV forms at the beginning of each half cycle and this develops into a ring vortex system as the wing continues its motion. At stroke reversal the wing pitches up in preparation for the next half cycle. As it does so, vorticity is generated at the trailing-edge, resulting in the formation of a rotational starting vortex (RSV). As the wing reverses direction, this RSV and the LEV and TV from the previous half cycle are shed from the wing. Consequently, the wing meets its own wake during the early stages of each half cycle. This is a separate unsteady mechanism known as wake capture (see §1.3.3).

1.3.1.2 Effect of Reynolds Number

Birch *et al.* (2004) undertook a DPIV experiment of a dynamically scaled fruit fly wing at two Reynolds numbers to gain further insight into the structure of the LEV and how it varies with Reynolds number. The experiment was conducted in mineral oil with two different viscosities in order to achieve Reynolds numbers of 120 and 1400. The
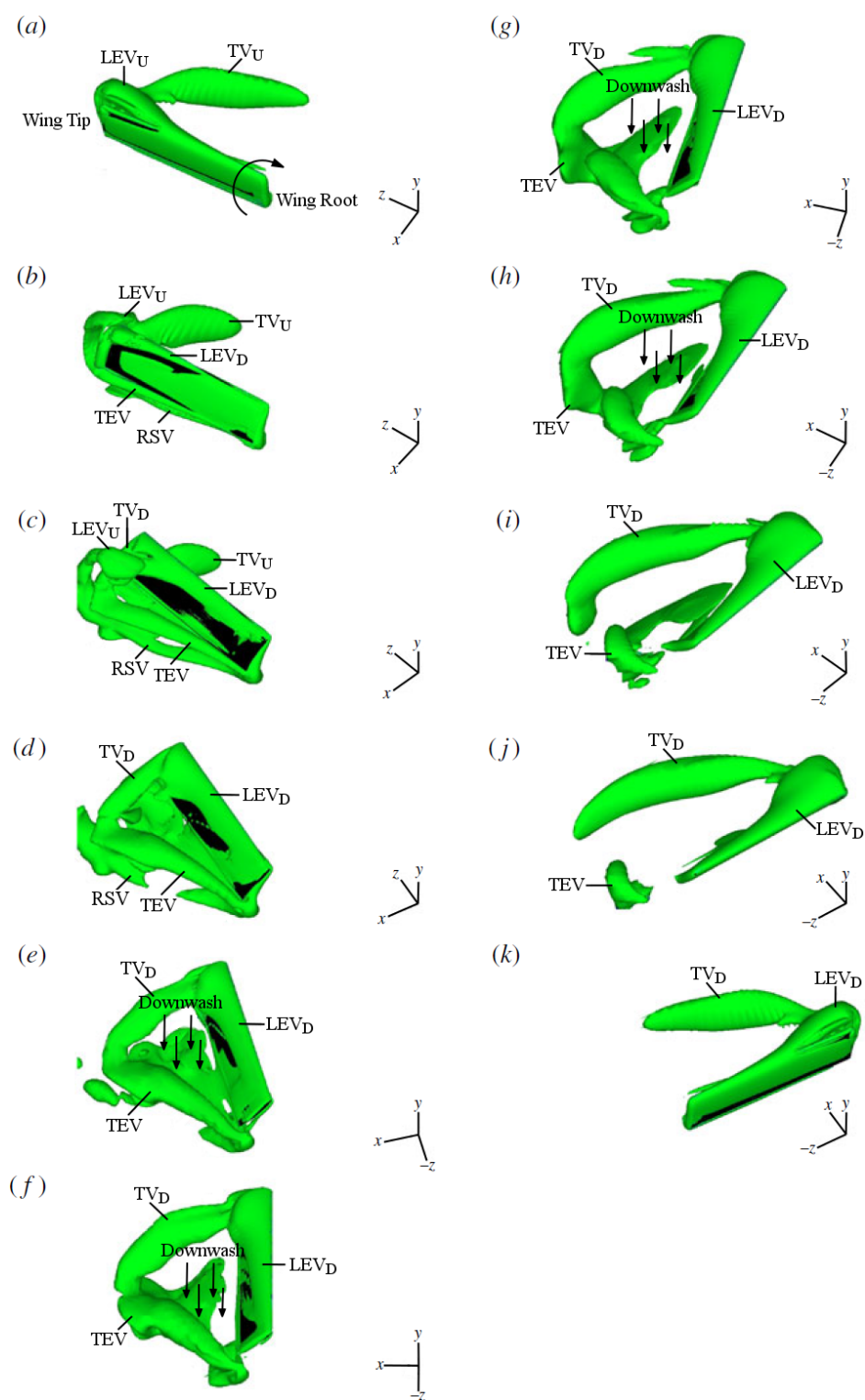
FIGURE 1.9: Development of vortex structures around a flapping rectangular wing during the downstroke of a simulated hovering cycle (from Jardin *et al.* 2012). The wing is shown in black and the vortex structures are visualised using iso-surfaces of λ_2 criterion coloured green. U and D subscripts indicate structures formed during the up- and downstrokes respectively.
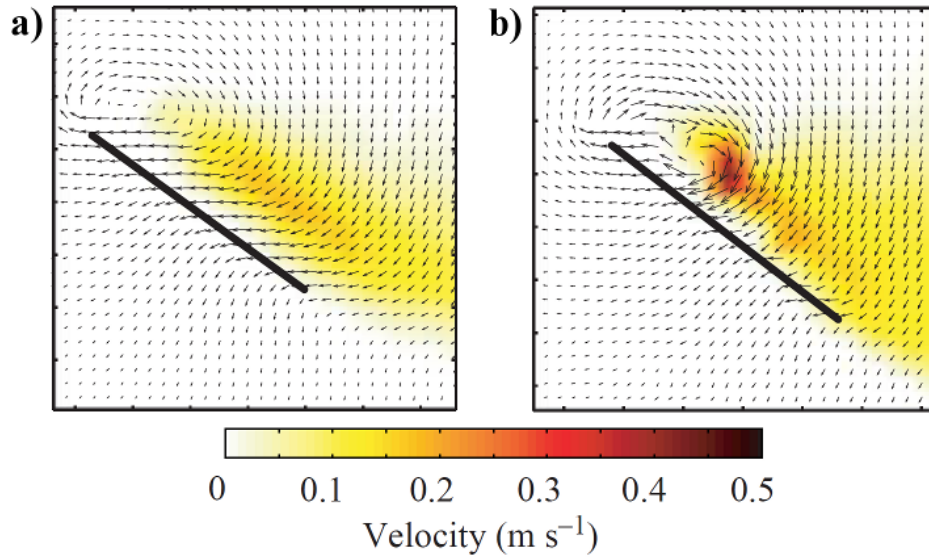
FIGURE 1.10: Sectional velocity field around a rotating wing at 45° angle of attack for (a) $Re = 120$ and (b) $Re = 1400$ (from Birch *et al.* 2004). In plane velocity vectors are superimposed over a contour plot of spanwise velocity. Images show the velocity field at 55% span.

wing motion was an impulsive start followed by constant angular velocity rotation at a fixed angle of attack and the kinematics were identical for both Reynolds numbers. Birch *et al.* showed that at a Reynolds number of 120, a region of spanwise flow formed over a broad region of the wing, where the peak in spanwise velocity occurs behind the LEV (see figure 1.10a). At a Reynolds number of 1400, an additional region of higher velocity flow within the core of the LEV was observed (figure 1.10b), superimposed over a broad spanwise flow that was similar in structure to that present at a Reynolds number of 120. At a Reynolds number of 1400 the maximum spanwise flow within the core of the LEV reached velocities as high as 150% of the wing tip speed.

In a later study, Lentink & Dickinson (2009b) undertook a similar experiment and using the results of their study, combined with observations from a thorough review of the available literature, they concluded that "the spanwise flow in the core of the LEV of an insect, when present, is most likely to be driven by the spanwise pressure gradient." They also concluded that "the spanwise flow in the extended viscous flow region behind the LEV can be explained best by centrifugal pumping, directly analogous to that found on spinning discs."

Both Birch *et al.* (2004) and Lentink & Dickinson (2009b) performed flow visu-
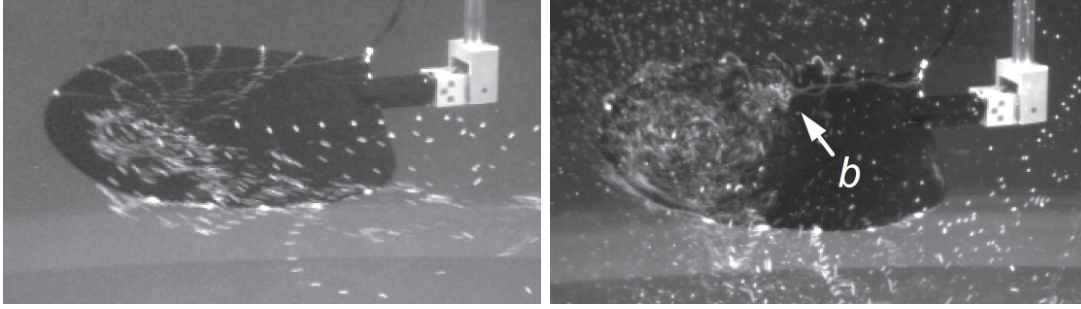
FIGURE 1.11: Air bubble flow visualisations of a rotating scaled robotic fruit fly wing at (left) $Re = 110$ and (right) $Re = 1400$ (from Lentink & Dickinson 2009b). The white arrow shows the breakdown point of the LEV. The wing has travelled eight and four chord lengths, measured at the wing's radius of gyration, in the left and right images respectively.

alisations by injecting air bubbles into the flow along the leading and trailing edge of the wing. The flow visualisations from Lentink & Dickinson (2009b) are shown in figure 1.11. At a Reynolds number of 110 the LEV did not form a tight spiral and was attached to the wing along its span to approximately the 70% span position, at which point it joined with the tip vortex as it separated from the wing. At a Reynolds number of 1400, a tight spiral LEV formed which broke down at approximately 60% span, which resulted in a region of unsteady flow near the wing tip. Vortex breakdown is an abrupt change in the structure of a vortex with a marked retardation of the flow in the axial direction and a corresponding divergence of the stream surface near the vortex axis (Hall 1972). The burst LEV remained coherent and stable with respect to the wing after it broke down and joined with the tip vortex at the wing tip (Lentink & Dickinson 2009b).

Shyy & Liu (2007) also investigated the effect of Reynolds number on the LEV by comparing simulations of a hovering hawkmoth ($Re = 6000$), fruit fly ($Re = 134$) and thrip ($Re = 10$). They observed similar changes in the LEV's structure between these Reynolds numbers and what was reported by Birch *et al.* (2004) and Lentink & Dickinson (2009b). At a Reynolds number of 6000, an intense, cone shaped LEV was observed along with substantial spanwise flow in the vortex core and the vortex was observed to break down at approximately three-quarter span. At a Reynolds number of 120, the LEV did not break down and the spanwise flow in the vortex core was also observed to become weaker. For the thrip ($Re = 10$), the LEV was shown to have more of a cylindrical than conical form, which suggests a more two-dimensional structure
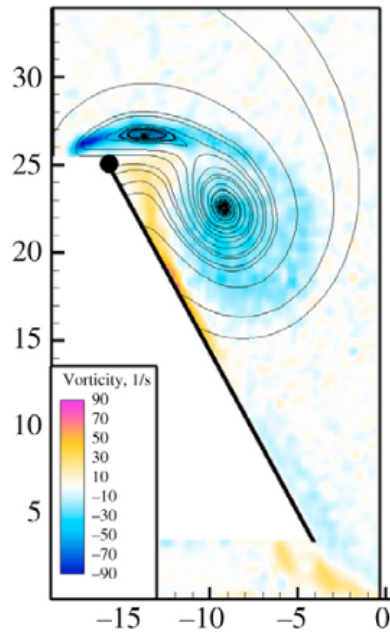
FIGURE 1.12: Sectional flow field at 29% wing span showing dual LEV structure on a flapping wing at $Re = 800$ and $\alpha = 60°$ (from Lu *et al.* 2006). Image shows streamlines (solid lines) superimposed on contours of spanwise vorticity.

with very little spanwise velocity in its core. This work was later extended by Liu & Aono (2009) to include a honeybee ($Re = 1000$), which showed a similar LEV structure to that of the hawkmoth.

Lu *et al.* (2006) undertook an experiment on a flapping wing at Reynolds numbers between 160 and 3200 using a higher resolution DPIV setup than that used by Birch *et al.* (2004). They showed that the structure of the LEV is more detailed at higher Reynolds numbers than previously thought. While the structure of the LEV was found to be similar at low Reynolds numbers, for Reynolds numbers of 640 and above a dual co-rotating LEV structure was observed to develop. An example of this dual LEV structure is shown in figure 1.12 and was found to be remarkably similar to the dual LEV structure that forms over non-slender delta wings (Gordnier & Visbal 2003; Taylor & Gursul 2004; Gordnier *et al.* 2009). This structure consisted of a small vortex located near the leading-edge of the wing and a larger vortex, which was further downstream and close to the wing's surface. The proximity of the larger vortex to the wing's surface induced a flow near the wing's surface, which generated a boundary layer of opposite sign vorticity to the vortex. This boundary layer separated from the wing near the leading-edge due to the adverse pressure gradient generated by the larger vortex

21

structure.

Lu *et al.* (2006) found that this dual LEV structure existed over a variety of wing shapes for angles of attack greater than 30° and for Reynolds numbers greater than 640. They therefore concluded that the dual LEV may be a basic flow structure of flapping wings. The dual LEV was observed by Lentink & Dickinson (2009b) for some $Re = 1400$ cases. Furthermore, this dual vortex structure has been seen in experiments on model flapping wings (Phillips *et al.* 2010) and over the wings of real butterflies (Srygley & Thomas 2002). Lu *et al.* (2006) suggested that improper locations of tracer release points, as well as inadequate spacial resolution of CFD and DPIV experiments, may be reasons why this dual LEV was not seen in earlier studies.

1.3.1.3   Attachment of the Leading-Edge Vortex

The formation of the LEV is often described as the delayed stall or dynamic stall mechanism, as its formation is similar to that of a two-dimensional impulsively started wing. Delayed stall occurs during the impulsive start of an aerofoil at an angle of attack beyond its steady-state stall angle (Walker 1931). A schematic of flow evolution during the early stages of the wing's motion is shown in figure 1.13. As the aerofoil begins to move, a starting vortex is shed from the trailing-edge, and an attached LEV develops due to flow separation at the leading-edge. The LEV allows the flow to reattach to the wing's surface and for the Kutta condition to be established at the trailing-edge. The formation of this LEV provides the wing with a temporary increase in lift that is greater than its steady state value. As the wing continues its motion the LEV grows in size until flow reattachment is no longer possible. At this point the Kutta condition breaks down and a trailing-edge vortex is formed as the LEV is shed into the wake. As a result, there is a drop in lift and the wing is said to have stalled. The trailing-edge vortex grows in size until it too can no longer remain attached to the wing. This dynamic process repeats, creating a wake of regularly spaced counter-rotating vortices known as a von Karman vortex street.

For this two-dimensional case, lift enhancement is limited to 3-4 chord lengths of travel (Dickinson & Gotz 1993), however many insects flap their wings further than this (Ellington 1999). Studies that have investigated three-dimensional translating wings at insect Reynolds numbers have also shown that the LEV is shed after a few chord lengths of travel (Miller & Peskin 2004; Taira & Colonius 2009). However, studies
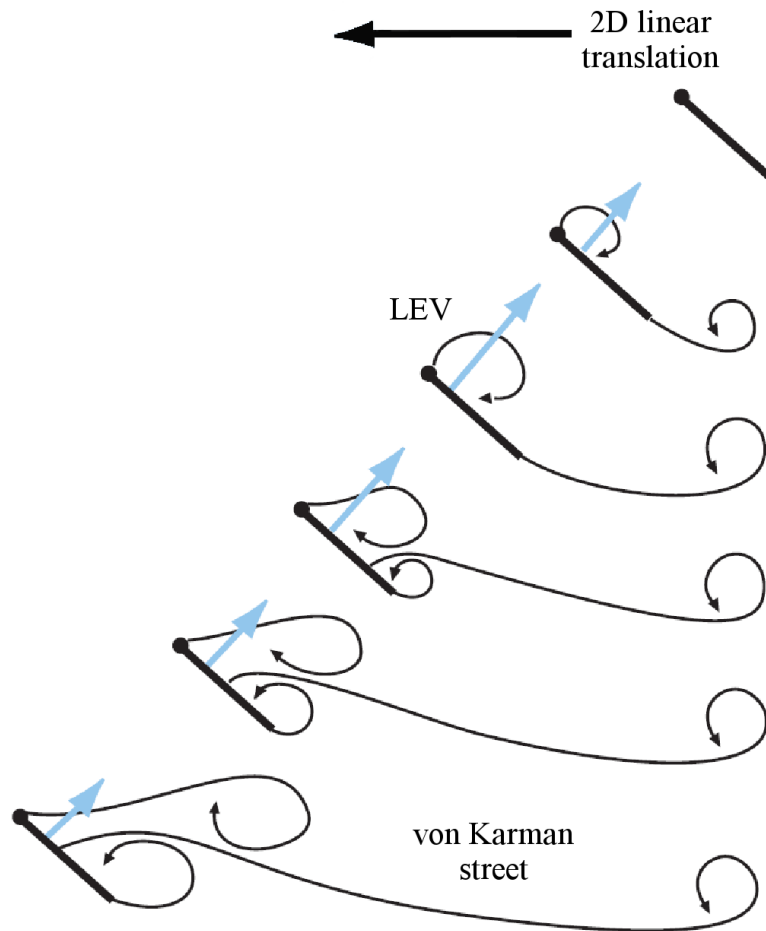
FIGURE 1.13: Schematic of the flow structure evolution for a two-dimensional impulsively started wing (from Sane 2003). Blue arrows are the net aerodynamic force vectors.

that have incorporated the rotation of the wing about its base have often found stable LEVs (Ellington *et al.* 1996; Usherwood & Ellington 2002a; Birch *et al.* 2004; Poelma *et al.* 2006), even after many chord lengths of travel. In this thesis the word "stable" and its derivatives are used to describe whether the LEV remains attached throughout the stroke (stable) or if it is shed (unstable), as it is commonly used in flapping wing literature (e.g. Ellington *et al.* 1996; Lentink & Dickinson 2009b; Shyy *et al.* 2010). It is not to be confused with "flow stability" in the classical sense that relates to the growth/decay of perturbations. In these rotating wing cases, a von Karman street is never created and the wing never stalls. Therefore, the ability for the LEV to remain attached to the wing is a key characteristic that is required in order to maintain high lift throughout the wing's stroke.

An important question is then what causes this prolonged attachment of the leading-

edge vortex? In their pioneering work, Ellington *et al.* (1996) remarked at the similarity of the LEV's structure and spanwise flow found on their flapping hawkmoth model to the spiral LEV and axial flow that forms on highly swept delta wings. The effect of sweepback on stabilisation of the LEV for delta-wing aircraft is well understood. Here, due to the wing's sweep, a component of velocity acts along the span of the wing. If the sweep angle is large enough, this component of velocity is sufficient to maintain the attachment of the LEV by drawing vorticity along the wing's span, away from the leading-edge. This limits the growth of the LEV and thus maintains its attachment to the wing (Wu *et al.* 1991). Ellington *et al.* (1996) therefore proposed that the LEV on insect wings is stabilised to the wing's surface by the spanwise flow in an analogous way to the LEVs found on delta wings.

Lentink & Dickinson (2009b) tested this hypothesis by translating a model fruit fly wing with varying degrees of sweep angle at insect Reynolds numbers. In all cases the LEV was shed and they therefore concluded that the "strict analogy of the mechanisms that operate to stabilize LEVs on swept wing aircraft does not appear to hold for insect wings." Furthermore, Beem *et al.* (2012) translated a swept rectangular planform wing with a NACA 0012 profile at slightly higher Reynolds numbers and also found that the spanwise flow that was generated due to the wing sweep was insufficient to maintain an attached LEV. Curiously though, wing sweep on a rotating wing can be used to modulate the LEV strength and possibly its stability (Rival & Wong 2013; Wong *et al.* 2013).

Birch & Dickinson (2001) attempted to block the spanwise flow on a scaled flapping fruit fly wing by using a variety of baffles. They found that these had no effect on the stability of the LEV. They therefore proposed an alternate hypothesis that the downward flow induced by strong tip vortices, associated with the low aspect ratio (AR) wings, stabilise the LEV by greatly lowering the effective angle of attack. Cheng *et al.* (2013) later analysed the vorticity dynamics in the flow behind a rotating wing and proposed that the downwash velocity that the tip vortex and wake structures create stabilises the LEV, as it limits the strength of the LEV by convecting and tilting vorticity into other components. Using a numerical model, Taira & Colonius (2009) showed that a steady flow state can be created for translating wings if the aspect ratio and angle of attack are low enough. However, for aspect ratios and angles of attack which are typical of insect flight the LEV is unsteady, resulting in either a periodic

or aperiodic wake. Additionally, Lentink & Dickinson (2009b) translated their model fruit fly wing ($AR = 2.9$) and found that the LEV was unstable at insect Reynolds numbers. They therefore concluded that tip effects alone are insufficient to generate a stable LEV.

Lentink & Dickinson (2009b) noted that the LEV's stability seemed to be related to the wing's rotation. They compared the results of an experiment in which a fruit fly wing was translated and rotated at the same angle of attack and Reynolds number, and where the velocity at the radius of gyration was matched between each case. Their results showed that while the translating wing sheds its LEV after a few chord lengths of travel, the rotating wing maintains an attached LEV (compare figure 1.14 with figure 1.11). This demonstrated that it is the propeller-like rotation of the wing which stabilises the LEV to the wing. Using this finding, Lentink & Dickinson (2009a,b) non-dimensionalised the Navier-Stokes equations cast in a rotating frame of reference. They showed that the centripetal and Coriolis accelerations are proportional with the inverse of the Rossby number (see §1.1). The Rossby number is the ratio of inertial to Coriolis forces and is therefore a measure of the wing's rotation compared to its translation. When the wing is rotating about its base the Rossby number is low and the centripetal and Coriolis accelerations are large. Conversely, when the wing is translating the Rossby number approaches infinity and therefore the rotational accelerations are negligible. As these states correlated with a stable and unstable LEV respectively, Lentink & Dickinson (2009b) concluded that it is the low Rossby number rotation of the wing, and particularly the large rotational accelerations that this creates, that stabilise the LEV to the wing.

Further analysis revealed that, fundamentally, it is a combination of the pressure-gradient, centripetal and Coriolis forces that result from the wing's rotation that generate the spanwise velocity seen on flapping and rotating wings at high angles of attack (Lentink & Dickinson 2009b). Because of this, Lentink & Dickinson remarked that the results of their study also support the hypothesis that it is the spanwise flow that stabilises the LEV through vorticity transport. However, they proposed an alternative explanation that the spanwise flow itself generates Coriolis accelerations that act in the direction of the wing's travel which stabilises the LEV.

Nevertheless, there is one set of work that is in disagreement with the idea that it is the wing's rotation that stabilises the LEV. In a series of studies, Jones & Babinsky
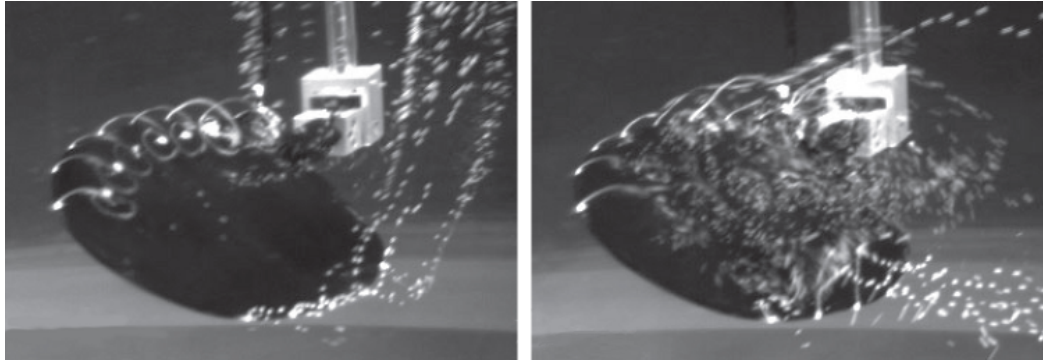
FIGURE 1.14: Air bubble flow visualisations of a translating fruit fly wing after (left) one chord length of travel and (right) three chord lengths of travel (from Lentink & Dickinson 2009b).

(2010, 2011) and Jones *et al.* (2011) undertook an experiment on a rotating rectangular planform wing at Reynolds numbers between 10,000 and 60,000. They found that the LEV was largely two-dimensional in structure and was shed from the wing during the early stages of the wing's motion, despite the fact that the wing was rotating at large angles of attack. However, their experimental setup, where the wing protruded through the fluid's free surface and the rotation point was located outside the fluid, may be the reason for their distinctly different findings.

1.3.1.4 Effect of Advance Ratio

The low Rossby number hypothesis of Lentink & Dickinson suggests that the LEV would become unstable under forward flight conditions (high Rossby numbers), however the change in the LEV's characteristics with flight speed is not well understood. While there have been numerous studies that have investigated pitching and plunging aerofoils in freestream flow, relatively few have looked into rotating wings in a uniform freestream flow. These latter studies pertain to insect flight, while the former more closely relate to bird flight.

Nagai *et al.* (2009) conducted both numerical and experimental investigations into the effect of advance ratio using a flapping bumblebee wing, whose stroke plane was set at $\beta = 45°$ to a uniform freestream flow. They found a similar variation in lift and drag coefficients throughout the flapping cycle as Dickson & Dickinson (2004) and demonstrated that at mid-downstroke the LEV was larger for higher advance ratios, but remained attached to the wing for all the advance ratios that were tested. Conversely,

the LEV was smaller during the upstroke for increasing advance ratios and only formed on the outer part of the wing due to the locally reversed flow in the inner part of the wing. Gopalakrishnan & Tafti (2010) computed the flow around a flapping aspect ratio 4 plate at an advance ratio of 0.5 where the wing's stroke plane angle was 90° to the freestream flow. They reported that the LEV was shed from the outer part of the wing mid-way through the downstroke. Bross *et al.* (2013) undertook a particle image velocimetry (PIV) experiment on a rotating wing ($AR = 2$) in a uniform freestream flow that was perpendicular to the wing's rotation plane ($\beta = 90°$). They found that if the effective angle of attack is matched then similar attached LEV structures are generated over a range of advance ratios.

1.3.2 Rapid Pitch Rotation

In an experimental study using a dynamically scaled robotic model, Dickinson *et al.* (1999) simulated the hovering flight of the fruit fly *Drosophila Melanogaster*. They found that the aerodynamic forces peaked in each half cycle just before stroke reversal. This was shown to be related to the rapid increase in pitch of the wing. If wing rotation occurs before stroke reversal (advanced rotation) the circulation around the wing is increased and lift is augmented. Conversely, if wing rotation occurs after stroke reversal (delayed rotation) then circulation is decreased resulting in reduced lift after reversal. In a later study, Sane & Dickinson (2002) termed this spike in force "rotational force" and demonstrated that the rotational force coefficient is proportional to the angular velocity of the wing's pitch rotation.

1.3.3 Wake Capture

A second force peak was also observed by Dickinson *et al.* (1999) from their robotic fruit fly experiments. This force peak occurred just after each stroke reversal and it was concluded that this was due to the wing interacting with its own wake that was created from the previous half cycle. These wing-wake interactions are commonly referred to as "wake capture".

The wake capture mechanism was first observed by Dickinson (1994) for a two-dimensional flapping wing, but was later found to also occur for three-dimensional flapping wings (Dickinson *et al.* 1999; Birch & Dickinson 2003). This mechanism is shown schematically in figure 1.15. As the wing transitions from a steady revolving motion (A) it pitches up in preparation for stroke reversal (B). This generates vorticity
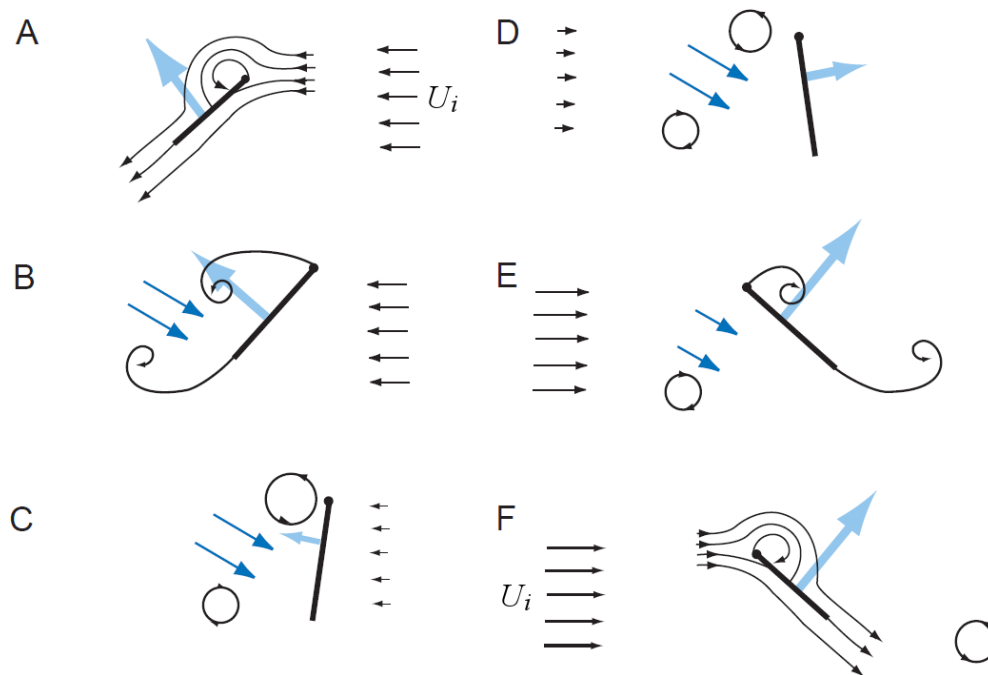
FIGURE 1.15: Schematic of the wake-capture mechanism as a wing reverses its stroke (from Sane 2003). Dark blue arrows indicate the velocity field generated by the wing's wake and the light blue arrows depict the aerodynamic force on the wing. U_i is the instantaneous relative velocity experienced by the wing.

at the trailing edge forming a RSV. This RSV and the LEV induce a strong velocity field between them. As the wing slows (B,C) and then reverses direction (D,E), it encounters this jet of high velocity fluid. This temporarily increases the relative velocity experienced by the wing and results in a peak in the aerodynamic forces.

1.3.4 Clap and Fling

During a study into the flight of a very small wasp *Encarsia Formosa*, Weis-Fogh (1973) found that unlike a normal insect's flap, the wasp clapped its two wings together at the end of the upstroke and then flung them apart at the beginning of the downstroke. This movement was called the clap and fling and can result in a modest lift enhancement.

A schematic of this process is shown in figure 1.16. During the clap phase (A-C), the leading-edges of the two wings touch before the trailing-edges. Each wing then rotates about its leading-edge and thus progressively closes the gap between them, pushing fluid out and generating additional lift. During this process, vorticity shed from the trailing-edge forms two stopping vortices and the strength of the LEVs diminish.
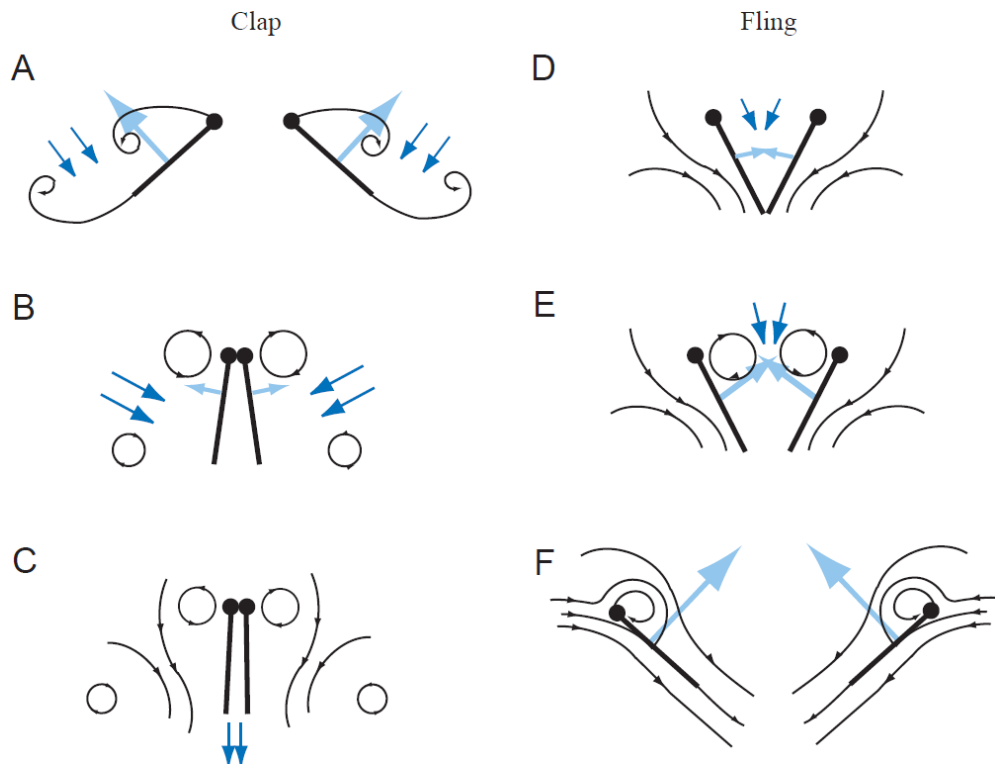
28

FIGURE 1.16: Section schematic of clap (A-C) and fling (D-F) mechanism (from Sane 2003). Dark blue arrows illustrate the induced velocity and the light blue arrows show aerodynamic force acting on the aerofoil.

The fling phase (D-F) consists of the two wings rotating around their trailing-edges before moving away from each other. As the leading-edges of each wing are displaced from each other, fluid rushes in to fill the gap which gives an initial boost in circulation around each wing, thus increasing lift. New LEVs are formed but the trailing-edge starting vortices are mutually annihilated as they are of opposite circulation.

While this mechanism is not as commonly implemented by insects as the LEV, rapid pitch rotation or wake capture mechanisms, a number of insect species have been shown to exploit its benefits, for example butterflies (Srygley & Thomas 2002), locusts (Cooter & Baker 1977), fruit flies (Ellington 1984c; Zanker 1990), wasps (Weis-Fogh 1973) and thrips (Ellington 1984c).

1.4 Wing Morphology

Insects employ a large variety of wing shapes in order to achieve their particular flight requirements, however relatively few studies have investigated the effect of wing shape

on the aerodynamics of flapping wings. One easily identifiable variation in wing morphology between different insect species is the diversity of wing planform shapes, and in particular the wing's aspect ratio. In addition, many insect wings are flexible and deform during flight as a result of the wing's passive response to the inertial and aerodynamic forces. Wing deformation is often observed as a combination of wing twist, camber and spanwise bending. A summary of studies that have dealt with these basic wing morphology parameters is presented below.

1.4.1 Wing Planform Shape

1.4.1.1 Aspect Ratio

The wing's aspect ratio is defined as the ratio of the wing's span to average chord length. In this thesis for convenience, we calculate the aspect ratio based on a single wing, i.e. the wing's span is measured from wing root to tip, as only a single wing is modelled in the numerical simulations. This is the most commonly reported aspect ratio in the literature, however some studies present the wing's aspect ratio in terms of a complete wing pair, i.e. the tip-to-tip wing span is used, as is conventional for large aircraft. The single wing aspect ratio is therefore approximately half the full aspect ratio. In order to compare between different studies the single wing aspect ratios are presented here.

A wide variety of aspect ratios can be observed across different insect species. For example, Ellington (1984b) presented data on various wing parameters for a range of insect species that include flies, beetles, moths, butterflies and dragonflies. Wing aspect ratios varied between 2.85 and 5.8, with a mean value of 4.15. Shyy *et al.* (2010) also reported wing aspect ratios for a wasp (2.12), fruit fly (3.06), honey bee (3.325), hawkmoth (2.65) and a hummingbird (4.5).

Usherwood & Ellington (2002b) were the first to investigate the effect of aspect ratio by varying the chord length of their rotating model hawkmoth wings ($2.265 \leq AR \leq 7.92$). They measured the aerodynamic forces using horizontal and vertical "propeller" force coefficients. They found that the maximum vertical force coefficient did not vary greatly with aspect ratio, however the initial rate of change of the vertical force coefficient with angle of attack did change significantly with aspect ratio, where higher aspect ratios had larger initial rates of change. Horizontal force coefficients were similar at angles of attack less than approximately 30° but differed significantly at
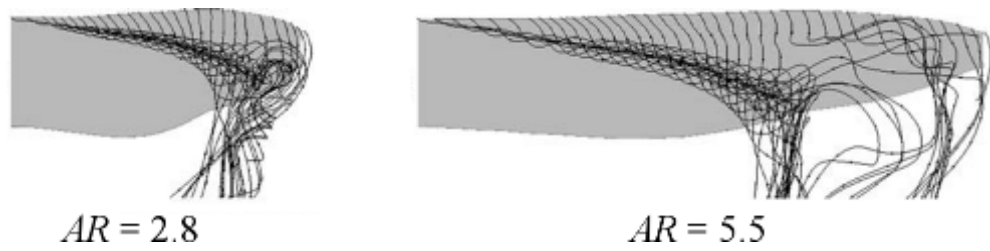
FIGURE 1.17: Instantaneous streamline plots for rotating hawkmoth wings of aspect ratios of 2.8 and 5.5 (from Luo & Sun 2005).

higher angles, with lower aspect ratio wings having larger horizontal force coefficients.

Luo & Sun (2005) investigated the effect of aspect ratio by varying the span of an impulsively started rotating hawkmoth wing using a computational model. They found that the mean aerodynamic force coefficients varied by 10% between aspect ratios of 2.8 and 5.5. They indicated that the LEV separated from the wing proportionally earlier along the wing's span for larger aspect ratios, and this resulted in a larger region of separated flow near the wing tip (see figure 1.17). Consequently, the non-dimensional lift distribution along the wing's span showed that the minimum pressure peak moved inboard and reduced in magnitude for higher aspect ratios.

Tsuzuki *et al.* (2007) measured the aerodynamic forces on rotating rectangular wings, where aspect ratios between 4 and 10 were created by increasing the wing's span. They used a figure of merit parameter, which was based on the thrust and torque coefficients, as a measure of the hovering aerodynamic performance of the rotor. They found that an optimum aspect ratio of 5.5 existed for which the figure of merit was the highest over all angles of attack.

As part of an extensive wing geometry study, Ansari *et al.* (2008) investigated the effect of aspect ratio ($1.25 \leq AR \leq 7.5$) on thirteen different wing planforms using a numerical model. Each wing was prescribed a similar flapping motion. They found that mean lift generally increased with aspect ratio and that lift on drag ratio reached a peak for most wings at an aspect ratio between 2.5 and 5 after which it did not change considerably. Additionally, the lift on torque ratio was found to reduce as aspect ratio increased. However, these results need to be treated with some caution as the simplistic numerical model that was used was based on a blade element method. This method solves the flow over two-dimensional wing sections and therefore cannot model three-dimensional effects such as spanwise flow or a tip vortex. As such, a stable LEV also

cannot be simulated (see §1.3.1.3). It is unclear as to how these limitations influenced their findings.

All of the above studies report different effects of aspect ratio on the wing's aerodynamic performance and in some cases the results are quite contradictory. This variation in results may be explained by differences in the way the wing aspect ratio is varied. Due to the wing's rotation, changing the aspect ratio either by stretching the wing in the chordwise or spanwise directions also varies the Reynolds number. This can be seen by considering equation 1.6, which defines the Reynolds number for a flapping or rotating wing. Modifying the wing's span alters the reference velocity as the distance from the wing's root to either the radius of gyration or wing tip is altered. Likewise, changing the wing's chord directly affects the Reynolds number. Thus, it doesn't matter how the aspect ratio is changed, it will also influence the Reynolds number. This issue is not addressed in any of the above studies and as such the reported effects of aspect ratio from these studies also include Reynolds number effects. Usherwood & Ellington (2002b) varied the aspect ratio by changing the wing's chord length, Luo & Sun (2005) and Tsuzuki *et al.* (2007) varied the wing's span, and Ansari *et al.* (2008) changed both the wing span and mean chord length. As each study varied the aspect ratio in a different way, variation in Reynolds number between each study is also different and therefore this could explain the variance in results. Nonetheless, this highlights that further investigation is needed to separate the effects of Reynolds number from those of aspect ratio.

A further consideration arises from the low Rossby number hypothesis of Lentink & Dickinson (2009b). Lentink & Dickinson theorised that the Rossby number is equivalent to the wing's aspect ratio for hovering flight, and therefore low aspect ratio wings would be required in order for the LEV to remain attached to the wing. However, few studies have investigated the change in the characteristics of LEV with aspect ratio. Wojcik & Buchholz (2012) used DPIV to measure the flow around rotating plates at two spanwise locations. Plates with aspect ratios of 2 and 4 were considered, where the aspect ratio was changed by increasing the wing's span. They attempted to avoid Reynolds number effects by maintaining a constant Reynolds number based on the tip velocity and the wing's chord length between each aspect ratio. They found that the lower aspect ratio plate had lower LEV circulation and that the LEV was stable for both aspect ratios at 25% and 50% span. Carr *et al.* (2013) also investigated the flow around rotating plates

of aspect ratio 2 and 4, where the change in aspect ratio was achieved by stretching the wing in both the chordwise and spanwise directions. Like Wojcik & Buchholz, they attempted to avoid Reynolds number effects by maintaining a constant Reynolds number at the wing's tip. The flow field along the entire wing span was reconstructed using DPIV and they found that for the higher aspect ratio wing the LEV broke down earlier in the wing's rotation and lifted-off from the wing's surface near the wing tip. The lower aspect ratio wing was observed to exhibit substantially higher spanwise vorticity and velocity, and showed a strong flux of spanwise vorticity in the outer part of the wing. Carr *et al.* suggested that this strong flux of vorticty into the tip vortex may account for the mitigation of LEV lift-off at this aspect ratio. It is worth noting that the results of Carr *et al.* were published after the first study into aspect ratio was conducted (see §1.5 below) and that the results of this study show that neither Wojcik & Buchholz nor Carr *et al.* were successful in eliminating Reynolds number effects from their data (see chapter 3).

1.4.1.2   Wing Shape

In addition to the aspect ratio, the wing's planform shape can be described by the spanwise variation in chord length. Due to the wing's rotation and the spanwise variation in velocity that this creates, the distribution of wing area can have a significant impact on the aerodynamic forces. This was demonstrated by Luo & Sun (2005) who examined the effect of wing planform shape on the aerodynamic forces produced by 10 different insect wing planforms which were modified such that they had the same wing span and aspect ratio. They found that when the forces were non-dimensionalised using the tip velocity the force coefficients varied significantly (by 33%) between the different wing planforms. In a quasi-steady analysis, the mean lift force is proportional to the second moment of wing area (Weis-Fogh 1973). Thus, by non-dimensionalising the aerodynamic forces using the velocity at the radius of the second moment of wing area (also referred to as the radius of gyration, r_g), wings with different area distributions can be compared equally. This was again evidenced by Luo & Sun (2005), who recalculated the force coefficients using this velocity and found that the variation in aerodynamic force coefficients was now less than 5%. This result highlights the potential variation in conclusions that can be reached depending on the reference velocity used.

Ansari *et al.* (2008) also studied the effects of wing shape by comparing the performance of thirteen different derived wing shapes using their flapping-wing numerical model. They concluded that wings with more area outboard, a straight leading-edge, and/or positive sweep at the leading-edge show better lift on torque versus lift ratios. However, again these results need to be treated with some caution for the same reasons outlined above. Additionally, the computed aerodynamic forces were not non-dimensionalised and, due to the restricted separation distance between the two wings, the variation of the wing's area distribution also resulted in a change in the flapping kinematics between planforms. This meant that the effect of one parameter was not clearly isolated and the effect of different flapping velocities is included in the aerodynamic force results.

Like Luo & Sun (2005), Wilkins (2008) tested three different planform shapes, which all had the same aspect ratio and wing span, using a CFD model of an impulsively started rotating wing. Wilkins reported a large variation in the lift coefficients, which were calculated using the tip velocity, but found little change in the flow structures between each wing. In addition, Phillips *et al.* (2010) undertook a DPIV experiment using these same wing planform shapes (and one additional) but at a higher Reynolds number. They measured the flow fields over the four planform shapes at the midstroke position of a flapping cycle. They also showed that a very similar dual LEV structure formed over each wing and therefore concluded that planform shape has little effect on the flow structure over a flapping wing.

1.4.2 Morphology due to Wing Deformation

Many insects have flexible wings which become bent, cambered and twisted during the course of a flapping cycle. Details of the fluid-structure interaction that cause this deformation is beyond the scope of this study. Refer to Shyy *et al.* (2010) for a review of works covering this topic. In this section, the work by Walker *et al.* (2010) will be used as an example of how these wing morphology parameters vary throughout the course of a flapping cycle and their effect on the aerodynamics of flapping wings will be discussed.

1.4.2.1 Wing Twist

Walker *et al.* (2010) used four high-speed digital video cameras to reconstruct the motion and distortion of the wings of free-flying hoverflies and a three dimensional
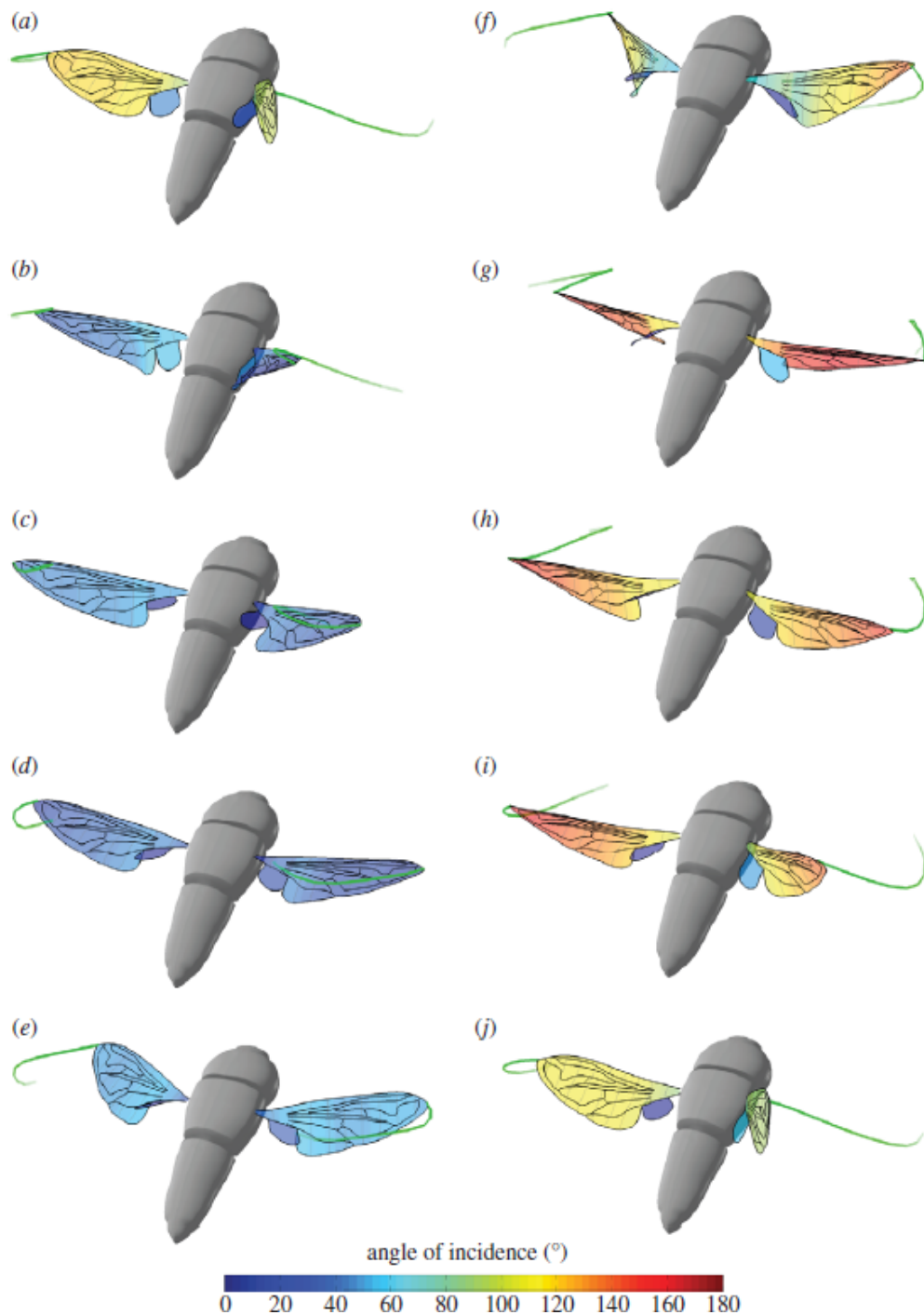
FIGURE 1.18: Three-dimensional projection of hoverfly wings throughout a flapping cycle (from Walker *et al.* 2010). (a-e) downstroke, (f-j) upstroke. The wings are coloured by the angle of incidence which was defined with respect to a rotating wing-axis system and is the angle between the wing's chord line and the horizontal. A scaled model of the hoverfly body is also shown for reference. The green wisps at the wing tips show the immediate time history of the wing tip position to convey a sense of the wing's motion.

representation of their results is shown in figure 1.18. The wing is coloured by the angle of incidence and shows that the wing was twisted throughout the flapping cycle. During both the upstroke and the downstroke the hoverfly's wings were twisted such that they had aerodynamic washout of approximately $10° − 20°$, i.e. the wing tip is at a lower angle of attack compared to the wing root. The wings were most noticeably twisted just after stroke reversal (figure 1.18f), where a torsional wave passes along the wing from wing tip to wing root.

Wing twist is often used on other rotating wings, such as propellers and wind turbines, to maintain a constant pitch for each blade section and is also used on fix wing aircraft to control the wing's aerodynamic loading in order to prevent wing tip stall (McCormick 1995). Wing twist has been observed in a number of studies on different insect species (e.g. Jensen 1956; Weis-Fogh 1973; Wootton 1981; Ellington 1984c). However it wasn't until Usherwood & Ellington (2002a) investigated its effects on a rotating model hawkmoth wing that its role in insect flight was studied. They revolved the rigid model hawkmoth wings at a constant rotational velocity and measured the aerodynamic forces using a custom made force balance. The twisted model wings were also compared to a non-twisted flat wing. It was found that $15°$ of wing twist did not affect the aerodynamic force coefficients significantly, however $32°$ of wing twist resulted in lower maximum force coefficients.

Du & Sun (2008) also studied the effects of wing twist using a numerical model of a fruit fly wing undergoing a hovering flapping motion. The wing did not deform due to the aerodynamic and inertial loads but had a prescribed time-varying twist. Their results again showed that twist had little impact on lift and drag coefficients, exhibiting only a 1-2% variation in mean aerodynamic force coefficients from a non-twisted wing.

In contrast, Nakata & Liu (2012) used a fluid-structure interaction computational model of a hovering hawkmoth with both rigid and flexible wings. Their results revealed that a combination of spanwise wing bending and wing twist produced increased aerodynamic forces and improved hovering efficiency for the flexible wing.

1.4.2.2   Wing Camber

Wing camber is the chordwise bending of the wing that produces either a convex shape (positive camber) or a concave shape (negative camber) of the wing's top surface. Walker *et al.* (2010) measured the time variation of the wing camber throughout the

flapping cycle of free flying hoverflies and found that it was positive for both half cycles, i.e. the wing reversed shape at stroke reversal. The magnitude of camber varied for each of the flies that was tested but was between 5-12% at midstroke. For each hoverfly the magnitude of camber was approximately constant across the majority of the wing's span.

For a conventional aircraft wing, which requires attached flow in order to operate, positive camber is beneficial as it increases the lift coefficient for a given angle of attack over the linear range of the lift coefficient versus angle of attack curve (McCormick 1995). However, for thin insect wings at high angles of attack the flow separates from the wing's leading-edge and therefore conventional reasoning for camber does not apply to insect flight (Usherwood & Ellington 2002a).

Early studies into the effect of camber on insect wings had mixed results. Jensen (1956) measured the aerodynamic force on locust wings in a wind tunnel and found that a cambered forewing produced more lift than a non-cambered forewing. Vogel (1967) also used a wind tunnel to measure the aerodynamic forces acting on model fruit fly wings. He found that a small amount of wing camber considerably increased lift with a small drag penalty. Conversely, Dickinson & Gotz (1993) measured the aerodynamic forces on flat and cambered two-dimensional wings using a towing tank and found negligible difference between the two. These studies ignored the effects of wing rotation, but later studies have shown that the wing's rotation is important for generation of an attached LEV (see §1.3.1.3).

Usherwood & Ellington (2002a) were the first to investigate the use of camber for a rotating insect wing. They used their rotating model hawkmoth wing rig to measure the aerodynamic forces on wings with 0%, 7% and 10% camber. The observed changes in force coefficients were found to be within the experimental error and so could not be attributed to aerodynamic effects.

In contrast, later rotating and flapping wing studies have shown that positive camber increases the aerodynamic performance of the wing. Altshuler *et al.* (2004) measured the forces on a revolving model hummingbird wing and found that when the wing model was cambered like a real hummingbird's wing (5% camber) the lift coefficients increased. Tsuzuki *et al.* (2007) measured the aerodynamic forces on rotating rectangular wings used for rotary-winged MAVs. They used a figure of merit parameter, which was based on the thrust and torque coefficients, as a measure of the hovering aerodynamic

37

performance of the rotor. Results showed an increased maximum figure of merit up to 10% camber, which reduced after that. The maximum figure of merit occurred around $20°$ angle of attack, however at angles between $30° - 50°$, at which insects typically fly, the figure of merit continued to increase up to 15% camber. Du & Sun (2008) used a numerical model of a fruit fly wing undergoing a flapping motion in hover to study the effects of wing twist and camber. The wing did not deform due to the aerodynamic and inertial loads but had a prescribed time-varying twist and camber. Their results showed that increasing camber up to 10% increased lift and the lift on drag ratio. They showed that by using a combination of $20°$ wing twist and 6% camber lift could be increased by 10-20% and that the lift on drag ratio could be increased by 10% compared to a rigid flat wing case. Two Reynolds numbers (200 and 4000) were considered and it was found that the effect of camber increased for the higher Reynolds number case. Gopalakrishnan & Tafti (2010) coupled a linear elastic membrane solver with an unsteady large eddy simulation (LES) to model the aerodynamic forces and deformation of a rectangular wing planform undergoing a vertical flapping motion in forward flight. They found that a wing with low pre-stress, which resulted in it deforming to 25% camber, produced 40% more thrust than a rigid wing. Lift production was also found to improve.

Conversely, Zhao *et al.* (2010) measured the aerodynamic forces on rotating flexible wings that created negative camber and showed that this degrades the wing's lift.

Despite the importance of the LEV for flapping flight, only a few studies have investigated the effect of wing camber on the vortex structures around a flapping or rotating wing. Zhao *et al.* (2011b,a) found that the degree of trailing-edge flexion strongly correlated with the magnitude of vorticity at the leading-edge. Du & Sun (2008) suggested that the LEV is distorted by positive wing camber, however details of what this distortion entailed were omitted. Gopalakrishnan & Tafti (2010) showed that for a rigid flat wing the LEV lifts off from the surface near the wing tip, which resulted in low force production in this region. They suggested that the increase in thrust and lift found in their models of flexible wings was due to the cambered wing maintaining an attached LEV along a larger proportion of the wing's span compared to the rigid flat wing.

1.5   Summary

In the last two decades or so, much work has been done that has significantly improved our understanding of the aerodynamics of insect flight. These studies have highlighted the importance of stroke kinematics in determining unsteady flight forces (Weis-Fogh 1973; Dickinson *et al.* 1999; Sane & Dickinson 2001) and the generation of a stable leading-edge vortex which provides insect wings with additional circulation and enhanced lift (Ellington *et al.* 1996; Usherwood & Ellington 2002a; Birch *et al.* 2004). However, despite the variety of wing shapes seen in nature, the effect of the wing's geometry on the aerodynamic performance of a flapping wing is still not understood. Furthermore, little effort has been made to link changes in wing morphology to variations in fluid structure. This information is vital in understanding the effect of such parameters.

1.5.1   Aspect Ratio

One critical wing design parameter for large aircraft is wing aspect ratio, however the effect of this parameter for flapping and rotating wings in insect-like flight regimes is not well understood. Noticeably, different insects have different wing aspect ratios and many insects have relatively low aspect ratio wings compared to most conventional fixed wing aircraft. Seemingly contradictory results have been reported in the literature (Usherwood & Ellington 2002b; Luo & Sun 2005; Tsuzuki *et al.* 2007; Ansari *et al.* 2008) and it is still unclear whether aspect ratio is a significant design parameter for optimal aerodynamic performance in insect/MAV flight.

Due to the wing's rotation, changing the wing's aspect ratio by stretching the wing in either the chordwise or spanwise directions also changes the Reynolds number. This issue is not addressed in any of the studies involving aspect ratio, and given the significant variation in the LEV's structure with Reynolds number this effect may account for the differences in reported forces with aspect ratio.

Moreover, it has been suggested that it is the low Rossby number rotation of the wing that is required for LEV stability, and that the Rossby number is equal to the wing's aspect ratio for hovering flight (Lentink & Dickinson 2009b). This indicates that there should indeed be a change in the LEV's characteristics with aspect ratio as low aspect ratio wings would be required in order for the LEV to be stable. However, the manner in which the LEV's structure changes with aspect ratio is not clear.

A study into the effect of wing aspect ratio has been undertaken in order to address these questions. This investigation has been split into two parts. The first part provides an initial investigation into the effect of aspect ratio on the structure of the LEV. The primary aim of this is to decouple the effects of aspect ratio from those of Reynolds number. This was achieved using a rotating-wing model (see §2.2) to simulate the flow around different aspect ratio wings at various Reynolds numbers and the results of this study are presented in chapter 3. The second part of this investigation applies what was learnt in the previous study to a more complex flapping-wing model (see §2.3) which is used to explore the change in vortex structures over various aspect ratio wings at different advance ratios. The aim of this study is to address the role that the wing aspect ratio plays in determining the stability of the LEV. Furthermore, the results of this study provide a more detailed description of the effect that wing aspect ratio has on the aerodynamic performance of a flapping wing, and therefore the significance of wing aspect ratio as a design parameter for insect/MAV flight is addressed. Chapter 4 of this thesis details the results of this study.

1.5.2 Wing Camber

Wing deformation is observed during the flight of some insect species (e.g. Weis-Fogh 1973; Wootton 1981; Ellington 1984c) and is a result of the wing's passive response to inertial and aerodynamic forces during flight. Wing deformation is observed as wing twist, camber and spanwise bending. Most investigations into the flow around flapping and rotating wings have been performed under the assumption that the wing is rigid and flat, and consequently, the effect of these wing deformations on the LEV is still unclear.

Wing camber is of particular interest because of its potential to improve the wing's aerodynamic performance (e.g. Tsuzuki *et al.* 2007; Du & Sun 2008; Young *et al.* 2009). For conventional aircraft with attached flow, positive wing camber is generally advantageous. However, for thin insect wings at high angles of attack the flow separates from the wing's leading-edge and therefore conventional reasoning for camber does not apply to insect flight (Usherwood & Ellington 2002a). Consequently, an alternative explanation is required. Furthermore, despite the importance of the LEV for flapping flight, few studies have investigated the effect of wing camber on the vortex structures around a flapping or rotating wing. A clear understanding of how the LEV varies with

camber is vital in order to formulate this explanation.

Therefore, a study into the effect of wing camber has been undertaken in order to address these questions. The aim of this study is to reveal how the vortex structures around the wing change with camber in order to understand how wing camber results in improved aerodynamic performance under insect flight conditions. The results of this study are presented in chapter 5 of this thesis.

Chapter 2

Methodology

This chapter presents an overview of the computational methods used for the simulations conducted for this thesis. Two computational fluid dynamics (CFD) models were developed, an impulsively started rotating-wing model and a flapping-wing model, using the commercial finite-volume based code ANSYS CFX. CFX was chosen for this study as it is a well validated and robust solver that has the ability to solve the governing equations in a rotating frame of reference. It is also capable of parallelization and a large number of high-performance computing licences were available at the time of this study.

In this chapter the governing equations and solution strategy are first introduced, which includes the discretization schemes that were employed for both CFD models. The details of the rotating-wing model are then outlined, followed by the flapping-wing model. For each computational model, the wing geometry and kinematics are introduced, followed by the specified boundary conditions and mesh generation. Validation studies were also undertaken for each model to check for mesh, timestep and domain size independence. The results of these studies are presented at the end of each model's section.

2.1   Numerical Method

As presented in §1.1, the flow around flapping and rotating wings is governed by the Navier-Stokes equations cast in a non-inertial rotating frame of reference. In order to minimise numerical error the "alternate rotation model" was used. In this model the flow solver advects the absolute frame velocity instead of the rotating frame velocity. This reduces the numerical error for simulations in which the absolute frame velocity is a constant but the relative frame velocity has a high swirl component (ANSYS 2010a).

Thus, the velocity in the advection and transient terms of the momentum equation were modified to involve the absolute frame velocity rather than the rotating frame velocity. The equations that were solved for both the rotating-wing model and the flapping-wing model were written in the form

$$\frac{\partial \rho \boldsymbol{u_{abs}}}{\partial t} + \boldsymbol{\nabla} \cdot (\rho \boldsymbol{u} \boldsymbol{u_{abs}}) = -\nabla p + \boldsymbol{\nabla} \cdot \boldsymbol{\tau} - \rho \boldsymbol{\Omega} \times \boldsymbol{u} - \rho \boldsymbol{\Omega} \times (\boldsymbol{\Omega} \times \boldsymbol{r}) \qquad (2.1)$$

and

$$\boldsymbol{\nabla} \cdot \boldsymbol{u} = 0. \qquad (2.2)$$

Here, $\boldsymbol{u}$ and $\boldsymbol{u_{abs}}$ are the velocity vectors in rotating and absolute frames respectively, and $\boldsymbol{\tau}$ is the stress tensor, which is defined as

$$\boldsymbol{\tau} = \mu(\boldsymbol{\nabla u} + (\boldsymbol{\nabla u})^T - \frac{2}{3}\boldsymbol{I}\boldsymbol{\nabla} \cdot \boldsymbol{u}), \qquad (2.3)$$

where $\boldsymbol{I}$ is the identity matrix. Note that the Coriolis and centrifugal terms have been moved to the right-hand side of equation 2.1 and the angular acceleration of the fluid is included in the transient term as $\boldsymbol{u_{abs}} = \boldsymbol{u} + \boldsymbol{\Omega} \times \boldsymbol{r}$.

Due to the relatively low Reynolds numbers ($120 \leq Re \leq 1500$) considered in this study, a direct numerical simulation (DNS) approach could be undertaken, without the need for complex turbulence models. Hence, these equations were solved directly using ANSYS CFX. CFX uses an element-based finite-volume method for the discretization of the governing equations onto the numerical grid. In a finite-volume method the relevant quantities, such as mass and momentum, are conserved locally within each control volume. The formally second-order accurate specified blend factor scheme (with $\beta = 1$) was used for the advection term, where the solution variable, ψ, is evaluated at each integration point using

$$\psi_{ip} = \psi_{up} + \beta \nabla \psi \cdot \Delta \boldsymbol{r}, \qquad (2.4)$$

where ψ_{up} is the value of the variable at the upwind node, $\nabla \psi$ is equal to the average of the adjacent nodal gradients and $\Delta \boldsymbol{r}$ is the vector from the upwind node to the integration point. A second-order backward Euler scheme was used for the time evolution term

$$\frac{\partial}{\partial t} \int \rho \psi dV \approx V \frac{1}{\Delta t} \left(\frac{3}{2}(\rho \psi)_n - 2(\rho \psi)_{n-1} + \frac{1}{2}(\rho \psi)_{n-2} \right), \qquad (2.5)$$

where Δt is the time step, n represents the solution value at the current time step and V is the integration volume. The spatial derivatives that are used to evaluate the

pressure gradient and diffusion terms were calculated using tri-linear shape functions. For more information see ANSYS (2010b).

The equations were solved iteratively until a convergence criterion was met, before being marched forward in time. This criterion was applied to the three components of velocity and the pressure field and was set to be when the root mean square of the residual value was below 1×10^{-5} for the impulsively started rotating-wing model and 5×10^{-5} for the flapping-wing model. This convergence criterion was typically achieved within three coefficient loop iterations for the rotating-wing model and four coefficient loop iterations for the flapping-wing model.

2.2 Impulsively Started Rotating-Wing Model

As discussed in §1.2.1, an impulsively started wing rotating about its base has been shown to be a good approximation to a half cycle of a typical insect flapping stroke except without the complication of stroke reversal (Poelma *et al.* 2006; Lentink & Dickinson 2009b). This model was selected for the first aspect ratio (chapter 3) study and the wing camber (chapter 5) study as this model allows a quasi-steady flow state to be developed and maintained for the majority of the wing's motion and thus the effects of these wing shape parameters during a simulated half cycle could be clearly identified.

2.2.1 Geometry and Kinematics

The wing was modelled as a rigid plate with square edges, with a thickness of 3% of the mean chord. The planform shape was based on a generic fruit fly wing (*Drosophila Melanogaster*). This planform was chosen as it has been studied extensively both computationally (Liu & Aono 2009; Kweon & Choi 2010) and experimentally (Birch & Dickinson 2001; Birch *et al.* 2004; Poelma *et al.* 2006; Lentink & Dickinson 2009b). The wing was scaled to have a wing span of 2.47mm and an aspect ratio of 2.91, similar to that of an actual fly's wing (Zanker 1990). For the aspect ratio study this wing shape was stretched to produce wings of different aspect ratios between 2.91 and 7.28 to reflect the variety seen in nature (for examples see Ellington 1984b; Shyy *et al.* 2010).

For the wing camber study the original $AR = 2.91$ wing was used throughout the study. The wing's camber was defined by the equations for the mean camber line (y_c)
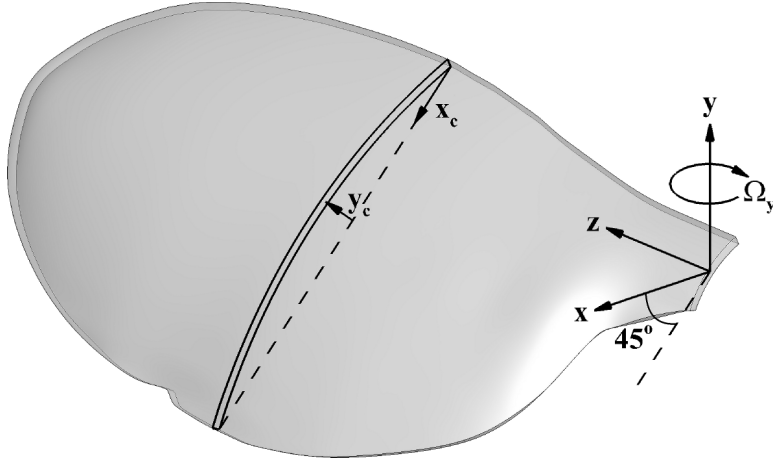
FIGURE 2.1: Schematic of the coordinate system and cambered fly wing geometry with $m/c = 0.1$ and $p/c = 0.5$.

of a NACA four-digit wing section, as given by

$$y_c = \begin{cases} \frac{m}{p^2}(2px_c - x_c^2), & x_c \leq p \\ \frac{m}{(1-p)^2}[(1 - 2p) + 2px_c - x_c^2], & x_c > p, \end{cases} \tag{2.6}$$

where m is the maximum ordinate of the camber line, p is the chordwise position of the maximum ordinate and x_c is the abscissa of a point on the chord line. This equation was applied locally along the wing's span in order to maintain the same planform shape between each wing. The magnitude of camber was varied in the interval $-0.15 \leq m/c \leq 0.2$ and three chordwise positions of maximum camber were considered, $p/c = 0.25, 0.5$ and 0.75. An example of a cambered fruit fly wing is shown in figure 2.1 as well as the wing fixed coordinate system used in this model.

For both studies, each wing was prescribed the same kinematic motion, which consisted of a rotation about the wing's base (y-axis) at a constant angle of attack of $45°$. The wing was initially at rest in still fluid ($\boldsymbol{u_{abs}} = 0$) and was accelerated over a period of $t = 0.084T$ before rotating at a constant rotational velocity Ω. This kinematic motion is described by equation 2.7 where T is the total simulation time,

$$\Omega_y(t) = \begin{cases} \frac{1}{2}\Omega(1 - \cos(\frac{\pi t}{0.084T})), & t < 0.084T \\ \Omega, & t \geq 0.084T. \end{cases} \tag{2.7}$$

The simulation was stopped after the angle through which the wing had rotated (ϕ) had reached $270°$. As will be shown in chapter 3, this allowed ample time for a quasi-steady flow state to become established.

46

In these simulations the Reynolds number was calculated using the velocity at the radius of gyration (U_{rg}) and the mean chord length ($\bar{c}$), and changes in Reynolds number were achieved by altering the fluid's viscosity in order to maintain the same kinematics. Reynolds numbers between 120 and 1500 where investigated using this model which correspond to fruit fly scale and house fly or bee scale respectively. Similarly, the lift, drag and net force coefficients were calculated as $C_L = 2L/\rho U_{rg}^2 S$, $C_D = 2D/\rho U_{rg}^2 S$ and $C_F = 2\sqrt{L^2 + D^2}/\rho U_{rg}^2 S$ respectively, where S is the wing area and L and D are the aerodynamic forces acting in the y and x directions respectively.

2.2.2 Domain Setup

The wing was located in the centre of a cylindrically shaped computational domain whose axis was coincident with the rotation axis of the wing. The domain size was selected from the domain sizing study (see §2.2.3.3) and resulted in a diameter of 18 times the wing span and a length of 48 times the average wing chord. The boundary condition on the outer cylindrical surface was a free-slip wall condition ($u_n = 0$), while for the top and bottom circular surfaces fluid was allowed to flow into and out of the domain with the average pressure across each boundary held at zero gauge pressure (see figure 2.2). A no-slip boundary condition was applied at the wing's surface.

The computational domain was meshed using an unstructured tetrahedral mesh with a region of triangular prism elements near the wing's surface. Four mesh refinement zones were used to control the mesh sizing around the wing. These refinement zones are shown in figure 2.3 and consist of a near wing region, near wake region, outer wing region and a far wake region. The size of each of the refinement boxes was adapted for the different aspect ratio and camber wings to ensure mesh consistency for each wing shape change. A maximum element size was prescribed for each of these zones and the mesh transitioned between each region at a growth rate of 1.2, except for both of the wake zones where a growth rate of 1.1 was applied. The final surface mesh on the wing's surface, the refinement zone boundaries and the domain boundary, as determined by the mesh resolution study, is shown in figure 2.4 to give an indication of the relative mesh size between each zone. Mesh was concentrated in the region of interest; around the wing and in the near wake box.

The size of the mesh on the wing's top and bottom surfaces was also controlled and was set to be half the element size of the near wing zone. Furthermore, the mesh size
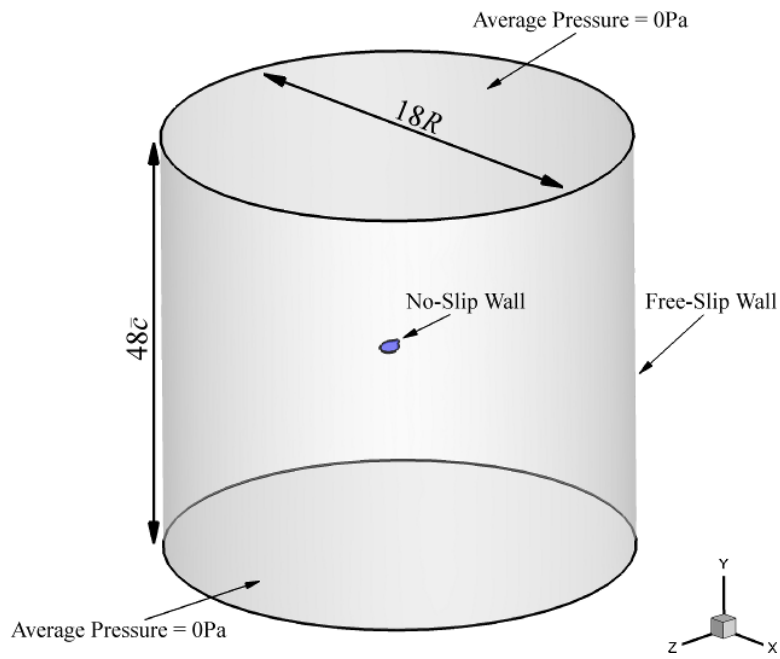
FIGURE 2.2: Computational domain and imposed boundary conditions. The wing is shown in blue.
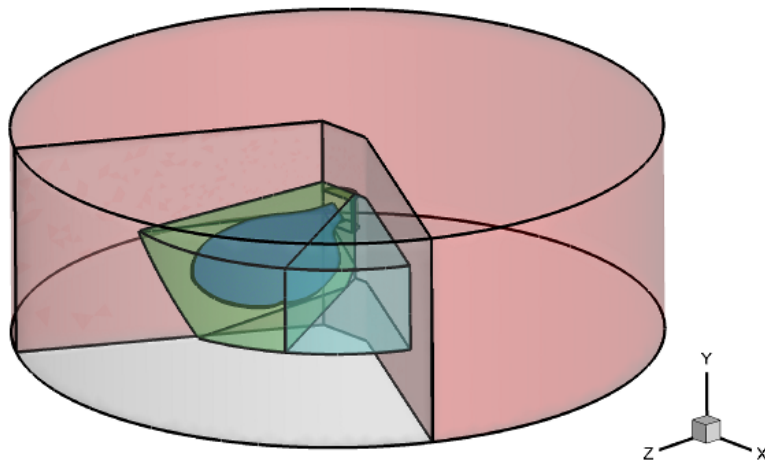

FIGURE 2.3: Mesh refinement zones around the wing; near wing (green), near wake (light blue), outer wing (light grey) and far wake (red). The wing is shown in blue.
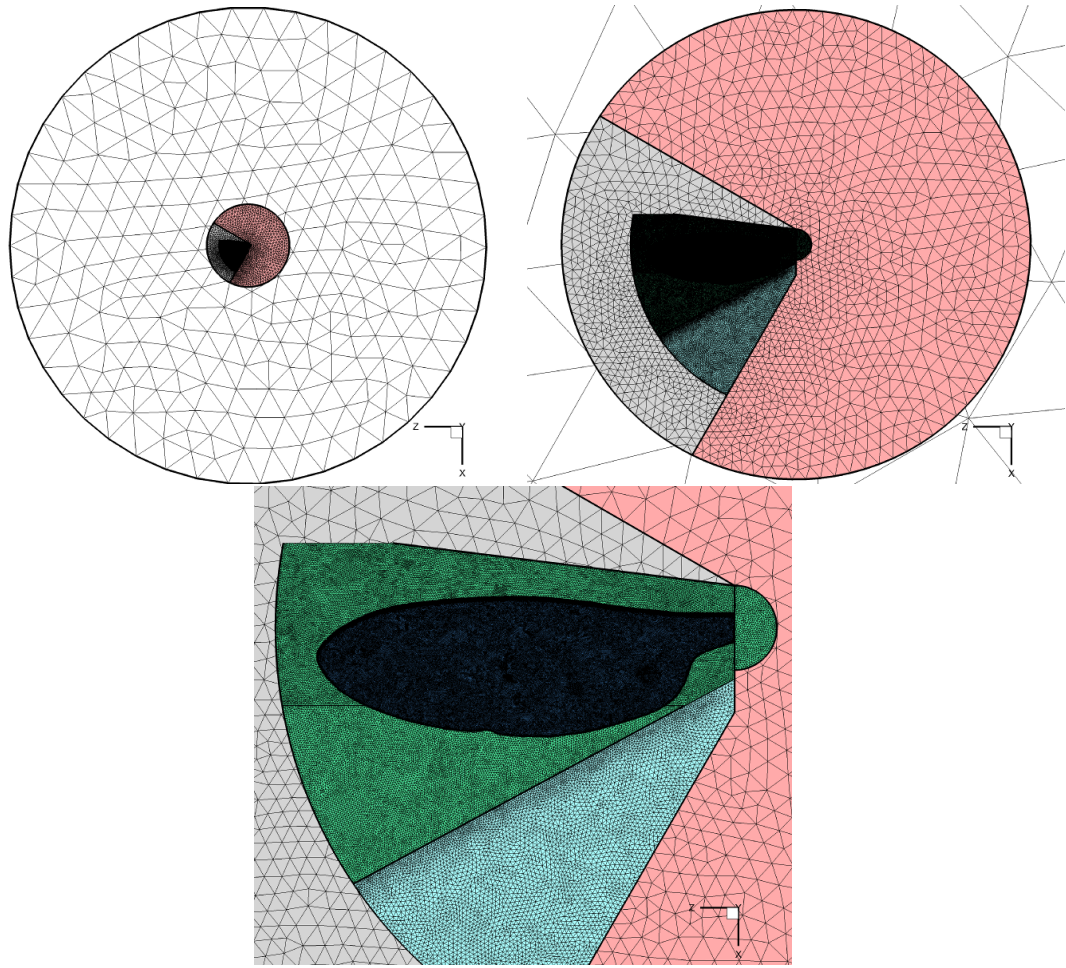
FIGURE 2.4: Successively zoomed in images of the surface mesh on the wing's surface, refinement zone boundaries and the domain boundary. Images show a top down view of the domain. The surface mesh colouring on the wing and the refinement zone boundaries is as in figure 2.3 and the domain boundary mesh is white.

around the wing's edge was set to half that again to ensure that there were sufficient elements across the wing's thickness. A region of triangular prism elements were meshed around the wing's surface in order to resolve the velocity gradients in this area. This boundary layer mesh was generated using 23 layers with a growth rate of 1.2 and a maximum thickness of 0.1mm. A cut through the volume mesh at approximately 50% span is shown in figure 2.5 which shows the boundary layer mesh on the wing, as well as the volume mesh in the surrounding refinement zones.
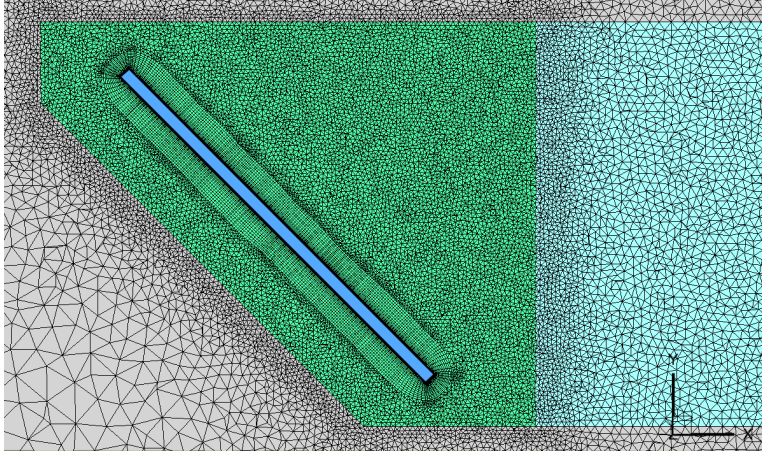
FIGURE 2.5: Volume mesh at approximately 50% wing span. Mesh colouring consistent with figure 2.3.

2.2.3 Validation Studies

Mesh, timestep and domain sizing studies were conducted to ensure that numerical errors were below an acceptable level. These errors were estimated using the *grid convergence index* (GCI) method outlined by Roache (1998, 2003). The validation studies were performed using a flat non-cambered wing with an aspect ratio of 2.91.

The GCI is based on generalized Richardson extrapolation and involves the comparison of discrete solutions at different grid spacings. The GCI is a measure of the percentage that the computed value is away from the asymptotic numerical value and can be used to provide an error band on the grid convergence of the solution. Between two successive grid refinements the GCI on the coarse and fine girds is calculated by

$$GCI_{coarse} = \frac{r^p F_s |\epsilon|}{r^p - 1} \qquad (2.8)$$

and

$$GCI_{fine} = \frac{F_s |\epsilon|}{r^p - 1} \qquad (2.9)$$

respectively. The relative error, ϵ, is given by

$$\epsilon = \frac{f_2 - f_1}{f_1}, \qquad (2.10)$$

where f_2 and f_1 are the solution values on the coarse and fine grids respectively, r is the grid refinement ratio, p is the order of convergence and F_s is a safety factor. For a minimal two grid convergence study the order of convergence cannot be estimated

and so a theoretical value of p based on the order of the discretization scheme must be used. In such a case Roache (2003) recommends a conservative value for the safety factor of $F_s = 3$. However, when three or more grids are used p can be estimated from the discrete solutions, and as such, a more appropriate safety factor of $F_s = 1.25$ can be used.

When three (or more) grids are used the solutions can be checked to see if they are in the asymptotic range by calculating

$$\frac{GCI_{23}}{r^p GCI_{12}} \approx 1, \tag{2.11}$$

where GCI_{23} and GCI_{12} are calculated using equation 2.9 and are the GCI values using grids 2 and 3, and 1 and 2 respectively. Grid 1 is the finest and 3 is the coarsest.

2.2.3.1 Mesh Resolution

To explore spatial resolution effects, three grids were generated such that the element size on the wing's surface and in the surrounding fluid zones were successively halved. As an unstructured grid was generated, the refinement ratio between two successive grids was estimated using an effective refinement ratio

$$r = \left(\frac{N_1}{N_2}\right)^{\frac{1}{3}}, \tag{2.12}$$

where N_1 and N_2 are the number of mesh elements for the fine and coarse grids respectively. The refinement ratio between grids 2 and 3 was $r_{23} = 1.53$ and between 1 and 2 was $r_{12} = 1.71$.

In order to calculate the GCI the observed order of convergence must first be calculated. As the refinement ratio is not constant, the order of convergence was calculated using the iterative technique outlined by Roache (1998), where

$$p = \omega \rho + (1 - \omega) \frac{\ln(\beta)}{\ln(r_{12})} \tag{2.13}$$

and

$$\beta = \frac{(r_{12}^\rho - 1)\epsilon_{23}}{(r_{23}^\rho - 1)\epsilon_{12}}, \tag{2.14}$$

where ρ is the previous iterate for p, ω is a relaxation factor and ϵ_{12} and ϵ_{23} are calculated from equation 2.10 using grids 1 and 2, and 2 and 3 respectively.

The aerodynamic force coefficients, along with the calculated GCI values, are shown in tables 2.1 and 2.2 for each mesh at Reynolds numbers of 120 and 1500 respectively.

51

Mesh	Surface Size	Elements (million)	C_L value	C_L GCI(%)	C_D value	C_D GCI(%)	Circulation $\Gamma_z/(U_{rg}R)$	Circulation GCI(%)
3	$0.02857\bar{c}$	1.538	1.540	0.547	1.620	0.940	-0.4514	1.36
2	$0.01449\bar{c}$	5.490	1.543	0.251	1.609	0.066	-0.4556	0.198
1	$0.00725\bar{c}$	27.36	1.545	0.094	1.608	0.002	-0.4563	0.017

TABLE 2.1: Mesh resolution study at $Re = 120$ for rotating-wing model.

Mesh	Surface Size	Elements (million)	C_L value	C_L GCI(%)	C_D value	C_D GCI(%)	Circulation $\Gamma_z/(U_{rg}R)$	Circulation GCI(%)
3	$0.02857\bar{c}$	1.538	1.834	0.286	1.719	1.51	-0.6441	14.0
2	$0.01449\bar{c}$	5.490	1.837	0.102	1.701	0.177	-0.7153	1.59
1	$0.00725\bar{c}$	27.36	1.838	0.028	1.699	0.012	-0.7240	0.102

TABLE 2.2: Mesh resolution study at $Re = 1500$ for rotating-wing model.

Mesh 1 was selected for this study and had a GCI of less than 0.1%. The dimensionless total circulation ($\Gamma_z/(U_{rg}R)$) of the LEV at 50% wing span was also calculated from the flow solution for each mesh and is shown in tables 2.1 and 2.2. The circulation of the LEV was calculated by integrating the spanwise vorticity over the area defined by a contour of the Q criterion. The GCI method was applied to the circulation values to give an indication of the convergence of the flow field. The GCI for Mesh 1 was 0.102% or less for both Reynolds numbers.

2.2.3.2 Timestep Resolution

The temporal error was estimated at a Reynolds number of 1500 in a similar manner to the mesh refinement, where the lift coefficient, drag coefficient and LEV circulation were calculated using three successive timestep sizes. Here a constant refinement ratio of 2 was used and thus the order of convergence could be calculated directly using equation 2.15 (Roache 1998),

$$p = \frac{\ln\left(\frac{f_3 - f_2}{f_2 - f_1}\right)}{\ln(r)}. \tag{2.15}$$

Table 2.3 shows the result of the timestep refinement study. A timestep of $\Delta t = T/540$ was selected for this study, with a GCI of 0.68% for both C_L and C_D, as the GCI for timestep 1 was only marginally better and not worth the added computational cost. Convergence of the LEV circulation was not seen in this timestep resolution study and thus the GCI method could not be applied to this data. However, all of the circulation values were within 0.52% of each other and therefore it was assumed that the LEV

Timestep	Timestep Size ($\Delta t/T$)	C_L		C_D		Circulation	
		value	GCI(%)	value	GCI(%)	$\Gamma_z/(U_{rg}R)$	$\Delta(\%)$
3	1/270	1.842	1.10	1.706	1.13	-0.7195	0.056
2	1/540	1.836	0.684	1.700	0.682	-0.7153	-0.520
1	1/1080	1.832	0.425	1.696	0.412	-0.7191	-

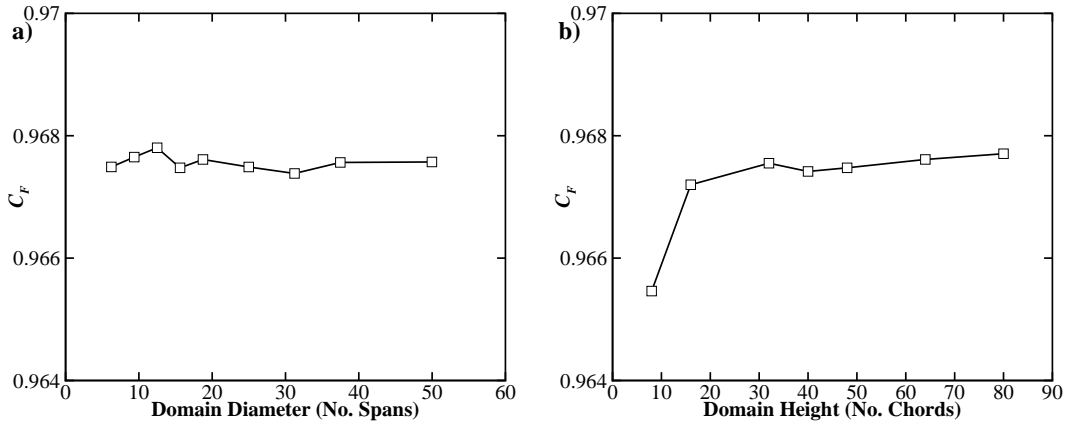TABLE 2.3: Timestep resolution study at $Re = 1500$ for rotating-wing model.

FIGURE 2.6: Variation of the net force coefficient with (a) the domain diameter and (b) the domain height.

circulation was independent of timestep size over the range of timesteps considered here.

2.2.3.3 Domain Size

For the domain size study both the height and diameter of the domain were independently varied. The variation in the net force coefficient with domain size is shown in figure 2.6. No clear trend was found between the aerodynamic force and the domain size, except at very small domain heights. At a domain height of 8 chord lengths the net force is only 0.23% below the value at a domain height of 80. The variation between the rest of the domain heights is less than 0.053% and the variation between the domain diameters is less than 0.024%. A domain height of 48 times the mean chord and a domain diameter of 18 times the wing span were chosen.

2.3 Flapping-Wing Model

While the rotating-wing model simulates hovering flight well, its implementation becomes problematic for forward flight due to the difference in relative velocities between
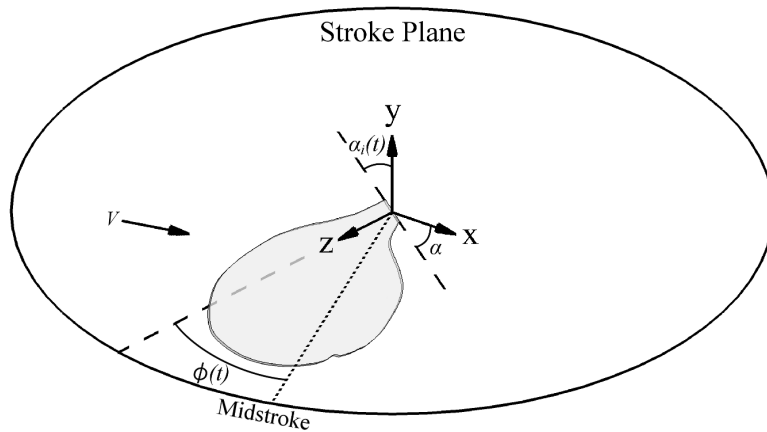
FIGURE 2.7: Schematic of fly wing geometry, kinematic angles and coordinate system. The origin of the coordinate system is located at the wing's root. The coordinate system rotates with the wing's stroke position (about the y-axis), but not the wing's pitch rotation (z-axis). Thus the zx-plane defines the wing's stroke plane with the z-axis aligned with the wing's span and the y-axis points vertically.

the up- and downstrokes. Therefore a flapping-wing model was developed for use in the second aspect ratio study (chapter 4), as this study investigated the effect of aspect ratio at different flight speeds. The flapping-wing model provides a more realistic representation of insect flight and also extends on the rotating-wing model as it includes the effects of stroke reversal.

2.3.1 Geometry and Kinematics

The wing was again modelled as a rigid plate with square edges with a thickness of 3% of the mean chord and the planform shape was based on a generic fruit fly wing. The wing was scaled to have a wing span of 2.47mm and an aspect ratio of 2.91, similar to that of an actual fly's wing (Zanker 1990). This wing shape was again stretched to produce wings of different aspect ratios between 2.91 and 7.28 to reflect the variety seen in nature. An example of the fruit fly wing is presented in figure 2.7 as well as the coordinate system used in this model.

In this study a "normal hovering" (Weis-Fogh 1973) type of kinematics was used as a simplification of a real insect's flapping stroke, where the wing's stroke plane is horizontal. The wing's motion can be described by the temporal variation of two kinematic angles; the stroke position angle ($\phi(t)$) and the angle of incidence ($\alpha_i(t)$). These angles are depicted in figure 2.7, where the stroke position angle is the angle
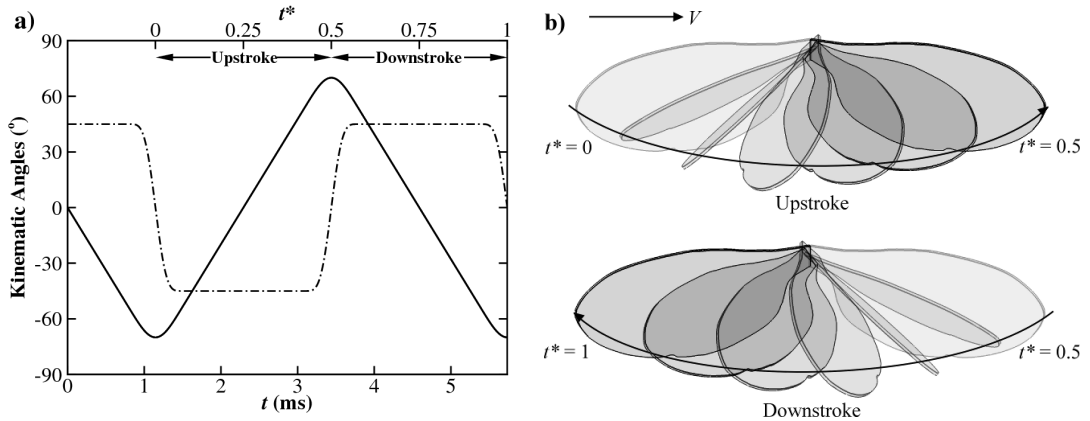
FIGURE 2.8: Wing kinematics plots. (a) Time variation of kinematic angles for the first 1.25 cycles. Dimensionless time (t^*) is also shown at the top where $t^* = 0$ at the beginning of the upstroke. Solid line is the stroke position angle ($\phi(t)$) and dashed line is the angle of incidence ($\alpha_i(t)$). (b) Schematic of the wing's motion and freestream velocity (V).

between the z-axis and the midstroke line, and the angle of incidence is the angle between the wing's chord line and the stroke plane's normal vector (y-axis). Figure 2.8a shows the temporal variation of these two kinematic angles over the first 1.25 cycles. A dimensionless time (t^*) is also defined that varies between zero and one for each flapping cycle, where the upstroke is between $0 \leq t^* \leq 0.5$ and the downstroke is between $0.5 \leq t^* \leq 1$. A schematic of the wing's motion is also shown in figure 2.8b, which highlights the relative motion of the wing for the up- and downstrokes compared to the freestream velocity (V).

Insects that use this type of flapping kinematics for hovering flight typically tilt their wing's stroke plane in order to produce thrust to achieve forward flight (e.g. Willmott & Ellington 1997a; Dudley & Ellington 1990). The amount of stroke plane tilt that is required at a particular flight speed depends on the thrust that is required to overcome the insect's body drag and can be quite large for high advance ratios. Additionally, under these forward flight conditions the wing's angle of attack is no longer constant along the wing's span due to the component of freestream velocity that acts normal to the stroke plane. Insects also adjust their wing's pitch angle kinematics to fit the advance ratio and stroke plane angle (Ellington 1999; Sun 2003). The degree to which the wing's angle of attack and stroke plane angle vary with advance ratio depends on the insect. As this study was of a more general nature, a simplification was made whereby all simulations were run with a horizontal stroke plane and constant wing kinematics,

regardless of the advance ratio. This was done to simplify the analysis as it allowed a constant stroke plane angle with advance ratio and for the wing's angle of attack to remain constant between advance ratios and along the wing's span.

The wing's kinematics consisted of a rotation about its base (y-axis), where the wing's stroke position ($\phi(t)$) followed a smoothed triangular motion (see figure 2.8). A smoothed triangular motion has been used previously to simulate a fruit fly's hovering stroke (Sane & Dickinson 2001; Poelma *et al.* 2006) and allowed a more direct comparison to the previously described impulsively started rotating-wing model (§2.2) than a sinusoidal motion. The wing's stroke position was described by equation 2.16 where t is the time from mid-downstroke,

$$\phi(t) = \begin{cases} -\Omega t, & t \leq \frac{T}{4} - t_r \\ 2t_r(\Omega t_1'^2 - \Omega t_1' + \frac{\Omega}{2\pi^2}\cos(2\pi t_1')) - \Omega(\frac{T}{4} - t_r + \frac{t_r}{\pi^2}), & \frac{T}{4} - t_r < t < \frac{T}{4} + t_r \\ \Omega t - \Omega\frac{T}{2}, & \frac{T}{4} + t_r \leq t \leq \frac{3T}{4} - t_r \\ -2t_r(\Omega t_2'^2 - \Omega t_2' + \frac{\Omega}{2\pi^2}\cos(2\pi t_2')) + \Omega(\frac{T}{4} - t_r + \frac{t_r}{\pi^2}), & \frac{3T}{4} - t_r < t < \frac{3T}{4} + t_r \\ -\Omega t + \Omega T, & t \geq \frac{3T}{4} + t_r, \end{cases}$$

(2.16)

where

$$t_1' = (t - \frac{T}{4} + t_r)/(2t_r)$$

(2.17)

and

$$t_2' = (t - \frac{3T}{4} + t_r)/(2t_r).$$

(2.18)

The constant rotational velocity of the wing (Ω) during the up- and downstroke is dependent on the peak to peak amplitude (Φ) of the wing's stroke and can be calculated by the function, $\Omega = \Phi/(\frac{T}{2} - t_r + \frac{4t_r}{\pi^2})$, where T is the period of a flapping cycle and t_r is half the stroke reversal time, i.e. around stroke reversal the function is smoothed over a period of $2t_r$. In order to completely define $\phi(t)$, values for the flapping frequency (n), peak to peak amplitude and stroke reversal time are required. Values of $n = 218\text{Hz}$ and $\Phi = 140°$ were chosen and are representative a real fruit fly's kinematics (Fry *et al.* 2005). A stroke reversal time of 16% of the flapping period was used, i.e. $2t_r = 0.16T$. This value is typical of similar flapping wing studies (e.g. Sane & Dickinson 2001; Poelma *et al.* 2006; Jardin *et al.* 2012).

The wing's angle of incidence ($\alpha_i(t)$) varied according to a smoothed trapezoidal motion (see figure 2.8). Note that for clarity $\alpha_i(t)$ is not the wing angle of attack (α).

The time variation of $\alpha_i(t)$ is described by,

$$\alpha_i(t) = \begin{cases} 90 - \alpha_0, & t \leq \frac{T}{4} - t_r \\ \begin{aligned} &\frac{4(90-\alpha_0)}{3\pi}\sin(2\pi t_1') - 2(90-\alpha_0)t_1' \\ &\quad - \frac{90-\alpha_0}{6\pi}\sin(4\pi t_1') + 90 - \alpha_0, \end{aligned} & \frac{T}{4} - t_r < t < \frac{T}{4} + t_r \\ -(90-\alpha_0), & \frac{T}{4} + t_r \leq t \leq \frac{3T}{4} - t_r \\ \begin{aligned} &-\frac{4(90-\alpha_0)}{3\pi}\sin(2\pi t_2') + 2(90-\alpha_0)t_2' \\ &\quad + \frac{90-\alpha_0}{6\pi}\sin(4\pi t_2') - (90-\alpha_0), \end{aligned} & \frac{3T}{4} - t_r < t < \frac{3T}{4} + t_r \\ 90 - \alpha_0, & t \geq \frac{3T}{4} + t_r, \end{cases} \tag{2.19}$$

where α_0 is the angle of attack at mid-downstroke and was equal to $45°$, t_1' and t_2' are given by equations 2.17 and 2.18 respectively, and t_r is half the flip reversal time. Equation 2.19 was written such that the wing's pitch rotation occurred symmetrically around stroke reversal and $2t_r$ was set to 16% of the flapping period so that the duration of the wing's flip occurred over the same period as stroke reversal. The wing's pitch rotation axis was the z-axis and was estimated to be located at the mid-point of the wing's root chord length for real fruit flies (see figure 2.7). This position corresponded to 21.5% of the wing's maximum chord length referenced from the leading-edge. Both equation 2.16 and equation 2.19 where written such that the functions are smooth up to their third derivative. This was done to avoid artificial spikes in the aerodynamic forces due to discontinuities in acceleration at the start and end of each stroke reversal.

In chapter 3 it is demonstrated that by scaling the flow using the wing's span as the characteristic length, Reynolds number effects can be decoupled from aspect ratio effects when comparing results between differently shaped wings. Therefore this scaling is adopted here and the Reynolds number was calculated using the average velocity at the wing tip ($\bar{U}_{tip}$) and the wing's span (R). This Reynolds number represents an approximate average over the entire flapping cycle, as the effect of the freestream velocity (V) on $\bar{U}_{tip}$ over a complete flapping cycle averages out to zero. At non-zero advance ratios, due to the freestream velocity, the instantaneous Reynolds number is increased during the downstroke and decreased for the upstroke (see §4.3.2.1). Two span-based Reynolds numbers, of 613 and 7668, were considered in this study, which correspond the span-based Reynolds numbers for fruit flies and house flies respectively. Changing the Reynolds number between simulations was achieved by altering the fluid's viscosity. The lift and drag coefficients were calculated as $C_L = 2L/\rho\bar{U}_{rg}^2 S$ and $C_D = 2D/\rho\bar{U}_{rg}^2 S$ respectively, where $\bar{U}_{rg}$ is the average flapping velocity at the radius of gyration, L is the aerodynamic force acting in the y direction and D is the force opposing

the wing's rotation in the zx-plane.

The advance ratio was calculated using equation 1.8 and was used to set the freestream velocity which was applied perpendicular to the midstroke line (see figure 2.1). The wing was initially at rest in quiescent fluid ($\boldsymbol{u_{abs}} = 0$). At the start of the simulation the freestream velocity was applied to the domain boundary (see §2.3.2) and the wing's motion was started from mid-downstroke. The simulation was run for four complete flapping cycles, as determined from the number of flapping cycles validation study (see §2.3.3.1), and the results of the fourth cycle were recorded.

2.3.2 Domain Setup

Two computational domains were employed to construct the flow field for this model, an outer "stationary" domain and an inner "rotating" domain (see figure 2.9). The outer domain consisted of a cube with sides of 18 times the wing's span in length. In this domain, the fluid dynamic equations were solved in an inertial frame that moved at the insect's flight speed (V), i.e. equations 2.1 and 2.2 with the rotational terms removed and where $\boldsymbol{u} = \boldsymbol{u_{abs}}$. The stationary domain was aligned with the freestream flow such that four of the faces were parallel to the freestream and two were perpendicular. The parallel faces were assigned free-slip wall boundary conditions ($u_n = 0$), while the freestream velocity was prescribed uniformly across the upstream face and the average pressure across the downstream boundary was set to zero gauge pressure. These boundary conditions were applied when $J > 0$, however for the hovering simulations, when $J = 0$, the fluid was allowed to flow into or out of all six faces with the average pressure across each boundary set to zero gauge pressure.

The rotating domain was spherical in shape, with a diameter 7 times the wing's span, and was located in the centre of the stationary domain. The wing was located in this domain such that its base was situated on the centre point of the domain. This domain rotated about the wing's rotation axis (y-axis) according to equation 2.16, and as such the fluid dynamic equations were solved in a non-inertial rotating frame of reference (equations 2.1 and 2.2). A no-slip boundary condition was applied on the wing's surface and a *general grid interface* (GGI) connection was applied between the rotating and stationary domains to allow fluid flow between the two. The GGI connection uses a physically based intersection algorithm to connect the grid topology across the interface. A control surface approach is then applied to perform the connection. By using this
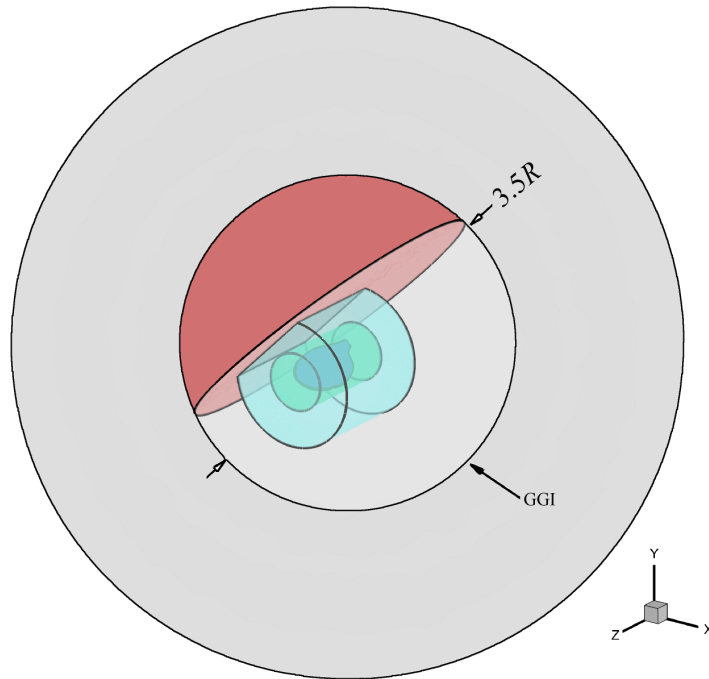
FIGURE 2.9: Computational domain and imposed boundary conditions for when $J > 0$. When $J = 0$ the boundary condition on all six outer faces is an average pressure of zero gauge pressure. The stationary domain is shown in light grey, the rotating domain is in dark grey and the wing is in blue.

approach strict conservation is maintained of the surface fluxes (mass, momentum, energy, etc.) for all equations across the interface. For more information see ANSYS (2010b).

The stationary domain was meshed using an unstructured tetrahedral mesh where the element size on the interface with the rotating domain was set to 0.25mm. The mesh was allowed to grow out from this surface at a rate of 1.4 until a maximum element size of 2mm was reached. The rotating domain was constructed using two non-conformal meshes. As shown in figure 2.10 the rotating domain consists of a smaller sphere of diameter 3.5 times the wing's span concentrically located inside the larger sphere. The mesh inside the small sphere was fixed to the wing and was allowed to rotate about the wing's spanwise axis (z-axis) according to equation 2.19. Thus an additional GGI connection was applied on the interface of the large and small spheres to enable the sliding mesh interface. The large sphere was meshed using a tetrahedral mesh with the element size on the interface set to 0.25mm, a growth rate of 1.4 and a maximum mesh size of 0.5mm. The small sphere was meshed with an unstructured tetrahedral

FIGURE 2.10: Mesh refinement zones within the rotating domain; near wing (green), near wake (light blue), far wake (light grey) and above wing (red). The wing is shown in blue.

mesh with a region of triangular prism elements near the wing's surface. Four mesh refinement zones were used to control the mesh size around the wing. These mesh refinement zones are shown in figure 2.10 and consist of a near wing region, near wake region, far wake region and an above wing region. The size of each of the refinement zones was adapted for the different aspect ratio wings to ensure mesh consistency for each wing shape change. A maximum element size was prescribed for each of these zones and the mesh transitioned between each region at a growth rate of 1.4. The size of the mesh on the wing's surfaces was also controlled and was set to be half the element size of the near wing zone for the top and bottom surfaces, and half that again around the wing's thickness. A region of triangular prism elements were meshed around the wing's surface in order to resolve the velocity gradients in this area. This boundary layer mesh was generated using 23 layers with a growth rate of 1.2 and a maximum thickness of 0.1mm. The tetrahedral mesh was allowed to grow out from the boundary layer mesh at a rate of 1.2 within the near wing region.

The surface mesh on the wing's surface, the refinement zone boundaries and the domain boundary, as determined by the mesh resolution study, is shown in figure 2.11
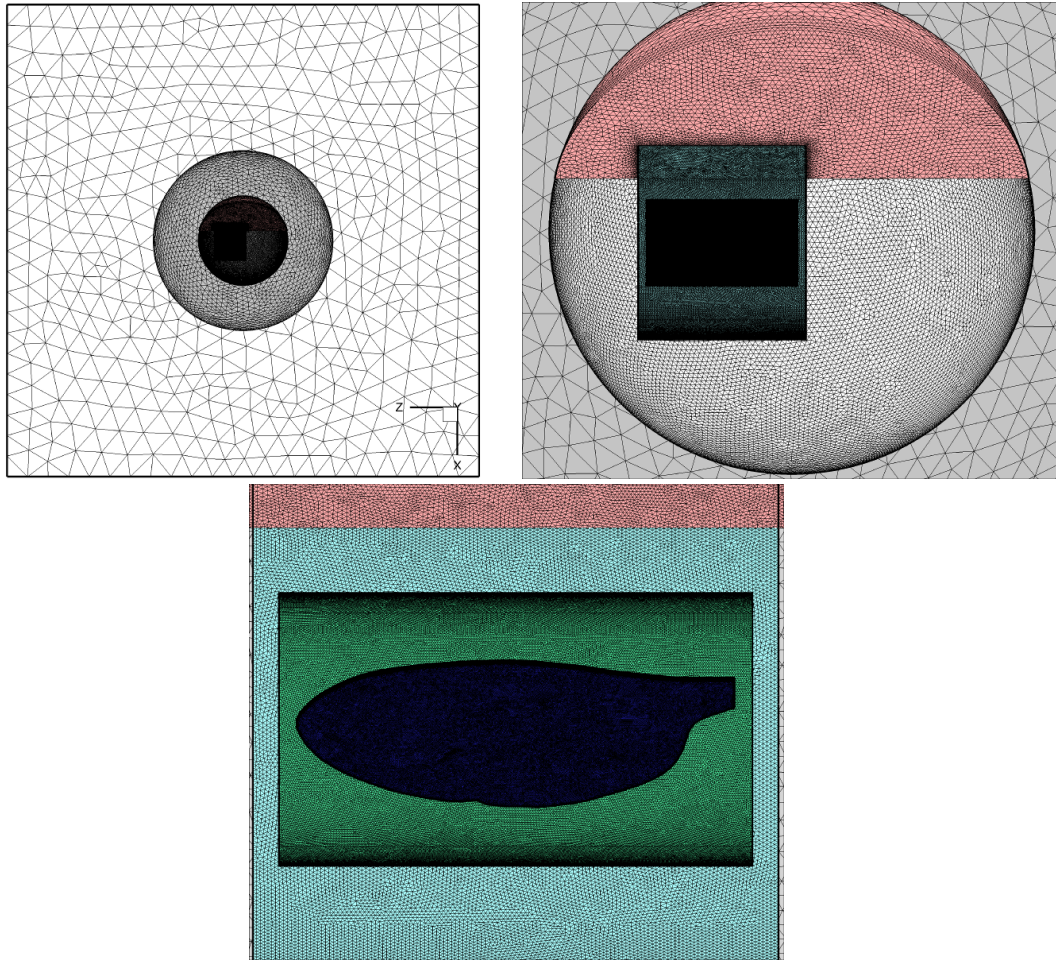
FIGURE 2.11: Successively zoomed in images of the surface mesh on the wing's surface, refinement zone boundaries and the domain boundary. Images show a top down view of the domain. The surface mesh colouring on the wing and the refinement zone boundaries is as in figure 2.10 and the domain boundary mesh is white.

to give an indication of the relative mesh size between each zone. Mesh was concentrated in the area of interest; around the wing and in the near wake region. A cut through the boundary layer mesh and the volume mesh in the surrounding refinement zones at approximately 50% span is also shown in figure 2.12.

2.3.3 Validation Studies

Mesh and timestep resolution studies were conducted to ensure that numerical errors were below an acceptable level. In addition, a study into the number of flapping cycles that are required to generate a stable flow field was conducted. The GCI method (Roache 1998, 2003), outlined in §2.2.3, was used to estimate the level of numerical
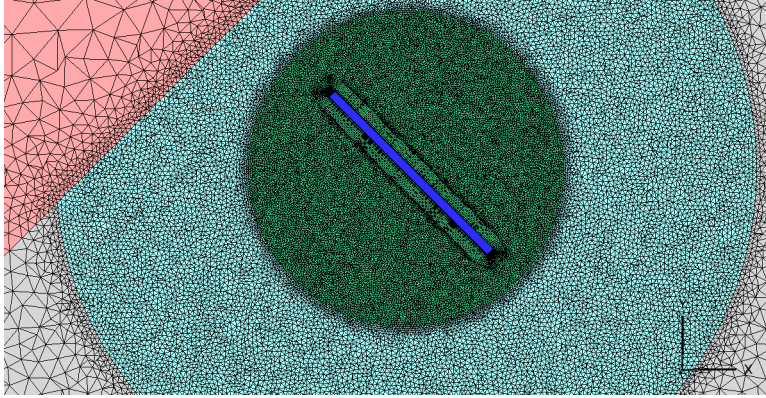
FIGURE 2.12: Volume mesh at approximately 50% wing span. Mesh colouring consistent with figure 2.10.

Number of Cycles	C_L		C_D		Circulation	
	ϵ	GCI(%)	ϵ	GCI(%)	$\Gamma_z/(U_{rg}R)$	GCI(%)
1	-	19.7	-	22.6	-0.6534	9.08
2	0.115	5.32	0.128	6.59	-0.7045	0.014
4	0.0308	1.43	0.0371	1.91	-0.7046	0.002

TABLE 2.4: Convergence of C_L, C_D and LEV circulation ($\frac{\Gamma_z}{U_{rg}R}$) with the number of flapping cycles.

error for these studies. These validation studies were performed using the fruit fly wing ($AR = 2.91$), however due to the increased computational cost of the flapping-wing model, these studies were limited to one Reynolds number ($Re_R = 7668$) and one advance ratio ($J = 0$).

2.3.3.1   Number of Flapping Cycles

Insects produce a strong downwash velocity jet below their wings that extends for approximately 1.5 times the insect's body length beneath the insect (Aono *et al.* 2008; Liu & Aono 2009). Naturally, it takes a number of flapping cycles to generate this far-field flow and this can affect the aerodynamic forces that are produced by the wing from cycle to cycle. The flapping-wing model was therefore run for four consecutive cycles, starting in quiescent fluid, to determine the number of cycles required to generate the far-field flow and to characterise the variation in lift and drag coefficients from cycle to cycle.

Table 2.4 shows the relative error and calculated GCI values for both the lift and drag coefficients for cycles 1, 2 and 4. The refinement ratio was based off the total

Mesh	Surface Size	Elements (million)	C_L		C_D		Circulation	
			ϵ	GCI(%)	ϵ	GCI(%)	$\Gamma_z/(U_{rg}R)$	GCI(%)
3	$0.02857\bar{c}$	4.099	-	9.27	-	10.6	-0.6496	12.4
2	$0.01449\bar{c}$	9.991	0.0339	5.04	0.0336	6.41	-0.7046	2.61
1	$0.00725\bar{c}$	49.26	0.0268	1.69	0.0305	2.60	-0.6911	0.160

TABLE 2.5: Mesh resolution study for flapping-wing model at $Re_R = 7668$.

simulation time and was therefore exactly two. Due to the significant fluctuation in aerodynamic forces throughout the flapping cycle, the relative error (equation 2.10) was calculated at each timestep throughout the flapping cycle and then averaged, and was not based off the cycle-averaged aerodynamic force coefficients. The GCI was calculated using equations 2.8 and 2.9. Table 2.4 shows a GCI of less than 2% for both lift and drag coefficients over the fourth cycle and thus the results of this model are taken from the fourth flapping cycle.

The circulation of the LEV was again used as a measure of the convergence of the flow field near the wing's surface. Here the circulation was calculated at 50% span and midway through the downstroke for each cycle. The computed dimensionless circulation for cycles 1, 2 and 4 are shown in table 2.4, which shows that by the fourth cycle the GCI was down to 0.002%.

2.3.3.2 Mesh Resolution

Mesh resolution was explored using three grids that were generated by halving the element size on the wing's surface and in the surrounding fluid zones. The refinement ratio was estimated from equation 2.12, which yielded a ratio of 1.35 between grids 2 and 3, and 1.70 between grids 1 and 2. The flow field was calculated on each mesh and the variation of the lift and drag coefficients throughout the fourth flapping cycle were compared. The relative errors for C_L and C_D were calculated at each timestep throughout the flapping cycle and then averaged, as was done for the number of flapping cycles study presented above. In addition, the circulation of the LEV was calculated at 50% wing span and at the mid-point of the downstroke of the fourth cycle. The order of convergence was again calculated using equations 2.13 and 2.14, and the GCI was calculated using equations 2.8 and 2.9.

The relative error and GCI values for both the lift and drag coefficients are shown in table 2.5 for the flapping-wing model at a Reynolds number of 7668, along with the
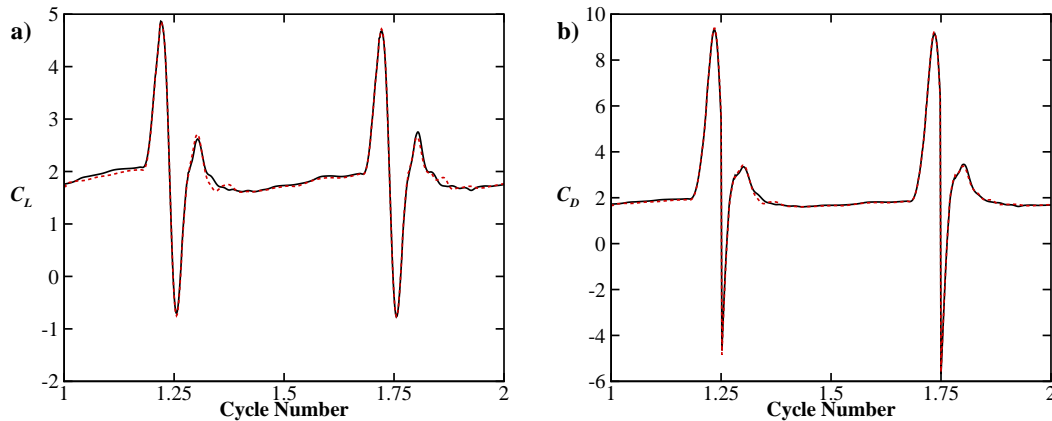
FIGURE 2.13: Comparison of lift and drag coefficients over the second cycle. Black line shows the results obtained using mesh 1 for both cycles. Red dotted line shows the results obtained after interpolating the solution from mesh 3 for the first cycle onto mesh 1 for the second cycle.

dimensionless LEV circulation and corresponding GCI estimates. The GCI value for the circulation of the LEV was calculated as 0.16% for mesh 1, while the GCI for the aerodynamic forces was found to be 2.6%. This mesh offered a significant improvement in numerical error over the intermediate mesh and was therefore selected for this study.

The choice of mesh 1 for this model, however, would have resulted in prohibitive computational cost if it was used for four complete flapping cycles. An alternative scheme was proposed whereby the simulation was run for 2.5 flapping cycles using mesh 3 in order to generate the far-field flow. The solution from this simulation would then be interpolated onto mesh 1 and the model would be run for a further 1.5 cycles. This would allow half a cycle (half the up stroke, dorsal reversal and half the downstroke) for the solution to "settle down" before the start of the fourth cycle. It was estimated that this approach would yield a 51% reduction in the total computational time of each simulation.

To test the validity of this method, a simulation was run in which mesh 3 was used for the first cycle and mesh 1 was used for the second cycle. The results from the second cycle were then compared to a simulation which used mesh 1 for both cycles. The difference in results from the second cycle is equivalent to the error introduced over the last half of cycle 3 and the first half of cycle 4 for the above mentioned scheme. A comparison of the lift and drag coefficients over the second cycle between these two solutions is shown in figure 2.13. While there is a slight difference in the lift and drag

Timestep	Timestep Size $(\Delta t/T)$	C_L		C_D		Circulation	
		ϵ	GCI(%)	ϵ	GCI(%)	$\Gamma_z/(U_{rg}R)$	GCI(%)
3	1/280	-	2.99	-	4.85	-0.6990	2.74
2	1/560	0.0178	0.763	0.0227	2.02	-0.7046	1.74
1	1/1120	0.0168	0.722	0.0190	1.69	-0.7082	1.10

TABLE 2.6: Timestep resolution study for flapping-wing model.

values in the first quarter of the cycle, after the first stroke reversal the two solutions follow each other very closely. At the half way point, the lift and drag coefficients are less than 1% off the "mesh 1 only" solution and the LEV circulation is less than 0.5% out. This point is equivalent to the start of the fourth cycle in a full simulation. A small variation between the two simulations can be seen in the lift coefficient after each stroke reversal, however a similar level of variation was also seen between half cycles over the fourth flapping cycle and is due to the complex wing-wake interaction that happens in this region of the flapping cycle. Furthermore, the average difference in aerodynamic forces over the last half a cycle is just 1.6%. It was therefore determined from these simulations that interpolating a coarse mesh solution onto the fine mesh only introduces a small amount of error and therefore the scheme to use mesh 3 for the first 2.5 cycles and mesh 1 for the next 1.5 cycles was adopted for this model.

2.3.3.3 Timestep Resolution

The effect of timestep resolution was investigated using a similar method to the mesh refinement. The variation of the lift and drag coefficients over the fourth flapping cycle were calculated using three successive timestep sizes. The refinement ratio between each timestep was 2 and so the order of convergence was calculated directly from equation 2.15. The relative error for the lift and drag coefficients were again calculated over the flapping cycle and averaged, while the LEV's circulation was calculated at 50% span, midway through the downstroke of the fourth cycle. The computed GCI values are shown in table 2.6. The GCI for the finest timestep was only marginally better than for timestep 2, but took twice the computational time to solve. As such timestep 2 was selected for this model. For a timestep of $\Delta t = T/560$ the largest estimate of the numerical error was 2% based on the drag coefficient.

Chapter 3

Aspect Ratio: Decoupling Aspect Ratio and Reynolds Number

3.1 Introduction

This chapter describes an investigation into the effect of aspect ratio on rotating wings at insect Reynolds numbers. The aim of this study is to decouple the effects of aspect ratio from those of Reynolds number in order to identify changes in the LEV's structure that are due to aspect ratio.

The impulsively started rotating-wing model was used for this study as it allowed a quasi-steady flow state to be developed on the wing. This made the effects of aspect ratio and Reynolds number clearly identifiable without the complication of stroke reversal. The effect of Reynolds number for a fruit fly wing ($AR = 2.91$) is first investigated and the change in the structure of the LEV with Reynolds number is highlighted. These results are also compared against the experimental investigations of Birch *et al.* (2004) and Lentink & Dickinson (2009b) to validate the numerical model.

The effect of aspect ratio at a constant Reynolds number is then explored. Due to the wing's rotation, changing the wing's aspect ratio either by chord or by span also changes the Reynolds number. To avoid this, the fluid viscosity was adjusted to maintain a constant Reynolds number between each aspect ratio wing. However, analysis of the vortex structures reveals that aspect ratio has the same effect as Reynolds number on the LEV. This finding shows that the aspect ratio results are still coupled with Reynolds number. An alternate scaling parameter is presented that decouples the effect of aspect ratio and Reynolds number. Finally, the applications to which this new scaling parameter can be employed are explored and a vortex breakdown criteria is tested.

3.2 Reynolds Number Effects for a Fly Wing

In this section, simulations of the fruit fly wing ($AR = 2.91$) are used to highlight the change in the aerodynamic forces and flow structures at various Reynolds numbers. Results at Reynolds numbers of 120 (fruit fly scale) and 1500 (house fly or bee scale) were used to validate the numerical model against similar experimental investigations.

3.2.1 Aerodynamic Forces

The time variation of lift and drag coefficients at Reynolds numbers of 120 and 1500 are compared to the experimental force measurements of Birch *et al.* (2004) in figure 3.1. Here, it should be noted that the current CFD model is not intended to be an exact replica of their experiment. The experimental wing had a cut-out at the wing's root to accommodate the force sensor. This was not included in the numerical model and so there are some differences in the wing's planform shape. In addition, the wing's angle of attack is 5° lower in the experiment, and in figure 3.1 the results are taken at Reynolds numbers of 1400 and 1500 for the experimental and numerical data respectively. Finally, the experimental wing reached a rotation angle of 240° compared to 270° in the CFD model, and the experimental data is truncated at some point between $\phi = 180°$ and $\phi = 240°$. This is why the experimental data stops at approximately $t/T = 0.75$. Nonetheless, the variation of the aerodynamic force is consistent with previously reported aerodynamic forces for impulsively started rotating wings (Dickinson *et al.* 1999; Birch *et al.* 2004), where there is an initial transient period in which the force coefficients reach a maximum, which is followed by a minimum, before the lift and drag coefficients recover and there is a period of approximately constant force production. The average lift coefficient over the period of steady force production for the CFD model is approximately 9% lower than the average experimental lift coefficient for both Reynolds numbers. Conversely, the mean drag coefficient is approximately 6% higher for both Reynolds numbers. In addition, the maximum lift and drag coefficients that are produced during the wing's initial acceleration are 12% and 3% lower respectively than the maximum experimental values.

Figure 3.1 shows that large steady lift coefficients are produced after the initial transient period. As will be shown below in §3.2.3, this is because a quasi-steady flow regime has developed where the LEV remains attached to the wing. As discussed in chapter 1, the development of this quasi-steady flow state is thought to be due to the
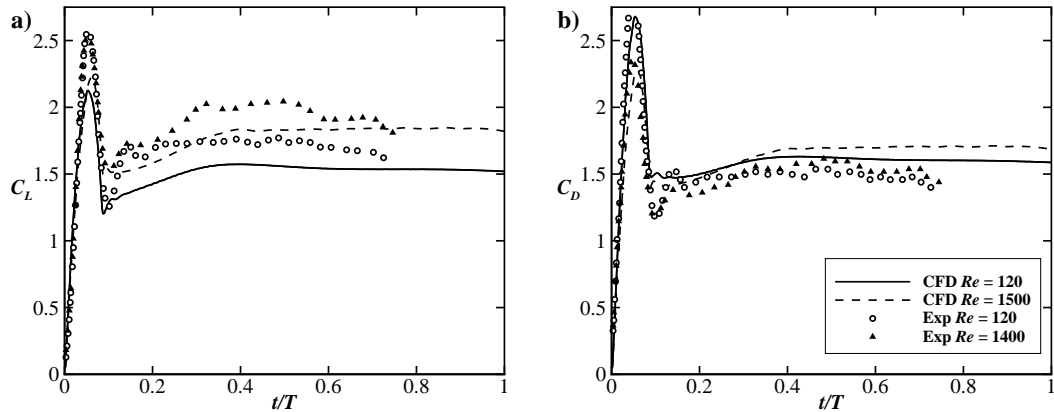
FIGURE 3.1: Time variation of the (a) lift coefficient and (b) drag coefficient throughout the simulation for $AR = 2.91$ wing at $Re = 120$ and $Re = 1500$. The experimental results of Birch *et al.* (2004) ($Re = 120$ and 1400, $\alpha = 40°$) are also included for comparison.

wing's rotation (Lentink & Dickinson 2009b) and has been observed in a number of rotating wing experiments (e.g. Dickinson *et al.* 1999; Poelma *et al.* 2006; Lentink & Dickinson 2009b).

3.2.2 Steady-State Flow Structures

To obtain a qualitative validation of the vortex structures that are present during the quasi-steady period, the results at Reynolds numbers of 120 and 1500 were used to compare to the air bubble flow visualisations of Lentink & Dickinson (2009b). To visualise the flow features in a similar manner, a particle tracking model was used to model the behaviour of neutrally buoyant particles ejected along the leading and trailing edges of the wing. These results are compared in figure 3.2 and show good agreement with the experimental visualisations at both Reynolds numbers. At a Reynolds number of 120 the LEV does not form a tight spiral (as for the high Reynolds number case) and is attached to the wing along its span to approximately the 70% span position, at which point it joins with the TV as it separates from the wing. Figure 3.3a shows a more detailed view of the vortex structures at this Reynolds number and demonstrates that the LEV grows in size in the spanwise direction. Additionally, the TEV separates from the wing slightly closer to the wing tip, thus forming a pair of counter-rotating vortices in the wake. This vortex structure was also observed by Poelma *et al.* (2006) in their PIV experiments on a flapping fruit fly wing.

At a Reynolds number of 1500, figures 3.2c and 3.2d show a tight spiral LEV which
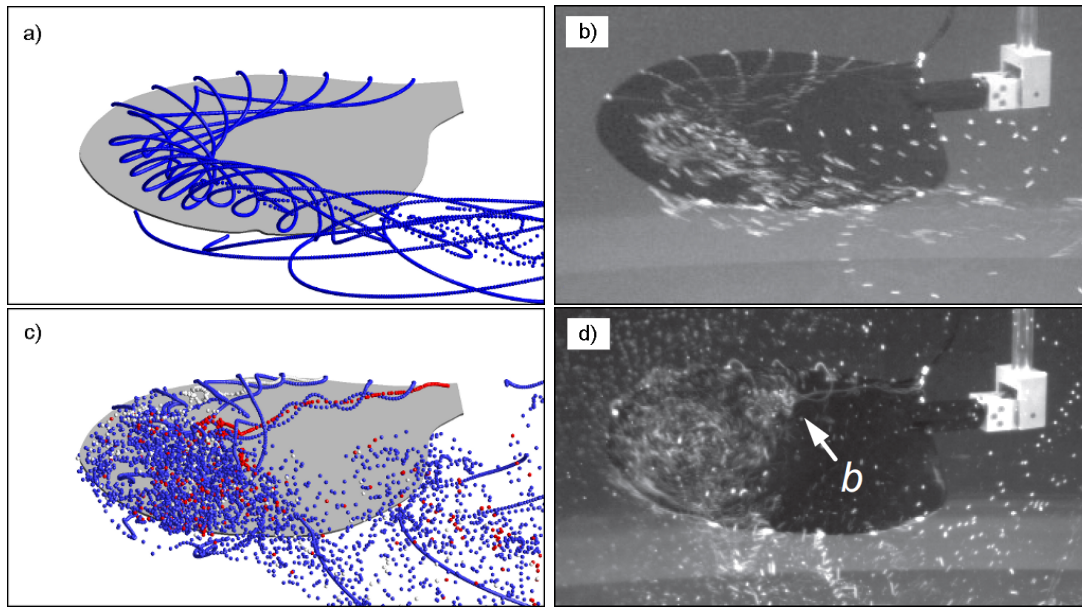
FIGURE 3.2: Comparison of numerical particle tracking flow visualisation results at (a) $Re = 120$ and (c) $Re = 1500$ with air bubble flow visualisations of Lentink & Dickinson (2009b) at (b) $Re = 110$ and (d) $Re = 1400$. Also see movies B.1 and B.2.

breaks down at approximately 60% span, resulting in an unsteady region of flow near the wing tip. Figure 3.2c shows a second vortex structure closer to the leading-edge which is not seen in figure 3.2d, however this dual LEV system was observed by Lentink & Dickinson (2009b) towards the end of the wing's stroke at a Reynolds number of 1400. A dual leading-edge vortex structure has been observed by Srygley & Thomas (2002) over butterfly wings during wing beats that resulted in very large accelerations of the butterfly. It has also been shown to exist under certain Reynolds number conditions and angles of attack for a range of wing shapes (Lu *et al.* 2006; Phillips *et al.* 2010).

Figure 3.3 shows the development of this dual LEV structure with Reynolds number, where the vortices are visualised using surfaces of constant Q criterion. The Q value is the second invariant of the velocity gradient tensor (Hunt *et al.* 1988) and is a measure of the magnitude of rotation rate relative to strain rate in a fluid. Positive values of Q represent areas where the local magnitude of rotation in the fluid dominates relative to strain and therefore can be used to highlight vortical structures. Figure 3.3 shows that as the Reynolds number increases, the iso-Q surfaces near the leading-edge split, revealing two co-rotating vortex structures (labelled LEV 1 and 2) separated by a smaller counter-rotating vortex (labelled SV). At high Reynolds numbers the vortex
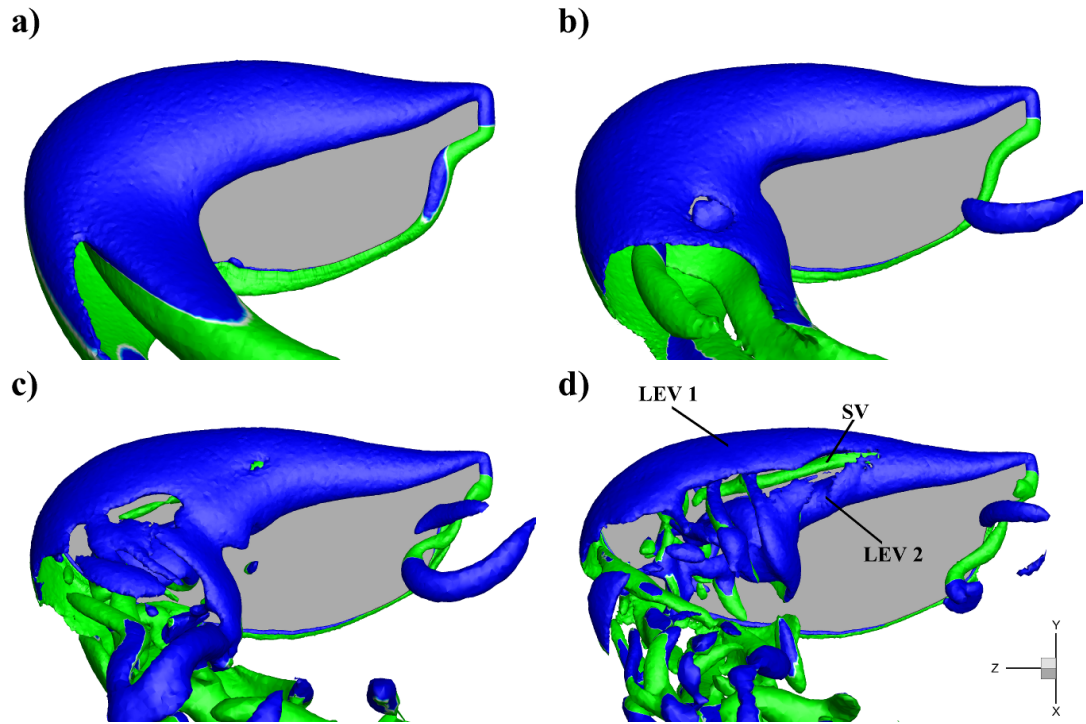
FIGURE 3.3: Development of vortex structures over a fruit fly wing ($AR = 2.91$) with Reynolds number; (a) $Re = 120$, (b) $Re = 300$, (c) $Re = 750$, (d) $Re = 1500$. Vortex structures are visualised using surfaces of constant Q criterion and are coloured by spanwise vorticity (ω_z) to indicate direction; blue is negative and green is positive. Images show the instantaneous flow structures at $270°$ of rotation and are taken perpendicular to the wing surface.

structure furthest away from the leading-edge of the wing (LEV 2) breaks down near the wing tip.

The development of this dual vortex structure with Reynolds number is further highlighted in figure 3.4, which shows the change in spanwise vorticity patterns at 50% span. At a Reynolds number of 120 a single region of strong negative (blue) vorticity is located near the leading-edge of the wing. As the Reynolds number is increased a region of negative vorticity develops further downstream of the leading-edge near to the wing's surface. At first ($Re = 300$) these two regions of negative vorticity are merged together forming a large region of vorticity near the leading-edge. As the Reynolds number is increased further ($Re = 750$ and 1500) the strength of the vorticity in the region furthest downstream of the leading-edge increases and the two regions split to form two distinct vortex cores. As this dual vortex structure forms, the proximity of LEV 2 to the wing's surface induces a flow near the wall. When the Reynolds number
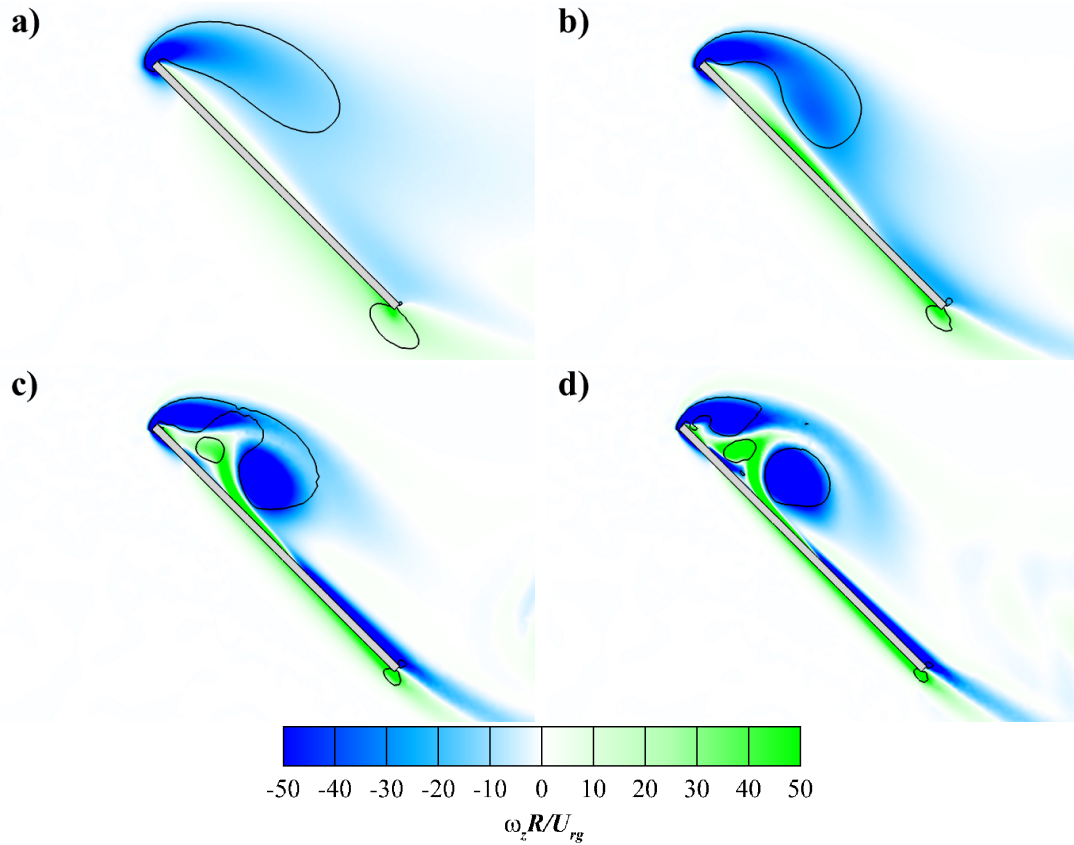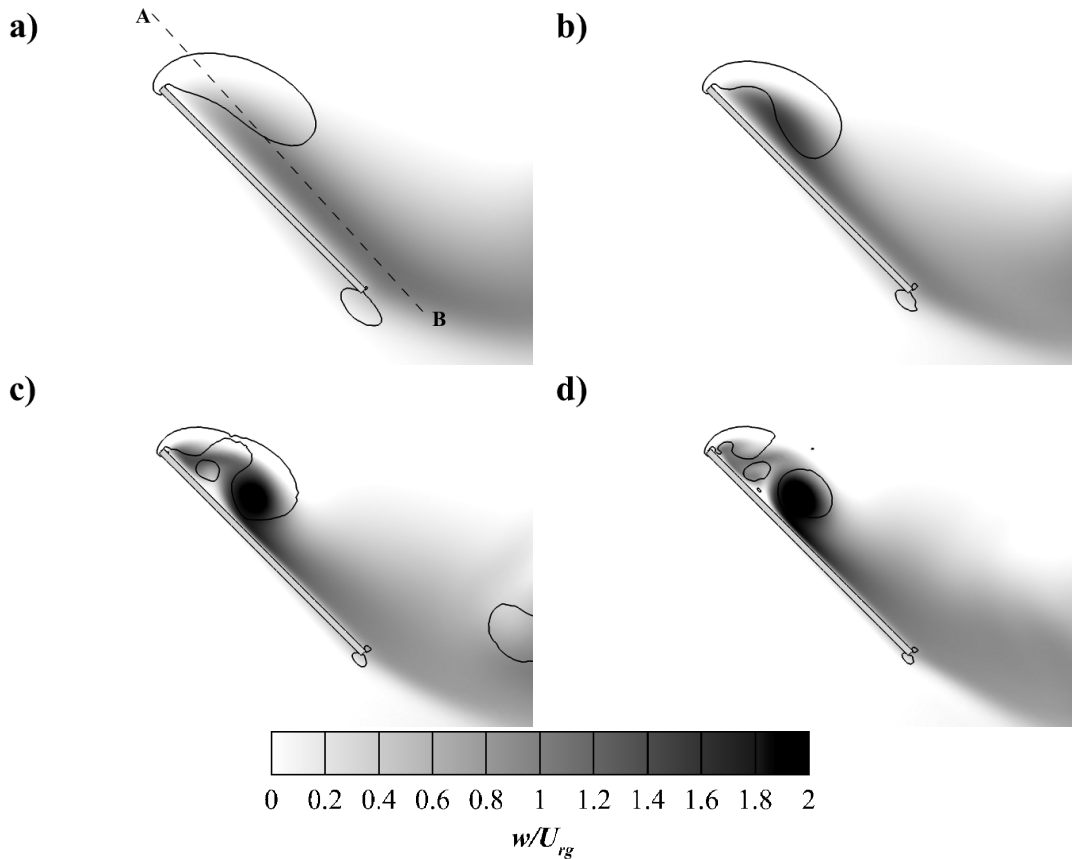
FIGURE 3.4: Contours of spanwise vorticity ($\omega_z R/U_{rg}$) at 50% span for Reynolds numbers of (a) 120, (b) 300, (c) 750 and (d) 1500. Solid lines are contours of constant Q criterion. Images show the instantaneous flow structures at 270° of rotation.

is increased and the strength of LEV 2 increases, this boundary layer separates due to the adverse pressure gradient generated by LEV 2 and forms a secondary region of positive vorticity between the two regions of negative vorticity. The formation of this counter-rotating vortex is similar to the vortex structure that forms for a vortex ring impacting a wall (Walker *et al.* 1987). Furthermore, the overall change in vorticity pattern with Reynolds number is very similar to that observed by Lu *et al.* (2006) for an $AR = 5.8$ flapping wing at 60 degrees angle of attack.

The vortex centre identification algorithm presented by Graftieaux *et al.* (2001) was employed to calculate the location of the LEV axis at various spanwise locations. This method calculates a scalar field, γ_1, which is a measure of the relative rotation about each grid point constrained to a definable interrogation window. The discrete scalar
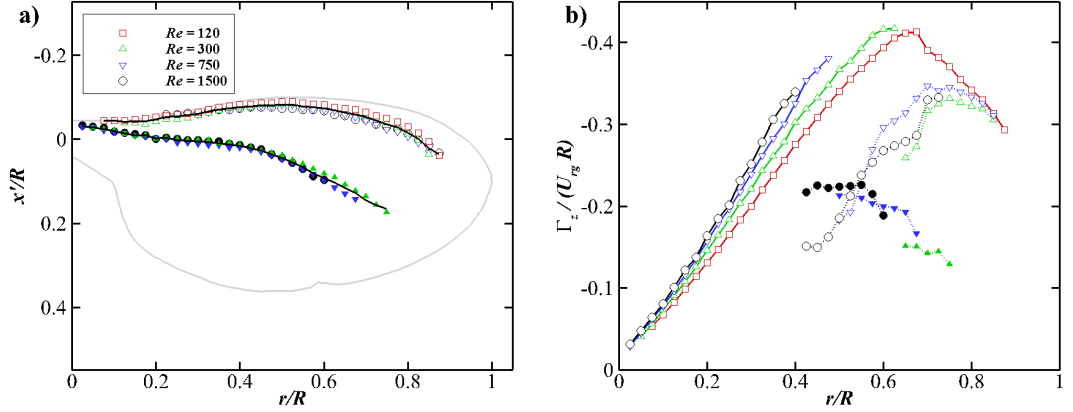
FIGURE 3.5: LEV plots of $AR = 2.91$ wing at various Reynolds numbers; (a) position of vortex axis plotted in the plane of the wing using wing coordinates and (b) the circulation ($\Gamma_z/U_{rg}R$) of the co-rotating vortices. Solid black lines in a) are the average vortex positions and the grey line is the wing outline. Solid lines in b) represent regions where vortex cores are merged and therefore are the combined circulation of the dual co-rotating vortices. Dotted lines show the circulation of the individual vortices after they have split. For both figures, open symbols are LEV 1 and filled symbols are LEV 2.

function is defined as

$$\gamma_1(P) = \frac{1}{N} \sum_M \frac{(\mathbfcal{R}_{PM} \wedge \mathbf{U_M}) \cdot \mathbf{z}}{|\mathbfcal{R}_{PM}| \cdot |\mathbf{U_M}|} = \frac{1}{N} \sum_M \sin(\theta_M), \tag{3.1}$$

where N is the number of grid points, M, within a bounded square region centered on grid point P. γ_1 is equivalent to the ensemble average of $\sin(\theta_M)$, where θ_M represents the angle between the velocity vector $\mathbf{U_M}$ and the radius vector $\mathbfcal{R}_{PM}$. The magnitude of γ_1 is bounded by 1 and is calculated on two-dimensional velocity planes in the chordwise direction, where $\mathbf{z}$ is the unit normal vector of the plane. The centre of a vortex core is identified as a local maximum of the $|\gamma_1|$ field. The location of each of the vortex centres across the span are plotted in figure 3.5a and highlight that the position of the dual vortex structure is independent of Reynolds number. LEV 1 largely follows the shape of the leading-edge, only deviating slightly as the spanwise position increases, while LEV 2 moves away from the leading-edge as it tracks across the wing.

The circulation of the dual vortex structure was calculated using the Graftieaux *et al.* (2001) vortex core identification algorithm, in which the previously defined scalar field is modified to take into account the local advection velocity $\mathbf{U_P}$ around P. The new field is

$$\gamma_2(P) = \frac{1}{N} \sum_M \frac{[\mathbfcal{R}_{PM} \wedge (\mathbf{U_M} - \mathbf{U_P})] \cdot \mathbf{z}}{|\mathbfcal{R}_{PM}| \cdot |\mathbf{U_M} - \mathbf{U_P}|}, \tag{3.2}$$

FIGURE 3.6: Contours of spanwise velocity (w/U_{rg}) at 50% span for Reynolds numbers of (a) 120 , (b) 300 , (c) 750 and (d) 1500. Solid lines are contours of constant Q criterion. Images show the instantaneous velocity fields at 270° of rotation. Dashed line in (a) represents the line along which the velocity comparison for figure 3.7 is made.

where $|\gamma_2|$ is again bounded by 1. Regions where $|\gamma_2| > \frac{2}{\pi}$ are locally dominated by rotation and therefore represent a vortex core. The spanwise vorticity within these regions was integrated to calculate the circulation of the dual LEV system which is plotted in figure 3.5b. The solid lines represent regions where the two vortex cores are merged together and therefore represents the combined circulation of the dual co-rotating vortices. Dotted lines show the circulation of the individual vortices after they have split. Figure 3.5b shows that the combined circulation initially increases approximately linearly with span. Except for a Reynolds number of 120, where only LEV 1 is present, the two vortex cores split at some point along the span and this point moves towards the wing root with increasing Reynolds number. After the split, the circulation of LEV 2 is fairly constant with span until it breaks down, which indicates that after the two vortex cores separate, vorticity is no longer fed into the second vortex.

74
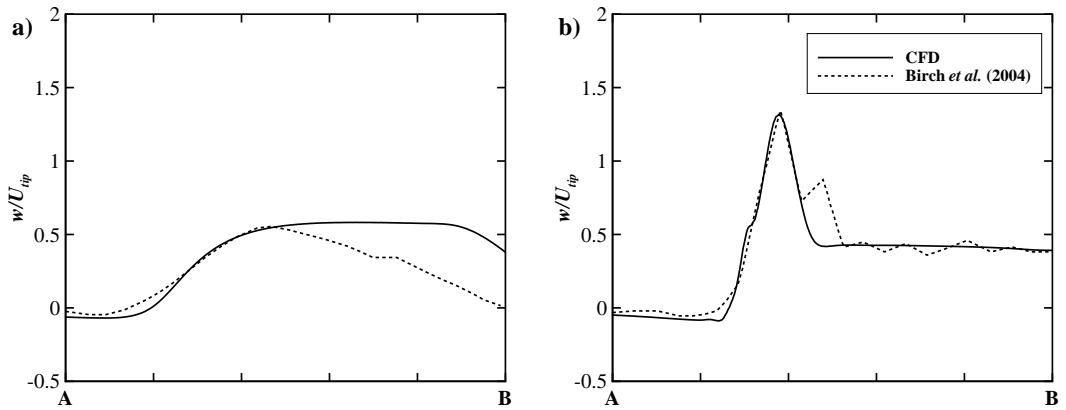
FIGURE 3.7: Spanwise (w/U_{tip}) velocity along the line shown in figure 3.6 at $r/R = 0.45$ for (a) $Re = 120$ and (b) $Re = 1500$. Experimental results from Birch *et al.* (2004) ($Re = 120$ and 1400) are included for comparison.

The circulation of LEV 1 continues to grow approximately linearly with span after the split up to about 70% span.

In addition to the development of a dual LEV structure, the spanwise velocity distribution over the wing is also influenced by Reynolds number. Figure 3.6 shows the change in spanwise velocity with Reynolds number at 50% span. At a Reynolds number of 120, a broad region of positive (root to tip) spanwise flow extends across the wing. While there is some positive velocity within the core of the LEV the maximum spanwise flow is located behind the LEV. As the Reynolds number is increased, and the dual vortex structure develops, the spanwise velocity increases within the core of the downstream vortex (LEV 2) such that the peak in spanwise velocity shifts to be within LEV 2. At high Reynolds numbers there is still significant spanwise velocity in the region behind the LEV system, however the spanwise flow within the core of LEV 1 is relatively weak.

Birch *et al.* (2004) used DPIV to measure the velocity at a number of spanwise locations for their rotating wing experiments and observed a similar change in spanwise velocity patterns with Reynolds number. They reported that at a Reynolds number of 1400 an additional region of higher velocity axial flow within the core of the LEV was clearly visible, superimposed over a broad flow that was similar in structure to that present at a Reynolds number of 120. Birch *et al.* (2004) plotted the variation of spanwise velocity along a line that passes through both the core of the LEV and the area

75

of maximum axial flow at 45% span. Figure 3.7 shows a comparison of the spanwise velocity along this line, which is shown in figure 3.6a, between these simulations and the experimental results of Birch *et al.* (2004). Figure 3.7a shows the velocity distribution at a Reynolds number of 120 and demonstrates that while there is a good match around the leading-edge of the wing, the numerical model maintains a high velocity for longer across the rear of the wing. The average difference between the experimental and numerical results is 14% at this Reynolds number. Figure 3.7b shows the distribution of spanwise velocity at a Reynolds number of 1500. Here good agreement in the distribution of spanwise velocity between the numerical and experimental data is observed across the whole wing, which leads to an average difference between the two of 6.1%. Figure 3.7 shows that the numerical model is capturing the same change in spanwise velocity distribution with Reynolds number that was observed in the DPIV experiments.

3.2.3 Temporal Development of Flow Structures

In this section the development of the vortex structures throughout the wing's motion is presented. The vortex structures near the wing's surface at six time instances for Reynolds numbers of 120 and 1500 are shown in figures 3.8 and 3.9 respectively. These figures combined with the lift and drag coefficient time histories (figure 3.1) show that a quasi-steady flow state has developed for the vortex structures around the wing by approximately $t/T = 0.36$, or after 90 degrees of wing rotation. This period of flow development is the same as that reported by Poelma *et al.* (2006).

Figure 3.8 shows the iso-Q surfaces during the wing's motion for a Reynolds number of 120. At the beginning of the wing's motion, a horseshoe-shaped vortex is formed that consists of the LEV, TV and TEV. As the wing continues to rotate, this vortex grows in size and the TEV is shed from the wing. Noticeably, the LEV enlarges towards the wing tip, which results in a three-dimensional vortex structure. This flow structure development is similar to that computed for the initial part of the downstroke of a hovering fruit fly (Aono *et al.* 2008). At $t/T = 0.267$ a second TEV can be seen to detach from the wing on the wing tip side of the TV. By $t/T = 0.363$ the growth of the LEV has stopped and the structure of the LEV remains steady for the rest of the simulation. The second TEV continues to develop in the wake, forming a counter-rotating vortex pair with the TV, however this does not have a significant impact on the aerodynamic forces.
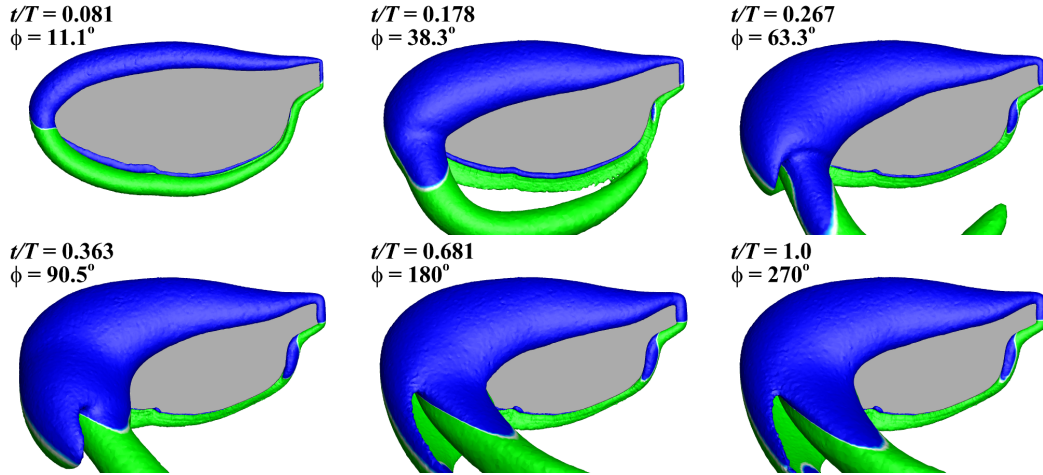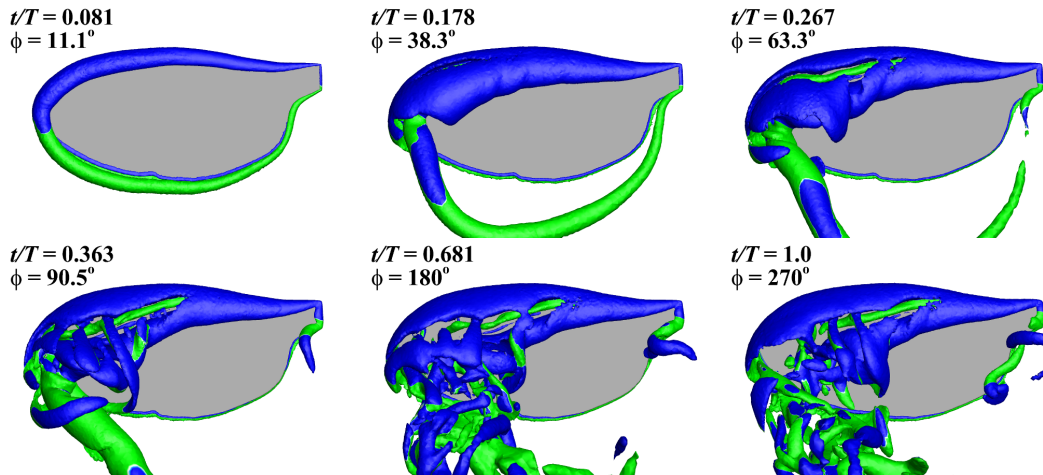
FIGURE 3.8: Temporal vortex structure development over a fruit fly wing ($AR = 2.91$) at $Re = 120$. Vortex structures are visualised using surfaces of constant Q criterion and are coloured by spanwise vorticity (ω_z) to indicate direction; blue is negative and green is positive. Images show the instantaneous flow structures throughout the wing's rotation and are taken perpendicular to the wing surface. Sequence progresses left to right. Also see movie B.3.
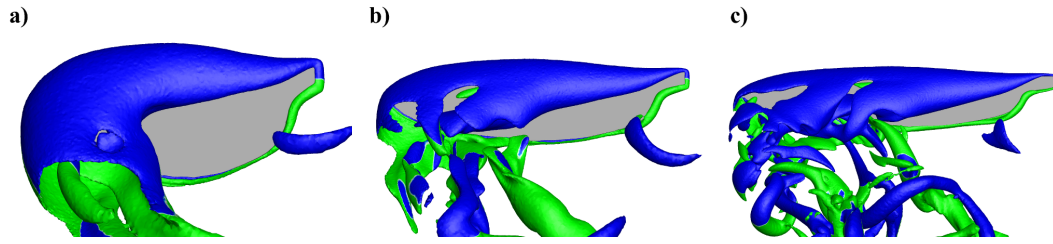

FIGURE 3.9: Temporal vortex structure development over a fruit fly wing ($AR = 2.91$) at $Re = 1500$. Vortex structures are visualised using surfaces of constant Q criterion and are coloured by spanwise vorticity (ω_z) to indicate direction; blue is negative and green is positive. Images show the instantaneous flow structures throughout the wing's rotation and are taken perpendicular to the wing surface. Sequence progresses left to right. Also see movie B.4.

FIGURE 3.10: Variation of vortex structures for different aspect ratio wings at $Re = 300$. (a) $AR = 2.91$, (b) $AR = 5.1$, (c) $AR = 7.28$. Vortex structures are visualised using surfaces of constant Q criterion and are coloured by spanwise vorticity (ω_z) to indicate direction; blue is negative and green is positive. Images show the instantaneous flow structures at 270° of rotation and are taken perpendicular to the wing surface.

The development of the vortex structures at a Reynolds number of 1500 is shown in figure 3.9. Initially, a similar horseshoe-shaped vortex structure is formed as was seen at a Reynolds number of 120. At $t/T = 0.178$ the TEV also separates from the wing in a similar manner, however here the iso-Q surface representing the LEV begins to split near the tip of the wing. By $t/T = 0.267$ a clear dual LEV structure has formed and by $t/T = 0.363$ LEV 2 has burst, resulting in smaller scale structures forming. These smaller scale structures are advected into the wake as the wing's motion continues, however the LEV structure appears to be fully developed and consistent in size and position from $t/T = 0.363$.

3.3 Effect of Aspect Ratio at Constant Reynolds Number

The fruit fly wing simulation at a Reynolds number of 300 was used as the basis for an initial investigation into the effect of aspect ratio. The wing was scaled to create wings of different aspect ratios while the fluid viscosity was adjusted to maintain a constant Reynolds number. Figure 3.10 visualises the vortex structures using surfaces of constant Q criterion and shows a significant change in the vortex structures with aspect ratio.

Increasing the aspect ratio results in the LEV structure evolving into dual vortices in a similar manner to that observed in §3.2.2 for increasing Reynolds number. This can be seen in figure 3.10 by the splitting of the iso-Q surface near the leading-edge into two co-rotating vortices and the formation of a secondary counter-rotating vortex as aspect ratio is increased. The development of the dual LEV system is also seen

78
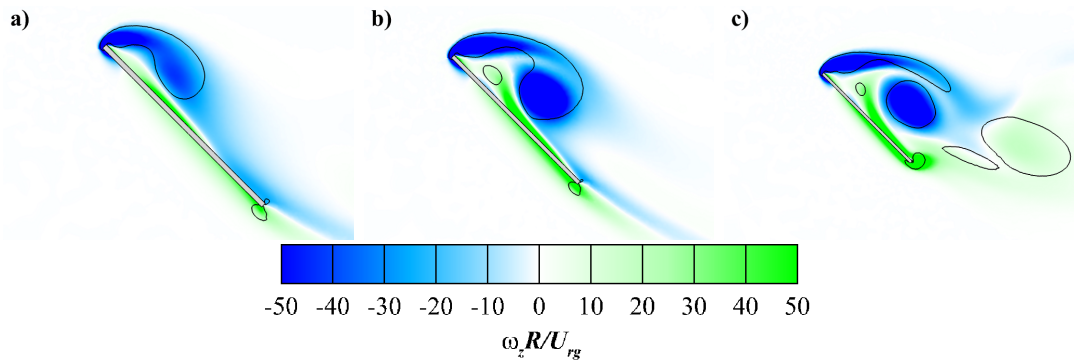
FIGURE 3.11: Contours of time averaged spanwise vorticity ($\omega_z R/U_{rg}$) at 50% span for wings at $Re = 300$. (a) $AR = 2.91$, (b) $AR = 5.1$ and (c) $AR = 7.28$. Solid lines are contours of constant Q criterion. Flow field has been averaged over the quasi-steady period ($0.36 \leq t/T \leq 1.0$).

in the time averaged contours of spanwise vorticity at 50% span shown in figure 3.11. Here the same changes in flow patterns are observed with aspect ratio as was found to occur with Reynolds number, namely the splitting of the negative vorticity region into two distinct vortex cores, an increase in strength of vorticity within the core of the downstream vortex and the formation of a region of positive vorticity between the two co-rotating vortex cores.

In addition to the formation of dual LEVs, higher aspect ratio wings have larger LEVs in proportion to the wing chord. Consequently, the trailing-edge of the wing is closer to the core of the downstream vortex (LEV 2) and this appears to result in the LEV interacting with the vorticity from the underside of the wing and the generation of unsteady vortex shedding out near the tip of the wing. This can be seen in figure 3.10 by the increase in complexity of the vortex structures in the wake with aspect ratio. A more detailed discussion of this effect of aspect ratio is presented in §3.4.2.

3.4 Wing Span as a Characteristic Length

The striking similarity between the change in flow structures with aspect ratio and those with Reynolds number indicates that the two sets of results are linked, and may be scaled in an alternative manner so as to yield similar vortex structures for a range of aspect ratios. Figure 3.3 gives a clue as to how these results may be scaled differently. It shows that the LEV develops along the span of the wing, both in terms of its size and its circulation (figure 3.5b). This is due to the wing's rotation and the spanwise

velocity, that exists both within the core of the LEV and in the region immediately behind the wing (figure 3.6), which convects vorticity towards the wing tip (Maxworthy 1979; Ellington *et al.* 1996; Lentink & Dickinson 2009b). Hence, the key characteristic of the wing shape seems to be the wing span and not the wing chord.

The hypothesis is therefore proposed that the wing span is a more useful characteristic length to use in the scaling of flapping and rotating wings at high angles of attack. In order to test this hypothosis, the Navier Stokes equations (1.1 and 1.2) are first non-dimensionalised using the method outlined by Lentink & Dickinson (2009a). Here the same scaling parameters as Lentink & Dickinson (2009a) are used except that the average wing chord ($\bar{c}$) is replaced with the wing span (R) as the characteristic length, thus the scaled variables become:

$$\boldsymbol{u}^* = \frac{\boldsymbol{u}}{U_{tip}}, \quad t^* = \frac{U_{tip}t}{R}, \quad \boldsymbol{\nabla}^* = R \cdot \boldsymbol{\nabla}, \quad \dot{\boldsymbol{\Omega}}^* = \frac{\dot{\boldsymbol{\Omega}}}{\dot{\Omega}}, \qquad (3.3a, b, c, d)$$

$$\boldsymbol{\Omega}^* = \frac{\boldsymbol{\Omega}}{\Omega}, \quad \boldsymbol{r}^* = \frac{\boldsymbol{r}}{R}, \quad p^* = \frac{p}{p_0}, \qquad (3.3e, f, g)$$

where U_{tip} is the wing tip velocity. Substituting equations 3.3 into equations 1.1 and 1.2 and normalising by $\rho U_{tip}^2/R$ results in the following dimensionless equations,

$$\frac{\mathrm{D}\boldsymbol{u}}{\mathrm{D}t} + \frac{\dot{\Omega}R^2}{U_{tip}^2}\dot{\boldsymbol{\Omega}} \times \boldsymbol{r} + \frac{\Omega^2 R^2}{U_{tip}^2}\boldsymbol{\Omega} \times (\boldsymbol{\Omega} \times \boldsymbol{r}) + \frac{\Omega R}{U_{tip}}2\boldsymbol{\Omega} \times \boldsymbol{u} = -\frac{p_0}{\rho U_{tip}^2}\boldsymbol{\nabla}p + \frac{\mu}{\rho U_{tip}R}\boldsymbol{\nabla}^2\boldsymbol{u}, \quad (3.4)$$

and

$$\boldsymbol{\nabla} \cdot \boldsymbol{u} = 0, \qquad (3.5)$$

where * is omitted for clarity. Equation 3.4 shows that when the Navier Stokes equations are scaled in this way, the Reynolds number becomes based on the wing span ($Re_R = \rho U_{tip}R/\mu$). Furthermore, the centripetal and Coriolis accelerations scale with $1/Ro^2$ and $1/Ro$ respectively, where $Ro = U_{tip}/\Omega R$ is the Rossby number. Lentink & Dickinson (2009b) propose that these rotational accelerations mediate LEV stability and therefore, if this argument is true, then the new definition of Rossby number should describe LEV stability and the span-based Reynolds number should determine the structure of the LEV. The effects of these two parameters are investigated below.

3.4.1 Scaling of Results using a Span-Based Reynolds Number

Simulations of the fruit fly wing scaled to different aspect ratios were re-run with the fluid viscosity adjusted to match the span-based Reynolds number for each wing. The results of these tests were assessed to determine the dependence of the LEV structure

on aspect ratio and span-based Reynolds number. Figure 3.12 shows a comparison of the vortex structures over different aspect ratio wings for two span-based Reynolds numbers of 613 and 7667. These two Reynolds numbers are equivalent to $Re = 120$ and 1500 for an aspect ratio of 2.91. Comparing the flow structures in this way shows a stronger correlation of the vortex structures between different aspect ratio wings at the same span-based Reynolds number. For $Re_R = 613$ (figure 3.12a,b,c), all three wings show a very similar vortex structure. A single LEV extends along the wing until approximately 70% span, where it separates and joins with the TV. Similarly, the iso-Q surfaces for $Re_R = 7667$ (figure 3.12d,e,f) show similar vortex structures. Here the dual LEV structure is clearly evident and is well developed for all aspect ratios. Similar consistency in flow structures was found for intermediate span-based Reynolds numbers between 613 and 7667.

Sectional slices of spanwise vorticity further show the similarity of the LEV structure for the different AR wings when scaled with the span-based Reynolds number. At a span-based Reynolds number of 613 (figure 3.13a,b,c) all aspect ratio wings have a single region of strong negative vorticity located near the leading-edge of the wing, while at a span-based Reynolds number of 7667 (figure 3.13d,e,f) the dual LEV structure consisting of two regions of negative vorticity separated by a region of positive vorticity can be seen.

The spanwise position of the point at which the vortex core identification algorithm (Graftieaux *et al.* 2001) first recognises two separate vortex cores is plotted against both the chord-based and span-based Reynolds numbers in figure 3.14. This shows that as the Reynolds number is increased the spanwise position at which two distinct vortex cores can be observed shifts towards the wing root. This can therefore be used as a measure of how much the dual LEV structure has developed for each wing. Figure 3.14a shows that the "splitting" point depends on both the chord-based Reynolds number and the wing aspect ratio. However, when these results are plotted against the span-based Reynolds number (figure 3.14b) the "splitting" point becomes independent of the wing aspect ratio, as shown by the collapsing of the data onto effectively a single curve. This further demonstrates that the development of the dual LEV system is characterised by the span-based Reynolds number.

As shown in figure 3.12, at high Reynolds numbers LEV 2 breaks down at some point along the span. Vortex breakdown is an abrupt change in the structure of a vortex
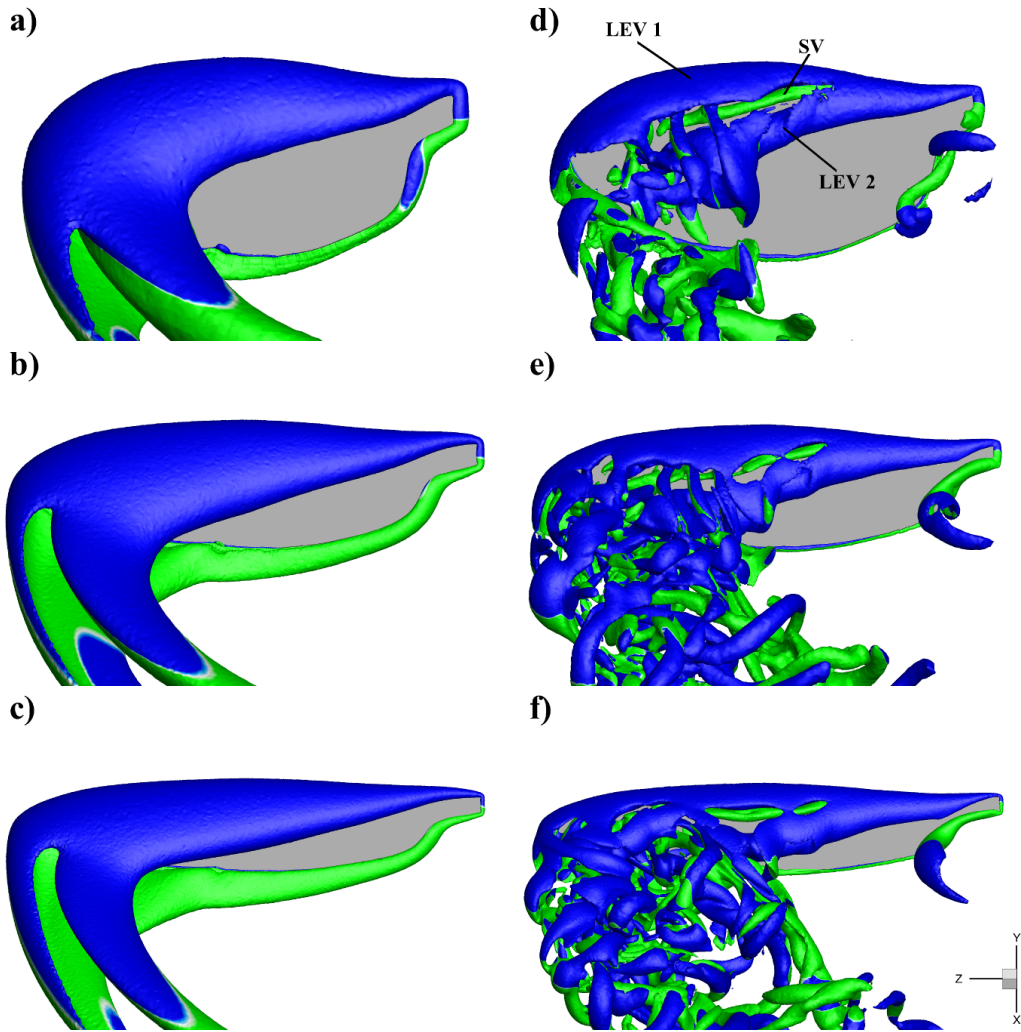
FIGURE 3.12: Vortex structures over different AR wings at span-based Reynolds numbers of (left) $Re_R = 613$ and (right) $Re_R = 7667$. (a,d) $AR = 2.91$, (b,e) $AR = 5.1$, (c,f) $AR = 7.28$. Vortex structures are visualised using surfaces of constant Q criterion and are coloured by spanwise vorticity (ω_z) to indicate direction; blue is negative and green is positive. Images show the instantaneous flow structures at $270°$ of rotation and are taken perpendicular to the wing surface.

with a marked retardation of the flow in the axial direction (Hall 1972). Figure 3.15 shows the spanwise location of the breakdown point plotted against both the chord-based and span-based Reynolds numbers. Here, the breakdown point is estimated as the point at which the spanwise velocity in the vortex core approaches zero. Figure 3.15 shows that as the Reynolds number is increased the burst point shifts towards the wing root and, like the "splitting" point, the spanwise position of the breakdown point can be described by the span-based Reynolds number for all aspect ratios.
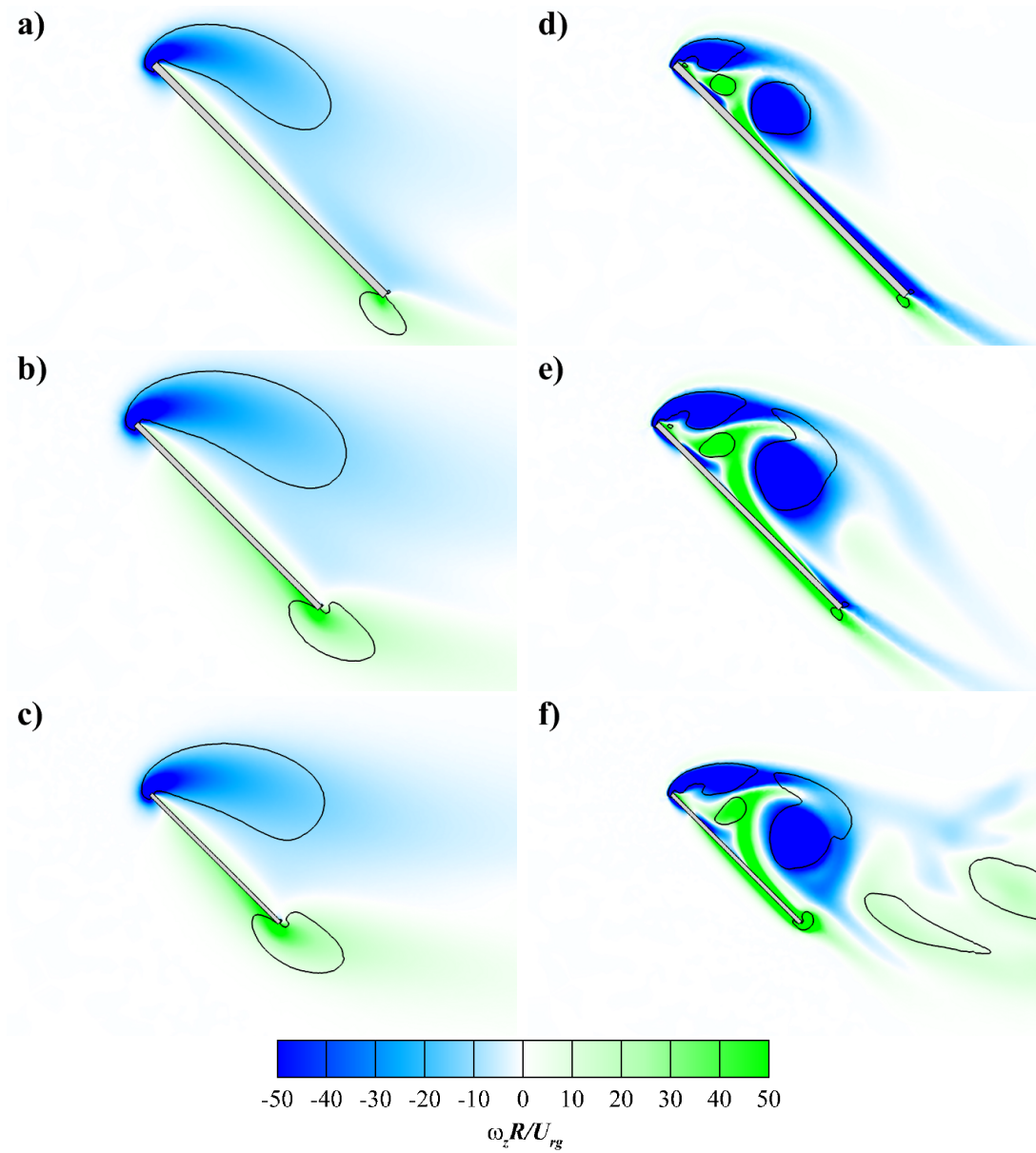
FIGURE 3.13: Contours of time averaged spanwise vorticity ($\omega_z R/U_{rg}$) at 50% span for different AR wings at span-based Reynolds numbers of (left) $Re_R = 613$ and (right) $Re_R = 7667$. (a,d) $AR = 2.91$, (b,e) $AR = 5.1$, (c,f) $AR = 7.28$. Solid lines are contours of constant Q criterion. Flow field has been averaged over the quasi-steady period ($0.36 \leq t/T \leq 1.0$).
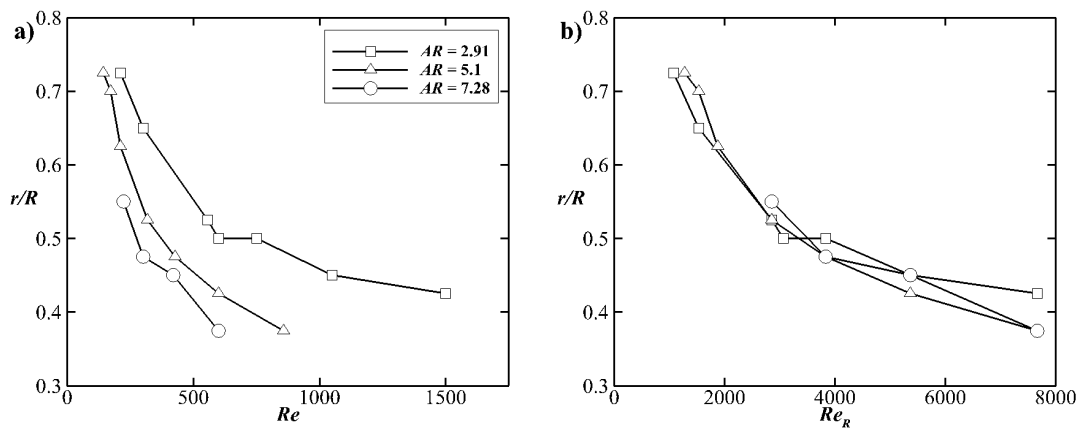
FIGURE 3.14: Normalised spanwise position (r/R) of the point at which two individual vortex cores are observed as a function of (a) Re and (b) Re_R.
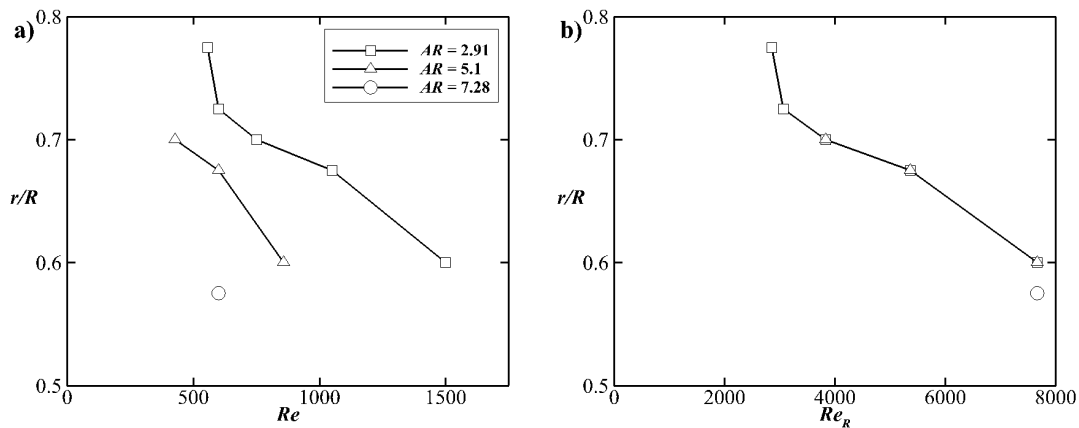
FIGURE 3.15: Normalised spanwise position (r/R) of the breakdown point of LEV 2 as a function of (a) Re and (b) Re_R.

3.4.2 Aspect Ratio Effects at Constant Span-Based Reynolds Number

The results of §3.4.1 show that the span-based Reynolds number does indeed describe the overall structure of the LEV. Furthermore, the effect of a change in the wing's aspect ratio no longer leads to changes in flow topology that are comparable to Reynolds number effects. Therefore, using the span-based scaling allows the influence of aspect ratio and Reynolds number to be separated. Any change in flow patterns at a constant span-based Reynolds number can now be attributed to changes in the wing's aspect ratio. The effect of wing aspect ratio on the flow structures and aerodynamic forces under simulated hovering conditions is discussed below.

84
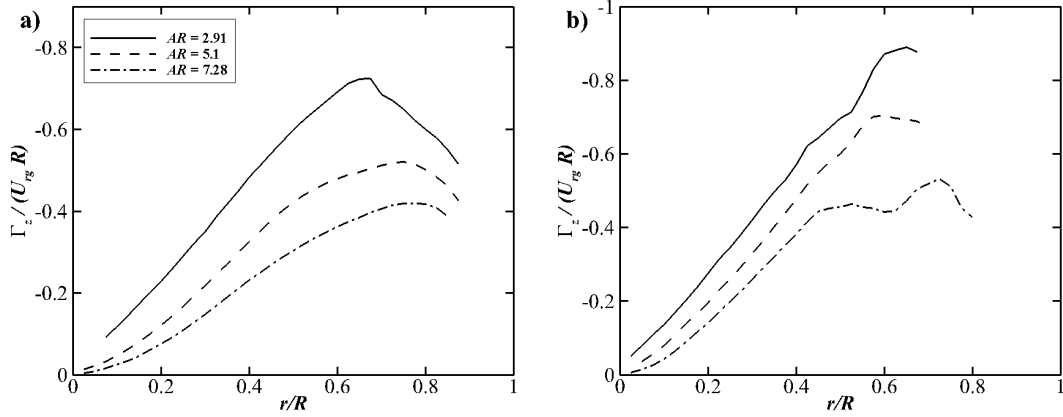
FIGURE 3.16: Combined circulation ($\Gamma_z/U_{rg}R$) of dual co-rotating LEVs for different aspect ratio wings at (a) $Re_R = 613$ and (b) $Re_R = 3833$. Note that only one vortex is present for $Re_R = 613$.

3.4.2.1 Steady-State Flow Structures

While the structure of the LEV is mainly dictated by the span-based Reynolds number, the wing's aspect ratio does influence the flow characteristics. The main effect of aspect ratio is to change the size of the LEV relative the wing's chord length. This can be seen in figures 3.12 and 3.13, which demonstrate that as the wing aspect ratio is increased the LEV increases in size relative to the chord length of the wing. This can be viewed as either an effective shortening of the wing's chord length compared to a fixed LEV size, or as the LEV's size growing with an increase in wing span.

At low span-based Reynolds numbers, when only LEV 1 is present, this does not have a significant impact on the structure of the LEV, however the dimensionless circulation of the LEV is reduced for higher aspect ratios (figure 3.16a). Additionally, the larger LEV structure pushes the flow reattachment point towards the trailing-edge of the wing. This is demonstrated in figure 3.17a-c by the half-saddle point on the upper surface of the wing moving towards the trailing-edge with increasing aspect ratio. As the LEV is conical in shape, the reattachment point reaches the trailing-edge in the outer part of the wing for high aspect ratios. It is known that for a two-dimensional translating wing, when the flow reattachment point reaches the trailing-edge the LEV is in danger of being shed from the wing (Dickinson & Gotz 1993), however figure 3.12a,b,c shows that the LEV is not shed at this Reynolds number.

At a span-based Reynolds number of 7667 the same increase in LEV size with aspect

85
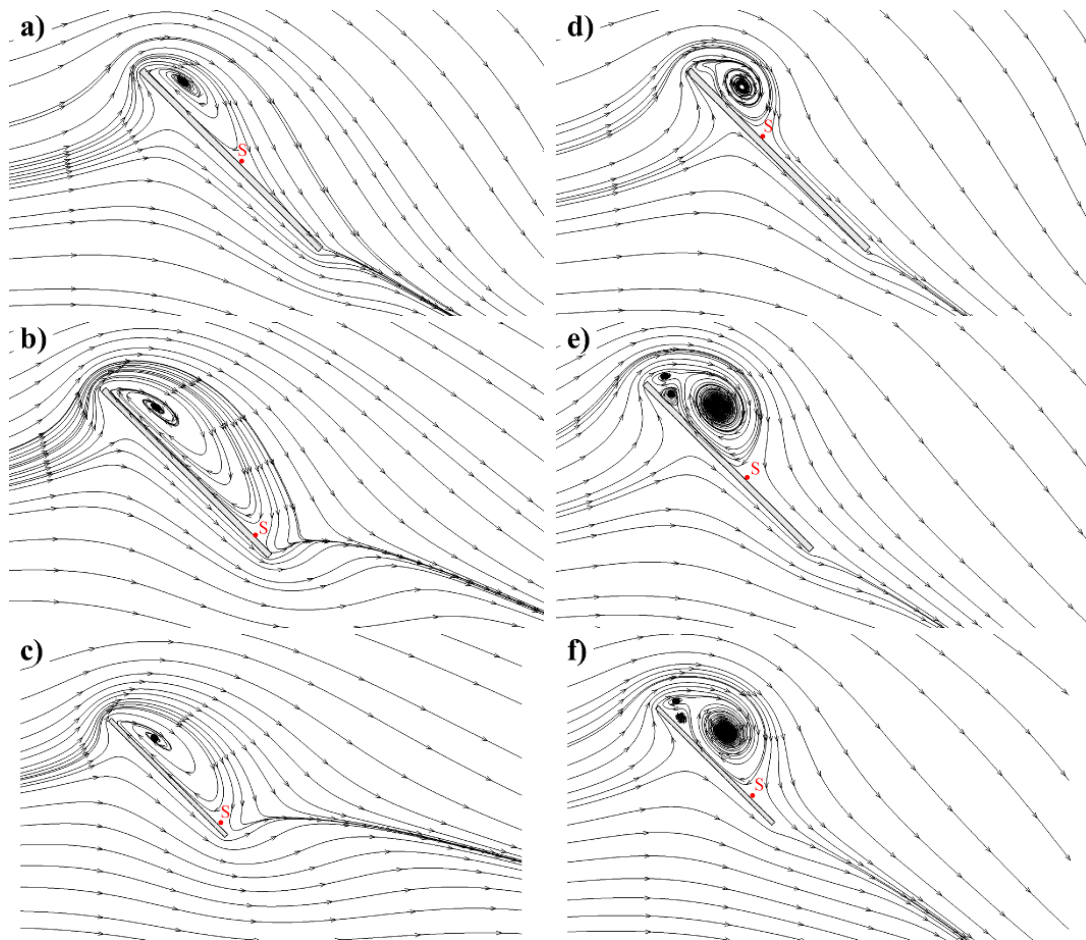
FIGURE 3.17: Two-dimensional streamlines at 30% wing span for different AR wings at span-based Reynolds numbers of (left) $Re_R = 613$ and (right) $Re_R = 7667$. (a,d) $AR = 2.91$, (b,e) $AR = 5.1$, (c,f) $AR = 7.28$. Streamlines show instantaneous flow patterns at $\phi = 270°$. "S" marks the half saddle point on the wing's top surface.

ratio can be seen. This again leads to the flow reattachment point moving towards the wing's trailing-edge with increasing aspect ratio (figure 3.17d-f). At this Reynolds number LEV 2 breaks down at approximately 60% span. After LEV 2 bursts, its core rapidly expands in size and a region of unsteady flow is developed over the outer part of the wing. Like Lentink & Dickinson (2009b), it was observed that the flow within the unsteady region is advected along the wing and into the TV for the aspect ratio 2.91 wing (see movie B.2). Furthermore, this is also found to occur for higher aspect ratios (see movie B.5) and therefore the LEV appears to be stable for all aspect ratios during the quasi-steady period. The TV covers approximately the outer 30% of the wing's span and therefore the small vortex structures seen in the wake of the wing in figure

86
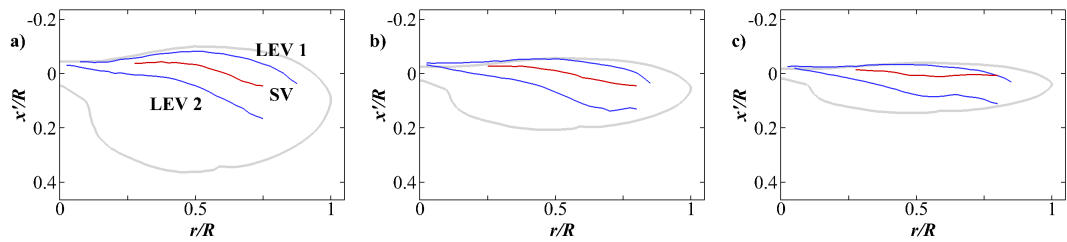
FIGURE 3.18: Position of vortex axis plotted in the plane of the wing using wing coordinates for aspect ratios of (a) 2.91, (b) 5.1 and (c) 7.28. Blue lines represent the co-rotating LEVs and the red lines depict the secondary counter rotating vortex. Grey line illustrates the wing's outline.

3.12d,e,f are due the breakdown of LEV 2 and the advection of the resulting unsteady flow that this creates into the TV.

A secondary effect of the wing aspect ratio is to change the position of LEV 2 on the wing. This can be seen at intermediate span-based Reynolds numbers, when the dual LEV structure is present, but LEV 2 does not break down until close to the wing's tip. This can be seen in figure 3.18 which shows the vortex centrelines for the LEVs at three aspect ratios. For the aspect ratio 2.91 wing, LEV 2 tracks across the wing gradually moving away from the leading-edge. For the high aspect ratio wings, LEV 2 tracks a similar path over the inner part of the wing but is deflected towards the tip when it reaches the trailing-edge. For the aspect ratio 7.28 wing this occurs around mid span. After LEV 2 has been deflected it follows the trailing-edge of the wing until it separates from the wing near the tip.

The deflection of LEV 2 creates a particular flow pattern for high aspect ratio wings at moderate span-based Reynolds numbers. For these cases, the proximity of LEV 2 to the trailing-edge causes LEV 2 to interact with the vorticity from the underside of the wing, which results in a region of unsteady flow developing in the outer part of the wing, even before LEV 2 has burst. In fact this interaction seems to suppress the breakdown of LEV 2 as will be discussed later. An example of when this occurs is for the aspect ratio 7.28 wing at a span-based Reynolds number of 3833. The instantaneous surfaces of the Q criterion at 270° of rotation are shown in figure 3.10c. This figure shows that the vortex structures are steady over the inner part of the wing, however beyond approximately 50% span the flow becomes unsteady as indicated by the complex vortex structures in the wake. It is over this same region of the wing where LEV 2 follows the
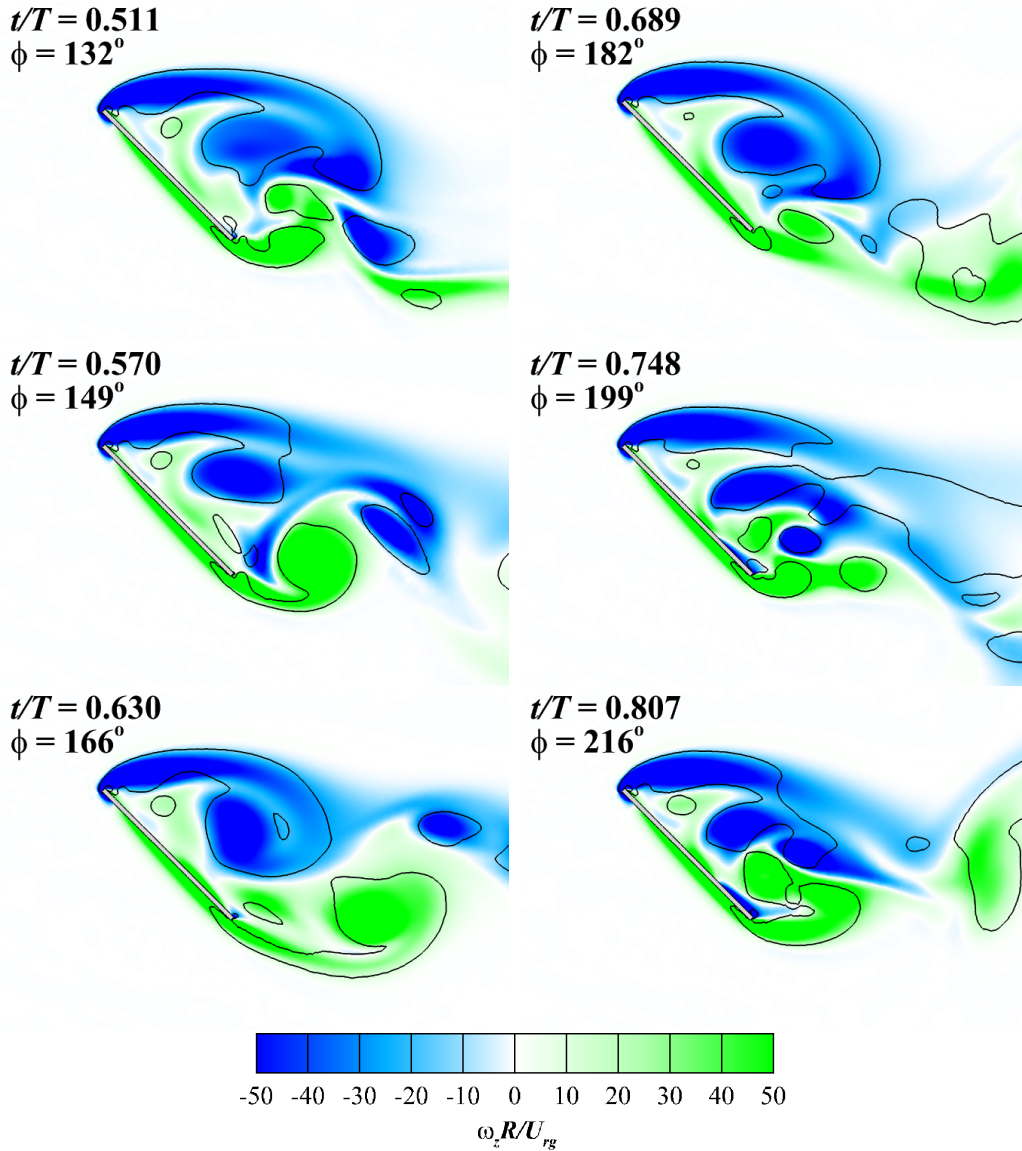
FIGURE 3.19: Time sequence of spanwise vorticity ($\omega_z R/U_{rg}$) at 70% span for $AR = 7.28$ and $Re_R = 3833$. Solid lines are contours of constant Q criterion and the sequence progresses top to bottom. Also see movie B.6.

trailing-edge (figure 3.18c). To show the fluctuation of the flow out near the wing tip more clearly, the time evolution of the spanwise vorticity at 70% span for the aspect ratio 7.28 wing at $Re_R = 3833$ is shown in figure 3.19 (also see movie B.6). Here, the proximity of LEV 2 to the trailing-edge causes the vorticity from the underside of the wing to roll up into a TEV which is later shed from the wing. LEV 2 also appears to be pushed up slightly towards the leading-edge and therefore interacts with the vorticity from the leading-edge in a similar manner, resulting in negative sign vortices being
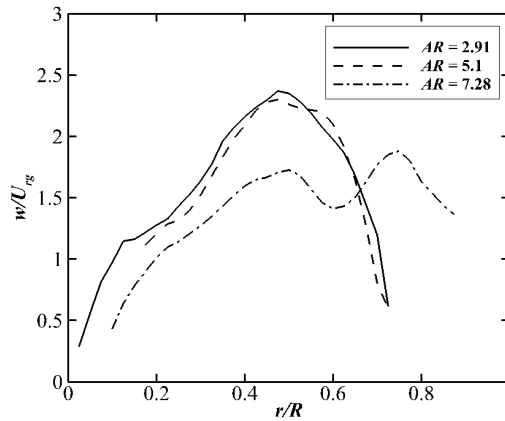
FIGURE 3.20: Spanwise velocity (w/U_{rg}) along the axis of LEV 2 at $Re_R = 3833$.

shed from the wing. This continual interaction results in unsteady fluctuation of the flow in the outer part of the wing. Nonetheless, the dual LEV structure can always be visualised in figure 3.19. The LEV is therefore not completely shed, as it would be for a purely translating wing, and remains attached to the wing throughout the wing's rotation. The LEV does, however, have reduced circulation in this section of the wing as is shown in figure 3.16b.

The interaction between LEV 2 and the vorticity at the trailing-edge also appears to suppress the breakdown of LEV 2. Figure 3.20 shows the spanwise velocity along the vortex axis at $Re_R = 3833$. At low aspect ratios, where LEV 2 is not influenced by the trailing-edge, the spanwise flow in the vortex rapidly drops towards zero beyond the mid-span, which indicates the formation of a stagnation point and the beginning of vortex breakdown (Hall 1972; Leibovich 1978). However at an aspect ratio of 7.28 the peak in spanwise velocity in the vortex core is reduced and beyond 50% span, where LEV 2 is following the trailing-edge of the wing, the spanwise velocity fluctuates around a mean value and does not rapidly drop towards zero. This results in the suppression of the breakdown of LEV 2 for high aspect ratios at moderate span-based Reynolds numbers. When the Reynolds number is high enough such that the breakdown location occurs at or before the point that LEV 2 meets the trailing-edge then the LEV still undergoes vortex breakdown. This is the case for the aspect ratio 7.28 wing at a span-based Reynolds number of 7667 as shown in figure 3.12f.
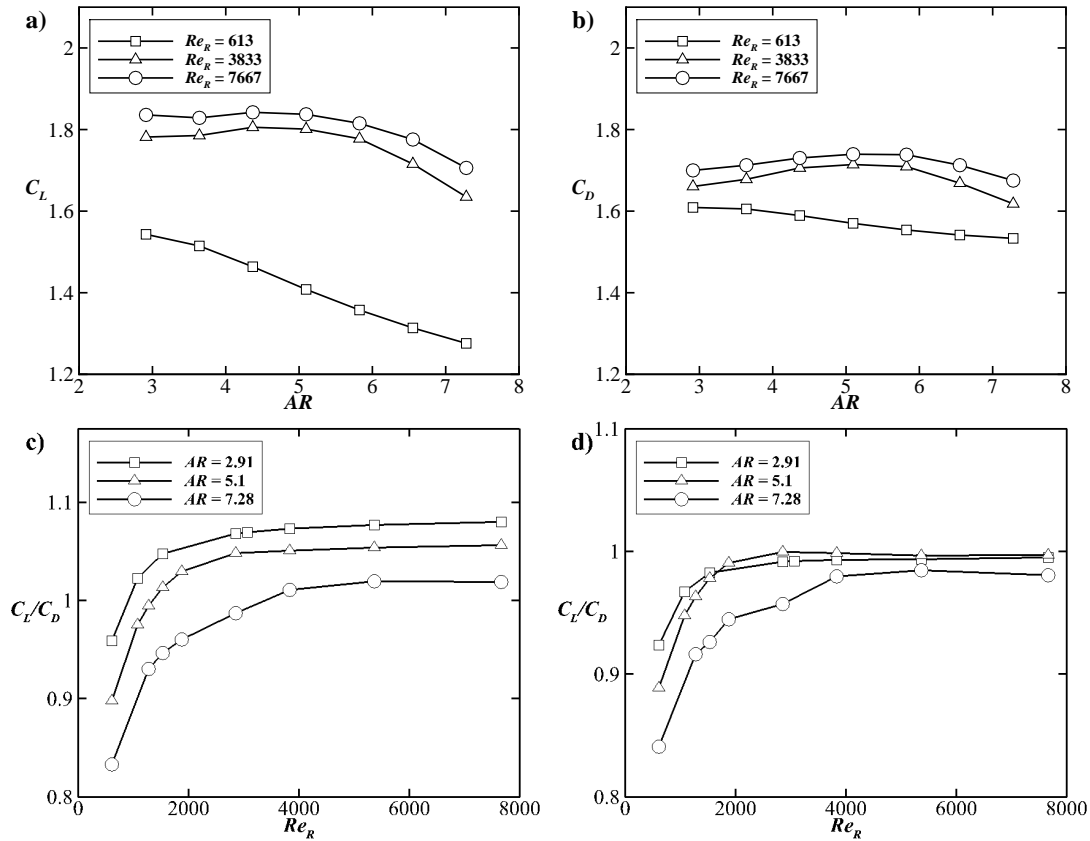
FIGURE 3.21: Aerodynamic force graphs; (a) lift coefficient as a function of aspect ratio for three span-based Reynolds numbers, (b) drag coefficient as a function of aspect ratio for three span-based Reynolds numbers, (c) average lift on drag ratio as a function of Re_R and (d) lift on drag ratio excluding wing thickness effects. Aerodynamic forces have been averaged over the quasi-steady period ($0.36 \leq t/T \leq 1.0$).

3.4.2.2 Aerodynamic Forces

The variation in average aerodynamic forces for different aspect ratio wings at varying span-based Reynolds numbers is shown in figure 3.21. These aerodynamic forces were calculated as the average values over the quasi-steady period ($0.36 \leq t/T \leq 1.0$) and therefore exclude the effects of the initial flow development. Figures 3.21a and 3.21b show the change in the lift and drag coefficients respectively with aspect ratio for three span-based Reynolds numbers. This shows that there is a different variation in the aerodynamic forces at high and low span-based Reynolds numbers.

At a span-based Reynolds number of 613, both the lift and drag coefficients can be seen to decrease with aspect ratio. Here, only LEV 1 is present and its gradient of circulation as a function of wing span is reduced for higher aspect ratios (figure 3.16a).

90

This reduces the lifting capacity across the whole wing and results in the reducing aerodynamic forces with increasing aspect ratio. At higher Reynolds numbers the lift coefficient is approximately constant with aspect ratio until around an aspect ratio of 5, after which it decreases. In addition, the drag coefficient increases slightly up to an aspect ratio of approximately 5 before reducing. Here the spanwise gradient of circulation of the LEV is not altered with aspect ratio over the inner part of the wing, but is reduced over the outer part of the wing for high aspect ratios due to the interaction of LEV 2 with the flow at the trailing-edge (figure 3.16b). Thus the lift and drag coefficients are not affected greatly until the reduced LEV circulation over the outer part of the wing begins to influence the aerodynamic forces at high aspect ratios.

Nevertheless, for all Reynolds numbers this change in aerodynamic forces leads to a reduction in the wing's performance for higher aspect ratios. This can be seen in figure 3.21c which shows the lift on drag ratio plotted against span-based Reynolds number for three aspect ratios. Figure 3.21c shows that the lift on drag ratio decreases for increasing aspect ratio. At low span-based Reynolds numbers the lift on drag ratio is less than one due to the high skin friction force. At this Reynolds number the skin friction force accounts for between 4% and 8.5% of the total lift and drag forces depending on the wing aspect ratio. Higher aspect ratio wings have proportionally higher skin friction drag and therefore the lift on drag ratio is reduced for increased aspect ratios. For higher span-based Reynolds numbers, the lift on drag ratio exceeds one for all wings. At these Reynolds numbers the skin friction force is insignificant, however the increased lift on drag ratio for lower aspect ratios is due to the pressure acting across the thickness of the wing's leading-edge. To highlight this, figure 3.21d shows the lift to drag ratio after this surface has been removed from the aerodynamic force calculation. This shows that when the wing's thickness is excluded the lift on drag ratios for each wing become approximately one for high span-based Reynolds numbers. Therefore the variation in lift on drag ratio with aspect ratio shown in figure 3.21c is partly an artefact of the proportionally thinner wings for higher aspect ratios.

3.4.3 Discussion of Leading-Edge Vortex Stability

The ability for the LEV to remain attached to the wing is a key characteristic that is required in order to maintain high lift throughout the wing stroke. Studies that have investigated 2D and 3D translating wings at insect Reynolds numbers and high angles

of attack have shown that the LEV is shed after a few chord lengths of travel (Dickinson & Gotz 1993; Miller & Peskin 2004; Taira & Colonius 2009). However, studies that have incorporated the rotation of the wing about its base have often found stable LEVs (Usherwood & Ellington 2002a; Birch *et al.* 2004; Lentink & Dickinson 2009b). Lentink & Dickinson (2009b) have proposed that the centripetal and Coriolis accelerations due to wing rotation mediate LEV stability. In their analysis, these accelerations scale with the inverse of the Rossby number and therefore they suggest that low Rossby numbers, of the order of one, are required for the LEV to be stable. Lentink & Dickinson proposed that the Rossby number is equal to the wing's aspect ratio for hovering flight and therefore low aspect ratio wing's are required in order for the LEV to be stable.

As shown in §3.4, scaling of the Navier-Stokes equation using wing span resulted in the Rossby number being $Ro = U_{tip}/\Omega R$, and for the centripetal and Coriolis accelerations to scale with $1/Ro^2$ and $1/Ro$ respectively. For a hovering wing, where $U_{tip} = \Omega R$, this results in a Rossby number of one for all aspect ratios. This indicates that a stable LEV is always possible under this flight regime. Furthermore, letting $U_{tip} = U_\infty + \Omega R$, where U_∞ is the flight velocity of the insect or MAV, results in $Ro = U_\infty/\Omega R + 1$. This suggests that only large flight speeds compared to the velocity due to rotation would result in high Rossby numbers and therefore an unstable LEV. This condition is not tested here (see chapter 4), however the stability of the LEV under hovering type conditions is.

All of the simulations show that the LEV remains attached to the wing when it is rotating at a constant rotational velocity. The words "stable" and "attached" are used interchangeably to mean that the structure is persistent throughout the wing's rotation and is not completely shed as it would be for a purely translating wing. At low span-based Reynolds numbers only LEV 1 is present and it remains attached to the wing for the majority of the span for all aspect ratios, only separating near the tip as it joins with the TV (see figure 3.12a,b,c). At higher Reynolds numbers when the dual LEV structure is present, LEV 1 still remains attached to the wing's leading-edge despite the flow becoming unsteady out near the tip of the wing (figure 3.12d,e,f). LEV 2 also remains attached to the wing up until the point at which it bursts (figure 3.12d,e,f), beyond which the flow continues to remain with the wing, suggesting that the vortex structure is persistent. Even at high aspect ratios and moderate Reynolds numbers, when the interaction between LEV 2 and the vorticity at the leading and trailing edges

results in unsteady flow and vortex shedding, the dual LEV structure remains attached to the wing.

The finding that the LEV is always stable regardless of the aspect ratio or span-based Reynolds number disagrees with the hypothosis proposed by Lentink & Dickinson (2009b) that high aspect ratio wings will have unstable LEVs. However, it agrees with the notion that the centripetal and Coriolis accelerations mediate LEV stability as the Rossby number (calculated using span-based scaling) is equal to one for all simulations. However, further investigation is required to confirm the behaviour of the LEV under forward flight conditions. This is explored in chapter 4.

3.4.4   Conditions for which Span-Based Scaling is Applicable

This chapter's results have shown that by using the wing's span rather than chord to scale the flow around a rotating wing allows the LEV structure to be characterised by a span-based Reynolds number. This scaling is useful when comparing the performance of wings with different planform shapes, as it allows each wing to have a comparable LEV structure. However, under what conditions is this scaling applicable? As explained above, this scaling comes about because of the spanwise development of the LEV, which is due to the wing's rotation. This rotation creates a spanwise gradient in the freestream velocity experienced by the wing and a strong spanwise component of velocity that dominates in the region immediately behind the wing.

The spanwise pressure gradient that results from the wing's rotation and the centripetal and Coriolis rotational accelerations are both mechanisms which have been suggested to drive this spanwise velocity (Ellington *et al.* 1996; Aono *et al.* 2008; Lentink & Dickinson 2009b). Clearly the wing's rotation is important for both mechanisms. Lentink & Dickinson (2009a) have proposed that moving the wing further away from its rotation axis is analogous to transitioning from pure rotation to only translation. It is therefore possible that increasing the offset distance will reduce the spanwise velocity compared to freestream velocity, which would be equivalent to increasing forward flight speed for a wing rotating about its base. Hence, the use of wing span as the characteristic length is likely to not apply for wings with large offset distances or large forward flight velocities. Another way of viewing this is simply that the span-based scaling may not apply when the Rossby number is high, as it is a measure of the wing's rotation compared to translation.

The strength of the spanwise velocity also seems to be linked the wing's angle of attack. Usherwood & Ellington (2002a) observed for their rotating model hawkmoth wings that at very low angles of attack there was no spanwise flow. Occasionally at small angles of attack, around 10 degrees, the flow separated from the leading-edge and travelled rapidly towards the tip and only at higher angles of attack did a consistent spanwise velocity form. Lu *et al.* (2006) also noted that considerable spanwise flows were only generated for angles of attack above 30 degrees. Finally, for angles of attack greater than 30 degrees, Ozen & Rockwell (2011) observed increasing maximum spanwise velocities with angle of attack. Hence, the wing's angle of attack appears to play a role in determining when the span-based scaling can apply, as sufficiently large angles of attack are required in order for the flow to separate from the leading-edge consistently and therefore allowing the spanwise velocity component to dominate behind the wing.

Many studies in the literature that have observed stable LEVs have reported a three-dimensional LEV structure along the wing's span as well as significant spanwise flows on the leeward side of the wing. Additionally, the simplified kinematic motion used in this study has been shown to be a good approximation of the beginning of a typical insect's flapping stroke (Poelma *et al.* 2006; Lentink & Dickinson 2009b) and thus generates similar structures to those seen on flapping wings. Therefore this span-based scaling has the potential to apply over a wide range of both flapping and rotating wing flows. The above discussion suggests that the wing's offset from it's rotation axis, angle of attack and flight velocity may all have an influence on when this scaling can apply. However, the extent to which these parameters influence this requires further investigation.

3.5   Prediction of Vortex Breakdown

In the past, several vortex breakdown criteria have been applied to both free swirling jets and swirling pipe flows in order to predict the onset of vortex breakdown. In this section, one of these criteria is applied to the rotating wing numerical data in an attempt to see if it can successfully predict vortex breakdown in a more complex flow. Here the swirl parameter proposed by Billant *et al.* (1998) is used. They derive the vortex breakdown criterion by considering the case of a free vortex undergoing conical breakdown in a flow of infinite extent. The Bernoulli equation is applied along the
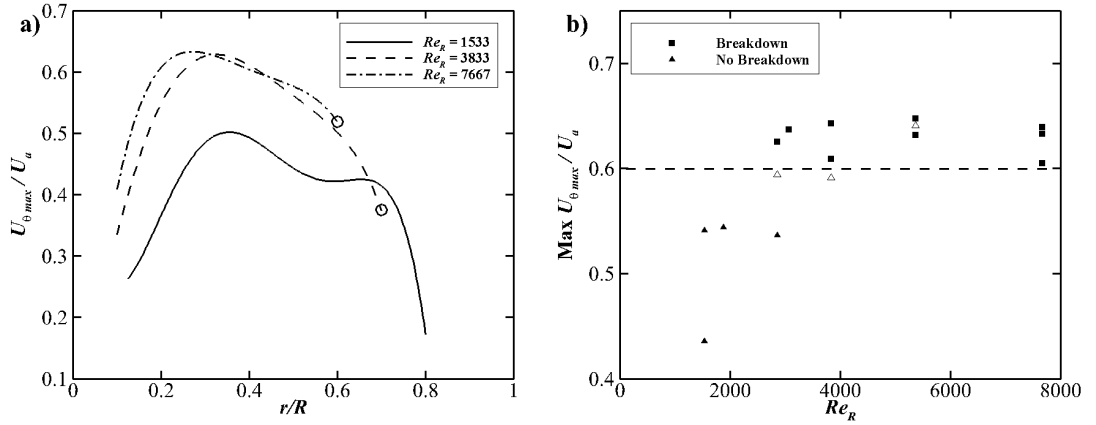
FIGURE 3.22: Swirl parameter graphs. (a) Variation of the swirl parameter along the wing's span for the aspect ratio 2.91 wing at three Re_R values. Open circles indicate the spanwise position of the breakdown point. (b) Maximum swirl parameter as a function of Re_R. Open symbols represent high aspect ratio cases where vortex breakdown is supressed due to the proximity of LEV 2 to the trailing-edge.

streamline on the vortex axis and the assumption is made that the stagnation region is directly connected to the surrounding quiescent fluid and therefore the pressure at stagnation is equal to the ambient pressure. This results in the following relation

$$\frac{\int_0^\infty \frac{U_\theta^2}{l} \mathrm{d}l}{U_a^2} = \frac{1}{2}, \tag{3.6}$$

where U_a is the axial velocity on the vortex axis, U_θ is the azimuthal velocity and l is the radial distance from the vortex axis. To simplify this further the particular case of a Rankine vortex is considered. Here, $U_\theta = \Omega_\theta l$ within the vortex core ($l \leq a$) and $U_\theta = \Omega_\theta a^2/l$ outside it ($l > a$), where a is the core radius and Ω_θ is the solid body rotational velocity of the vortex. Thus this criterion reduces to

$$\frac{U_{\theta max}}{U_a} = \frac{1}{\sqrt{2}}, \tag{3.7}$$

where $U_{\theta max}$ is the maximum azimuthal velocity.

This swirl criterion is applied to LEV 2 in figure 3.22a, which shows the variation of this parameter along the span for the aspect ratio 2.91 wing at three span-based Reynolds numbers. For high span-based Reynolds numbers where LEV 2 is observed to break down, the swirl parameter rapidly increases near the root of the wing and reaches a maximum value before reducing more slowly with span until the point of breakdown (as indicated by the open circles). For these Reynolds numbers, the maximum swirl criterion that is reached is of a comparable value. For the lowest span-based

95

Reynolds number, vortex breakdown was not observed to occur and the swirl parameter is generally much lower across the whole span. Figure 3.22b shows a plot of the maximum swirl parameter with span-based Reynolds number applied to all cases where a dual LEV system was observed over a portion of the wing. It shows that for all cases where vortex breakdown occurs the maximum swirl parameter exceeded a value of approximately 0.6, which suggests that this is the critical value for this flow regime. This critical value is, however, in the order of 15% lower than the theoretical limit of $1/\sqrt{2}$. Nevertheless, the assumptions of an infinite flow extent and of the stagnation pressure being equal to the ambient pressure, which are made in the derivation of equation 3.7, do not apply to this flow regime and could account for the lower critical value. It is worth noting, however, that maximum swirl values of around 0.6 or higher were calculated for some cases but no vortex breakdown was seen to occur. These are shown in figure 3.22b by the open symbols and correspond to high aspect ratios where vortex breakdown is suppressed because of the interaction of LEV 2 with the trailing-edge. Under these conditions the prediction of vortex breakdown failed and so the application of this breakdown criterion to these simulations was only partially successful.

3.6 Summary

In this chapter, the flow structures over rotating wings with different aspect ratios for a range of Reynolds numbers have been investigated. Simulations of a fruit fly wing ($AR = 2.91$) were conducted at Reynolds numbers between 120 and 1500. Over this Reynolds number range a dual LEV structure was found to develop, where the LEV split into two co-rotating vortex structures separated by a smaller counter-rotating vortex. Results at higher aspect ratios revealed that the same dual LEV structure develops with increasing aspect ratio at a fixed Reynolds number.

Analysis of the flow structures suggested that these results could be scaled in an alternative manner so as to decouple the effects of Reynolds number and aspect ratio. It was found that by using the wing's span as the characteristic length, rather than chord, that these results could be scaled using a span-based Reynolds number to yield similar LEV structures for different aspect ratio wings. The span-based Reynolds number was able to independently describe the location where two co-rotating vortices could be observed as well as the breakdown point of the downstream vortex.

This scaling proved to be useful when comparing the performance of different wing

shapes and was used in this study to assess the impact of aspect ratio on the flow structures and aerodynamic forces. The main effect of aspect ratio is to increase the size of the LEV relative to the wing's chord length, which results in the flow reattachment point downstream of the LEV being closer to the trailing-edge. At low span-based Reynolds numbers, this leads to higher aspect ratio wings having reduced LEV circulation and therefore decreased lift and drag. At high span-based Reynolds numbers, when the dual LEV structure had developed, it was found that high aspect ratio wings altered the direction of the downstream LEV near the wing tip. When the aspect ratio was large enough, such that a significant portion of the LEV was affected, this resulted in reduced lift and drag coefficients due to the LEV losing circulation in the outer part of the wing. This finding reveals that low aspect ratio wings do in fact outperform high aspect ratio wings under these conditions.

The span-based scaling also resulted in a new definition for the Rossby number. Using the low Rossby number hypothesis of Lentink & Dickinson (2009b), this Rossby number suggested that the LEV should always be stable under hovering flight conditions regardless of the wing's aspect ratio. Analysis of the flow structures revealed this to be the case for the range of aspect ratios tested and therefore the results of this study agree with the low Rossby number theory. However, it was shown that increasing the flight speed will increase the Rossby number and therefore the LEV could become unstable. This was not tested in this chapter but is explored in chapter 4.

Chapter 4

Aspect Ratio: Leading-Edge Vortex Stability

4.1 Introduction

The attachment of the LEV is essential for the wing's performance, however the mechanism that stabilises the LEV is not well understood. A number of hypotheses have been proposed as to how the stability of the LEV is maintained. These include spanwise vorticity transport due to the spanwise component of velocity (Maxworthy 1979; Ellington *et al.* 1996; van den Berg & Ellington 1997), vortex tilting due to the downwash velocity (Birch & Dickinson 2001; Cheng *et al.* 2013) and rotational accelerations due to the low Rossby number rotation of the wing (Lentink & Dickinson 2009b).

In chapter 3, it was demonstrated that the LEV remained attached over a range of wing aspect ratios under hovering flight conditions and that similar LEV structures could be produced if the flow field is scaled using the wing's span. This scaling resulted in a span-based Reynolds number and Rossby number. Combining this new Rossby number and the low Rossby number hypothesis of Lentink & Dickinson (2009b) suggests that the LEV would become unstable at some point under forward flight conditions. However, the change in the LEV's characteristics with flight speed is not well understood. The flight speed of an insect is defined by the advance ratio (equation 1.8), which is the ratio of the flight velocity relative to the wing tip flapping velocity. Both Nagai *et al.* (2009) and Bross *et al.* (2013) reported stable LEVs at various advance ratios over flapping and rotating wings respectively, but Gopalakrishnan & Tafti (2010) reported that the LEV was shed from the outer part of the wing mid-way through the downstroke at an advance ratio of 0.5. Moreover, all of these studies where conducted at different stroke plane angles and for different aspect ratio wings, and given the LEV size

99

relationship with aspect ratio (see §3.4.2), this could explain the difference in findings.

This chapter describes an investigation into the effect of aspect ratio and advance ratio on the characteristics and stability of the LEV for flapping wings at insect Reynolds numbers. The aim of this study is to determine the role that wing aspect ratio plays, if any, in determining the stability of the LEV. In addition, this investigation aims to provide a more in-depth description of the change in the LEV's characteristics with advance ratio.

The flapping-wing model was used for this study as it provided a more realistic description of the flow under forward flight conditions. The wing is prescribed a simplified flapping motion and the freestream velocity is adjusted to achieve the desired advance ratio. The results of this model are first validated against the experimental force measurements of Sane & Dickinson (2001). The span-based scaling was used for this investigation, and the effects of advance ratio and aspect ratio were explored at two span-based Reynolds numbers. The results for a span-based Reynolds number of 613 are first presented. Here the time evolution of the LEV structure throughout a flapping cycle under hovering conditions is highlighted. The changes in the characteristics of the LEV with advance ratio are then explored, with particular emphasis being given to the downstroke. This model is extended to different aspect ratio wings and the effect of advance ratio and aspect ratio on the stability of the LEV is discussed. The effects of advance ratio and aspect ratio at a span-based Reynolds number of 7668 are then presented, and it is shown that stability of the LEV is still dependent on these parameters at this Reynolds number. Finally, the results of this study are discussed in relation to LEV stability theories.

4.2 Validation

In order to compare the results of the flapping-wing numerical model to the experimental force measurements of Sane & Dickinson (2001), a simulation with slightly different kinematics was constructed to those defined in §2.3. Sane & Dickinson used a dynamically scaled model of a fruit fly wing to study how changes in wing kinematics influence the aerodynamic forces acting on the wing throughout the flapping cycle. A set of these experimental results were used as a point of comparison to validate the numerical model. The kinematics consisted of a smoothed triangular motion for the wing's stroke position and a smoothed trapezoidal motion for the wing's angle of incidence with a
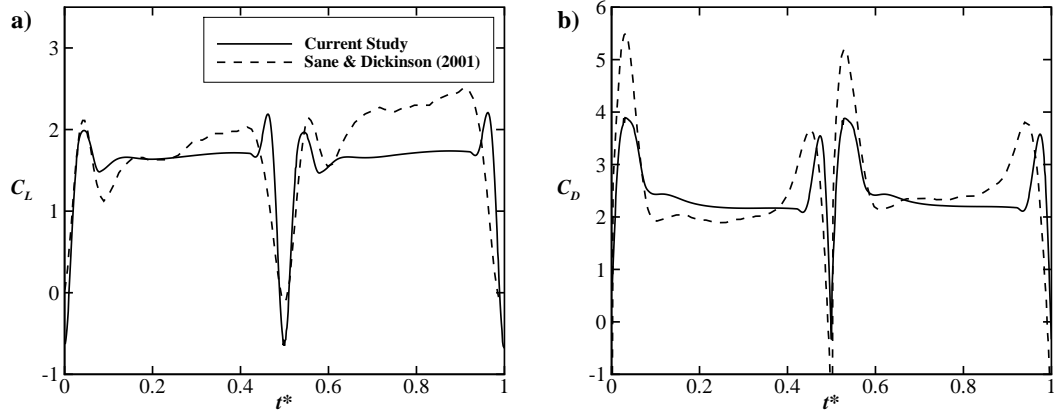
FIGURE 4.1: Variation of the lift and drag coefficients over a flapping cycle ($\Phi = 180, \alpha_0 = 50°, Re = 110$). Comparison of the current study with the experimental results of Sane & Dickinson (2001).

flip duration of 16% of the flapping period. The peak to peak amplitude was $\Phi = 180°$ and the angle of attack of the wing at mid-stroke was $\alpha_0 = 50°$.

Sane & Dickinson did not specify an exact Reynolds number for this experiment as it varied between the different kinematic motions considered, however they stated that it was in the range of 100. Nonetheless, the Reynolds number was estimated, based on the mean wing chord length, to be 110 using their wing's geometry and fluid's kinematic viscosity for this particular set of kinematics. This Reynolds number was matched in the computational model.

The comparison between the experimental and numerical lift and drag coefficients over the flapping cycle is shown in figure 4.1. The aerodynamic forces are plotted as a function of dimensionless time (t^*) from the beginning of the upstroke. Both the experiment and the numerical model were performed in hovering conditions and therefore the variation in aerodynamic forces is symmetric for both the up- ($0 \leq t^* \leq 0.5$) and downstrokes ($0.5 \leq t^* \leq 1.0$) for the numerical simulations. Some asymmetry can be observed in the experimental results, particularly in the lift coefficient measurements, which Sane & Dickinson (2001) suggest is due to "small asymmetries in the stroke pattern introduced by the gearbox of the model." Overall, better agreement is seen between the numerical and experimental results for the upstroke, where the average lift coefficient is 1.81% lower and the drag coefficient is 0.38% higher than the experimental values. This is compared to 17.43% and 7.12% lower for the mean lift

101

and drag coefficients respectively for the downstroke. Nonetheless, the variation in the aerodynamic forces is consistent throughout the cycle, where the peaks in aerodynamic forces, both before and after each stroke reversal due to rapid pitch rotation and wake capture respectively, are clearly seen in the numerical data. The timing of the force peak after stroke reversal, associated with wake capture, is in good agreement with the experimental results, however the rapid pitch rotation force peak is slightly delayed compared to the experimental results. This suggests that there may be a difference in kinematics in this portion of the flapping cycle in which the experimental wing begins its pitch rotation earlier in the cycle compared to the numerical model.

4.3   Results at Low Reynolds Number

4.3.1   Hovering

A number of studies have investigated the vortex structures that form over a flapping wing under hovering conditions (e.g. Poelma et $al.$ 2006; Aono et $al.$ 2008; Liu & Aono 2009; Jardin et $al.$ 2012). The change in flow structures over the wing throughout the downstroke at zero advance ratio for this study is shown in figure 4.2 (also see movie B.7). The formation of flow structures observed here is comparable to that reported in these earlier studies, and due to the symmetric flapping kinematics, this flow pattern is repeated for the upstroke but with the vortex structures having opposite directions of rotation.

At the beginning of the downstroke ($t^* = 0.5$) the LEV_U and TV_U system from the previous upstroke can be seen, along with the rotational starting vortex (RSV) that is created by the pitch rotation of the wing. This RSV is shed from the wing as it continues its pitch rotation and the LEV_U is also shed as the wing reverses its direction ($t^* = 0.54$). At this point a horseshoe shaped vortex is formed around the wing comprising of a new LEV_D, TV_D and TEV_D. As the wing's motion continues this horseshoe vortex grows in size, particularly towards the wing's tip, which results in a conically shaped LEV. The previously shed LEV_U and TV_U from the upstroke are swept underneath the wing and the newly formed TEV_D is shed from the wing ($t^* = 0.6$). These vortex structures are left behind in the wake of the wing as it continues to rotate. From about $t^* \approx 0.83$ the flow structures on the wing remain more or less steady until the wing begins its pitch up at the end of the stroke, at which point a new RSV is created at the trailing-edge.
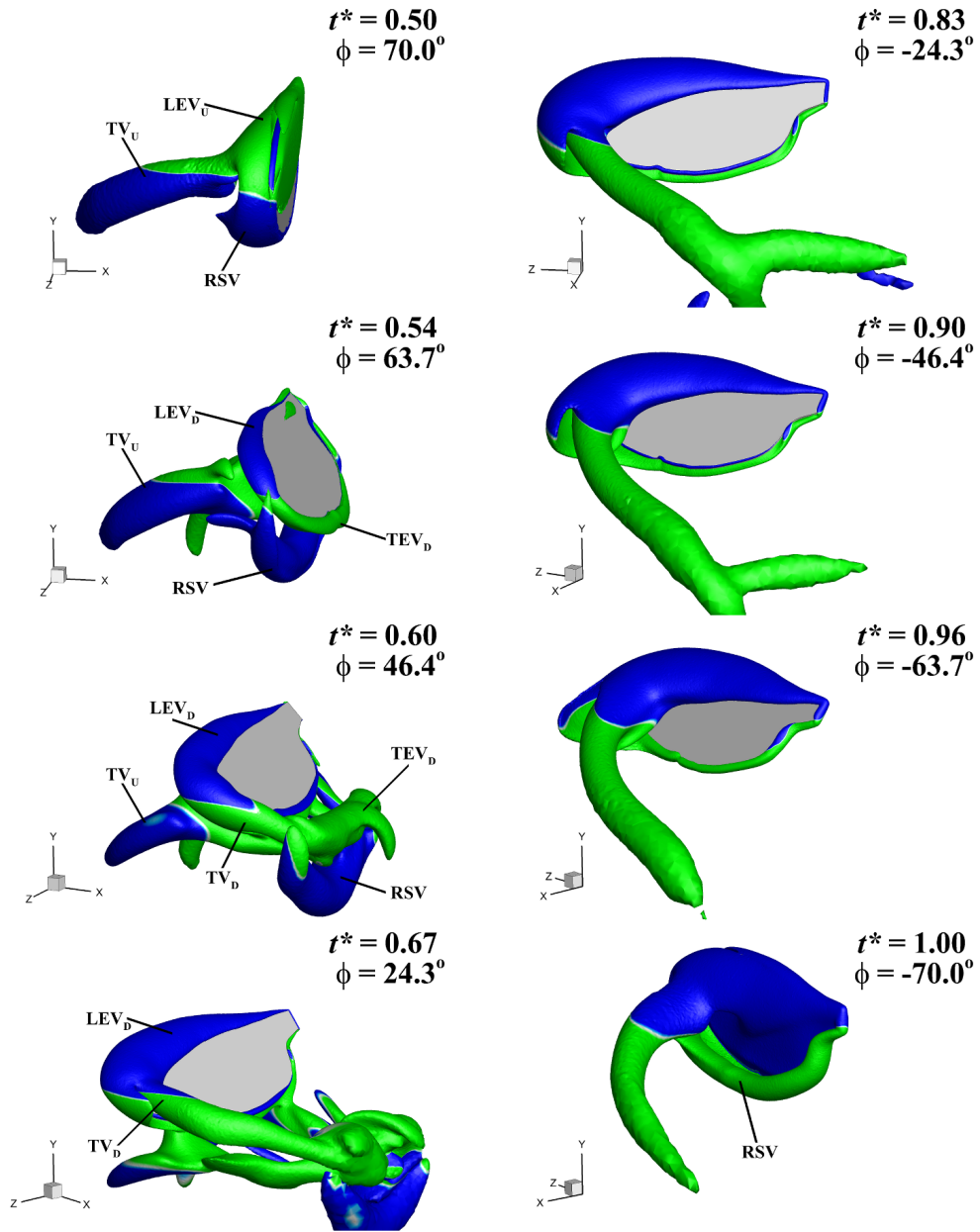
FIGURE 4.2: Stationary view of the wing's motion (clockwise rotation) and the generated flow structures during the downstroke for hovering conditions ($J = 0, AR = 2.91, Re_R = 613$). Vortex structures are visualised by iso-Q surfaces coloured by spanwise vorticity to indicate direction, green is positive and blue is negative. The sequence progresses from top to bottom. Also see movie B.7.
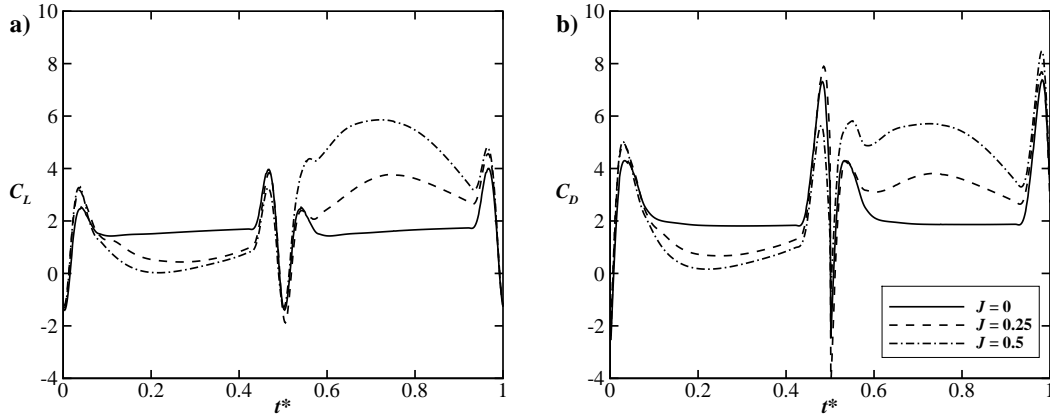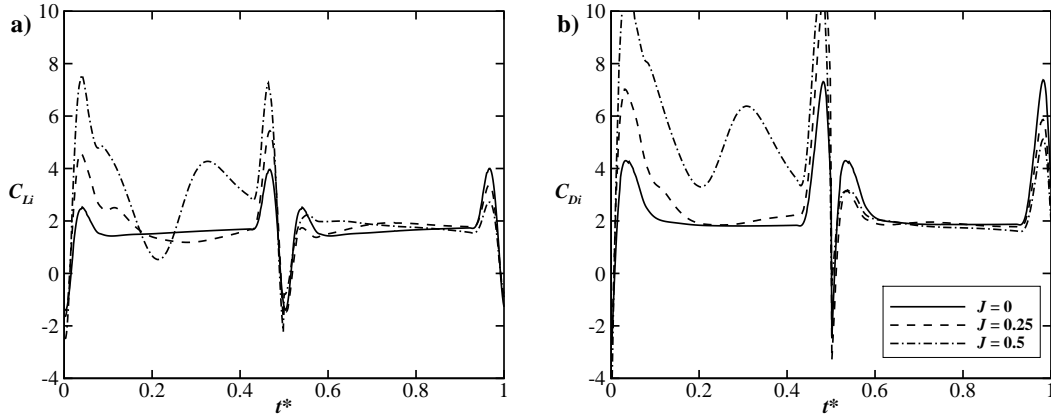
FIGURE 4.3: Change in lift and drag coefficients throughout a flapping cycle with advance ratio. Results are for the $AR = 2.91$ wing at $Re_R = 613$ and the lift and drag coefficients are based on average flapping velocity at the radius of gyration ($\bar{U}_{rg}$).

4.3.2 Effect of Advance Ratio

4.3.2.1 Aerodynamic Forces

The effect of advance ratio is to generally create an asymmetry between the upstroke and the downstroke. This can be seen in both the aerodynamic forces and flow structures that are generated for each half cycle. This asymmetry is induced by the change in relative velocity experienced by the wing, where the relative velocity is increased during the downstroke but is reduced for the upstroke (Dickson & Dickinson 2004). Increasing the advance ratio increases this imbalance and thus for high advance ratios the aerodynamic forces are much larger for the downstroke compared to the upstroke (Ellington 1999; Dickson & Dickinson 2004; Nagai *et al.* 2009). This can be seen in figure 4.3 which shows the variation in lift and drag coefficients throughout the cycle at $J = 0, 0.25$ and 0.5. The aerodynamic force coefficients are reduced during the upstroke ($0 \leq t^* \leq 0.5$) but are augmented during the downstroke ($0.5 \leq t^* \leq 1.0$) for increasing advance ratio. Note that the coefficients here are calculated using the average flapping velocity at the radius of gyration (see §2.3) and therefore the effect of the freestream velocity is not incorporated into the calculation as it averages out to zero over a complete flapping cycle.

Nagai *et al.* (2009) reported that advance ratio changes the effectiveness of the pitch rotation and wake capture mechanisms, which can also be seen in these simulations. Outside of these stroke reversal periods the wing produces approximately constant
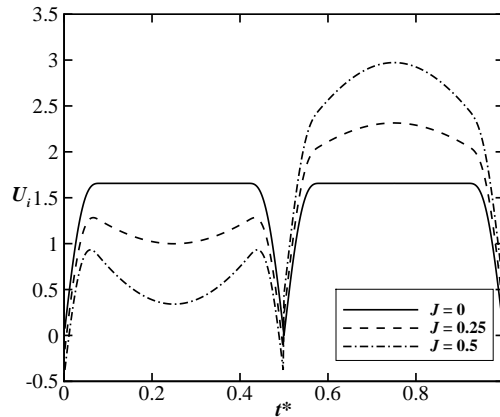
FIGURE 4.4: Time variation of the relative velocity at the wing's radius of gyration throughout a flapping cycle for different advance ratios.

lift and drag coefficients under hovering conditions ($J = 0$). For non-zero advance ratios, the aerodynamic forces are no longer constant and vary throughout each half cycle such that there is a minimum around mid-upstroke and a maximum around mid-downstroke. This was first observed by Dickson & Dickinson (2004) in their rotating wing experiments where they demonstrated that the aerodynamic forces depended on both the advance ratio and the wing's stroke position.

Dickson & Dickinson (2004) suggested that the variation in aerodynamic forces could be accounted for by using the wing tip velocity ratio, which they defined as the ratio of the chordwise components of flow velocity at the wing tip due to translation and revolution. The tip velocity ratio varies between $-J$ at mid-upstroke and J at mid-downstroke. Using this ratio in the calculation of the lift and drag coefficients effectively computes a force coefficient that is based on the instantaneous relative velocity seen by the wing. For the flapping wing simulations, the time variation in relative velocity at a particular spanwise location (r) is given by $U_i = r|\frac{\mathrm{d}\phi(t)}{\mathrm{d}t}| \pm V\cos(\phi(t))$, where the two velocity components are added together for the downstroke and are subtracted for the upstroke. The variation in this velocity throughout the wing's stroke for different advance ratios is presented in figure 4.4. U_i is positive when the velocity is in the opposite direction to the wing's motion. Increasing the advance ratio results in higher relative velocities experienced by the wing during the downstroke and lower velocities for the upstroke. However, due to the variation in the angle between the wing and the freestream velocity, the relative velocity also changes such that it is a maximum at

FIGURE 4.5: Change in instantaneous lift and drag coefficients throughout a flapping cycle with advance ratio. Results are for the $AR = 2.91$ wing at $Re_R = 613$ and the lift and drag coefficients are calculated using the instantaneous velocity at the radius of gyration (U_i).

mid-downstroke and a minimum at mid-upstroke.

To test Dickson & Dickinson's idea on a typical flapping wing motion, the lift and drag coefficients were re-calculated for the flapping wing simulations using the instantaneous relative velocity. This was computed at the wing's radius of gyration ($r = 0.57R$), so that the force coefficients returned the same values for $J = 0$ as calculated previously. The variation in the instantaneous lift and drag coefficients are shown in figure 4.5 where the lift and drag coefficients are labelled as C_{Li} and C_{Di} respectively to denote the use of U_i. Note that here the relative velocity is approximated to be $U_i \approx r\Omega \pm V\cos(\phi(t))$, where Ω is the rotational velocity of the wing at mid-stroke as defined in §2.3. This was done to avoid excessive spikes in the coefficients around stroke reversal where the velocities are low. Figure 4.5 reveals that the instantaneous lift and drag coefficients are more comparable during the downstroke between advance ratios, but there is still some variation in coefficients outside of the stroke reversal times. This can be particularly seen in the instantaneous lift coefficient, which reduces by 18.6% between $t^* = 0.6$ and 0.9 for $J = 0.5$ but increases by 20.4% and 18.9% for $J = 0$ and 0.25 respectively. Note that over this period ($0.6 \leq t^* \leq 0.9$) the wing is rotating at a constant rotational velocity and at a constant angle of attack, as in Dickson & Dickinson's experiment. For the upstroke the instantaneous lift and drag coefficients vary markedly with advance ratio. Thus, the use of the instantaneous velocity to collapse the force coefficients does not seem to apply for a normal flapping

106

motion. This is likely due to the wing's acceleration and the re-establishment of the flow structures which are introduced by the flapping motion due to stroke reversal. These transient effects where purposely avoided in Dickson & Dickinson's rotating wing experiment. This highlights that the change in aerodynamic forces throughout a typical flapping cycle at non-zero advance ratios (figure 4.3) is not purely due to the relative velocity experienced by the wing, but also incorporates a change in flow structures that alter the wing's performance. The variations in vortex structures during the up- and downstrokes for non-zero advance ratios are investigated below.

4.3.2.2 Downstroke Flow Structures

The added relative velocity seen by the wing during the downstroke at non-zero advance ratios causes an increase in the growth rate of circulation of the LEV. This can be seen in figure 4.6a, which shows the time variation in circulation of the LEV at 25% span. This was calculated by integrating the vorticity within an area defined by a contour of the Q criterion. Figure 4.6a reveals a much more rapid increase in the LEV circulation for higher advance ratios, particularly in the early to mid downstroke. Due to the wing's rotation, a spanwise velocity is generated that acts from the wing's root to tip. This spanwise flow drains vorticity generated at the leading-edge into the TV (Ellington *et al.* 1996; Lentink & Dickinson 2009b) and therefore the time evolution of circulation of the LEV is dependent on the balance between vorticity generation at the leading-edge and vorticity transport due to the spanwise component of velocity. An increased rate of accumulation of circulation in the LEV is caused by either an increase in vorticity generation or by a reduction in vorticity transport. Figure 4.6b shows the average spanwise velocity within the vortex core, which demonstrates that during the early to mid downstroke there is increased vorticity transport with advance ratio. Thus, the increase in circulation seen in figure 4.6a must be due to enhanced vorticity production at the leading-edge due to the increased relative velocity experienced by the wing, and this increased production must out-weigh the increased vorticity transport.

To investigate this further, the generation of vorticity near the wing's leading-edge was assessed. Vorticity is generated at the boundary between the wing's surface and the fluid due to tangential pressure gradients and the tangential acceleration of the wing's surface (Morton 1984). The generated vorticity is then diffused into the fluid and advected around the leading-edge, into the LEV. The method used to calculate these two
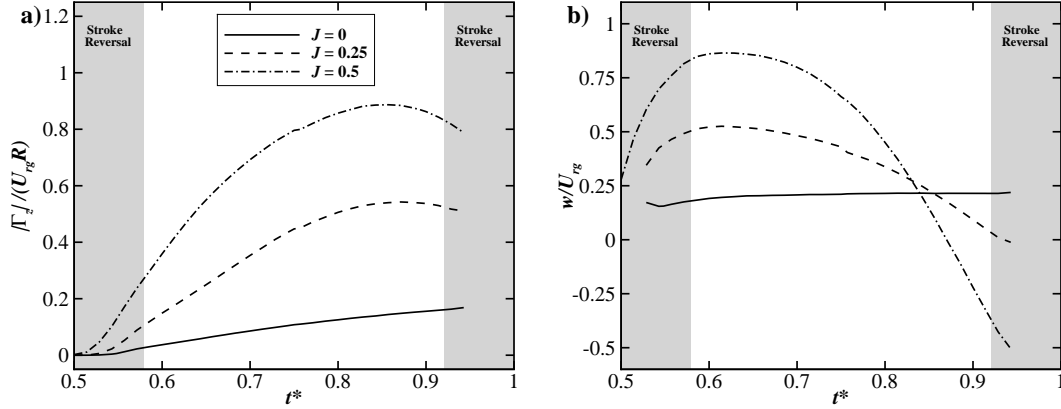
FIGURE 4.6: Time variation of (a) magnitude of LEV circulation ($|\Gamma_z|/U_{rg}R$) and (b) average spanwise velocity within the LEV (w/U_{rg}) at 25% span throughout the downstroke ($AR = 2.91, Re_R = 613$).

production mechanisms is detailed in Appendix A and the results of this analysis are presented in figure 4.7, where the vorticity production is given as the temporal gradient of LEV circulation per unit span that is due to the generated vorticity. Figure 4.7a shows the influence that the tangential pressure gradient has on the production of vorticity at the leading-edge throughout the downstroke at 25% span. During the period of constant velocity rotation the pressure gradient, and therefore the generated vorticity, increases with increasing advance ratio. Furthermore, the production of vorticity follows a similar curve to the relative velocity, which leads to maximum vorticity production occurring around mid-downstroke for non-zero advance ratios. The vorticity generation due to the wing's acceleration is plotted in figure 4.7b. Here the wing's acceleration produces negative vorticity for the first half of the downstroke and positive vorticity for the second half. However, the magnitude of the rate of generated circulation due to the wing's acceleration is four orders of magnitude lower than that due to tangential pressure gradients. Hence, the pressure gradients around the wing's leading-edge dominate the generation of vorticity and the overall vorticity generation follows the curves shown in figure 4.7a. This further demonstrates that increasing the advance ratio, and therefore the relative velocity, causes increased production of vorticity during the downstroke, which leads to an increased rate of accumulation of circulation in the LEV.

Due to the low Reynolds number and therefore high viscous diffusion, the higher
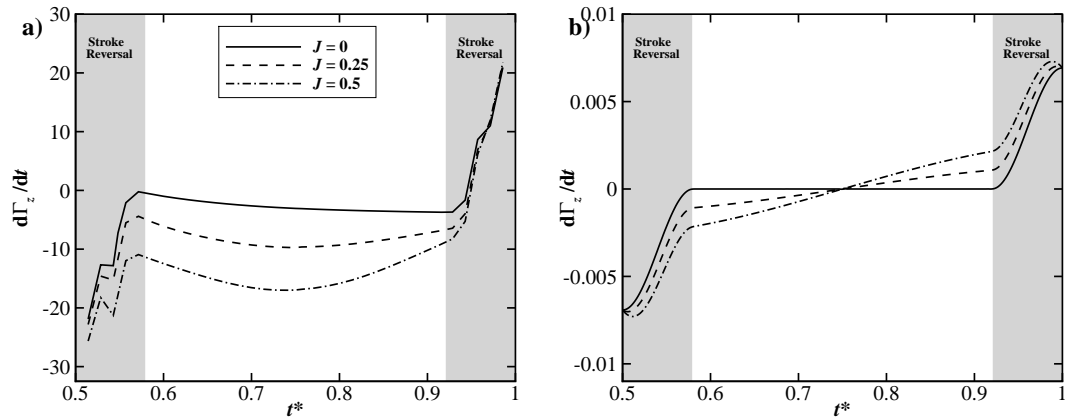
FIGURE 4.7: Change in vorticity generation throughout the downstroke for different advance ratios at 25% span. The vorticity generation is plotted as the time rate of change of circulation due to vorticity production per unit span ($\frac{d\Gamma_z}{dt}$), where (a) is the component due to the tangential pressure gradient on the wing's surface and (b) is the component due to the tangential acceleration of the wing's surface. Appendix A details the calculation of these two quantities.

LEV circulation for non-zero advance ratios results in an increase in the size of the LEV. This can be seen in figure 4.8, which illustrates the change in vortex structures near the wing at three instances during the downstroke for three advance ratios. The left column is for a hovering ($J = 0$) aspect ratio 2.91 wing, and the middle and right columns are for advance ratios of 0.25 and 0.5 respectively at the same aspect ratio. Figure 4.8 shows that at each point in the downstroke, the higher the advance ratio the larger the LEV is. The tip and root vortices also enlarge with increasing advance ratio and as the wing progresses through the downstroke. The increased growth rate of the LEV and TV leads to these vortices becoming so large for high advance ratios that they almost completely cover the entire wing in the latter stages of the downstroke (e.g. $t^* = 0.9, J = 0.5$).

When the LEV becomes too large, the flow no longer reattaches to the wing's top surface. This can be seen in the left hand side images of figure 4.9, which depicts the change in two-dimensional streamlines throughout the downstroke at 50% span for the $J = 0.5$ case. Early in the downstroke, when the LEV is small, the flow separates from the leading-edge but reattaches to the wing just downstream of the LEV, as demonstrated by the half saddle point on the top surface of the wing. As the wing moves through the downstroke the LEV enlarges and this pushes the reattachment

109
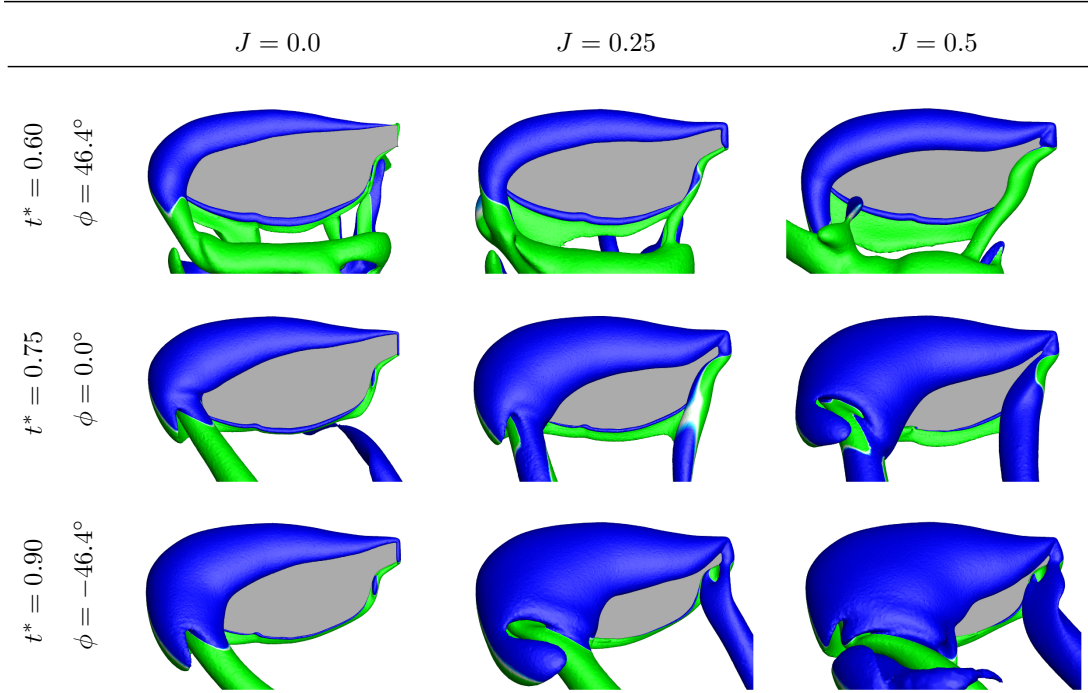
FIGURE 4.8: Flow structures during the downstroke for (left) $J = 0$, (middle) $J = 0.25$ and (right) $J = 0.5$. Images are taken perpendicular to the wing's top surface and are shown for (top) early downstroke, (middle) mid-downstroke and (bottom) late downstroke ($AR = 2.91, Re_R = 613$). Vortex structures are visualised by iso-Q surfaces coloured by spanwise vorticity to indicate direction, green is positive and blue is negative. Also see movie B.7 and movie B.8 for the $J = 0$ and $J = 0.5$ cases respectively.

point towards the trailing-edge. Eventually the saddle point reaches the trailing-edge ($t^* = 0.75$) and the flow no longer reattaches to the wing. This leads to a breakdown of the Kutta condition and the formation of a TEV ($t^* = 0.90$).

The right hand side of figure 4.9 shows the surface streamlines on the wing's top surface. During the early part of the downstroke a positive bifurcation line extends from the wing root to tip, which is associated with the reattachment of the flow downstream of the LEV. Because the LEV is conical in shape, as it grows in size the flow reattachment first reaches the trailing-edge near the wing tip. As it continues to enlarge and the TV extends from the wing tip, the bifurcation line is shifted towards the trailing-edge and the wing's root. This results in the bifurcation line reaching the trailing-edge earlier along the wing's span, which indicates that the flow does not reattach to the wing over a larger proportion of the wing's span. By the end of the downstroke ($t^* = 0.9$) almost the entire wing experiences fully separated flow. The significance of this finding will be discussed further in §4.3.4 and §4.3.5.

110
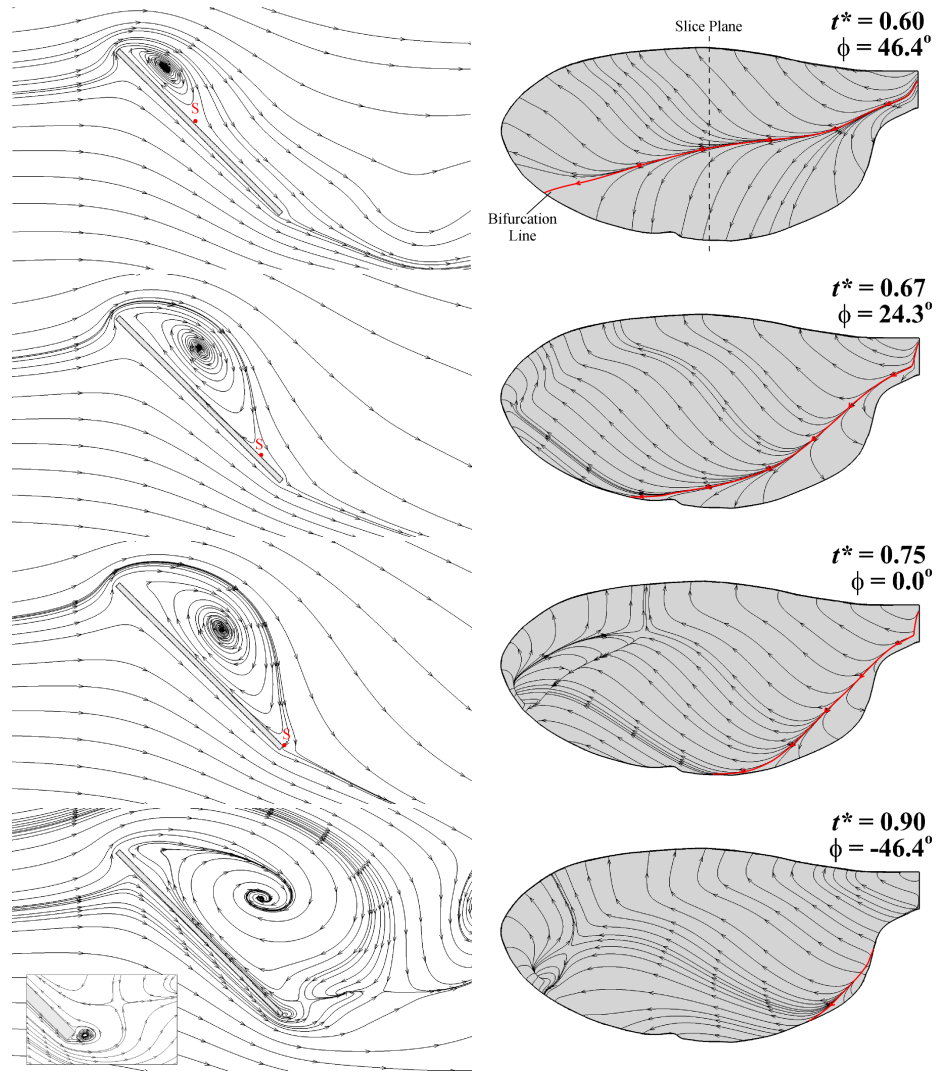
FIGURE 4.9: Flow topology images throughout the downstroke for the $AR = 2.91$ wing at $J = 0.5$ and $Re_R = 613$. (Left) Two dimensional streamlines at 50% span. "S" marks the half saddle point on the wing's top surface and the inset in the bottom image displays a close up of the flow topology at the wing's trailing-edge. (Right) Surface streamlines.

4.3.2.3 Upstroke Flow Structures

The variation in relative velocity for the upstroke is the opposite to the downstroke in that it decreases with increasing advance ratio. Figure 4.4 illustrates that for the upstroke ($0 \leq t^* \leq 0.5$) the velocity experienced by the wing is not only reduced for higher advance ratios, but it also varies throughout the upstroke such that it is a maximum just before and after each stroke reversal, and it is a minimum at mid-upstroke. This therefore leads to both an overall reduction in vorticity generation

111
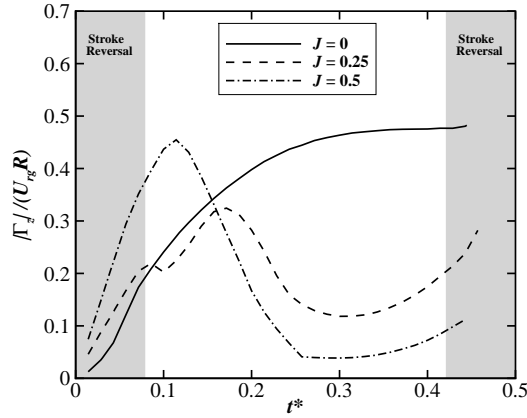
FIGURE 4.10: Time variation of the magnitude of total LEV circulation ($|\Gamma_z|/U_{rg}R$) at 60% span throughout the upstroke ($AR = 2.91, Re_R = 613$).

at the leading-edge with increasing advance ratio and a significant drop in vorticity production around mid-upstroke for non-zero advance ratios. The higher the advance ratio the larger the variation in vorticity production throughout the upstroke.

This results in a significant variation in the circulation of the LEV throughout the upstroke for non-zero advance ratios. This is highlighted in figure 4.10, which shows the variation in LEV circulation at 60% span for three advance ratios. For the hovering case, the time variation in LEV circulation is the same as for the downstroke, although note that the circulation is higher in figure 4.10 than in figure 4.6 as the former is calculated further out along the wing's span. Here the LEV's circulation increases during the early to mid upstroke and then flattens out to become approximately constant towards the end of the stroke. Increasing the advance ratio results in an initial increase in the growth rate of circulation in the early part of the stroke due to the enhanced wake capture mechanism observed for the upstroke with increasing advance ratio (see figure 4.3). However, as the wing approaches mid-upstroke the circulation in the LEV rapidly drops as the vorticity production reduces. After mid-upstroke the LEV's circulation grows again as the relative velocity and vorticity generation increase.

The time variation in vorticity generation and LEV circulation causes a substantial change in the vortex structures around the wing during the upstroke for non-zero advance ratios. Figure 4.11 depicts the change in vortex structures near the wing at three instances during the upstroke for three advance ratios. The left column is for a hovering ($J = 0$) aspect ratio 2.91 wing, which demonstrates that the upstroke flow structures

112
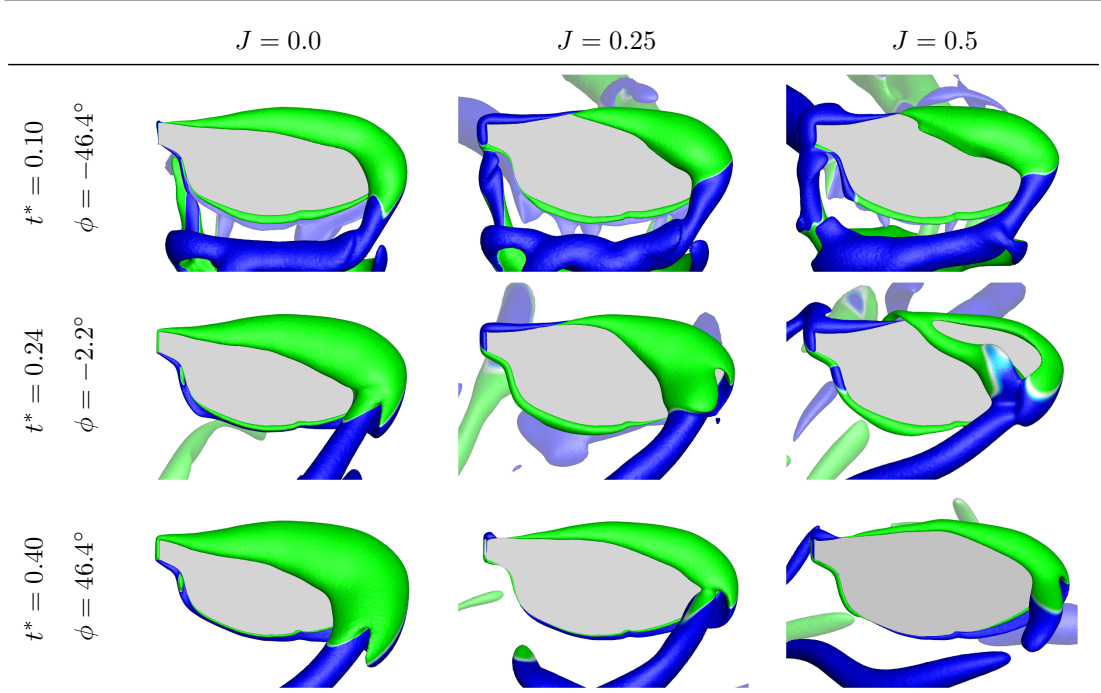
FIGURE 4.11: Flow structures during the upstroke for (left) $J = 0$, (middle) $J = 0.25$ and (right) $J = 0.5$. Images are taken perpendicular to the wing's surface and are shown for (top) early upstroke, (middle) mid-upstroke and (bottom) late upstroke ($AR = 2.91, Re_R = 613$). Vortex structures are visualised by iso-Q surfaces coloured by spanwise vorticity to indicate direction, green is positive and blue is negative. Faded vortex structures are left over from the previous downstroke and are behind the wing.

are identical to the downstroke except with opposite sign of rotation. The middle and right columns are for advance ratios of 0.25 and 0.5 respectively. As the freestream velocity is acting with the wing's rotation, a region of reversed flow is created near the wing's root and thus the LEV is restricted to being in the outer part of the wing for non-zero advance ratios. In the early upstroke ($t^* = 0.1$) the LEV is larger due to the enhanced wake capture mechanism. However, by middle to late upstroke the LEV is smaller for larger advance ratios. Increasing the advance ratio also allows the TV and wake structures to remain close to the wing.

At an advance ratio of 0.5 the iso-Q surface representing the LEV can be seen to split, revealing a dual LEV structure. This dual vortex structure was only observed at this advance ratio and must be due to the very low relative velocity around mid-upstroke at this advance ratio. Around mid-upstroke, the low relative velocity causes both low vorticity generation and a low advection velocity. This allows the LEV that is created from wake capture earlier in the stroke to break away from the leading-edge. A
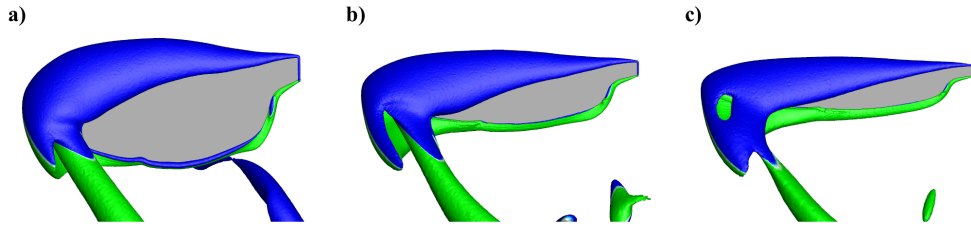
FIGURE 4.12: Vortex structures at mid-downstroke ($t^* = 0.75$) for three aspect ratio wings ($J = 0, Re_R = 613$); (a) $AR = 2.91$, (b) $AR = 5.10$ and (c) $AR = 7.28$. Images are taken perpendicular to the wing's top surface and vortex structures are visualised by iso-Q surfaces coloured by spanwise vorticity to indicate direction, green is positive and blue is negative.

new LEV is created behind it resulting in the dual vortex structure. As the downstream LEV is no longer fed vorticity from the leading-edge, it quickly cross-annihilates with a region of opposite sign vorticity on the wing's surface and possibly with the TV due to its close proximity. Hence by the late upstroke ($t^* = 0.4$) the downstream LEV has gone, leaving only the smaller LEV near the leading-edge. This variation in flow structures throughout the upstroke explains the significant change in instantaneous force coefficients observed in figure 4.5.

4.3.3 Effect of Aspect Ratio

Here the effect of aspect ratio at an advance ratio of zero is considered, however the effect of aspect ratio applies equally to other flight speeds. Figure 4.12 shows the vortex structures near the wing at mid-downstroke for three different aspect ratio wings. As was found in the first aspect ratio study (chapter 3) and can also be seen here, by scaling the flow using a span-based Reynolds number a very similar vortex structure is created over each of the different aspect ratio wings. Figure 4.12 demonstrates that the size of the LEV is approximately constant relative to the wing's span between each aspect ratio wing. Thus, modifying the wing's aspect ratio can be seen as effectively changing the wing's chord length relative to a fixed LEV size. This leads to the LEV being much larger in proportion to the wing for higher aspect ratios.

It doesn't matter how the wing's aspect ratio is changed, either by stretching the wing in the chordwise or spanwise directions, this condition is still met if the flow is scaled using the span-based Reynolds number. If the span-based Reynolds number is not maintained and either the conventional chord-based Reynolds number is used or no scaling is made, then increasing the aspect ratio still leads to a larger LEV relative

the wing's size but it also includes a change in the structure of the LEV due to an alteration of the span-based Reynolds number (see §3.3).

4.3.4 Leading-Edge Vortex Stability

In this section, a case in which the effects of advance ratio and aspect ratio are combined is first considered. It was found that at high aspect ratios and high advance ratios the LEV becomes unstable and is shed from the wing during the downstroke. An example of this can be seen in figure 4.13, which shows the change in spanwise vorticity during the early stages of the downstroke at 70% span for an $AR = 7.28$ wing at $J = 0.5$. The black lines are a single contour of the Q criterion. At the beginning of the downstroke ($t^* = 0.54$) the LEV and TEV form. The TEV is soon shed from the wing and the LEV quickly grows to become as large as the wing's chord length. At this point ($t^* = 0.64$) the flow can no longer reattach to the wing's top surface. The Kutta condition breaks down and vorticity forms at the trailing-edge. As the wing continues through the downstroke, the LEV is eventually shed into the wake ($t^* = 0.71$) and the TEV grows in size.

This process is remarkably similar to the initial flow patterns created by a translating wing, as described by Dickinson & Gotz (1993) from their two-dimensional wing towing tank experiments. However, figure 4.14 (also see movie B.9) shows a three-dimensional view of this shedding process which illustrates that it is not two-dimensional. Figure 4.14 reveals that the LEV and TEV form part of a vortex loop that is shed from the wing. In the early stages of the downstroke ($t^* = 0.6$) the TEV_1 is shed from the wing and the LEV_1 quickly grows to envelop the entire wing. The LEV_1 and TEV_1 are connected by the TV to form a ring vortex that extends back to the wing's root. As the wing continues to rotate the LEV_1 peels away from the outer part of the wing and a new TEV_2 begins to form. By mid-stroke ($t^* = 0.75$) LEV_1 has completely shed from the outer 50% of the wing. For this aspect ratio wing, at this advance ratio, the shedding of the LEV seems to be confined to the outer half of the wing. A new LEV_2 has begun to form in its place and the second TEV_2 has separated from the wing near the wing tip. The shed LEV_1 and TEV_1 form a counter-rotating vortex pair in the wake of the wing and are part of a vortex loop that remains connected to the wing. Note that the change in colour of LEV_1 and TEV_1 in figure 4.14 at $t^* = 0.83$ is due to their change in orientation relative to the wing and not due to a change in sign.
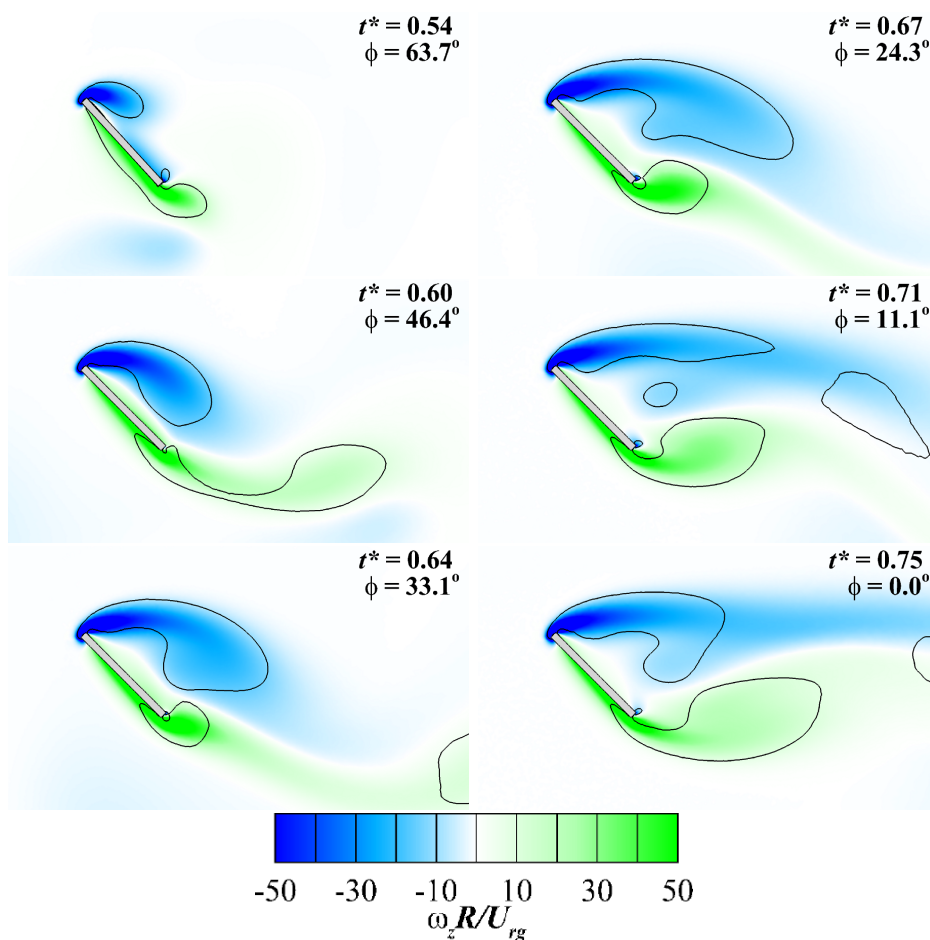
FIGURE 4.13: Spanwise vorticity contours at 70% span for $AR = 7.28$ wing at $J = 0.5$ and $Re_R = 613$. Solid line is a single contour of the Q criterion. The sequence progresses from top to bottom.

For this particular case, this shedding process is repeated two more times before the end of the downstroke, where LEV_2 and TEV_2 are shed from the wing as part of a vortex loop that peels away from the wing tip with the TEV leading the detachment. A third vortex loop is formed, consisting of LEV_3 and TEV_3, and it is also shed before the end of the wing's motion.

It was found that under hovering conditions ($J = 0$) the LEV remains attached to the wing for a variety of aspect ratios. However, at high advance ratios the LEV is stable for low aspect ratio wings (figure 4.8) but is unstable for high aspect ratio wings (figure 4.14). Therefore the stability of the LEV is dependent upon both the advance ratio and the wing's aspect ratio. This relationship is shown in figure 4.15 which maps the stability of the LEV from the CFD simulations. It can be seen that for a particular
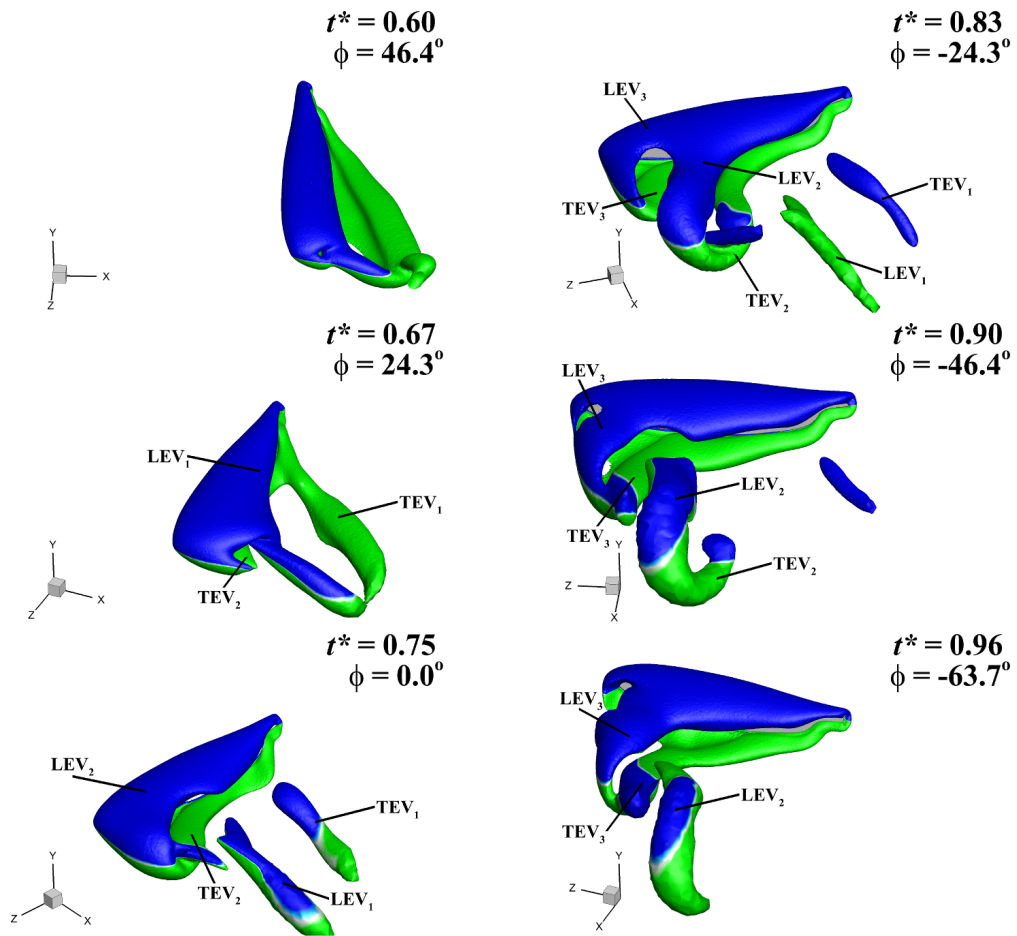
FIGURE 4.14: Stationary view of the wing's motion (clockwise rotation) and the generated flow structures during the downstroke for an $AR = 7.28$ wing at $J = 0.5$ and $Re_R = 613$. Vortex structures are visualised by iso-Q surfaces coloured by spanwise vorticity to indicate direction, green is positive and blue is negative. The sequence progresses from top to bottom. Also see movie B.9.

aspect ratio, if the advance ratio is increased the LEV can become unstable. Likewise, for a constant advance ratio if the wing aspect ratio is increased to be large enough the LEV can become unstable.

For a two-dimensional translating wing, the LEV becomes unstable once it grows too large for the wing, such that the flow can no longer reattach to the wing's top surface (Dickinson & Gotz 1993). When this occurs the Kutta condition breaks down and a TEV forms. If the wing continues its motion the LEV is eventually shed and the wing is said to have stalled. The stability of the LEV is therefore related to the size of the LEV relative to the wing's chord length. Figures 4.13 and 4.14 depict this same shedding process for the numerical simulations but it is now modified to be three-dimensional
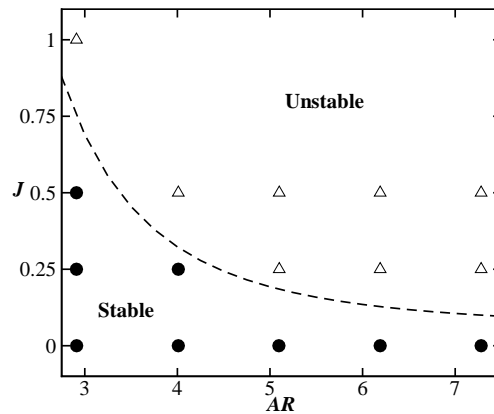
FIGURE 4.15: Stability of the LEV for a range of AR and J at $Re_R = 613$. Symbols ($\triangle$) and ($\bullet$) denote cases where LEV shedding is and is not observed respectively during the downstroke. The dashed line represents the approximate boundary between the two states.

due to the wing's rotation and finite span.

In §4.3.2.2 it was revealed that increasing the advance ratio increased the growth rate of the LEV and in §4.3.3 it was shown that increasing the wing aspect ratio effectively shortens the wing's chord. Both of these parameters have the same end effect of creating a LEV that is a larger proportion of the wing's chord length. Therefore, combining these two mechanisms together can cause situations in which the LEV becomes too large for the wing. The higher the advance ratio or aspect ratio the earlier in the downstroke that the LEV becomes as large as the wing's chord length and thus the LEV can be shed if there is sufficient rotation left in the downstroke. In figure 4.15, the points below the line represent cases where the LEV is either smaller than the wing's chord length or just reaches a comparable size late in the downstroke. Points above the line constitute instances when the LEV becomes as large as the wing's chord earlier in the downstroke and thus the LEV is shed before the end of the downstroke. The further above and to the right of the line the more unstable the LEV is, which can lead to it being shed multiple times.

Thus, the stability of the LEV is dependent on the growth rate of the LEV (determined by J) and the relative size of the LEV compared to the wing's chord length (determined by AR).

4.3.5 Aerodynamic Performance

Dickinson & Gotz (1993) reported that for their two-dimensional translating wing,

the lift force decreased as the Kutta condition broke down and a TEV formed, as the wing became less effective at imparting a steady downward momentum to the fluid (Sane 2003). After the LEV was shed from the wing the time-averaged lift had reached a minimum and the wing was said to have stalled. This observation from a two-dimensional flow can be applied to the flapping wing simulations to explain the variation in wing performance.

In §4.3.2.1 it was shown that the instantaneous lift coefficient decreased throughout the downstroke at an advance ratio of 0.5, but increased for lower advance ratios (figure 4.5). In §4.3.2.2 it was found that for this high advance ratio case, a larger proportion of the wing developed fully separated flow as the LEV grew and the wing moved through the downstroke (figure 4.9). Thus the gradual reduction in instanteous lift coefficient throughout the downstroke is due to the wing becoming less effective at producing lift in the region of the wing that experiences fully separated flow. As this region enlarges, the wing's overall performance drops. At lower advance ratios the LEV growth is slower and hence less of the wing experiences fully separated flow and a loss in performance.

This idea can be extended further to understand the effect of aspect ratio on the wing's performance. Figure 4.16a-b shows the variation in average lift and drag coefficients respectively with aspect ratio for three advance ratios. The white filled symbols are the average values during the downstroke, the black filled symbols are for the upstroke and the grey filled symbols are the average values over the whole flapping cycle. Figure 4.16a-b demonstrates that the force coefficients are increased with increasing advance ratio for the downstroke but are reduced for the upstroke due to the change in relative velocity. At a particular advance ratio, the aerodynamic forces are roughly constant for the upstroke over a range of aspect ratios. However, for the downstroke the aerodynamic forces reduce with increasing aspect ratio. This variation in aerodynamic forces can be explained by the development of separated flow across the wing. Figure 4.9 illustrates that for the $AR = 2.91$ wing at $J = 0.5$ almost the entire wing experiences fully separated flow late in the downstroke. As explained in §4.3.3, increasing the wing aspect ratio effectively shortens the wing's chord length and thus this state is reached earlier in the downstroke for higher aspect ratios. Therefore, higher aspect ratios have lower aerodynamic performance over a greater proportion of the downstroke. Furthermore, in §4.3.4 it was shown that higher aspect ratios can shed the LEV from the outer part of the wing and this further reduces lift. Consequently, higher aspect
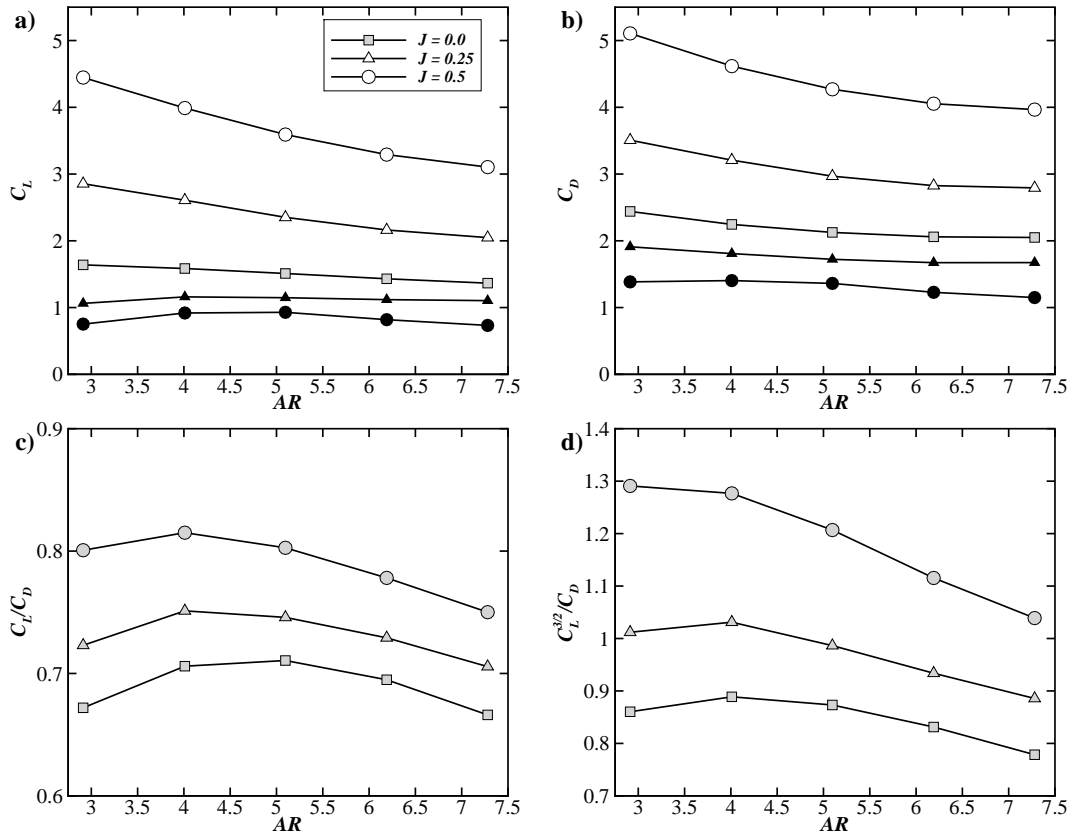
FIGURE 4.16: Aerodynamic force graphs ($Re_R = 613$); average (a) lift coefficient, (b) drag coefficient, (c) lift on drag ratio and (d) power factor. White filled symbols are average values for the downstroke, black filled symbols are for the upstroke and grey filled symbols are the average values over the full flapping cycle.

ratio wings have lower average aerodynamic forces over the downstroke. This effect is more pronounced for higher advance ratios due to the increased growth rate of the LEV.

The lower aerodynamic forces associated with higher aspect ratios leads to these wings having reduced aerodynamic performance during the downstroke. As the downstroke dominates the force balance at non-zero advance ratios this leads to a reduction in the overall wing performance for higher aspect ratios. This can be seen in figure 4.16c-d, which plots the full cycle average values of the lift on drag ratio (C_L/C_D) and power factor ($C_L^{3/2}/C_D$) respectively over a range of aspect ratios. The power factor is inversely proportional to the power required to generate a certain amount of lift (Wang 2008) and therefore maximising it maximises aerodynamic performance. Figure 4.16d shows that aspect ratios of 3 to 4 have increased power factors compared to higher

120

aspect ratios. This highlights that lower aspect ratio wings out-perform high aspect ratios under insect-like flight regimes as they are able to maintain a smaller attached LEV over a wider range of advance ratios.

4.4 Results at High Reynolds Number

It is well known that the characteristics of the LEV change with Reynolds number. The effects of Reynolds number are detailed in §3.2, but are summarised here for simplicity. As the Reynolds number is increased, the LEV forms a much tighter spiral structure compared to at low Reynolds numbers and a strong axial velocity develops in its core (Birch *et al.* 2004; Liu & Aono 2009). The LEV is often observed to break down at some point along the wing's span (Lu *et al.* 2006; Lentink & Dickinson 2009b; Venkata & Jones 2013). A second co-rotating LEV structure has also been reported to form as the primary LEV develops with Reynolds number (Lu *et al.* 2006). This vortex forms between the leading-edge and the primary LEV, which results in a dual LEV structure. All of these changes in flow structure are observed in the current study as the Reynolds number is increased from 613 to 7668, including the formation of the dual LEV structure. In this section the effects of advance ratio and aspect ratio are investigated at the higher Reynolds number of 7668.

4.4.1 Effect of Advance Ratio

The effect of advance ratio at the higher Reynolds number is essentially the same as at the lower Reynolds number. The added freestream velocity reduces the relative velocity experienced by the wing for the upstroke and increases it for the downstroke. The increased relative velocity for the downstroke enhances vorticity production which leads to an increased growth rate of LEV circulation with increasing advance ratio. This can be seen in figure 4.17a which shows the LEV circulation at 25% span throughout the downstroke for three advance ratios.

At this Reynolds number, however, the increased circulation of the LEV does not result in a larger LEV structure due to viscous diffusion, as the effect of viscosity is markedly reduced due to the higher Reynolds number. Instead, the increased circulation leads to an earlier breakdown of the primary LEV. Vortex breakdown is an abrupt change in the structure of a vortex with a marked retardation of the flow in the axial direction (Hall 1972). When a vortex breaks down, the vortex core expands downstream
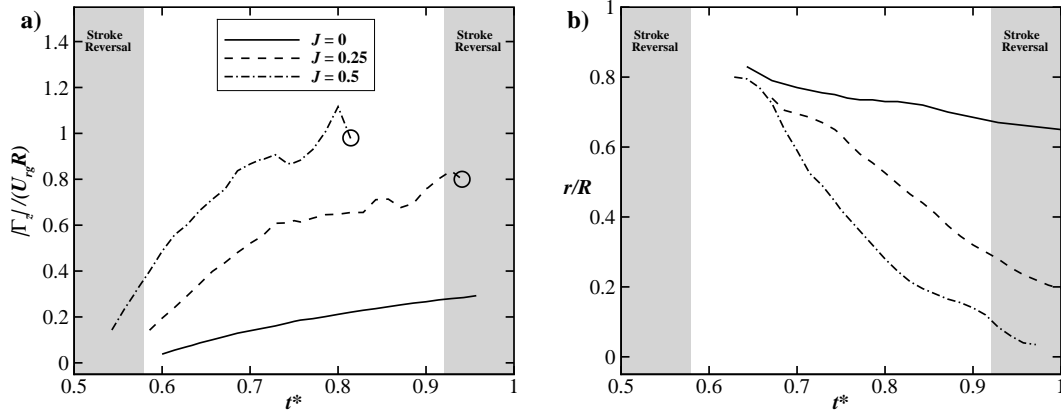
FIGURE 4.17: LEV graphs at $Re_R = 7668$ for the $AR = 2.91$ wing. (a) Time variation of the magnitude of total LEV circulation ($|\Gamma_z|/U_{rg}R$) at 25% span throughout the downstroke. Open circles show the point in the downstroke that the breakdown point of the LEV reaches 25% span. (b) Variation in the spanwise location of LEV breakdown (r/R) throughout the downstroke.

of the breakdown point and the flow within it becomes turbulent (Leibovich 1978). This can be seen in figure 4.18, which shows the change in the vortex structures at three instants during the downstroke for $J = 0$, 0.25 and 0.5. At a particular instant in downstroke (e.g. $t^* = 0.75$), the spanwise position of the breakdown location of the LEV moves towards the wing root with increasing advance ratio. When the LEV breaks down, the vortex core rapidly expands in size and a region of unsteady flow is generated across the rest of the wing's span. Thus the growth of the LEV appears to be through vortex breakdown at this Reynolds number, rather than viscous diffusion.

Breakdown is observed to occur once a critical swirl ratio or swirl angle is reached, which is calculated from the ratio of the azimuthal velocity to the axial velocity in the vortex (Hall 1972). As the size of the LEV upstream of the breakdown point does not change significantly with advance ratio at this Reynolds number, the increased circulation results in an increase in the azimuthal velocity in the vortex core. This increases the swirl ratio and leads to the LEV breaking down closer to the wing's root. Thus, the increased growth rate of circulation for non-zero advance ratios during the downstroke results in the breakdown location moving from the wing tip to the wing root more rapidly for higher advance ratios. This is shown in figure 4.17b and can also be seen in figure 4.18. Under hovering conditions the LEV begins to break down near the wing tip at approximately $t^* = 0.64$. The breakdown location slowly moves towards

122

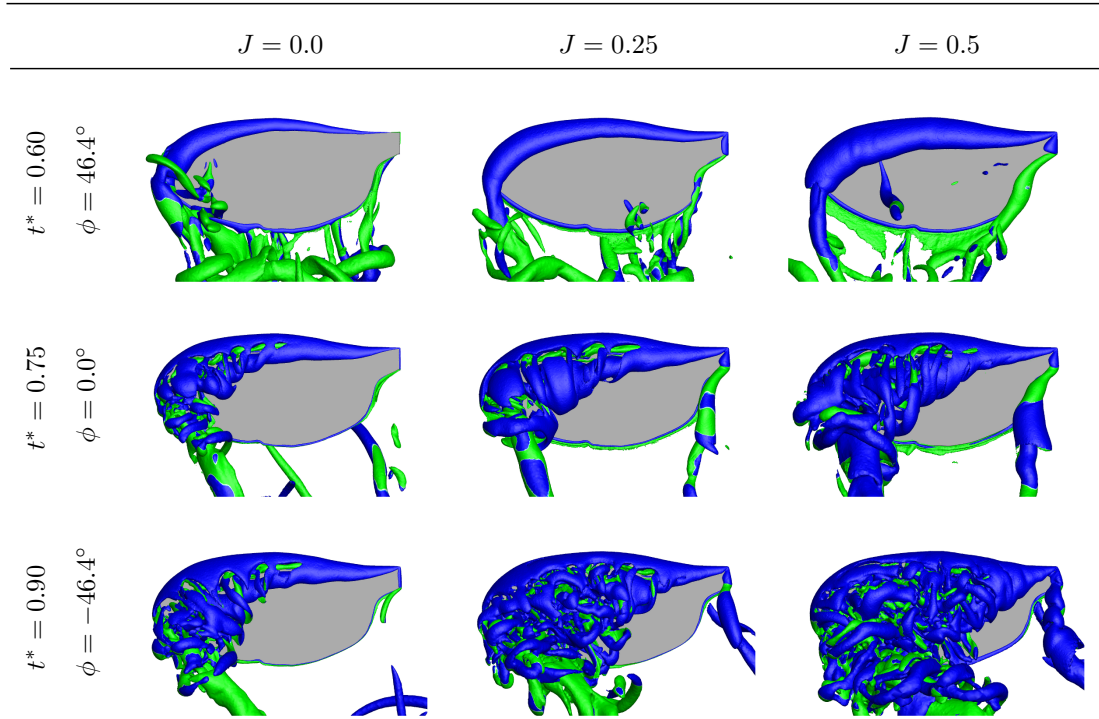|	$J = 0.0$	$J = 0.25$	$J = 0.5$
$t^* = 0.60$ $\phi = 46.4°$			
$t^* = 0.75$ $\phi = 0.0°$			
$t^* = 0.90$ $\phi = -46.4°$			

FIGURE 4.18: Flow structures during the downstroke for (left) $J = 0$, (middle) $J = 0.25$ and (right) $J = 0.5$. Images are taken perpendicular to the wing's top surface and are shown for (top) early downstroke, (middle) mid-downstroke and (bottom) late downstroke ($AR = 2.91, Re_R = 7668$). Vortex structures are visualised by iso-Q surfaces coloured by spanwise vorticity to indicate direction, green is positive and blue is negative. Also see movie B.10 and movie B.11 for the $J = 0$ and $J = 0.5$ cases respectively.

the wing's root as the LEV circulation builds and by the end of the downstroke the spanwise breakdown position is approximately 65% wing span. Increasing the advance ratio increases the rate at which the breakdown point moves towards the wing's root, and as such the breakdown location is closer to the wing's root by the end of the downstroke for higher advance ratios. At an advance ratio of 0.5, late in the downstroke the breakdown location is very close to the wing's root and therefore a coherent LEV structure can no longer be seen on the wing, as all of the flow within the vortex has become unsteady (figure 4.18, $t^* = 0.9$, $J = 0.5$). The burst LEV structure once again can be seen to cover almost all of the wing at this point in the downstroke for high advance ratios. Hence, the increased circulation associated with higher advance ratios does still lead to an expansion of the LEV, but it is through vortex breakdown.

4.4.2 Effect of Aspect Ratio

The effect of wing aspect ratio at the higher span-based Reynolds number is the same as at the lower Reynolds number, where increasing the aspect ratio shortens the wing's chord length relative to the LEV's size. When the LEV breaks down the vortex rapidly grows in size and therefore combining this with a larger aspect ratio can result in vortex shedding. This can be seen in figure 4.19 which shows the vortex structures during the downstroke for the high aspect ratio ($AR = 7.28$) high advance ratio ($J = 0.5$) case at $Re_R = 7668$ (also see movie B.12). At the beginning of the downstroke ($t^* = 0.6$), the vortex loop consisting of the LEV, TV and TEV can be seen. As the wing moves through the downstroke the LEV breaks down, initially near the wing tip but it rapidly moves towards the wing's root from then on. As it does so the TV also moves in towards the root. This creates a very similar counter rotating vortex pair in the wake of the wing ($t^* = 0.75$) as was seen at the lower Reynolds number (see figure 4.14), which suggests that the LEV is again shed from the outer part of the wing for this case. Beyond the breakdown point the flow is highly unsteady and instead of large coherent vortex loops being shed from the wing, many smaller vortex structures are shed from both the leading and trailing edges. Towards the end of the downstroke the LEV has completely burst, resulting in a flow which resembles highly unsteady separated flow. Hence, the LEV appears to be shed from the wing for this case.

At this advance ratio, but for the lower aspect ratio wing, the LEV is not shed (see right hand column of figure 4.18). Instead the burst LEV structure closely resembles the LEV from the same case at the lower Reynolds number (figure 4.8). Therefore the stability of the LEV is again dependent on both the wing's aspect ratio and advance ratio in the same way as described in §4.3.4, except that at this Reynolds number the shedding of coherent vortex structures is not observed due to the breakdown of the LEV and the unsteady flow this creates.

4.5 Discussion

As highlighted in the introduction, a number of different theories have been proposed as to how the stability of the LEV is maintained on insect wings. These include spanwise vorticity transport due to the spanwise component of velocity (Maxworthy 1979; Ellington *et al.* 1996; van den Berg & Ellington 1997), vortex tilting due to the downwash velocity (Birch & Dickinson 2001; Cheng *et al.* 2013) and rotational accelerations due
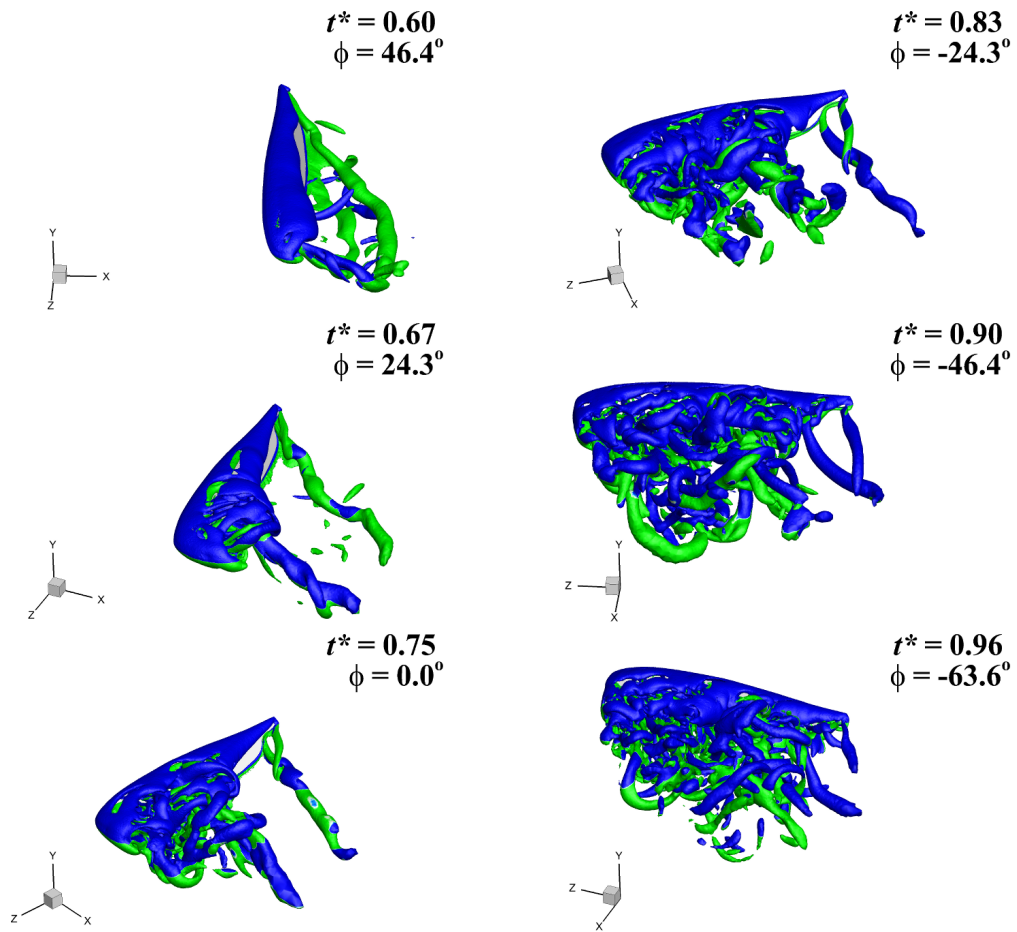
FIGURE 4.19: Stationary view of the wing's motion (clockwise rotation) and the generated flow structures during the downstroke for an $AR = 7.28$ wing at $J = 0.5$ and $Re_R = 7668$. Vortex structures are visualised by iso-Q surfaces coloured by spanwise vorticity to indicate direction, green is positive and blue is negative. The sequence progresses from top to bottom. Also see movie B.12.

to the low Rossby number rotation of the wing (Lentink & Dickinson 2009b). These hypotheses generally attempt to explain the mechanism through which the growth of the LEV is controlled. In this chapter, none of these theories were directly tested, but it has been shown that the LEV becomes unstable and is shed from the wing under certain conditions that are dictated by the advance ratio and wing's aspect ratio. The advance ratio controls the growth rate of the LEV during the downstroke, while the aspect ratio defines the maximum size that the LEV can become before flow separation occurs and the Kutta condition breaks down.

As LEV stability is partly determined by the advance ratio, which is a measure of the wing's rotation relative to its translation, a comment on the conformity of these results

with the low Rossby number hypothesis of Lentink & Dickinson can be made. In chapter 3, it was demonstrated that when the span-based scaling is used the Rossby number is equal to $Ro = U_{tip}/\Omega R$. Letting $U_{tip} = \Omega R \pm V$, where the velocities are summed for the downstroke and subtracted for the upstroke, results in $Ro = 1 \pm V/\Omega R \approx 1 \pm J$. Thus, the Rossby number is dependent on the advance ratio. It is equal to one for hovering flight, but is increased during the downstroke and reduced during the upstroke for non-zero advance ratios. Applying the low Rossby number hypothesis of Lentink & Dickinson predicts that the LEV would be unstable during the downstroke at high advance ratios. This prediction matches the findings of this study and therefore these results support the low Rossby number theory, at least in a general sense. However, the details of this theory have not been tested. The wing's rotation generates rotational accelerations and a spanwise pressure gradient that together produce the spanwise velocity, which is one candidate for LEV stability. But whether the Coriolis acceleration itself directly provides stability for the LEV, as proposed by Lentink & Dickinson, has not been confirmed.

Regardless of the mechanism through which the growth of the LEV is controlled, the shedding of the LEV is clearly a modification of the same delayed stall process seen on a two dimensional translating wing (Dickinson & Gotz 1993). In this chapter it has been demonstrated that the time it takes for the LEV to reach the critical size of one chord length depends on both the advance ratio and the wing's aspect ratio. If this timescale is shorter than the half cycle period then the LEV can be shed. Therefore, it can also be ascertained that the LEV stability would be dependent on the wing's stroke amplitude, as this determines the absolute size that the LEV can reach by the end of the downstroke. While different stroke amplitudes have not been tested here, changing the amplitude while maintaining a constant rotational velocity can be viewed as altering the half cycle period (i.e. the flapping frequency must also change). Smaller amplitudes would therefore limit the vortex size and thus allow the LEV to remain attached to the wing for higher advance ratios and for larger aspect ratios. The idea that the LEV stability is dependent on the relative timescales of the delayed stall mechanism compared to the flapping motion has been proposed previously (Wang 2005), based on two dimensional flapping wing simulations. Furthermore, as the wing's performance is affected by the LEV's stability, smaller stroke amplitudes may improve the aerodynamic performance of larger aspect ratio wings.

Finally, a comment needs to be made on the assumption of a constant stroke plane angle with flight speed that was made in the setup of these simulations. As explained in §2.3, this assumption was made in order to simplify the analysis by taking out some of the complexity associated with including a variation in stroke plane angle with advance ratio. However, insects tilt their stroke plane significantly in order to achieve forward flight. In these simulations the stroke plane angle was set to $0°$, which has also been used by Dickson & Dickinson (2004). Other studies have investigated the effect of advance ratio at different stroke plane angles. Nagai *et al.* (2009) studied a flapping bumblebee wing ($AR \approx 3$) for advance ratios of $0 \leq J \leq 0.47$ at a stroke plane angle of $45°$. They observed that a large but stable LEV formed during the downstroke. Gopalakrishnan & Tafti (2010) computed the flow around a flapping $AR = 4$ plate at $J = 0.5$ where the freestream flow was perpendicular to the wing's stroke plane. They reported that the LEV was shed from the outer part of the wing mid-way through the downstroke. Bross *et al.* (2013) also investigated the effect of advance ratio at a stroke plane angle of $90°$. They used PIV to measure the flow around a rotating $AR = 2$ plate. They found that the LEV was stable for all advance ratios tested ($0 \leq J \leq 0.537$), but they also observed that the streamline patterns departed from an attached flow state for large values of advance ratio and rotation angles. Combining all these observations together it is concluded that the effects of advance ratio and wing aspect ratio in determining the stability of the LEV are likely to apply to other stroke plane angles, and thus also to the flight of real insects. However, further investigation is warranted, especially considering the additional complexity that a varying non-zero stroke plane angle adds to the problem.

4.6   Conclusion

In this chapter the change in the LEV characteristics throughout a simulated flapping cycle has been investigated over a range of aspect ratios and advance ratios using a numerical model of a flapping fruit fly wing. Due to the symmetric flapping kinematics between the up- and downstrokes, under hovering flight the vortex structures that are created for each half cycle are identical, except with opposite signs of rotation. However, at non-zero advance ratios the change in relative velocity experienced by the wing for each half cycle leads to very different vortex structures being created between the up- and downstrokes.

It was demonstrated that the relative velocity affected vorticity production on the wing. For the upstroke the relative velocity was reduced with increasing advance ratio which resulted in less vorticity generation, particularly around mid-upstroke. This created smaller and weaker LEV structures for the upstroke at high advance ratios, that were confined to the outer portion of the wing due to a region of reversed flow at the wing's root. For the downstroke, the relative velocity was increased with increasing advance ratio, which caused enhanced vorticity production. At low span-based Reynolds numbers this resulted in a larger and stronger LEV being formed at higher advance ratios, where the LEV rapidly grew in size throughout the downstroke.

It was found that changing the wing aspect ratio had the effect of shortening the wing's chord length relative to the LEV's size. When the effects of wing aspect ratio and advance ratio were combined the LEV quickly grew to envelop the entire wing during the downstroke and eventually it was shed as part of a vortex loop that peeled away from the wing's tip. Thus, the stability of the LEV is dependent on both the advance ratio and wing aspect ratio, which control the growth rate of the LEV and the relative size of the LEV compared to the wing's chord length respectively. The higher the aspect ratio or advance ratio the more unstable the LEV becomes.

It was shown that the mean downstroke lift coefficient reduces as the wing aspect ratio is increased. This was due to the wing stalling, and therefore becoming less effective at producing lift, when the LEV became too large and was shed from the wing. This further displays that low aspect ratio wings therefore outperform higher aspect ratios, particularly at non-zero advance ratios.

At higher span-based Reynolds numbers, the primary LEV was observed to break down at some point along the wing's span. Beyond the breakdown point, the LEV expands in size and the flow within the vortex core is highly unsteady. During the downstroke, the increased LEV circulation for non-zero advance ratios was found to cause the LEV to break down earlier along the wing's span. This created a burst LEV structure that closely resembled the LEV from the lower Reynolds number, except that the flow was now unsteady due to the LEV breakdown. At high advance ratios and high aspect ratios, the burst LEV was shed from the wing resulting in a region of highly unsteady separated flow being developed on the wing. Thus, a similar dependency of the LEV stability on the advance ratio and aspect ratio was observed at this Reynolds number, except that the growth of the LEV is through vortex breakdown rather than

viscous diffusion. Hence the findings of this study are likely to apply across a wide range of Reynolds numbers.

Chapter 5

Wing Camber

5.1 Introduction

In this chapter, the results and findings from an investigation into the effect of wing camber on impulsively started rotating wings at insect Reynolds numbers are reported. The aim of this study is to uncover how the vortex structures around the wing change with camber in order to understand how wing camber results in improved aerodynamic performance under insect flight conditions.

For a real insect, wing camber varies throughout the course of the flapping cycle and can also vary along the wing's length (Walker *et al.* 2009, 2010) due to the complex interaction of the wing's structural properties with the forces induced from the wing's kinematics. In order to isolate the effect on the aerodynamic forces and flow structures due to the wing's shape, the wing was defined as being rigid with constant camber along its span (see §2.2.1). The wing's motion was also simplified to an impulsively started rotational motion. These two simplifications deviate from real insect flight, but allowed the effects of the wing's structure and kinematics to be eliminated, while still mimicking insect flight conditions.

The effects of both positive (convex top surface) and negative (concave top surface) camber on the aerodynamic forces at a chord-based Reynolds number of 1500 ($Re_R = 7667$) are first discussed, as well as the effect of the chordwise location of maximum camber. These results agree with the findings of Altshuler *et al.* (2004), Tsuzuki *et al.* (2007) and Du & Sun (2008) in showing a significant improvement in aerodynamic performance with positive camber. The variation of the LEV's structure with camber is then presented. These results reveal how changes in the wing's shape result in a significant alteration of the LEV's structure. The impact that this modified LEV structure has on the aerodynamic forces, in combination with the change in wing shape,

131
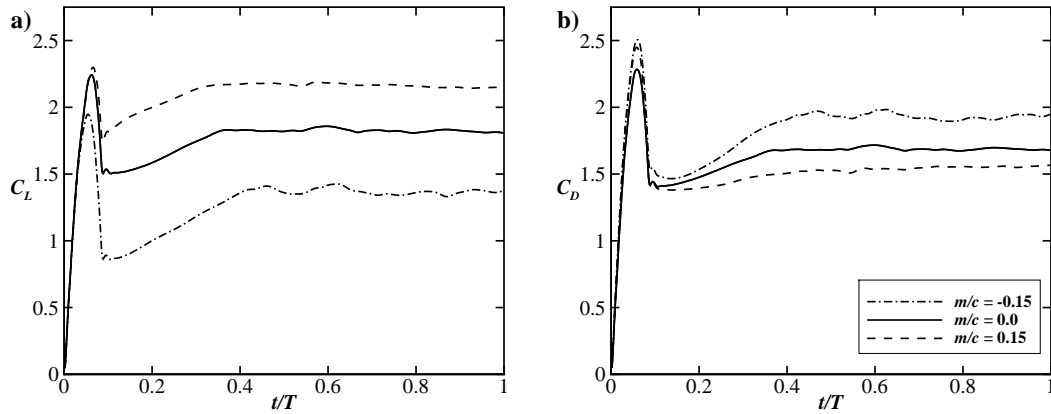
FIGURE 5.1: Time variation of the (a) lift coefficient and (b) drag coefficient throughout the simulation for -15%, 0% and 15% camber wings at $Re = 1500$.

is then discussed. Finally the effect of camber at a Reynolds number of 120 ($Re_R = 613$) is investigated and it is shown that the mechanism through which camber improves the wing's performance is the same at this lower Reynolds number as at the higher value. In particular, it is due to tilting of the force vector as the camber is increased.

5.2   Aerodynamic Forces

The variation in the lift and drag coefficients with time at a Reynolds number of 1500 for different magnitudes of wing camber are shown in figure 5.1. In these simulations, steady aerodynamic forces for the 0% camber wing are produced from approximately $t/T = 0.36$ or after the wing has rotated through 90°. Figure 5.1 shows that this point occurs significantly later for wings with negative camber (e.g. $t/T = 0.407$, $\phi = 103°$ at -15% camber) and slightly earlier for wings with positive camber (e.g. $t/T = 0.341$, $\phi = 84°$ at 15% camber). The estimated settling times and corresponding angles of rotation at different magnitudes of camber are shown in table 5.1. Figure 5.1 also shows that the 15% camber wing produced not only higher lift coefficients during the period of steady lift production but it also produced a higher minimum lift coefficient and a slightly increased maximum lift coefficient. Conversely, the -15% camber wing produced lower lift coefficients all round.

Figure 5.2a shows the variation in the average lift and drag coefficients with camber, where the coefficients are the average values calculated over the period given by the values in table 5.1 to the end of the wing's rotation. Figure 5.2a shows that positively

132

m/c	t/T	ϕ
-0.15	0.407	103
-0.10	0.391	98
-0.05	0.375	94
0	0.359	89
0.05	0.353	88
0.10	0.347	86
0.15	0.341	84
0.20	0.335	82

TABLE 5.1: Estimated settling times (t/T) and corresponding rotation angles (ϕ) for different magnitudes of camber (m/c).
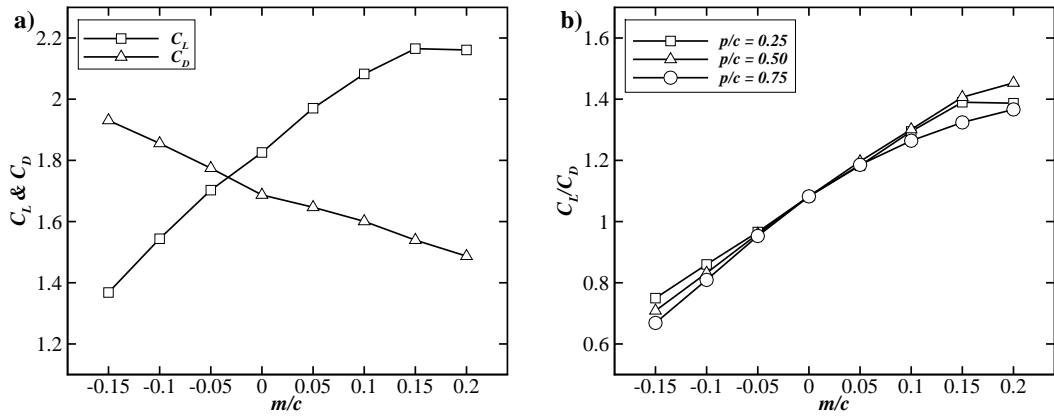
FIGURE 5.2: Average aerodynamic force graphs at $Re = 1500$. (a) Change in lift and drag coefficients with magnitude of camber, m/c (for $p/c = 0.5$). (b) Variation in lift on drag ratio with magnitude of camber for $p/c = 0.25$, 0.5 and 0.75.

cambered wings have increased lift coefficients and decreased drag coefficients compared to a flat wing. On the other hand, negative camber has the opposite effect, reducing the lift coefficient and increasing the drag coefficient. It was found that 15% camber ($p/c = 0.5$) increased the wing's lift on drag ratio by 30.0% compared to a flat wing, while -15% camber ($p/c = 0.5$) reduced the lift on drag ratio by 34.5% (see figure 5.2b). These results agree with the findings of Altshuler *et al.* (2004), Tsuzuki *et al.* (2007) and Du & Sun (2008), and show that positive wing camber could be used to improve aerodynamic performance of flapping and rotating wing MAVs.

In addition, the chordwise location of the maximum camber was investigated and found to have a small influence on the wing's performance, particularly at high magnitudes of camber. For positively cambered wings, having the point of maximum camber located at the mid-chord was found to be optimum. For negatively cambered wings,

$p/c = 0.25$ produced the highest lift on drag ratios, with degrading performance as the location of maximum camber moves towards the wing's trailing-edge.

5.3 Flow Structures

5.3.1 Negative Camber

In this section the vortex structures that are formed around negatively cambered wings are investigated. The change in vortex structures are compared to a non-cambered wing, therefore a brief recap of the flow structures around such a wing is first presented (see also §3.2.2). At this Reynolds number ($Re=$ 1500), a rigid wing with no camber produces a dual co-rotating LEV structure. This dual LEV structure is shown in figure 5.3a and consists of two co-rotating vortices (labelled LEV 1 and 2) separated by a smaller counter-rotating vortex (labelled SV). LEV 1 follows the leading-edge of the wing while LEV 2 moves away from the leading-edge as it tracks out along the wing's span and eventually breaks down at approximately 60% span.

Negatively cambered wings were found to produce very similar vortex structures. Figure 5.3 shows the variation in the spanwise vorticity contours at $\phi = 270°$ with increasing negative camber. Here a dual co-rotating LEV structure can be seen on all the wings as depicted by the two distinct regions of negative vorticity near the leading-edge. One notable difference in the LEV's structure between the negatively cambered wings is that LEV 2 breaks down closer to the wing's root as the wing becomes more negatively cambered. The position of the breakdown point along the wing's span (r/R) as a function of the magnitude of camber is shown in figure 5.4, where the breakdown point is estimated as the point at which the spanwise velocity in the vortex core approaches zero.

The development of a dual LEV structure throughout the wing's motion for a flat non-cambered wing has been previously reported in §3.2.3 (see also movie B.4). Perhaps unsurprisingly the development of the dual LEV structure over a negatively cambered wing is very similar to that for a flat wing. Figure 5.5 shows the time variation in surfaces of the Q criterion throughout the simulation for a -15% cambered wing (see also movie B.13). At the beginning of the wing's motion a horseshoe-shaped vortex is formed, which consists of the LEV, TV and TEV. As the wing continues to rotate, the LEV grows in size and the TEV is shed from the wing. The LEV enlarges more rapidly towards the wing tip, which results in a three-dimensional vortex structure.
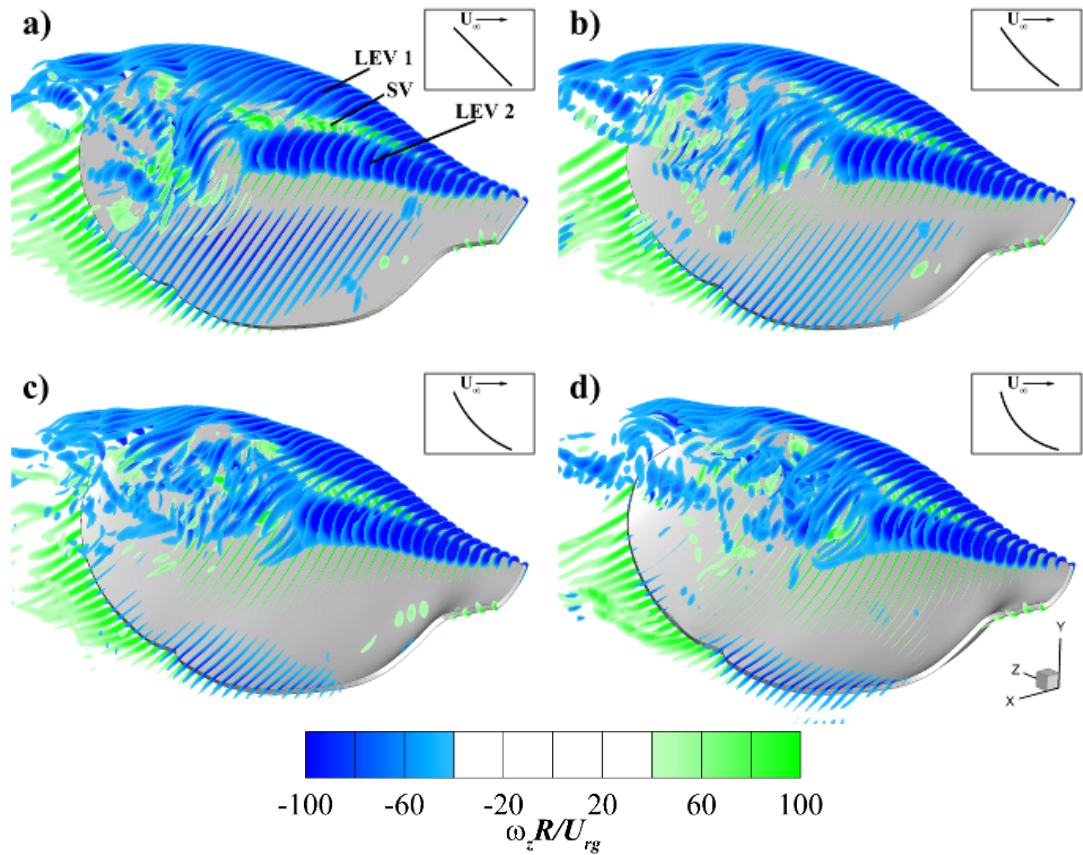
FIGURE 5.3: Change of spanwise vorticity contours ($\omega_z R/U_{rg}$) with decreasing magnitude of camber at $Re = 1500$; (a) 0%, (b) -5%, (c) -10%, (d) -15% ($p/c = 0.5$). Images show flow structures at $\phi = 270°$. The insets show a cross-sectional view of the wing's shape.
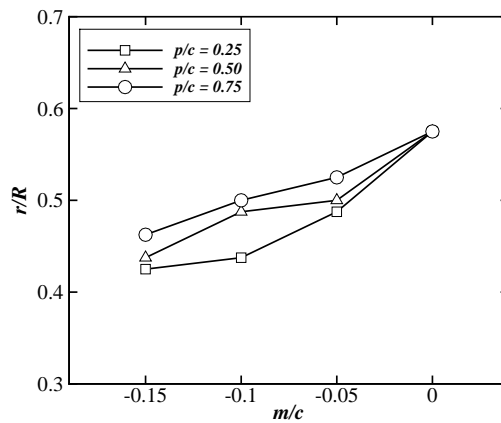

FIGURE 5.4: Spanwise position (r/R) of breakdown location as a function of the magnitude of camber (m/c).
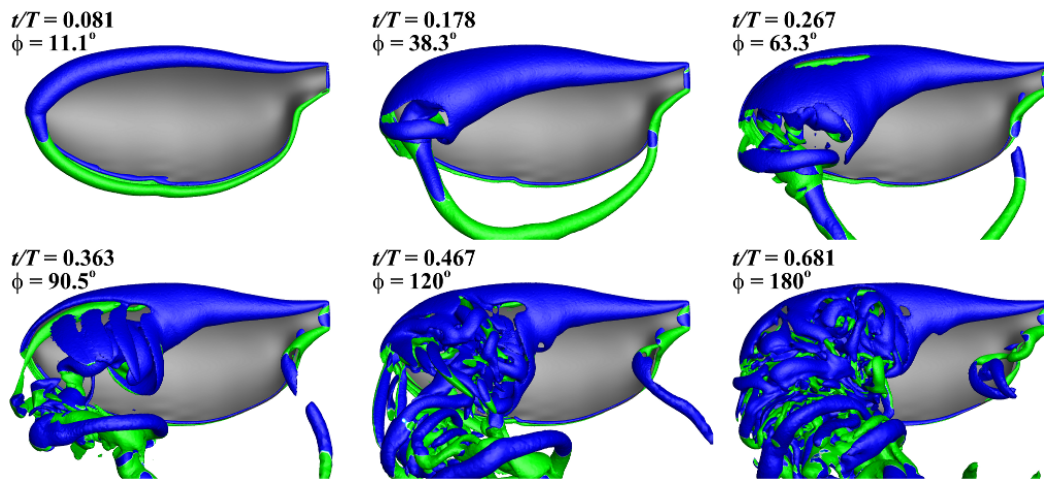
FIGURE 5.5: Temporal development of vortex structure over a -15% camber wing ($p/c = 0.5$, $Re = 1500$). Vortex structures are visualised using surfaces of constant Q criterion and are coloured by spanwise vorticity (ω_z) to indicate direction; blue is negative and green is positive. Images show flow structures throughout the wing's rotation and are taken perpendicular to the wing's surface. Sequence progresses left to right. Also see movie B.13.

This flow structure development is similar to that computed for the initial part of the downstroke of a hovering fruit fly, honeybee and hawkmoth (Liu & Aono 2009). At $t/T = 0.267$ the iso-Q surface representing the LEV begins to split in the outer part of the wing indicating that the dual LEV has formed. By $t/T = 0.363$ LEV 2 has burst, resulting in smaller scale structures being formed which are advected into the TV as the wing's motion continues. Figure 5.5 shows that a quasi-steady state is reached for $0.363 \leq t/T \leq 0.467$, which corresponds to the settling time of $t/T = 0.407$ shown in table 5.1.

5.3.2   Positive Camber

In contrast to wings with negative camber, positively cambered wings were found to dramatically influence the make-up of the LEV's structure. Increasing wing camber resulted in the initially coherent LEV becoming less distinct and the formation of multiple streamwise oriented vortex structures. The development of these vortex structures with increasing camber is shown in figure 5.6, where the vortices are visualised using surfaces of constant Q criterion. As described previously, for the flat wing (figure 5.6a) a dual co-rotating LEV structure forms over the wing. Increasing the wing's camber to 5% results in a similar dual LEV structure. However, two small streamwise oriented
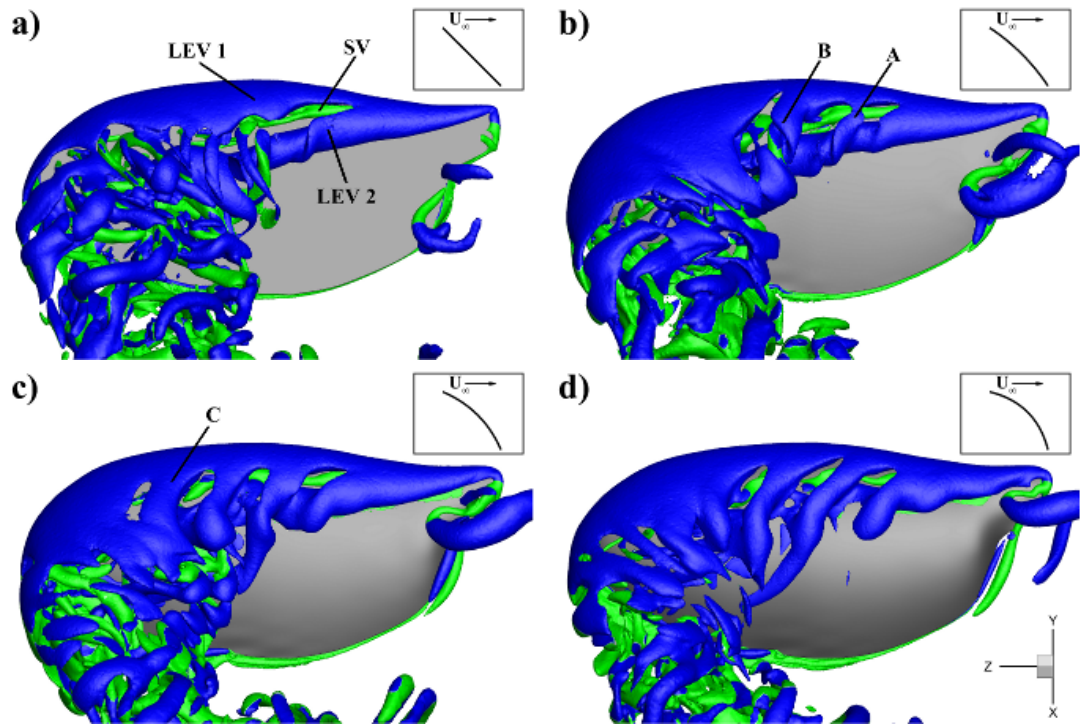
FIGURE 5.6: Change in vortex structures with increasing magnitude of camber at $Re = 1500$; (a) 0%, (b) 5%, (c) 10%, (d) 15% ($p/c = 0.5$). Vortex structures are visualised using surfaces of constant Q criterion and are coloured by spanwise vorticity (ω_z) to indicate direction; blue is negative and green is positive. Images show flow structures at $\phi = 270°$ and are taken perpendicular to the wing's surface. The insets show a cross-sectional view of the wing's shape.

vortex structures also form (labelled A and B in figure 5.6b). These structures originate from the wing's leading-edge and appear to be entrained into LEV 2. A further increase in wing camber to 10% results in these streamwise structures becoming more coherent and for a third streamwise vortex to be observed (labelled C in figure 5.6c). All of these streamwise vortices feed into the TV. At 15% camber the streamwise vortices appear to dominate the flow topology and significantly inhibit the development of LEV 2 across the wing and at this point LEV 2 is now entrained into vortex A.

The change in the vortex structure over wings with increasing magnitude of camber is further highlighted in figure 5.7, which shows the change in both spanwise and streamwise vorticity patterns at 270° of rotation. For the non-cambered wing (figure 5.7a), two distinct regions of negative spanwise vorticity can be seen, signalling the presence of a dual LEV structure, where one is near the leading-edge of the wing and the other is further downstream close to the wing's surface. Beyond approximately

60% span the region of concentrated spanwise vorticity representing LEV 2 breaks up, indicating that LEV 2 has burst. The streamwise vorticity contours in figure 5.7b show a large region of negative vorticity over the inner part of the wing, close to the leading-edge. Increasing the wing's camber to 5% results in this region of negative streamwise vorticity beginning to split into three separate regions. Another weaker region of negative vorticity can also be seen to form closer to the wing tip, extending out from the wing's leading-edge. As the wing's camber is increased from 5 to 15%, two distinct regions of negative streamwise vorticity form over the middle portion of the wing (labelled A and B in figure 5.7h) and the region of negative streamwise vorticity near the wing tip strengthens (labelled C in figure 5.7h), resulting in three co-rotating streamwise vortices. The region of negative streamwise vorticity near the wing's root is also seen to reduce in size and strength.

As these streamwise vortices form, they begin to influence the development of LEV 2 as it extends across the wing. At 5% wing camber (figure 5.7c) the spanwise vorticity contours for LEV 2 are distorted slightly around the wing's mid-span. Increasing the camber to 10 and 15% results in further distortion and stretching of the spanwise vorticity patterns in the chordwise direction where vortices A and B have formed. This is as a result of these streamwise structures interacting with LEV 2 as they begin to dominate the flow. The spanwise vorticity contours in figure 5.7 show that this interaction results in LEV 2 reducing in size and strength with increased camber, and appears to be confined to the inner part of the wing at high magnitudes of camber.

In an earlier study, Du & Sun (2008) compared the spanwise vorticity patterns of a flat wing to a 10% cambered wing at 50% span. They suggested that the LEV is distorted by positive wing camber, but details of what this distortion entailed were omitted. Figure 5.8 displays the variation in spanwise vorticity contours at 50% span with increasing camber. Figure 5.8 shows that the position of the outer extent of the region of negative vorticity is not altered by the increase in wing camber, and as such the downstream LEV is "squashed" between the wing's surface and the freestream flow, as shown by the reduction in size of the vortex with increasing camber. Figure 5.8 demonstrates that even at high magnitudes of camber at this angle of attack the flow still separates from the leading-edge. The flow then reattaches to the wing just downstream of the LEV but separates again near the trailing-edge for highly cambered wings.
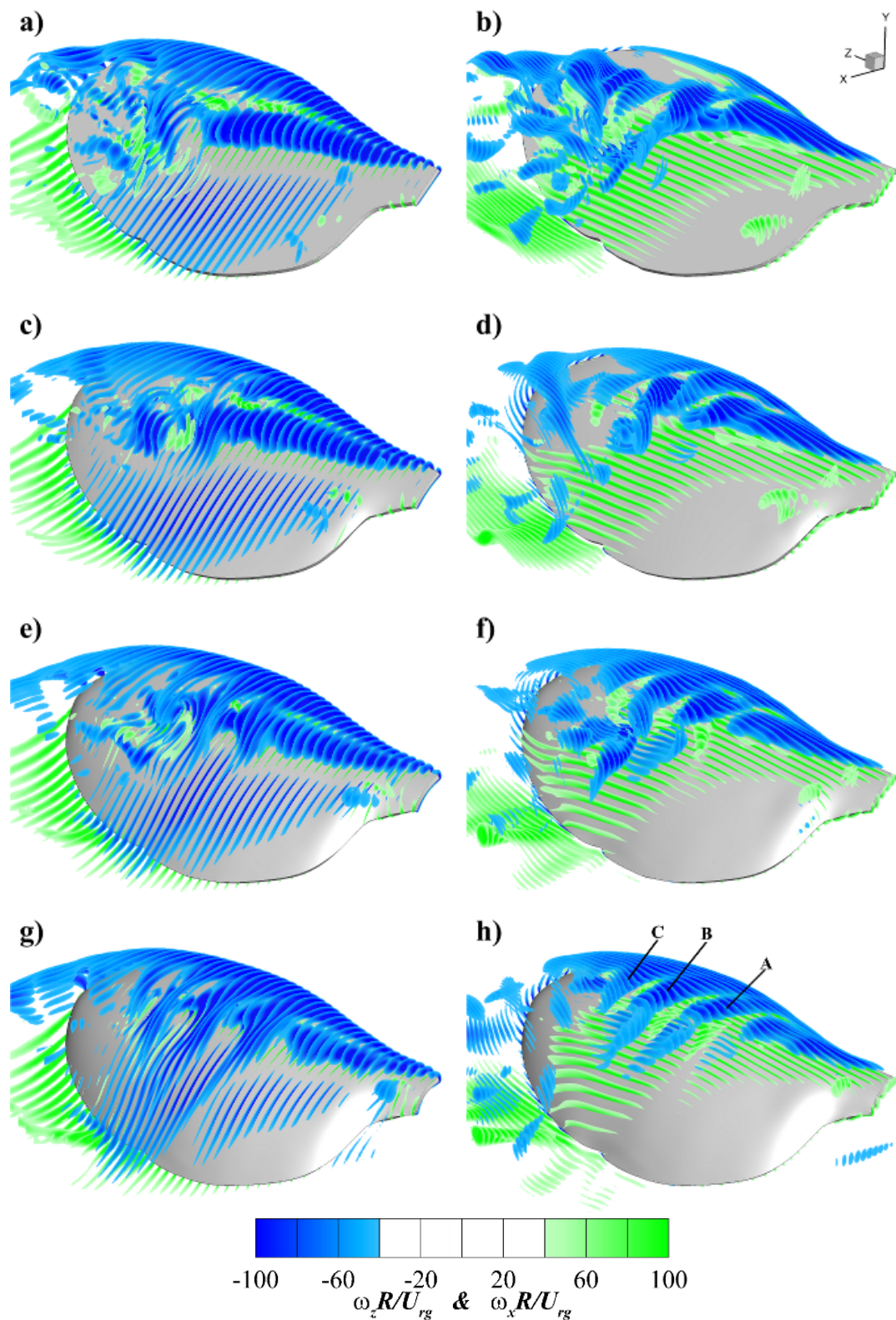
FIGURE 5.7: Change in spanwise vorticity contours ($\omega_z R/U_{rg}$, left) and streamwise vorticity contours ($\omega_x R/U_{rg}$, right) with increasing magnitude of camber at $Re = 1500$; (a,b) 0%, (c,d) 5%, (e,f) 10%, (g,h) 15% ($p/c = 0.5$). Images show flow structures at $\phi = 270°$.
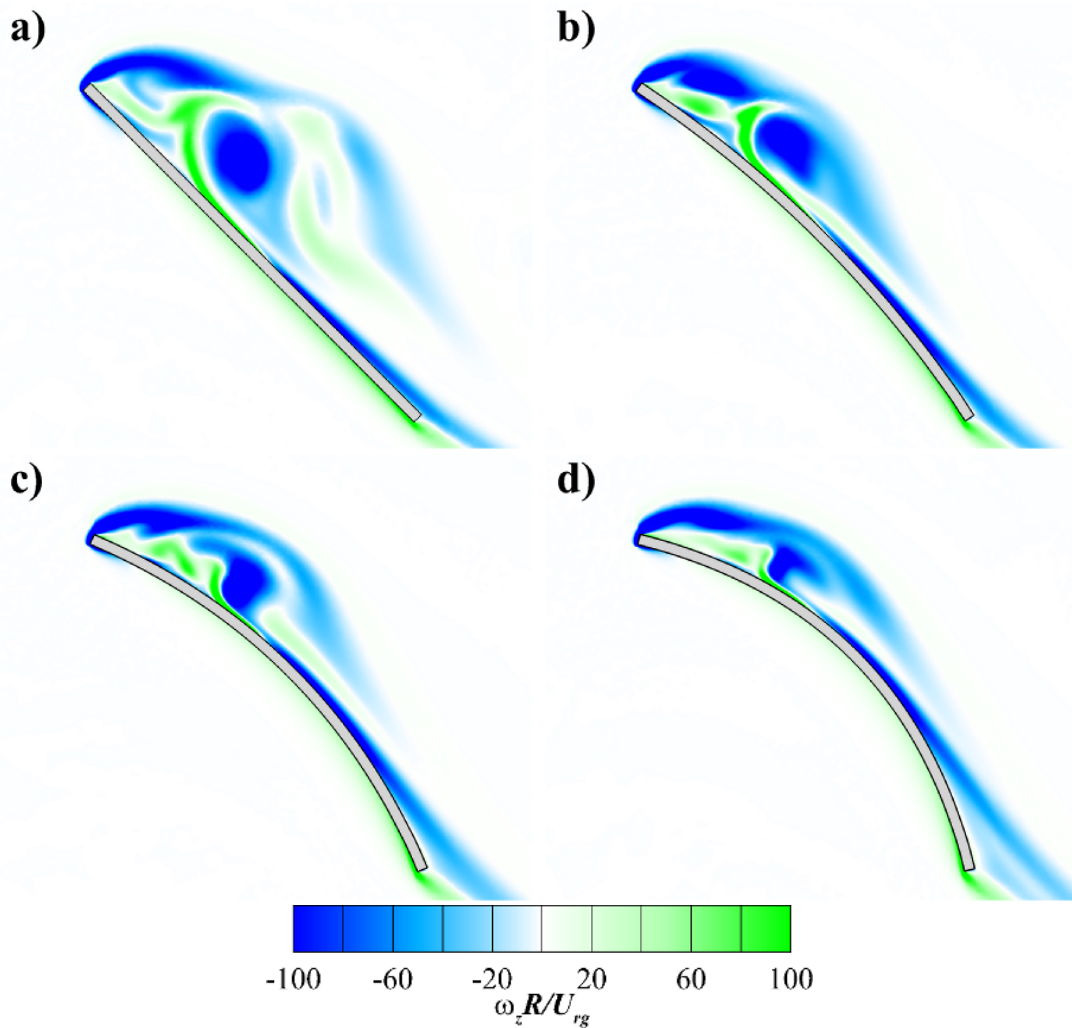
FIGURE 5.8: Spanwise vorticity contours ($\omega_z R/U_{rg}$) at 50% span for positively cambered wings at $Re = 1500$; (a) 0%, (b) 5%, (c) 10%, (d) 15% ($p/c = 0.5$). Images show flow structures at $\phi = 270°$.

In addition to the change in vorticity patterns, the spanwise velocity distribution over the wing is also influenced by the wing's camber, as is shown by figure 5.9. For a flat non-cambered wing at a Reynolds number of 1400, Birch *et al.* (2004) found that a strong spanwise velocity existed within the core of the LEV as well as a broad region of moderate spanwise velocity behind it. This can also be seen in these simulations (figure 5.9a). The velocity within the core of LEV 2 reaches a maximum value of around three times the velocity at the radius of gyration. This spanwise velocity is thought to help stabilise the LEV to the wing's surface by draining circulation out into the TV (Ellington *et al.* 1996; Lentink & Dickinson 2009b). However, figure 5.9 shows

140
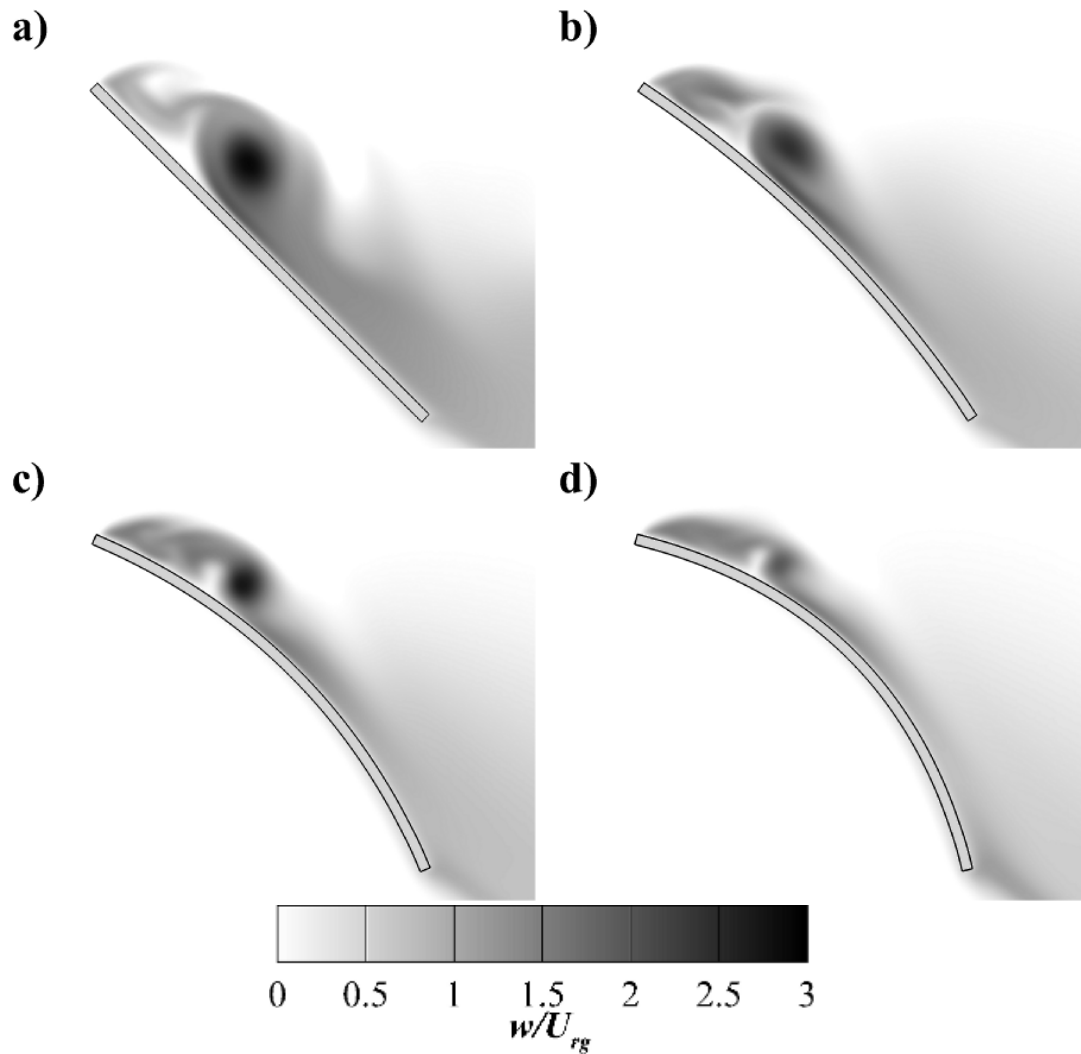
FIGURE 5.9: Change in spanwise velocity (w/U_{rg}) at 50% span for positively cambered wings at $Re = 1500$; (a) 0%, (b) 5%, (c) 10%, (d) 15% ($p/c = 0.5$). Images show the velocity contours at $\phi = 270°$.

that as the wing's camber is increased the strength of the spanwise velocity within the LEV reduces. Nonetheless, highly cambered wings still have some spanwise velocity (of the order of the velocity at the radius of gyration) near the wing's leading-edge where the LEV structures exist, and this appears to be sufficient in maintaining the attachment of the streamwise vortex structures that have formed. Figure 5.6 shows that these structures still drain into the TV and, as will be shown below, a quasi-steady state is still reached for highly cambered wings.

The development of the vortex structures over a 15% cambered wing throughout the simulation is shown in figure 5.10 (see also movie B.14). The initial temporal
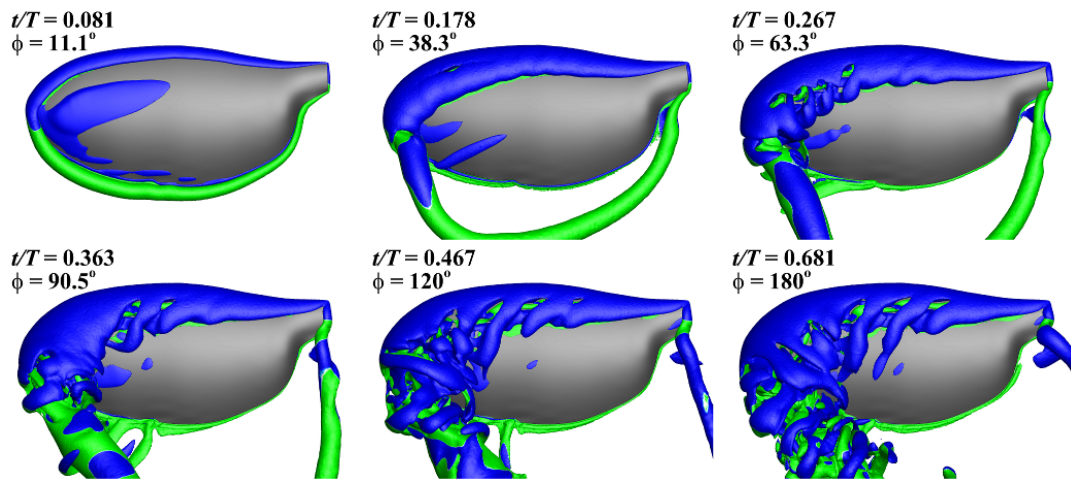
FIGURE 5.10: Temporal vortex structure development over a 15% camber wing ($p/c = 0.5$, $Re = 1500$). Vortex structures are visualised using surfaces of constant Q criterion and are coloured by spanwise vorticity (ω_z) to indicate direction; blue is negative and green is positive. Images show flow structures throughout the wing's rotation and are taken perpendicular to the wing's surface. Sequence progresses left to right. Also see movie B.14.

evolution of the vortex structures over the wing is the same as that for a non-cambered or negatively cambered wing, where a horseshoe-shaped vortex is formed around the wing's edge. As the wing continues to rotate the LEV grows in size and the TEV is shed from the wing. However, at $t/T = 0.267$, as the dual LEV begins to form, the iso-Q surface representing LEV 2 becomes rippled, particularly near the wing tip, indicating that the streamwise vortex structures are beginning to form and are being entrained into LEV 2. By $t/T = 0.363$ the aerodynamic forces have reached an approximately steady value as shown in figure 5.1, and yet the vortex structures over the wing continue to develop. Here the streamwise vortices have strengthened further and begin to inhibit the development of LEV 2 across the wing. At $t/T = 0.467$ the three streamwise vortex structures can be seen. Comparison of figure 5.6d with figure 5.10 shows that a quasi-steady vortex system is established over the wing by approximately $t/T = 0.467$ or after $120°$ of rotation.

5.3.3 Location of Maximum Camber

The chordwise location of maximum camber was found to have a relatively minor impact on the LEV's structure compared to the magnitude of camber. For both positively and negatively cambered wings, the influence of the chordwise location of camber was found
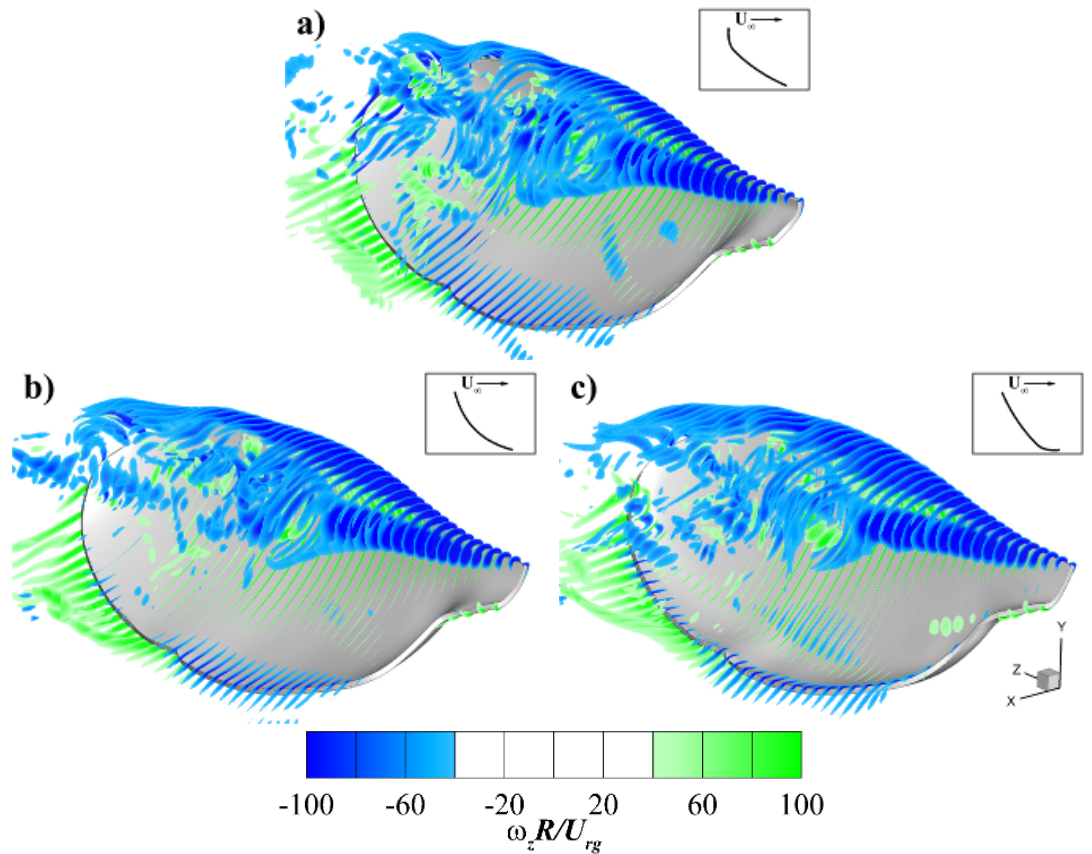
FIGURE 5.11: Change in spanwise vorticity contours ($\omega_z R/U_{rg}$) with chordwise location of maximum camber for a negatively cambered wing at $Re = 1500$; (a) 25%, (b) 50%, (c) 75% ($m/c = -0.15$). Images show flow structures at $\phi = 270°$. The insets show a cross-sectional view of the wing's shape.

to be similar to varying the magnitude of camber but with a more subtle impact on the flow structures.

An example of this is shown in figure 5.11, which shows the variation in the spanwise vorticity contours for three different positions of maximum camber for a -15% cambered wing. Figure 5.11 shows that the dual LEV structure remains persistent between $0.25 \leq p/c \leq 0.75$. There is, however, a slight variation in the breakdown location of LEV 2, which is more clearly shown in figure 5.4. Figure 5.4 shows that moving the location of maximum camber towards the trailing-edge of the wing moves the breakdown location towards the wing tip. This effect is similar to reducing the magnitude of negative camber and may be due to the reduction in curvature near the leading-edge of the wing seen in both instances.

Similarly, for positively cambered wings moving the location of maximum camber
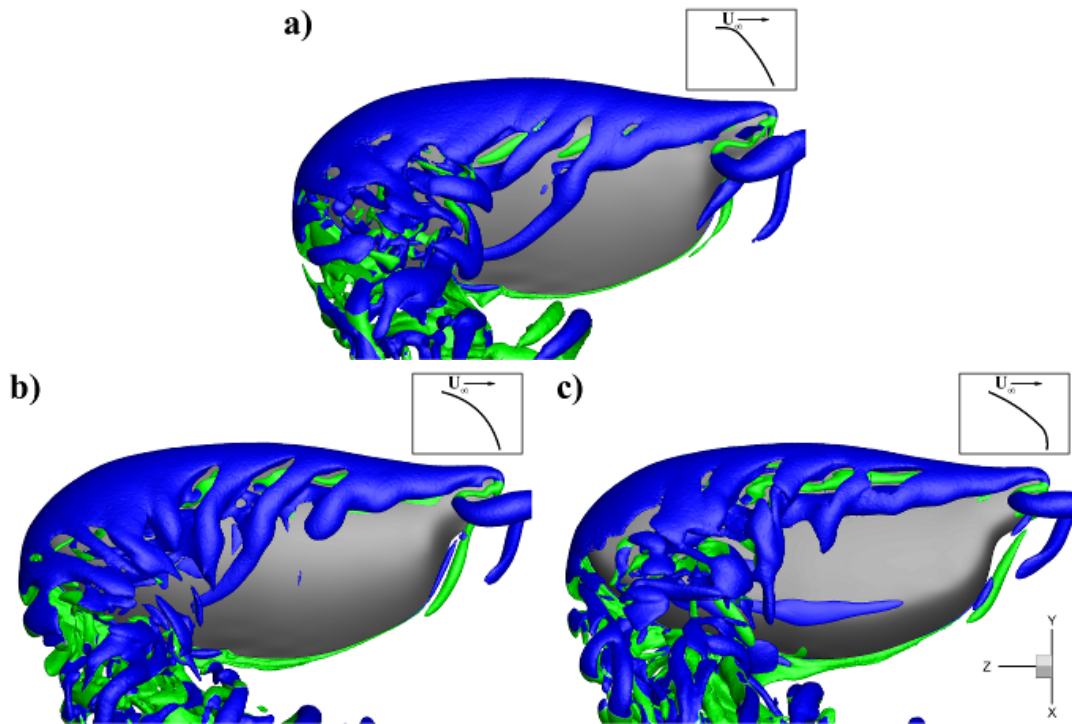
FIGURE 5.12: Change in vortex structures with chordwise location of maximum camber for a positively cambered wing at $Re = 1500$; (a) 25%, (b) 50%, (c) 75% ($m/c = 0.15$). Vortex structures are visualised using surfaces of constant Q criterion and are coloured by spanwise vorticity (ω_z) to indicate direction; blue is negative and green is positive. Images show flow structures at 270° of rotation and are taken perpendicular to the wing's surface. The insets show a cross-sectional view of the wing's shape.

towards the trailing-edge was found to be akin to reducing the magnitude of positive camber slightly. This can be seen from figure 5.12 which shows the variation in iso-surfaces of the Q criterion with the location of maximum camber for a 15% camber wing. Figure 5.12 shows that for $p/c = 0.5$ the development of the streamwise vortex structures is such that they limit the development of LEV 2 across the wing's span. However, for $p/c = 0.75$ the development of LEV 2 is not inhibited and it extends further across the wing. This flow structure state is similar to a 10% camber, $p/c = 0.5$ wing as shown in figure 5.6c. In addition, moving the location of maximum camber towards the leading-edge (figure 5.12a) results in the streamwise structures moving towards the wing root, which is also seen for a 20% camber $p/c = 0.5$ wing.
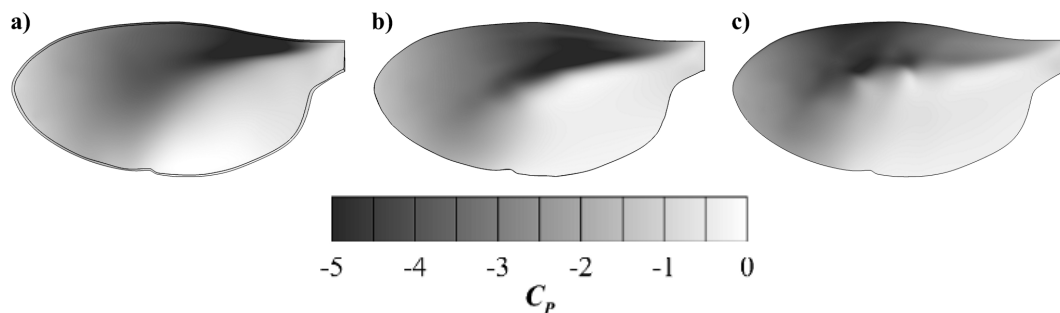
FIGURE 5.13: Average surface pressure coefficients on the top surface for (a) $m/c = -0.15$, (b) $m/c = 0$ and (c) $m/c = 0.15$ wings ($p/c = 0.5$, $Re = 1500$). Surface pressures have been averaged over the quasi-steady period.

5.4 Relating Forces, Flow Structures and Camber

In §§5.3.1 and 5.3.2 above, it was shown that positively and negatively cambered wings produce very different vortex structures. Despite negatively cambered wings maintaining a strong coherent LEV structure they produce less lift and more drag than a flat wing. On the other hand, highly positively cambered wings have increased aerodynamic performance but do not generate a strong coherent LEV. In this section how wing camber influences the aerodynamic performance of the wing is explored.

For a conventional aircraft wing, which requires attached flow in order to operate, camber is beneficial as it increases the lift coefficient for a given angle of attack over the linear range of the lift coefficient versus angle of attack curve. Usherwood & Ellington (2002a) argue that conventional reasoning for camber is flawed for thin flapping and rotating wings at high angles of attack as the flow separates from the wing's leading-edge. Therefore an alternative explanation must be found. Usherwood & Ellington (2002a) also demonstrate that for these wings the pressure force dominates and consequently the resultant force on a flat wing acts perpendicular to the wing's surface. This is further explored by Birch et $al.$ (2004), who show that at a Reynolds number of 1400 the angle of the net force vector to the wing's surface quickly reaches $90°$ as the angle of attack of the wing is increased from $0°$. This state is reached more slowly at a Reynolds number of 120 due to the added skin friction force.

For these simulations, at a Reynolds number of 1500, the skin friction force makes up between 0.26% - 1.3% of the total aerodynamic force and therefore the pressure force does indeed dominate. Therefore, a flat wing at a $45°$ angle of attack should have
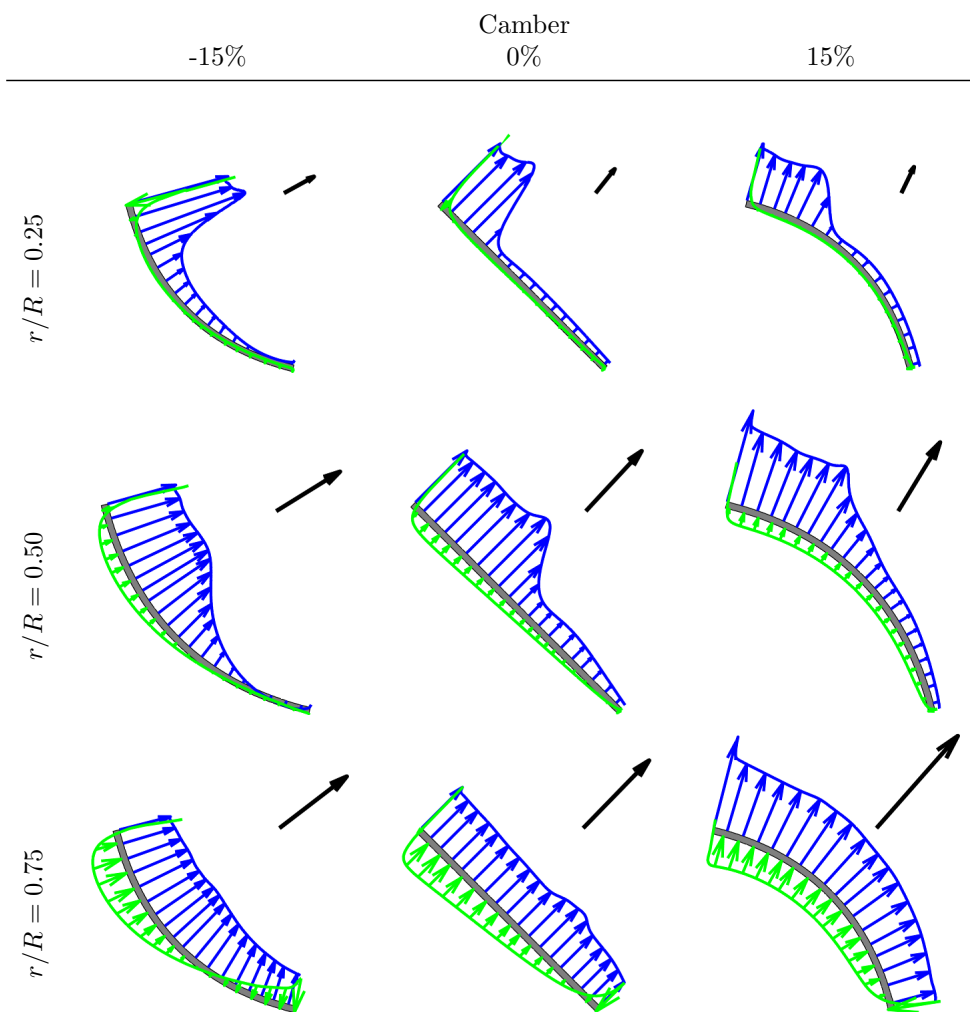
145

FIGURE 5.14: Force vectors due to surface pressure distribution at three spanwise locations for $m/c = -0.15$, 0 and 0.15 camber wings ($p/c = 0.5$, $Re = 1500$). The upper surface vectors are shown in blue and the lower surface vectors in green. Leading and trailing edge vectors are not shown. The black arrow is the scaled net force vector for that cross-section.

a lift on drag ratio of approximately one. Figure 5.2b shows that the lift on drag ratio for a flat wing is 1.08. This slightly elevated lift on drag ratio is due to low pressure acting across the wing's thickness at the leading-edge. Hence, leading-edge suction is not insignificant and makes up 3.97% of the wing's overall force.

In order to explain how increasing camber improves the aerodynamic performance of the wing, the pressure distribution over the wing first needs to be highlighted. This is shown in figure 5.13 for the -15%, 0%, and 15% camber wings. Figure 5.13b shows that for a flat wing from about the wing's root up until approximately 60% span there is an intense region of low pressure near the wing's leading-edge, which is associated

with the proximity of a strong coherent LEV to the wing's surface. Below this region the pressure rapidly increases and thus the wing does not produce much lift (or drag) in this area. Beyond 60% span, after LEV 2 has burst, the chordwise variation in surface pressure evens out across the wing. Figure 5.13a shows that this general description for the surface pressure remains the same for negatively cambered wings except that the pressure distribution begins to even out earlier along the span due to the earlier breakdown of LEV 2. For positively cambered wings it can be seen that the intense region of low pressure moves to the outer part of the wing due to the formation of the streamwise vortex structures and consequently there is an increase in pressure over the inner portion of the wing near the leading-edge as LEV 2 reduces in strength. However, figure 5.13 shows that for all wings the majority of the pressure force is produced in the first half of the wing's chord.

The effect of wing camber can then be understood by considering the chordwise pressure distribution on the wing and its relation to the wing's curvature. This is shown in figure 5.14 for the -15%, 0% and 15% camber wings at 25%, 50% and 75% wing span. Over the inner portion of the wing (e.g. $r/R = 25\%$ and 50%) most of the force due to surface pressure is produced near the wing's leading-edge. Positively cambered wings have surfaces which are flatter with respect to the horizontal in this portion of the wing. This allows the pressure force to act more vertically in this region, resulting in an upward tilting of the net force vector. Conversely, negatively cambered wings cause this region of low pressure to act more horizontally, lowering the net force vector and therefore reducing lift and increasing drag. In the outer part of the wing, where the pressure distribution is more even across the wing's chord, the effect of camber is minimal as the curvature of the wing near the leading-edge is balanced out by the curvature near the trailing-edge. This results in an angle of the net force vector to the wing's chord line of approximately 90° for all wings in this region. Therefore, positive wing camber allows the wing to produce lift more effectively over the inner portion of the wing, which consequently improves the wing's overall aerodynamic performance. The reduced suction near the wing's root due to the reduction in LEV 2's strength is outweighed by the effect of the wing's curvature and the formation of streamwise vortices lowers the surface pressure further out along the wing's span, aiding in lift production.
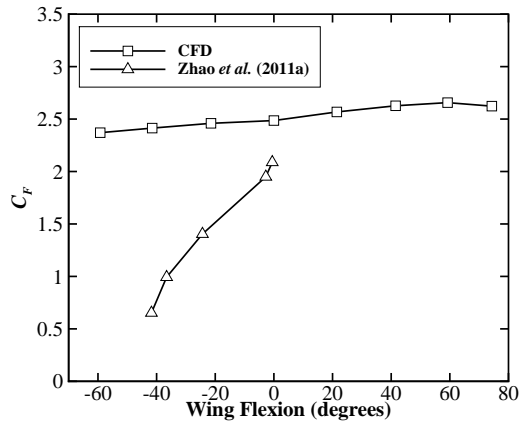
FIGURE 5.15: Variation of net force coefficient with wing flexion. Negative wing flexion corresponds to negative wing camber while positive wing flexion is positive wing camber. Comparison to experimental data from Zhao *et al.* (2011a).

5.5   Wing Camber and Net Force Correlation

In an earlier rotating wing experiment, Zhao *et al.* (2011a,b) hypothesised that trailing-edge flexion directly influences leading-edge vorticity and consequently the magnitude of the aerodynamic forces on flexible wings. Their experiment consisted of a flexible wing rotating at a constant rotational velocity. The leading-edge of the wing was fixed at an angle of attack of 45° while the rest of the wing was free to deform. They found that as the wing's flexural stiffness was reduced, the wing bent into a negatively cambered shape and there was a reduction in net force coefficient. The degree of wing deformation was measured as wing flexion, which they defined as the angle between the leading-edge tangent and the trailing-edge tangent. Their data has been reproduced in figure 5.15.

To compare their data with these simulations, the flexion angle and the net force coefficient were calculated for the cambered wings. The net force coefficient was calculated as $C_F = 2F/\rho U_{rg}^2 S$, where F is the net aerodynamic force. As shown in figure 5.2, it was found that increasing the magnitude of negative wing camber results in a reduction in lift coefficient but an increase in drag coefficient. This corresponds to a roughly constant net force coefficient with increasing flexion (figure 5.15). The numerical data shows just a 4.6% drop in the net force coefficient from 0° to −60° of flexion. These findings are markedly different from those of Zhao *et al.* (2011a,b), who found a 68.8% drop in the net force coefficient between 0° to −40° of flexion.

148

A possible explanation for this difference in trends could be due to a change in the wing's angle of attack in the experiments. Previous studies that have investigated the effect of angle of attack have shown that the net force reduces with decreasing angle of attack (Dickinson *et al.* 1999; Usherwood & Ellington 2002a; Birch *et al.* 2004). In these simulations the angle of attack (angle between the mean chord line and the freestream flow) is kept constant as the wing's camber is varied, while Zhao *et al.* (2011a,b) fix the leading-edge angle and allow the wing's trailing-edge to deform to the flow. Consequently, the angle of attack of the wing reduces as the wing flexes and their data therefore include a change in angle of attack as well as a change in wing shape. It is therefore likely that their results are dominated by the reduction in angle of attack experienced by the wing and are not due to the change in wing camber. The CFD results show that there is only a weak correlation between wing camber and the magnitude of the net aerodynamic force.

5.6   Effect of Camber at Low Reynolds Numbers

It is well known that the characteristics of the LEV change with Reynolds number. Birch *et al.* (2004) showed that at a Reynolds number of 1400 the LEV forms a tight spiral structure with a strong axial velocity in its core, but at a Reynolds number of 120 it does not. Ellington *et al.* (1996) reported a similar conical spiral LEV with an intense spanwise flow within its core for hovering hawkmoth flight ($Re \approx 5000$), while Shyy & Liu (2007) and Liu & Aono (2009) reported a similar change in the LEV's structure between a hovering fruit fly ($Re = 134$), honeybee ($Re = 1123$) and hawkmoth ($Re = 6300$) using a computational model. Lu *et al.* (2006) found that for Reynolds numbers greater than 640 a dual co-rotating LEV structure forms in which the primary vortex has a tight spiral structure.

The results of this study were performed at a Reynolds number of 1500 where a clear dual LEV structure exists for a flat wing. The above literature shows that the LEV's structure does not change greatly for Reynolds numbers higher than this, and therefore the effect of wing camber should be similar. However, at lower Reynolds numbers the LEV's structure does change significantly and therefore the effect of camber at these Reynolds numbers needs to be explored. How camber affects the wing's performance and flow structures at a Reynolds number of 120 is investigated below.

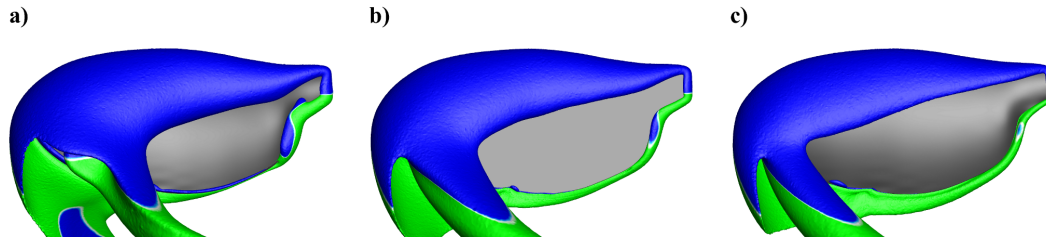The variation in the vortex structures between Reynolds numbers of 120 and 1500 for

FIGURE 5.16: Vortex structures at $Re = 120$ for (a) -15%, (b) 0% and (c) 15% camber ($p/c = 0.5$). Vortices are visualised using surfaces of constant Q criterion and are coloured by spanwise vorticity (ω_z) to indicate direction; blue is negative and green is positive. Images show flow structures at $\phi = 270°$ and are taken perpendicular to the wing's surface.
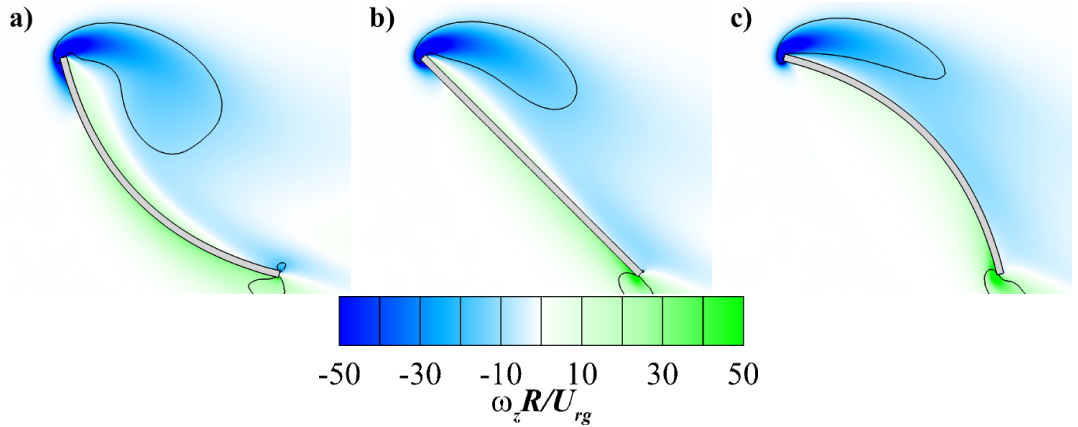

FIGURE 5.17: Spanwise vorticity contours ($\omega_z R/U_{rg}$) at 50% span for (a) -15%, (b) 0% and (c) 15% camber wings ($p/c = 0.5$) at $Re = 120$. Solid black lines represent a contour of the Q criterion of the same value as the iso-surfaces shown in figure 5.16. Images show flow structures at $\phi = 270°$.

a flat wing has been previously reported in §3.2.2 and is consistent with the observations described above. At this low Reynolds number ($Re = 120$) a single, less intense, LEV forms over the wing with reduced spanwise velocity in its core. Unlike at higher Reynolds numbers, here only minor changes in the LEV's structure are seen for both positive and negative camber. Figure 5.16 shows iso-surfaces of the Q criterion over -15%, 0% and 15% camber wings. A similar vortex system is seen for all wings where the single LEV extends across the wing and connects with the TV. A TEV forms and is seen to remain attached to the wing, only separating from the wing near the wing tip, outside the TV, thus forming a pair of counter-rotating vortices in the wake. This vortex structure was also observed by Poelma *et al.* (2006) in their PIV experiments
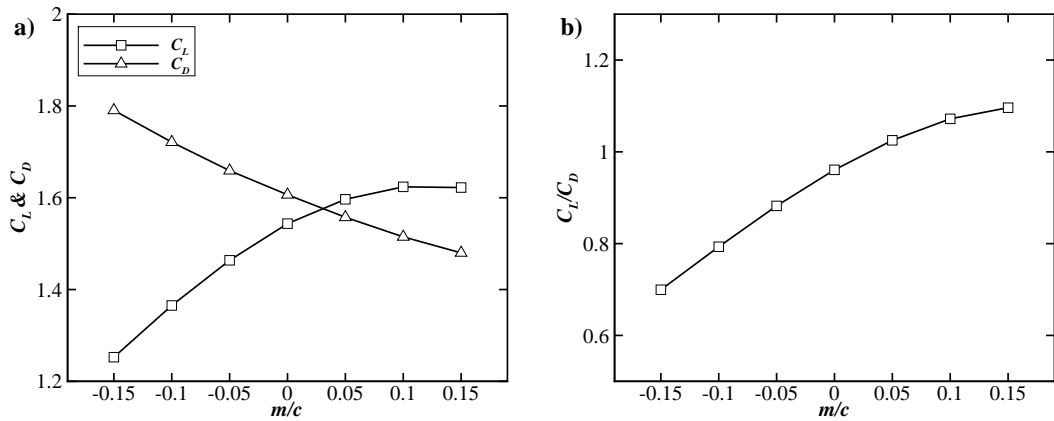
FIGURE 5.18: Average aerodynamic force graphs at $Re = 120$. (a) Change in lift and drag coefficients with magnitude of camber, m/c ($p/c = 0.5$). (b) Variation in lift on drag ratio with magnitude of camber.

on a revolving fruit fly wing.

One change that can be seen with camber is that the TV moves outboard slightly with increasing camber. The LEV also becomes compressed with increased camber, which is shown in figure 5.17 by the black line representing a contour of the Q-criterion. At -15% camber the LEV is fuller and more rounded, but as the camber is increased the LEV becomes elongated in the streamwise direction. Overall, the area enclosed by the iso-Q contour increases by 50.3% and reduces by 11.1% for the -15% and 15% camber cases respectively, compared to the non-cambered wing. The corresponding circulation change is 25.8% and -15.2% respectively.

A substantial increase in the wing's performance is seen for positively cambered wings at this Reynolds number. The variation in aerodynamic forces with camber at a Reynolds number of 120 is shown in figure 5.18 and reveals that a similar increase in lift coefficient and a decrease in drag coefficient are observed with increasing camber as was seen at the higher Reynolds number. Here a 14% increase in the lift on drag ratio was found at 15% camber compared to a flat wing. This percentage increase is about half that at $Re = 1500$, which shows that camber has a reduced effect at lower Reynolds numbers. A decreased benefit of positive camber at lower Reynolds numbers was also found by Du & Sun (2008) for a flapping wing.

The mechanism through which camber improves the wing's performance is the same at $Re = 120$ as it is at $Re = 1500$. The pressure force still dominates, making up between 94% - 99% of the total aerodynamic force depending on the magnitude of
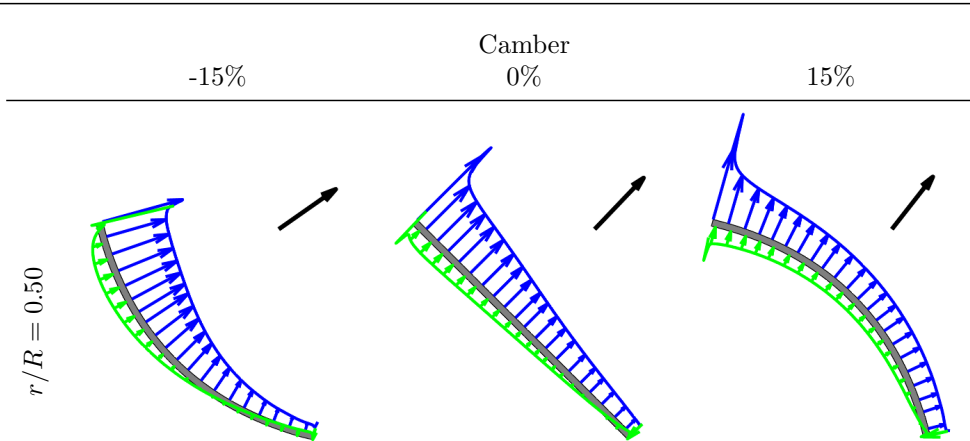
FIGURE 5.19: Force vectors due to surface pressure distribution at 50% span for $m/c = -0.15$, 0 and 0.15 camber wings ($p/c = 0.5$) at $Re = 120$. The upper surface vectors are shown in blue and the lower surface vectors in green. Leading and trailing edge vectors are not shown. The black arrow is the scaled net force vector for that cross-section.

camber and, while weaker, the LEV still produces a region of lower pressure near the leading-edge of the wing. Thus increasing the wing's camber allows this low pressure to act more vertically, which results in a tilting of the net force vector (figure 5.19). In fact the net force coefficient varies by less than 2% between -15% and 15% wing camber at this Reynolds number and therefore the variation in lift and drag coefficients that are seen are purely due to the angling of the net force vector and not from a change in its magnitude.

5.7   Summary

In this chapter the aerodynamic forces and flow structures that are produced by stiff cambered rotating insect wings were investigated by solving the Navier-Stokes equations cast in a rotating reference frame. These simulations were calculated at Reynolds numbers of 120 and 1500 and both the magnitude and the chordwise location of maximum camber were examined.

At a Reynolds number of 1500, a flat non-cambered wing produces a dual LEV structure which consists of two co-rotating spanwise oriented vortex structures that are separated by a smaller counter-rotating vortex. It was found that negatively cambered wings maintain this dual LEV structure, but the wing's concave shape allows the downstream vortex to break down earlier along the wing's span.

On the other hand, positively cambered wings produce very different LEV structures

to flat or negatively cambered wings. Here an increase in wing camber results in multiple streamwise vortex structures forming at the leading-edge. Initially these structures are weak and are entrained into the main LEV, but as the wing's camber is increased they begin to dominate the flow and prevent the dual LEV structure from developing across the wing's span. Despite a reduction in the magnitude of spanwise velocity, corresponding to the degradation of the main LEV, a significant spanwise velocity still exists for highly positively cambered wings. This allows the streamwise vortices to feed into the TV, and as such a quasi-steady state is still reached for these wings.

For both positively and negatively cambered wings, the influence of the chordwise location of camber was found to be akin to varying the magnitude of camber but with a more subtle impact on the flow structures. Moving the location of maximum camber towards the trailing-edge of the wing produced similar changes in flow structures to reducing the magnitude of positive or negative camber, which was attributed to the associated reduction in curvature near the leading-edge of the wing.

The relationship between the flow structures and the aerodynamic forces was also assessed. In agreement with previous studies, it was found that positive camber improved the wing's aerodynamic performance (Altshuler *et al.* 2004; Tsuzuki *et al.* 2007; Du & Sun 2008). It was revealed that both positively and negatively cambered wings produce chordwise pressure distributions that have a region of low pressure near the leading-edge for most of the wing's span. This pressure distribution combined with the curvature near the leading-edge results in a tilting of the net force vector, either more vertically for positive camber or more horizontally for negative camber, which leads to the variation in aerodynamic forces that are seen. This improved understanding explains why insects can benefit from wing camber.

The effect of camber at a Reynolds number of 120 was also investigated. It was found that at this Reynolds number only minor changes in the LEV's structure were observed, but an improvement in the wing's lift on drag ratio was still obtained for positively cambered wings. It was shown that it is the same mechanism (the pressure distribution combined with the wing's curvature) that acts to improve aerodynamic performance at this low Reynolds number as at a Reynolds number of 1500. Therefore camber is beneficial for flapping and rotating wings at Reynolds numbers between 120 and 1500, and possibly higher.

153

Chapter 6

Conclusions

In this thesis the effect of two wing morphological parameters, namely aspect ratio and camber, on the aerodynamic forces and flow structures of rotating and flapping wings has been investigated. The aim of this study was to provide a better understanding of the role that these parameters play in determining the wing's aerodynamic performance under insect-like flight regimes. The results from this study have helped to explain why many insects have evolved to have low aspect ratio wings and why many exploit flexible wing structures. They also provide the basis from which flapping and rotating MAV wings can be designed. These findings are detailed below.

6.1 Aspect Ratio

6.1.1 Decoupling Aspect Ratio and Reynolds Number

The wing aspect ratio investigation was split into two separate studies, the first of which was aimed at isolating the effects of aspect ratio from those of Reynolds number. A rotating-wing numerical model was used to solve the flow around different aspect ratio wings at various Reynolds numbers. This study revealed that the traditional use of the wing's chord length in scaling of the flow was inadequate for flapping and rotating wings under insect-like flight regimes. When the wing's chord length is used, changing the wing's aspect ratio also changes the Reynolds number, as these two parameters are linked due to the wing's rotation. Thus, modifying the wing's aspect ratio resulted in flow structure changes that included Reynolds number effects.

It was shown that for rotating and flapping wings the LEV develops in the spanwise direction due to the wing's rotation. Hence, a new hypothesis was proposed that the wing's span is a better characteristic length to use in the scaling of flapping and rotating wings under insect-like flight regimes.

This hypothesis was tested by re-scaling the simulations using the wing's span. This resulted in a new span-based Reynolds number and Rossby number. It was demonstrated that by scaling the flow using the span-based Reynolds number, matching vortex structures could be observed across a range of wing aspect ratios. Indeed, universal behaviour was found for the location where two co-rotating vortices could be first observed as well as the breakdown point of the downstream vortex using this scaling. It was therefore concluded that by using the span-based Reynolds number the effects of aspect ratio and Reynolds number can be decoupled. Thus, this span-based scaling should be used when scaling the flow around flapping or rotating wings under insect-like flight regimes, particularly when comparing the performance of different wing planform shapes as it allows each wing to be evaluated on an equal basis. This technique was used in this study to assess the impact of aspect ratio on the flow structures around rotating wings and it was found that the main effect of aspect ratio is to increase the size of the LEV relative to the wing's chord length, which brings the flow reattachment point downstream of the LEV closer to the trailing-edge.

Furthermore, the limitations of using wing span as a characteristic length were assessed and determined to be restricted to flapping and rotating wings revolving about their base at high angles of attack, such that the flow separates from the leading-edge and a strong spanwise velocity is generated on the leeward side of the wing. These conditions are typical of those seen in nature, and hence this scaling could be applied to investigations involving insects and birds as well as nature-mimicking MAVs.

6.1.2   Leading-Edge Vortex Stability

The second aspect ratio study was aimed at uncovering the effect of aspect ratio at different flight speeds and to determine weather or not it plays a role in dictating the stability of the LEV. Here, a flapping-wing numerical model was used to simulate the flow around different aspect ratio wings over a range of advance ratios. It was shown that for non-zero advance ratios the freestream velocity alters the relative velocity experienced by the wing for the up- and downstrokes. This affects vorticity production on the wing and therefore leads to different vortex structures being formed on the wing between the up- and downstrokes, where the LEV is larger and stronger for the downstroke and smaller and weaker for the upstroke.

At high advance ratios the LEV rapidly grew in size throughout the downstroke.

156

When this was combined with a larger aspect ratio wing the LEV quickly grew to envelop the entire wing during the downstroke and eventually it was shed as part of a vortex loop that peeled away from the wing's tip. Thus, it was found that the stability of the LEV is dependent on both the advance ratio and wing aspect ratio, where the advance ratio controls the growth rate of the LEV and the aspect ratio dictates the relative size of the LEV compared to the wing's chord length. The higher the aspect ratio or advance ratio the more unstable the LEV becomes. This dependency of LEV stability on the advance ratio and aspect ratio was shown to exist at both low and high span-based Reynolds numbers and therefore the findings from this study are likely to apply across a wide range of Reynolds numbers that are typical for insect flight.

This finding helps to explain why many insects have evolved to have low aspect ratio wings, as low aspect ratios avoid LEV shedding over a wider range of advance ratios. Indeed, it was shown that the wing's aerodynamic performance reduces as the wing aspect ratio is increased. This was due to the wing stalling, and therefore becoming less effective at producing lift, when the LEV became too large and was shed from the wing. It was therefore revealed that low aspect ratio wings do in fact outperform higher aspect ratios under insect-like flight regimes, particularly at non-zero advance ratios. Hence, many insect species have evolved to have low aspect ratio wings compared to conventional aircraft as they are more efficient in this flight regime. Furthermore, this research has shown that MAV designers who wish to employ an insect-like flapping or rotating wing mechanism should use low aspect ratio wings for optimal aerodynamic efficiency over a wide range of flight speeds.

6.2   Camber

In this thesis the effect of wing camber was investigated. The rotating-wing numerical model was used to solve the flow around rigid wings with different magnitudes of both negative and positive camber. These simulations showed that positively cambered wings produce higher lift coefficients and lower drag coefficients compared to flat or negatively cambered wings, and therefore positive wing camber improves the wing's aerodynamic performance. While it was found that aerodynamic performance was still increasing at 20% camber, this magnitude of camber is likely to be beyond what is typically observed in insect flight. However, these results show that even a small increase in wing camber would result in a significant improvement in aerodynamic performance for

insects. Moreover, MAV designers may wish to use more aggressive camber to exploit its benefits.

Analysis of the flow structures revealed that positive wing camber had a large effect on the structure of the LEV at high Reynolds numbers, causing it to break up into multiple smaller vortices. In addition, negative wing camber resulted in the breakdown point of the LEV moving closer to the wing's root. However, only a small impact on the LEV's structure was observed due to either positive or negative camber at low Reynolds numbers.

The relationship between the flow structures and the aerodynamic forces was assessed. It was revealed that the chordwise pressure distribution combined with the curvature near the leading-edge results in a tilting of the net force vector, either more vertically for positive camber or more horizontally for negative camber, which leads to the variation in aerodynamic forces that are seen. This finding provides a new understanding as to the mechanism through which camber acts in insect flight and helps to explain how insects can benefit from wing camber. This mechanism was observed to apply at both high and low Reynolds numbers, which shows that camber is beneficial for flapping and rotating wings across a wide range of Reynolds numbers that are typical for insect flight.

6.3 Directions for Future Work

There are a number of possible directions to extend the work presented in this thesis. These are discussed below.

The aspect ratio studies in this thesis revealed that there are two possible avenues for further work in this area. The first relates to selecting the optimal aspect ratio for flapping flight. It was determined that the optimal aspect ratio will depend on both the flight speed envelope of the insect/MAV (range of advance ratios) and the wing's stroke amplitude. Therefore further investigation into the effects of advance ratio, stroke amplitude and aspect ratio is recommended in order to provide guidelines as to the optimal aspect ratio and stroke kinematics selection for a particular operational flight envelope.

The second avenue is to investigate the effect of the stroke plane angle on the stability of the LEV. As discussed in chapter 4, insects typically tilt their stroke plane angle in order to achieve forward flight. This stroke plane tilt was not included in

this investigation for simplicity, but given the sensitivity of LEV stability to the insect's flight speed a follow up investigation into the effect of the stroke plane angle is recommended. Changing the stroke plane angle could easily be incorporated in the flapping-wing model described in §2.3 by rotating the stationary domain to change the angle of the freestream velocity relative to the stroke plane.

A natural extension of the investigation into wing camber would be to include non-zero advance ratios. This could be done by incorporating camber changes into the flapping-wing model described in §2.3. Due to the wing's flapping motion, this would require either a prescribed time varying camber to be specified or for a fluid structure interaction solver to be incorporated in the model. Both methods will most likely require re-meshing to be done throughout the flapping cycle, which will add considerable computational expense to the model. However, undertaking this study would broaden the findings of the current investigation to include the effect of wing camber under forward flight conditions.

In addition to continuing to investigate the wing shape parameters that were examined in this thesis, future work could also be expanded to study other wing shape parameters. Potential wing morphological parameters were highlighted in chapter 1 and include the distribution of wing area, spanwise bending and wing twist.

Appendix A

Vorticity Generation

Vorticity is generated at the boundary between a body's surface and the fluid. The flux of vorticity from these boundaries, as reported by Morton (1984), is given by,

$$-\nu(\boldsymbol{n} \cdot \boldsymbol{\nabla}\boldsymbol{\omega}) = -\rho^{-1}(\boldsymbol{n} \times \nabla)p - \boldsymbol{n} \times \boldsymbol{a}, \tag{A.1}$$

where ν is the kinematic viscosity, $\boldsymbol{n}$ is the wall unit normal vector, $\boldsymbol{\omega}$ is the vorticity vector and $\boldsymbol{a}$ is the acceleration vector of the boundary. This equation is evaluated at the surface and shows that vorticity is generated from tangential pressure gradients and the tangential acceleration of the boundary (Morton 1984).

Equation A.1 was used to estimate the vorticity being generated at one spanwise location on the wing's surface for the flapping wing simulations. Figure A.1 presents a schematic of a typical two-dimensional streamline pattern of the flow around a flapping wing. The flow stagnates on the wing's lower surface at A. The fluid above A flows over the leading-edge while the fluid below A travels along the underside of the wing. Therefore, any vorticity that is generated between A and C is advected over the leading-edge and into the LEV. By integrating equation A.1 along the wing's surface from A to C the time rate of change of LEV circulation per unit span due to the generation of vorticity can be calculated. This results in,

$$\frac{\mathrm{d}\Gamma_z}{\mathrm{d}t} = \rho^{-1}\int_A^C \frac{\partial p}{\partial s}\,\mathrm{d}s + \int_A^B \frac{\mathrm{d}U_i}{\mathrm{d}t}\sin(|\alpha_i|)\,\mathrm{d}s - \int_B^C \frac{\mathrm{d}U_i}{\mathrm{d}t}\cos(|\alpha_i|)\,\mathrm{d}s. \tag{A.2}$$

The first term on the right hand side of equation A.2 is the vorticity generation due to the pressure gradient and the other two terms account for the vorticity generation due to the tangential acceleration of the wing's bottom surface and leading-edge respectively. As we are primarily interested in the generation of vorticity outside of the stroke reversal, the acceleration of the wing's surface due to the pitch rotation of the wing
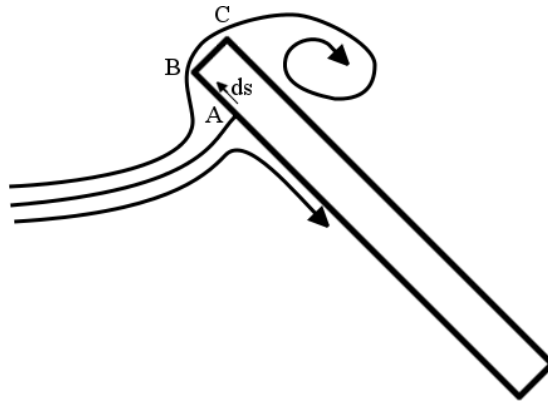
FIGURE A.1: Schematic of a typical two-dimensional streamline pattern at one point along the wing's span.

has been neglected. The acceleration of each point on the wing's surface can therefore be approximated as the time rate of change of the relative velocity at that spanwise location (i.e. $a = \frac{\mathrm{d}U_i}{\mathrm{d}t}$). As the wing's acceleration is in the x-direction, this needs to be modified to calculate the component that acts tangentially to each surface. Hence the use of $\sin(|\alpha_i|)$ and $\cos(|\alpha_i|)$ in equation A.2, where α_i is given by equation 2.19. Equation A.2 has been written for the downstroke and in terms of the coordinate system shown in figure 2.7. Therefore a negative pressure gradient results in the generation of negative vorticity, and a positive time rate of change of U_i causes positive vorticity to be generated on the wing's bottom surface and negative vorticity to be generated on the leading-edge. For the upstroke this description of vorticity generation is reversed, due to the change in orientation of the wing, and therefore the time rate of change of circulation is the negative of equation A.2.

Equation A.2 was evaluated at 25% span for the downstroke and the results are presented in figure 4.7, where figure 4.7a is the computed value of the pressure gradient term and figure 4.7b is the sum of the acceleration terms.

Appendix B

Movies

The videos generated for this thesis are detailed below. Movie files can be found on the CD at the back of thesis.
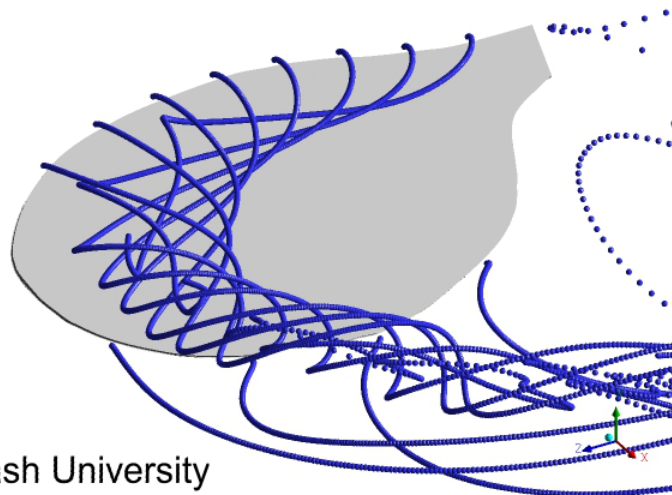
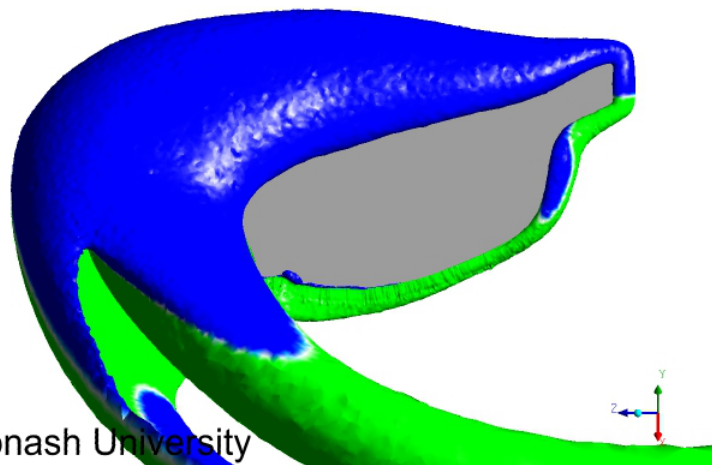MOVIE B.1: Particle tracking flow visualisation at $Re = 120$ for $AR = 2.91$ wing. Results from the rotating-wing model.
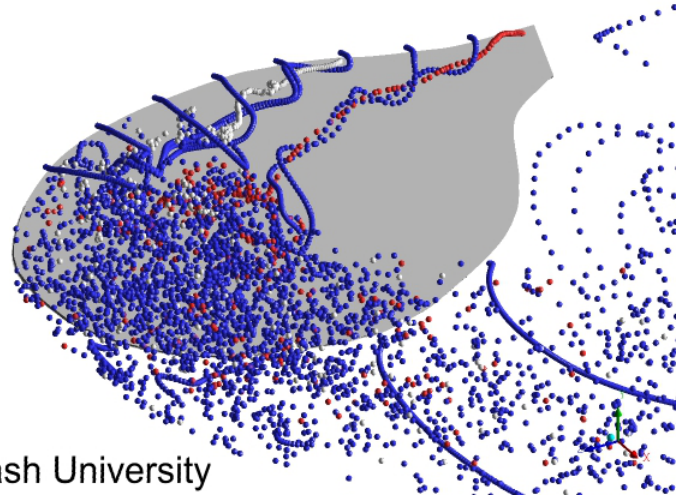
MOVIE B.2: Particle tracking flow visualisation at $Re = 1500$ for $AR = 2.91$ wing. Results from the rotating-wing model.
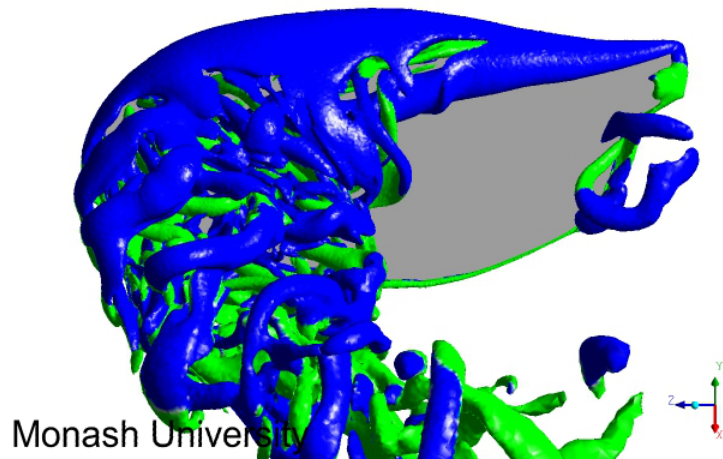

MOVIE B.3: Vortex structure development over a $AR = 2.91$ wing at $Re = 120$. Results from the rotating-wing model. Vortex structure are visualised using surfaces of constant Q criterion, coloured by spanwise vorticity to indicate direction; blue is negative and green is positive.

MOVIE B.4: Vortex structure development over a $AR = 2.91$ wing at $Re = 1500$. Results from the rotating-wing model. Vortex structure are visualised using surfaces of constant Q criterion, coloured by spanwise vorticity to indicate direction; blue is negative and green is positive.
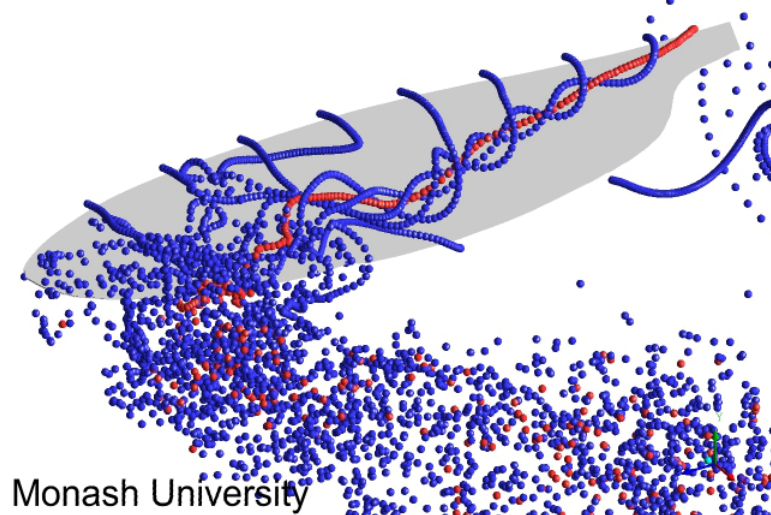
MOVIE B.5: Particle tracking flow visualisation at $Re_R = 7667$ for $AR = 7.28$ wing. Results from the rotating-wing model.
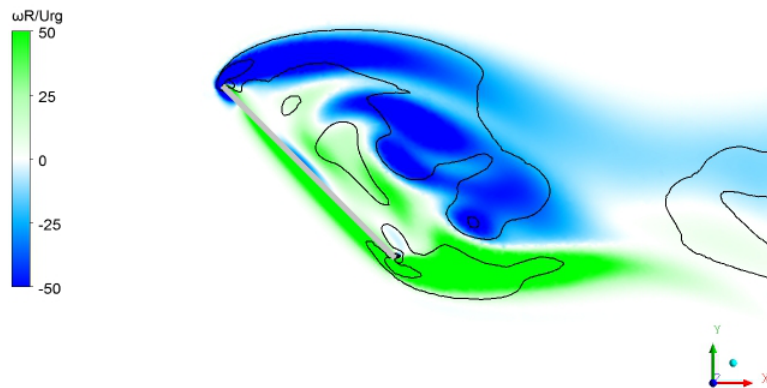
Movie B.6: Spanwise vorticity contours at 70% span for a $AR = 7.28$ wing at $Re_R = 3883$. Results from the rotating-wing model. Solid lines are contours of constant Q criterion.
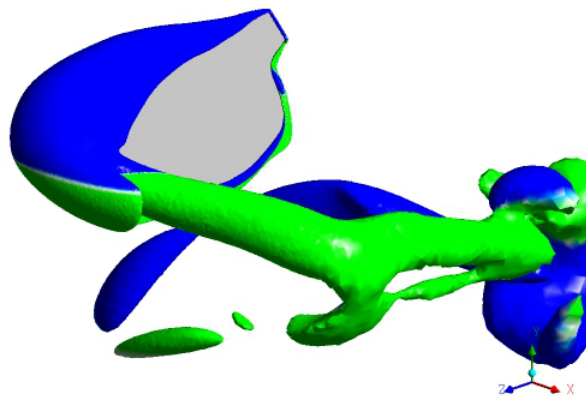
Movie B.7: Stationary view of the wings motion and the generated flow structures during the downstroke for $J = 0$, $AR = 2.91$ and $Re_R = 613$. Vortex structures are visualised by iso-Q surfaces coloured by spanwise vorticity to indicate direction, green is positive and blue is negative.
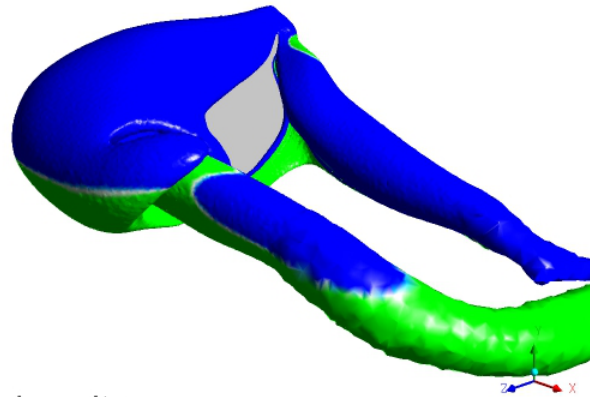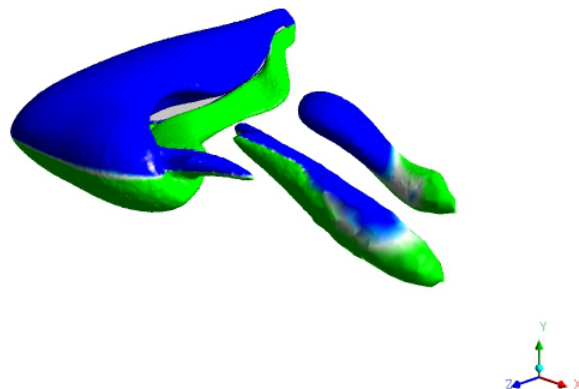
Monash University

MOVIE B.8: Stationary view of the wings motion and the generated flow structures during the downstroke for $J = 0.5$, $AR = 2.91$ and $Re_R = 613$. Vortex structures are visualised by iso-Q surfaces coloured by spanwise vorticity to indicate direction, green is positive and blue is negative.
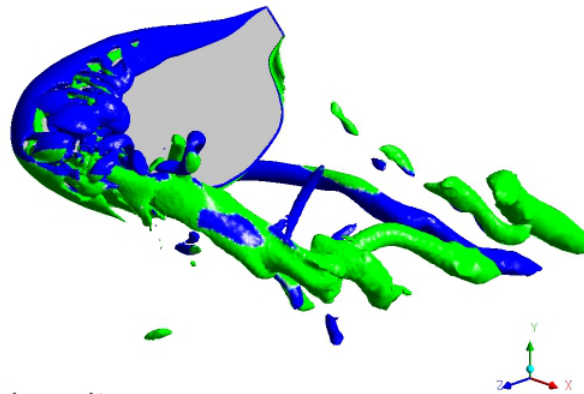

t* = 0.75
Φ = 0.00152996 [degree]

Monash University

MOVIE B.9: Stationary view of the wings motion and the generated flow structures during the downstroke for $J = 0.5$, $AR = 7.28$ and $Re_R = 613$. Vortex structures are visualised by iso-Q surfaces coloured by spanwise vorticity to indicate direction, green is positive and blue is negative.
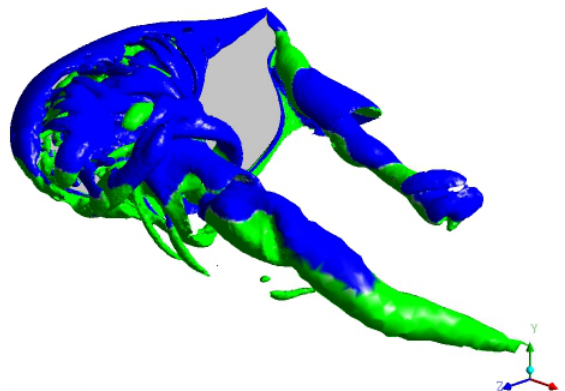
MOVIE B.10: Stationary view of the wings motion and the generated flow structures during the downstroke for $J = 0$, $AR = 2.91$ and $Re_R = 7668$. Vortex structures are visualised by iso-Q surfaces coloured by spanwise vorticity to indicate direction, green is positive and blue is negative.

MOVIE B.11: Stationary view of the wings motion and the generated flow structures during the downstroke for $J = 0.5$, $AR = 2.91$ and $Re_R = 7668$. Vortex structures are visualised by iso-Q surfaces coloured by spanwise vorticity to indicate direction, green is positive and blue is negative.
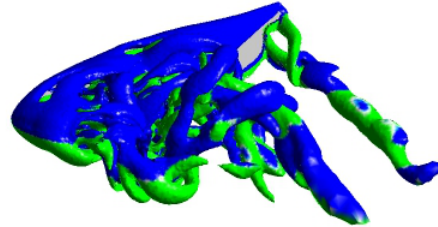
Movie B.12: Stationary view of the wings motion and the generated flow structures during the downstroke for $J = 0.5$, $AR = 7.28$ and $Re_R = 7668$. Vortex structures are visualised by iso-Q surfaces coloured by spanwise vorticity to indicate direction, green is positive and blue is negative.
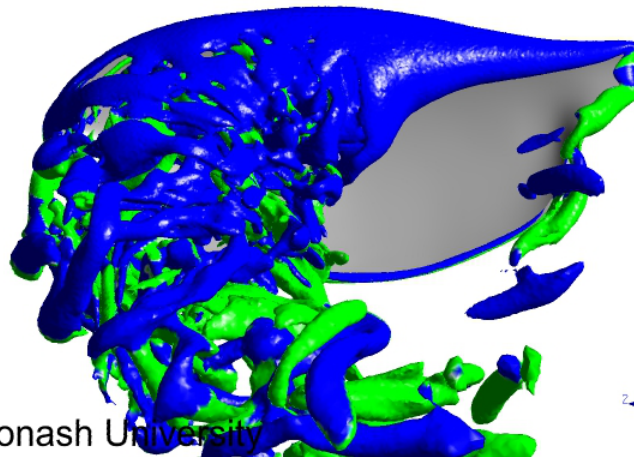

Movie B.13: Temporal development of vortex structure over a -15% camber wing ($p/c = 0.5$, $Re = 1500$). Vortex structures are visualised using surfaces of constant Q criterion and are coloured by spanwise vorticity (ω_z) to indicate direction; blue is negative and green is positive. Results from the rotating-wing model.
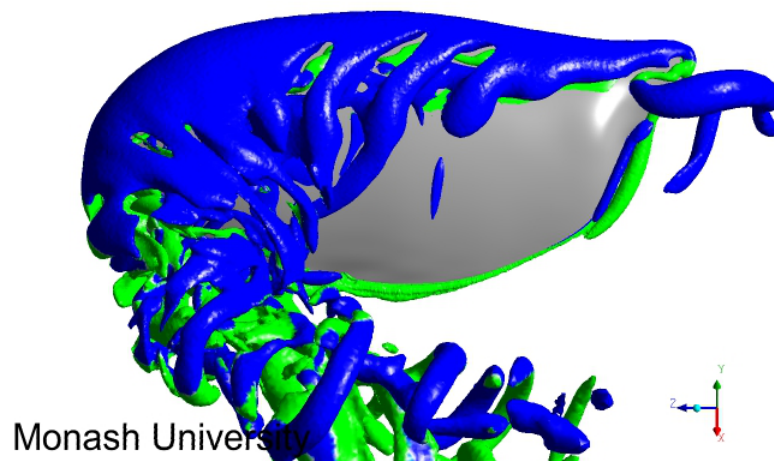
MOVIE B.14: Temporal development of vortex structure over a 15% camber wing ($p/c = 0.5$, $Re = 1500$). Vortex structures are visualised using surfaces of constant Q criterion and are coloured by spanwise vorticity (ω_z) to indicate direction; blue is negative and green is positive. Results from the rotating-wing model.

170

Bibliography

ALTSHULER, D. L., DUDLEY, R. & ELLINGTON, C. P. 2004 Aerodynamic forces of revolving hummingbird wings and wing models. *Journal of Zoology* **264**, 327–332.

ANSARI, S. A., KNOWLES, K. & ZBIKOWSKI, R. 2008 Insectlike flapping wings in the hover part 2: Effect of wing geometry. *Journal of Aircraft* **45** (6), 1976–1990.

ANSYS 2010a ANSYS CFX-Modeling Guide. *Tech. Rep.* Release 13.0. ANSYS Inc.

ANSYS 2010b ANSYS CFX-Solver Theory Guide. *Tech. Rep.* Release 13.0. ANSYS Inc.

AONO, H., LIANG, F. & LIU, H. 2008 Near- and far-field aerodynamics in insect hovering flight: an integrated computational study. *The Journal of Experimental Biology* **211**, 239–257.

BEEM, H. R., RIVAL, D. E. & TRIANTAFYLLOU, M. S. 2012 On the stabilization of leading-edge vortices with spanwise flow. *Experiments in Fluids* **52** (2), 511–517.

VAN DEN BERG, C. & ELLINGTON, C. P. 1997 The three-dimensional leading-edge vortex of a 'hovering' model hawkmoth. *Philosophical Transactions of the Royal Society B: Biological Sciences* **352** (1351), 329–340.

BILLANT, P., CHOMAZ, J. & HUERRE, P. 1998 Experimental study of vortex breakdown in swirling jets. *Journal of Fluid Mechanics* **376**, 183–219.

BIRCH, J. M. & DICKINSON, M. H. 2001 Spanwise flow and the attachment of the leading-edge vortex on insect wings. *Nature* **412**, 729–733.

BIRCH, J. M. & DICKINSON, M. H. 2003 The influence of wing-wake interactions on the production of aerodynamic forces in flapping flight. *Journal of Experimental Biology* **206**, 2257–2272.

BIRCH, J. M., DICKSON, W. B. & DICKINSON, M. H. 2004 Force production and flow structure of the leading edge vortex on flapping wings at high and low Reynolds numbers. *Journal of Experimental Biology* **207** (7), 1063–1072.

BROSS, M., OZEN, C. A. & ROCKWELL, D. 2013 Flow structure on a rotating wing: effect of steady incident flow. *Physics of Fluids* **25** (8).

CARR, Z. R., CHEN, C. & RINGUETTE, M. J. 2013 Finite-span rotating wings: three-dimensional vortex formation and variations with aspect ratio. *Experiments in Fluids* **54** (2).

CHENG, B., SANE, S. P., BARBERA, G., TROOLIN, D. R., STRAND, T. & DENG, X. 2013 Three-dimensional flow visualization and vorticity dynamics in revolving wings. *Experiments in Fluids* **54** (1).

COOTER, R. J. & BAKER, P. S. 1977 Weis-Fogh clap and fling mechanism in Locusta. *Nature* **269**, 53–54.

DICKINSON, M. H. 1994 The effects of wing rotation on unsteady aerodynamic performance at low reynolds numbers. *Journal of Experimental Biology* **192** (1), 179–206.

DICKINSON, M. H. & GOTZ, K. G. 1993 Unsteady aerodynamic performance of model wings at low Reynolds numbers. *Journal of Experimental Biology* **174** (1), 45 – 65.

DICKINSON, M. H., LEHMANN, F.-O. & SANE, S. P. 1999 Wing rotation and the aerodynamic basis of insect flight. *Science* **284** (5422), 1954–1960.

DICKSON, W. B. & DICKINSON, M. H. 2004 The effect of advance ratio on the aerodynamics of revolving wings. *Journal of Experimental Biology* **207** (24), 4269–4281.

DU, G. & SUN, M. 2008 Effects of unsteady deformation of flapping wing on its aerodynamic forces. *Applied Mathematics and Mechanics* **29** (6), 731–743.

DUDLEY, R. & ELLINGTON, C. P. 1990 Mechanics of forward flight in bumblebees. I. Kinematics and morphology. *Journal of Experimental Biology* **148**, 19–52.

ELLINGTON, C. P. 1984a The aerodynamics of hovering insect flight. I. The quasi-steady analysis. *Philosophical Transactions of the Royal Society B: Biological Sciences* **305** (1122), 1–15.

ELLINGTON, C. P. 1984b The aerodynamics of hovering insect flight. II. Morphological parameters. *Philosophical Transactions of the Royal Society B: Biological Sciences* **305** (1122), 17–40.

ELLINGTON, C. P. 1984c The aerodynamics of hovering insect flight. III. Kinematics. *Philosophical Transactions of the Royal Society B: Biological Sciences* **305** (1122), 41–78.

ELLINGTON, C. P. 1984d The aerodynamics of hovering insect flight. IV. Aerodynamic mechanisms. *Philosophical Transactions of the Royal Society B: Biological Sciences* **305** (1122), 79–113.

ELLINGTON, C. P. 1984e The aerodynamics of hovering insect flight. V. A vortex theory. *Philosophical Transactions of the Royal Society B: Biological Sciences* **305** (1122), 115–144.

ELLINGTON, C. P. 1984f The aerodynamics of hovering insect flight. VI. Lift and power requirements. *Philosophical Transactions of the Royal Society B: Biological Sciences* **305** (1122), 145–181.

ELLINGTON, C. P. 1999 The novel aerodynamics of insect flight: applications to micro-air vehicles. *The Journal of Experimental Biology* **202**, 3439–3448.

ELLINGTON, C. P., VAN DEN BERG, C., WILLMOTT, A. P. & THOMAS, A. L. R. 1996 Leading-edge vortices in insect flight. *Nature* **384** (19), 626–630.

FRY, S. N., SAYAMAN, R. & DICKINSON, M. H. 2005 The aerodynamics of hovering flight in Drosophila. *Journal of Experimental Biology* **208**, 2303–2318.

GOPALAKRISHNAN, P. & TAFTI, D. K. 2010 Effect of wing flexibility on lift and thrust production in flapping flight. *AIAA Journal* **48** (5), 865–877.

GORDNIER, R. E. & VISBAL, M. R. 2003 Higher-order compact difference scheme applied to the simulation of a low sweep delta wing flow. In *41st AIAA Aerospace Sciences Meeting and Exhibit*.

GORDNIER, R. E., VISBAL, M. R., GURSUL, I. & WANG, Z. 2009 Computational and experimental investigation of a nonslender delta wing. *AIAA Journal* **47** (8), 1811–1825.

GRAFTIEAUX, L., MICHARD, M. & GROSJEAN, N. 2001 Combining PIV, POD and vortex identification algorithms for the study of unsteady turbulent swirling flows. *Measurement Science and Technology* **12**, 1422–1429.

HALL, M. G. 1972 Vortex breakdown. *Annual Review of Fluid Mechanics* **4** (1), 195–218.

HUNT, J. C. R., WRAY, A. A. & MOIN, P. 1988 Eddies, streams, and convergence zones in turbulent flows. *Tech. Rep.* CTR-S88. Center for Turbulence Research.

JARDIN, T., FARCY, A. & DAVID, L. 2012 Three-dimensional effects in hovering flapping flight. *Journal of Fluid Mechanics* **702**, 102–125.

JENSEN, M. 1956 Biology and physics of locust flight. III. The aerodynamics of locust flight. *Philosophical Transactions of the Royal Society B: Biological Sciences* **239** (667), 511–552.

JONES, A. R. & BABINSKY, H. 2010 Unsteady lift generation on rotating wings at low Reynolds numbers. *Journal of Aircraft* **47** (3), 1013–1021.

Jones, A. R. & Babinsky, H. 2011 Reynolds number effects on leading edge vortex development on a waving wing. *Experiments in Fluids* **51** (1), 197–210.

Jones, A. R., Pitt Ford, C. W. & Babinsky, H. 2011 Three-dimensional effects on sliding and waving wings. *Journal of Aircraft* **48** (2), 633–644.

Jones, K., Bradshaw, C., Papadopoulos, J. & Platzer, M. 2004 Improved performance and control of flapping-wing propelled micro air vehicles. In *42nd AIAA Aerospace Sciences Meeting and Exhibit*.

Kweon, J. & Choi, H. 2010 Sectional lift coefficient of a flapping wing in hovering motion. *Physics of Fluids* **22** (7), 071703.

Leibovich, S. 1978 The structure of vortex breakdown. *Annual Review of Fluid Mechanics* **10**, 221–246.

Lentink, D. & Dickinson, M. H. 2009a Biofluiddynamic scaling of flapping, spinning and translating fins and wings. *Journal of Experimental Biology* **212** (16), 2691–2704.

Lentink, D. & Dickinson, M. H. 2009b Rotational accelerations stabilize leading edge vortices on revolving fly wings. *Journal of Experimental Biology* **212** (16), 2705–2719.

Liu, H. & Aono, H. 2009 Size effects on insect hovering aerodynamics: an integrated computational study. *Bioinspiration & Biomimetics* **4**, 015002.

Lu, Y., Shen, G. X. & Lai, G. J. 2006 Dual leading-edge vortices on flapping wings. *Journal of Experimental Biology* **209**, 5005–5016.

Luo, G. & Sun, M. 2005 The effects of corrugation and wing planform on the aerodynamic force production of sweeping model insect wings. *Acta Mechanica Sinica* **21** (6), 531–541.

Maxworthy, T. 1979 Experiments on the Weis-Fogh mechanism of lift generation by insects in hovering flight. Part 1. Dynamics of the fling. *Journal of Fluid Mechanics* **93** (01), 47 – 63.

McCormick, B. W. 1995 *Aerodynamics, aeronautics, and flight mechanics*, 2nd edn. John Wiley & Sons.

Miller, L. A. & Peskin, C. S. 2004 When vortices stick: an aerodynamic transition in tiny insect flight. *The Journal of Experimental Biology* **207**, 3073–3088.

Morton, B. R. 1984 The generation and decay of vorticity. *Geophysical & Astrophysical Fluid Dynamics* **28** (3), 277–308.

MUELLER, T. J. & DELAURIER, J. D. 2003 Aerodynamics of small vehicles. *Annual Review of Fluid Mechanics* **35**, 89–111.

NAGAI, H., ISOGAI, K., FUJIMOTO, T. & HAYASE, T. 2009 Experimental and numerical study of forward flight aerodynamics of insect flapping wing. *AIAA Journal* **47** (3), 730–742.

NAKATA, T. & LIU, H. 2012 Aerodynamic performance of a hovering hawkmoth with flexible wings: a computational approach. *Proceedings of the Royal Society B: Biological Sciences* **279** (1729), 722–731.

OSBORNE, M. F. M. 1951 Aerodynamics of flapping flight with application to insects. *Journal of Experimental Biology* **28** (2), 221–245.

OZEN, C. A. & ROCKWELL, D. 2011 Flow structure on a rotating plate. *Experiments in Fluids* **52**, 207–223.

PHILLIPS, N., KNOWLES, K. & LAWSON, N. J. 2010 Effect of wing planform shape on the flow structures of an insect-like flapping wing in hover. In *27th Inernational Congress of the Aeronautical Sciences*.

PINES, D. J. & BOHORQUEZ, F. 2006 Challenges Facing Future Micro-Air-Vehicle Development. *Journal of Aircraft* **43** (2), 290–305.

POELMA, C., DICKSON, W. B. & DICKINSON, M. H. 2006 Time-resolved reconstruction of the full velocity field around a dynamically-scaled flapping wing. *Experiments in Fluids* **41** (2), 213–225.

POLHAMUS, E. C. 1971 Predictions of vortex-lift characteristics by a leading-edge suction analogy. *Journal of Aircraft* **8** (4), 193–199.

RIVAL, D. E. & WONG, J. G. 2013 Measurements of vortex stretching on two-dimensional rotating plates with varying sweep. In *10th International Symposium on Particle Image Velocimetry*.

ROACHE, P. J. 1998 Verification of codes and calculations. *AIAA Journal* **36** (5), 696–702.

ROACHE, P. J. 2003 Error bars for CFD. In *41st AIAA Aerospace Sciences Meeting and Exhibit*.

SANE, S. P. 2003 The aerodynamics of insect flight. *Journal of Experimental Biology* **206**, 4191–4208.

SANE, S. P. & DICKINSON, M. H. 2001 The control of flight force by a flapping wing: lift and drag production. *Journal of Experimental Biology* **204**, 2607–2626.

SANE, S. P. & DICKINSON, M. H. 2002 The aerodynamic effects of wing rotation and a revised quasi-steady model of flapping flight. *The Journal of Experimental Biology* **205**, 1087–1096.

SHYY, W., AONO, H., CHIMAKURTHI, S. K., TRIZILA, P., KANG, C. K., CESNIK, C. E. S. & LIU, H. 2010 Recent progress in flapping wing aerodynamics and aeroelasticity. *Progress in Aerospace Sciences* **46** (7), 284–327.

SHYY, W., LIAN, Y., TANG, J., LIU, H., TRIZILA, P., STANFORD, B., BERNAL, L., CESNIK, C., FRIEDMANN, P. & IFJU, P. 2008 Computational aerodynamics of low reynolds number plunging, pitching and flexible wings for MAV applications. In *46th AIAA Aerospace Sciences Meeting and Exhibit*.

SHYY, W. & LIU, H. 2007 Flapping wings and aerodynamic lift: the role of leading-edge vortices. *AIAA Journal* **45** (12), 2817–2819.

SRYGLEY, R. B. & THOMAS, A. L. R. 2002 Unconventional lift-generating mechanisms in free-flying butterflies. *Nature* **420**, 660–664.

STANFORD, B., IFJU, P., ALBERTANI, R. & SHYY, W. 2008 Fixed membrane wings for micro air vehicles: Experimental characterization, numerical modeling, and tailoring. *Progress in Aerospace Sciences* **44** (4), 258–294.

SUN, M. 2003 Aerodynamic force generation and power requirements in forward flight in a fruit fly with modeled wing motion. *Journal of Experimental Biology* **206** (17), 3065–3083.

SUN, M. 2004 A computational study of the aerodynamic forces and power requirements of dragonfly (Aeschna juncea) hovering. *Journal of Experimental Biology* **207**, 1887–1901.

TAIRA, K. & COLONIUS, T. 2009 Three-dimensional flows around low-aspect-ratio flat-plate wings at low Reynolds numbers. *Journal of Fluid Mechanics* **623**, 187–207.

TAYLOR, G. S. & GURSUL, I. 2004 Buffeting flows over a low-sweep delta wing. *AIAA Journal* **42** (9), 1737–1745.

TSUZUKI, N., SATO, S. & ABE, T. 2007 Design guidelines of rotary wings in hover for insect-scale micro air vehicle applications. *Journal of Aircraft* **44** (1), 252–263.

USHERWOOD, J. R. & ELLINGTON, C. P. 2002a The aerodynamics of revolving wings I. Model hawkmoth wings. *Journal of Experimental Biology* **205** (11), 1547–1564.

USHERWOOD, J. R. & ELLINGTON, C. P. 2002b The aerodynamics of revolving wings II. Propeller force coefficients from mayfly to quail. *Journal of Experimental Biology* **205** (11), 1565–1576.

VENKATA, S. K. & JONES, A. R. 2013 Leading-edge vortex structure over multiple revolutions of a rotating wing. *Journal of Aircraft* **50** (4), 1312–1316.

VOGEL, S. 1967 Flight in drosophila III. Aerodynamic characteristics of fly wings and wing models. *Journal of Experimental Biology* **46**, 431–443.

WALKER, J. D. A., SMITH, C. R., CERRA, A. W. & DOLIGALSKI, T. L. 1987 The impact of a vortex ring on a wall. *Journal of Fluid Mechanics* **181**, 99–140.

WALKER, P. B. 1931 Experiments on the growth of circulation about a wing and an apparatus for measuring fluid motion. *Tech. Rep.* 1402. Aeronutical Research Committee.

WALKER, S. M., THOMAS, A. L. R. & TAYLOR, G. K. 2009 Deformable wing kinematics in the desert locust: how and why do camber, twist and topography vary through the stroke? *Journal of the Royal Society: Interface* **6** (38), 735–47.

WALKER, S. M., THOMAS, A. L. R. & TAYLOR, G. K. 2010 Deformable wing kinematics in free-flying hoverflies. *Journal of the Royal Society: Interface* **7** (42), 131–142.

WANG, Z. J. 2005 Dissecting insect flight. *Annual Review of Fluid Mechanics* **37**, 183–210.

WANG, Z. J. 2008 Aerodynamic efficiency of flapping flight: analysis of a two-stroke model. *The Journal of Experimental Biology* **211** (2), 234–238.

WEIS-FOGH, T. 1973 Quick estimates of flight fitness in hovering animals, including novel mechanisms for lift production. *Journal of Experimental Biology* **59**, 169–230.

WILKINS, P. C. 2008 Some unsteady aerodynamics relevant to insect-inspired flapping-wing micro air vehicles. PhD thesis, Cranfield University.

WILLMOTT, A. P. & ELLINGTON, C. P. 1997a The mechanics of flight in the hawkmoth Manduca Sexta. I. Kinematics of hovering and forward flight. *Journal of Experimental Biology* **200**, 2705–2722.

WILLMOTT, A. P. & ELLINGTON, C. P. 1997b The mechanics of flight in the hawkmoth manduca sexta II. Aerodynamic consequences of kinematic and morpholofical variation. *Journal of Experimental Biology* **200**, 2723–2745.

WOJCIK, C. J. & BUCHHOLZ, J. H. J. 2012 The dynamics of spanwise vorticity on a rotating flat plate. In *50th AIAA Aerospace Sciences Meeting*.

WONG, J. G., KRIEGSEIS, J. & RIVAL, D. E. 2013 An investigation into vortex growth and stabilization for two-dimensional plunging and flapping plates with varying sweep. *Journal of Fluids and Structures* pp. 1–12.

WOOTTON, R. J. 1981 Support and deformability in insect wings. *Journal of Zoology* **193**, 447–468.

WU, J. Z., VAKILI, A. D. & WU, J. M. 1991 Review of the physics of enhancing vortex lift by unsteady excitation. *Progress in Aerospace Sciences* **28** (2), 73–131.

YOUNG, J., WALKER, S. M., BOMPHREY, R. J., TAYLOR, G. K. & THOMAS, A. L. R. 2009 Details of insect wing design and deformation enhance aerodynamic function and flight efficiency. *Science* **325** (5947), 1549–1552.

ZANKER, J. M. 1990 The wing beat of Drosophila Melanogaster. I. Kinematics. *Philosophical Transactions of the Royal Society B: Biological Sciences* **327** (1238), 1–18.

ZHAO, L., DENG, X. & SANE, S. P. 2011a Modulation of leading edge vorticity and aerodynamic forces in flexible flapping wings. *Bioinspiration & Biomimetics* **6** (3), 036007.

ZHAO, L., DENG, X. & SANE, S. P. 2011b Trailing edge flexion influences leading edge vortices and aerodynamic forces in flapping wings. In *49th AIAA Aerospace Sciences Meeting*.

ZHAO, L., HUANG, Q., DENG, X. & SANE, S. P. 2010 Aerodynamic effects of flexibility in flapping wings. *Journal of the Royal Society: Interface* **7** (44), 485–497.